LASER DOPPLER VELOCITY AND VORTICITY MEASUREMENTS IN TURBULENT SHEAR LAYERS

Thesis by

Daniel Bernard Lang

In Partial Fulfillment

of the Requirements for the Degree of

Doctor of Philosophy

California Institute of Technology

Pasadena, California

1985

(Submitted November 12,1984)

Dedicated to my parents,

Leonard L. and Regis C. Lang

ACKNOWLEDGEMENTS

This project required the assistance of many people, whose aid was essential, and I would now like to thank these people. I appreciate the help of Mr. Herb Gaebler, who helped with the construction of the overhead assembly, and Mr. Jack Kingan who, along with Mr. Gaebler, helped run the FSWT facility. I am thankful for the aid of Dr. Manooch Koochesfahani, who designed and built the shear layer insert. I would also like to thank the many other people who assisted me; Mr. Harry Hamaguchi for his excellent photography, Mrs. Betty Wood for her fine draftsmanship, Mr. Clarence Hemphill for his electrical work, and the Aeronautics Machine Shop, including Mr. George Lundgren, Mr. Howard McDonald, Mr. Robert Seguine, and Mr. George Willson. I am also grateful for the aid of Mrs. Linda Malaby, who helped with the typing of the thesis.

Last, but not least, special thanks goes to my advisor, Dr. Paul Dimotakis, who helped define the goals of the project and provided me with much assistance and advice over the course of the project. The financial support of the Fannie and John Hertz Foundation and the California Institute of Technology is gratefully acknowledged. This project was supported by the NSF and AFOSR.

ABSTRACT

A Laser Doppler Velocimeter (LDV) system was developed to measure the instantaneous spanwise vorticity, $-\omega_z$, in a turbulent shear layer. It was necessary to design and fabricate the LDV optics and processing electronics, as no commercially available LDV systems met the specifications of measuring the velocity at four closely spaced points to the requisite accuracy. Measurements were also made of the instantaneous u, v, u', v' and $-u'v'$. The instantaneous vorticity was processed to obtain an estimate of its probability density function, from which the mean and rms values were estimated. It was also possible to separate the irrotational fraction of the flow ($-\omega_z \approx 0$) from the rotational (intermittent) fraction of the flow ($-\omega_z \neq 0$). The development of the intermittency profiles, based on vorticity, as a function of the downstream distance from the splitter plate was studied. A notable feature is that the vorticity is found to have values opposite the mean sense of rotation, i.e., $-\omega_z(t) < 0$, a significant fraction of the time. Additionally, a detailed study was performed to evaluate the approximation of $-\partial v/\partial x$, in terms of various local temporal derivatives $\partial v/u(y)\partial t$. The optimum choice for u(y) can be found and is influenced by the relative local convection velocities of the small and large scale structures.

TABLE OF CONTENTS

LIST OF FIGURES

LIST OF SYMBOLS

Symbol	Description
$B_1 - B_{10}$	curve fit parameters, equation 3.2
C	total input capacitance, Appendix D.1
d_o	diameter of core of vortex
e_a	amplifier input noise voltage, Appendix D.1
f	bandwidth in Hz, Appendix D.1
G	amplifier gain, Appendix D.1
h	spacing between opposite focal volumes
i_a	amplifier input noise current, Appendix D.1
I_L	photodiode leakage current, Appendix D.1
I_S	signal current, Appendix D.1
i_t	total noise current, Appendix D.1
k	Boltzmann's constant, Appendix D.1
ℓ	fringe spacing of focal volume
N_{max}	maximum number of fringes in a burst, Appendix D.3
N_{min}	minimum number of fringes in a burst, Appendix D.3
p	pressure
q_e	electronic charge, Appendix D.1
r	velocity ratio, U_2/U_1
Re	Reynolds number
Re_{δ_ω}	Reynolds number based on δ_ω, $\frac{\Delta U\ \delta_\omega}{\nu}$
R_L	load resistance, Appendix D.1

s	standard deviation
s_m	standard deviation of the mean
T	absolute temperature, Appendix D.1
t_n	time of n^{th} zero crossing, Appendix D.3
t_n	time of n^{th} velocity measurement, Appendix F
u	local U velocity, also $(u_1 + u_2)/2$
U_c	large scale convection velocity, $(U_1 + U_2)/2$
U_{cm}	$(U_1 + U_m)/2$
U_m	minimum $\bar{u}$ velocity in the profile
U_{opt}	optimum velocity for "frozen" convection approximation
u_w	wake component of velocity profile, equation 3.2
u_1	velocity measured by upper focal volume, Figure 1.1
U_1	high speed free stream U velocity
u_2	velocity measured by lower focal volume, Figure 1.1
U_2	low speed free stream U velocity
u'	U velocity fluctuation from mean, $u - \bar{u}$
$-\overline{u'v'}$	Reynolds stress
v	local V velocity
v_{corr}	corrected V velocity data, equation 3.6
V_L	level crossing threshold voltage, Appendix D.2
V_{max}	large particle rejection voltage, Appendix D.2
v_1	velocity measured by right focal volume, Figure 1.1
V_1	high speed free stream V velocity
v_2	velocity measured by left focal volume, Figure 1.1
V_2	low speed free stream V velocity

v'	V velocity fluctuation from mean, $v - \overline{v}$
x	streamwise coordinate, Figure 4.8
x_o	virtual origin of shear layer
y	transverse coordinate, Figure 4.8
y_c	center of step velocity profile, equation 3.1a
y_h	Y position at upper or lower focal volume, equation 3.2
y_m	Y position of minimum of $\overline{u}$, where $\overline{u} = U_m$
y_t	Y position of center of profile, equation 3.2
y_o	virtual origin of shear layer
z	spanwise coordinate
α	angle between laser beams
Δf	frequency difference, Appendiix C
δu	measurement error in U component velocity
ΔU	velocity difference, $U_1 - U_2$
ΔU_m	velocity difference, $U_1 - U_m$
δv	measurement error in V component velocity
$\delta \omega$	measurement error in vorticity
δ_ω	vorticity thickness of shear layer
ϵ	ratio test criterion, Appendix D.3
η	similarity variable, $(y - y_o)/(x - x_o)$
θ	integral thickness, equation 3.1
θ_1	momentum thickness of high speed boundary layer
λ	wavelength of laser light
ν_D	Doppler frequency
ρ	density of working fluid (water)

τ	average time between LDV measurements
τ_f	full width of filter profile at 1/e points
τ_n	time between zero crossings, Appendix D.3
τ_s	time between samples of uniformly sampled data
ϕ	rotation to correct V velocity data, equation 3.6
ω	frequency in radians/sec, Appendix D.1
$-\omega_z$	spanwise (z) component of vorticity
$-\omega_{zo}$	mean vorticity at centerline of shear layer
ω_o	vorticity in core of vortex
DMA	direct memory access
FET	field effect transistor, Appendix D.1
FIFO	first in, first out buffer
FSWT	free surface water tunnel
h.s.	high speed side
LDV	laser Doppler velocimeter
l.s.	low speed side
RMS	root mean square (about the mean)

CHAPTER 1

INTRODUCTION

1.1 Background

One of the most exciting recent developments in the field of fluid mechanics and turbulence in particular has been the realization that a turbulent flow field is not an isotropic random mess that can only be described in a stochastic sense. Experimental results in the last few years indicate that within the obvious randomness of turbulence there exist flow patterns and large scale structures that appear dominant in determining the overall characteristics of such flows. A notable example can be found in the discovery that the turbulent free shear layer is inhabited by a more or less organized vortical structure (Brown & Roshko 1971, Brown & Roshko 1974, Winant & Browand 1974, Roshko 1976, Dimotakis & Brown 1976, Konrad 1976, Browand & Weidman 1976, and subsequently others).

This discovery is responsible for a radical change of our conception of turbulence. Within what would classically have been considered the "turbulent region" of the flow we are now forced to differentiate between the large scale structures that drive the turbulence and a portion of the fluid that is irrotational and passively driven. This distinction is not new conceptually (Corrsin & Kistler 1955) and is presently reflected in measurements of the

"intermittency" of the flow. Such measurements are implemented, at present, by sensing some component of the velocity vector, computing a time derivative of the velocity signal, and generating an intermittency signal when the derivative exceeds a predefined trigger threshold. This technique has yielded valuable results to date, but the changing outlook of turbulent flow identifies serious shortcomings with this type of measurement.

The prevailing view of turbulence (Tennekes & Lumley 1972, Townsend 1976) assumed the existence of a time and space varying interface boundary that separates a relatively simply connected turbulent region from the outer irrotational flow. The velocity fluctuations were considered to be essentially confined within the region enclosed by this turbulent - non turbulent interface boundary. It was, conceptually at least, a simple matter to recognize the passage of this boundary over a given point by placing a single hot wire anemometer at that point and identifying the interior of the turbulent region with the presence of the velocity fluctuations. The difficulty arises because it appears that the interior of the turbulent region is considerably more complicated than earlier views may have led us to believe. It is safe to say that the incursions of irrotational fluid into the turbulent region are to be associated with the full spectrum of scales present in the flow. Such a picture would suggest that it may be inappropriate to speak of a turbulent - non turbulent interface that separates the outer irrotational flow from the inner turbulent

flow (Roshko 1976, Dimotakis & Brown 1976, Falco 1974, Willmarth & Bogar 1977, Dimotakis et al. 1983).

In addressing this difficulty, one is forced to re-examine whether intermittency is the proper tool for probing turbulent shear flows. The dynamics of turbulent shear flow appear to be determined by large scale flow structures, so an investigation of these flows requires a tool that is capable of probing the large scale flow structures. It appears that the structures in turbulent shear flow that have been identified or are suspected to exist are vortical and unsteady in nature. This suggests the use of the instantaneous vorticity as a quantity that is more closely coupled to the dynamics of the flow. In fact, the instantaneous vorticity can be used to determine which parts of the flow are irrotational and which parts are turbulent (vortical or intermittent). Consequently, it was decided to measure the instantaneous vorticity for what is perhaps the best understood shear flow, the two-dimensional shear layer.

1.2 Attempts to Date

At least 3 different techniques to measure one or more components of the instantaneous vorticity have been used in the past by various experimenters. These three methods are:

1. A physical probe consisting of rotating vanes,
2. A direct optical probe using a flow seeded with spherical particles having embedded reflectors,

and,

3. Multipoint measurements using hot wires that estimate the circulation around a closed loop.

Each method has its own set of advantages and disadvantages, but they all have problems that have prevented them from becoming general purpose tools.

1.2.1 Rotating Vane Probe

The simplest technique is a physical probe containing vanes that rotate with the vorticity (McCormak et al. 1968, Holdeman & Foss 1975, Wigeland et al. 1978). In the absence of bearing friction, the vanes should rotate with an angular velocity equal to 1/2 the component of vorticity parallel to the axis of rotation. The angular rotation of the vanes can be detected by an optical detector, or in the work of Wigeland et al. (1978), by using a hot wire probe downstream of the vanes to detect the passage of the wakes from the vanes. Operational difficulties include nonlinear response, requiring calibration, and finite response time. The most serious limitation, however, is the requirement that the probe be placed parallel to the flow, limiting the measurement to the streamwise component of vorticity. In the case of the shear layer, the spanwise component of vorticity is of greater fundamental interest, especially before the transition to 3-dimensional turbulence.

1.2.2 Direct Optical Probe

The direct optical probe involves seeding a flow with small spherical particles that have small mirrors embedded in them and using a laser beam as the probe (Frish & Webb 1981). The small spherical particles will rotate with an angular velocity equal to 1/2 the local vorticity vector. A particle containing an imbedded mirror will reflect the laser beam when the particle passes through it. While the particle rotates within the laser beam, the angle of the reflected beam will change at twice the rotation rate of the particle. A major limitation of this technique is the requirement that the indices of refraction for the fluid and the particles must be matched in order to avoid refraction at the fluid/particle interface. Since the particles have an index of refraction of 1.49, this eliminates the use of water as the working fluid. The second major limitation is the relatively low sampling rate. Only about 4% of the reflections from the particles are intercepted by the detection optics, necessitating a very high seeding density (several percent by volume) to obtain an adequate data rate. The high seeding density restricts the extent to which a laser beam can propagate in the flow and limits the technique to flows near a surface, such as the boundary layer, as opposed to the shear layer.

1.2.3 Multiple Hot Wires

One method for measuring a time resolved component of the vorticity is to measure the velocities for at least three non-collinear (but coplanar) points and estimating the circulation of the area enclosed by the points by the method of finite differences. Prior attempts have been made to measure the time resolved vorticity using hot wires. The first effort was by Kovasznay (1954) using a Wheatstone bridge of four hot wire probes. A theoretical analysis using hot wire probes was made by Wyngaard (1969). Other attempts were made by Foss (1976), Kastrinakis et al. (1979), Foss (1979), Foss (1981), and Vukoslavčević & Wallace (1981). These prior efforts, based on hot wires, have had limited success due, in part, to mutual interference effects between the probes. Good spatial resolution requires close spacing of the probes, but close spacing of the probes causes the flow seen by the downstream probes to be disturbed by the upstream probe wakes. A second difficulty is associated with the resolution that a heat transfer gauge (hot wire) can measure a selected velocity component in fully developed turbulent flow. These methods require that the difference in velocity, as measured by different hot wire probes, be statistically significant, a specification that in practice, in view of the resolution limitations, restricts the potential of such techniques.

1.3 The Laser Doppler Method

It was decided to use the method of measuring the velocities of at least 3 non-collinear (but coplanar) points and estimating the circulation, since this method is the most general and gives the instantaneous u and v velocities as a side benefit. It order to avoid the problem of probe wakes, it was decided to use a non-intrusive means of measurement, specifically, the laser Doppler velocimeter (LDV), which a careful feasibility analysis had indicated was also capable of overcoming the velocity measurement resolution restrictions of heat transfer gauge systems.

It was decided to use a four point measurement volume (rather than a three point measurement volume) because the transmitting and receiving optics are simpler for the four point measurement volume. The four point measurement volume also simplifies mathematical analysis and improves accuracy over a three point measurement volume. The geometry of the measurement volume is shown in Figure 1.1. The vorticity is obtained by the following approximation:

$$-\omega_z = \frac{\partial u}{\partial y} - \frac{\partial v}{\partial x} \approx \frac{u_1 - u_2}{h} - \frac{v_1 - v_2}{h} \quad . \tag{1.1}$$

The spacing between the focal volumes, h, could be varied from 1 mm to 4 mm and was set to approximately 1.9 mm for the measurements reported here. Shown also in Figure 1.1, superimposed on the measurement geometry, is the outline of the silicon quadrant detector used to detect the scattered light collected from the focal volumes by the

receiving optics (one quadrant per focal volume).

The random sampling nature of the laser Doppler velocimeter was overcome by using a sampling rate that was high compared to the reciprocal of the flow transit time through the measurement volume

$$\tau^{-1} \gg \frac{\bar{u}}{h} = \frac{\overline{u_1} + \overline{u_2}}{2h} \quad . \tag{1.2}$$

The average time between measurements is τ, and the local mean velocity of the flow is $\bar{u}$ ($u = (u_1 + u_2)/2$). Finally, data were uniformly sampled in time and then digitally filtered by convolving the uniformly sampled data with a Gaussian filter kernel having a full width at the 1/e points of $h/\bar{u}$. Note that the full width of the Gaussian filter kernel is large compared to the uniform sampling interval. The algorithm is slightly modified from the one used by Koochesfahani et al. (1979) to give greater accuracy at low data rates and to avoid having to subtract the mean from the data before filtering. This permits an optimization of the incoming data rate with respect to the desired signal-to-noise ratio of the measured velocity components and also permits a graceful solution to the problem of evaluating the four velocities at the same instants in time for the purposes of estimating the vorticity with the aid of equation 1.1. See Appendix F for a more detailed discussion of the algorithms used for the data reduction.

CHAPTER 2

EXPERIMENTAL FACILITY AND INSTRUMENTATION

This research was conducted in the Free Surface Water Tunnel (FSWT) of the Hydrodynamics Lab at Caltech. Figure 2.1 shows an overview of the experimental setup including:

1. Free Surface Water Tunnel (FSWT) test section
2. Shear layer insert
3. Laser Doppler Velocimeter optical system
4. Signal processing electronics
5. Data acquisition system.

2.1 Free Surface Water Tunnel

The GALCIT Free Surface Water Tunnel (FSWT) was used for the experiment because it provides a large test section (20" wide by 20" deep by 8 feet long) and a steady continuous flow. Figure 2.2 (Ward 1976) shows a diagram of the entire facility, of which only the initial contraction (nozzle) and test section (working section) are visible in Figure 2.1. Figure 2.3 (Ward 1976) shows the test section in greater detail. Note that the boundary layer skimmer was removed for this experiment, since it interfered with the shear layer insert. The boundary layer from the upper surface of the Free Surface Water Tunnel was not important since it was well separated from the mixing layer region. The walls of the test section are made out of lucite

(plexiglas), allowing access to the test section using Laser Doppler Velocimeter techniques. The test section has a pair of air bearing surfaces at the top of the vertical lucite walls. The air bearing surfaces allow even a heavy apparatus (1000 lbs.) equipped with air bearings to be easily moved along the length of the test section (in the streamwise direction).

The facility can be operated at velocities ranging from below a centimeter per second to 7.6 meters per second. It is also equipped with a continuously running filter that removes debris and algae from the water. It was necessary initially to filter the water completely and then turn the filter off for the duration of each run, adding a seeding agent (3μm Al_2O_3) in order to have sufficient scattering particles of approximately uniform size for the laser Doppler velocity measurements.

2.2 Shear Layer Insert

The Free Surface Water Tunnel (FSWT) generates a highly uniform flow throughout the test section away from the wall boundary layers. A recent velocity survey of the tunnel by H. Gaebler and Dr. M. Koochesfahani is shown in Figure 2.4. Since the object of the present research involved the study of a shear layer, an insert was designed and placed in the upstream portion of the test section (see diagram in Figure 2.5 and photograph in Figure 2.6). In order to avoid the instantaneous streamwise velocity reversal that has been documented to

occur in high velocity ratio shear layers (Dimotakis et al. 1981), a new insert was designed and built by Dr. M. Koochesfahani with a design velocity ratio of the order of 2 to 1. The insert follows the design of Dimotakis & Brown (1976) and occupies the first 30 inches of the test section, leaving 66 inches of the test section downstream of the splitter plate for the resulting shear layer to develop. It should be noted that while an instantaneous streamwise velocity component reversal could be accommodated by Bragg cell shifting all four pairs of beams of the LDV system (see discussion below), it was decided to utilize a 2:1 shear layer in the interest of simplifying the LDV system for this first set of vorticity measurements.

The insert contains a curved piece of lucite that accelerates the flow below it, and decelerates the flow above it. A perforated plate and a screen placed in the upper part of the flow is responsible for a head loss that matches the Bernoulli pressure drop in the lower part of the flow. This equalization is necessary to maintain the incoming dividing streamline approximately horizontal to avoid separation near the curved plate leading edge and produce a well-behaved dividing streamline at the splitter plate trailing edge (see also discussion in Dimotakis & Brown 1976). A splitter plate with a trailing angle of 6.5 degrees is attached to the trailing edge of the curved piece of lucite. The angle on the high speed side is 2.0 degrees, and the angle on the low speed side is 4.5 degrees. This choice of angles makes the V velocity components on the high and low speed sides just after the

splitter plate approximately equal and opposite. The resulting shear layer has a velocity ratio of between 2.0 to 1 and 2.1 to 1. The velocity ratio decreases slightly as the velocity is increased due to the weak Reynolds number dependence of the perforated plate and screen pressure coefficients. See Appendix A for additional details on the shear layer insert and the resulting flow quality.

2.3 Three-axis Positioner and Overhead Assembly

The LDV system is mounted on a overhead assembly that, in turn, is mounted on a three-axis positioner (see diagram in Figure 2.7 and photograph in Figure 2.8). The three-axis positioner is mounted on top of the Free Surface Water Tunnel (FSWT) test section using a set of air bearings.

2.3.1 Three-axis Positioner

The three-axis positioner (manufactured by Mc. Bain Instruments, designed and supervised by Prof. D. Coles) allows movement of the entire overhead/LDV assembly in increments of .001 inches under either manual control or remote control from a computer (through an IEEE-488 interface, designed and built by Mr. R. Morrison). The three-axis positioner has a range of movement of 18 inches in the x direction (streamwise), 12 inches in the y direction (transverse, also across the shear layer), and 12 inches in the z direction (spanwise, across the tunnel). When a range of travel greater than 18 inches was needed in

the x direction, the air bearings allowed the three-axis positioner to be easily moved to a new x location. Mounting the positioner on top of the FSWT test section also has the advantage of minimizing positioning errors and vibrations of the assembly relative to the FSWT test section. An obstruction above the FSWT test section limited the measurement range in the x direction to a maximum of 39 inches downstream of the splitter plate. A pair of air cylinders on the three-axis positioner counter-balanced the static weight of the overhead assembly (250 pounds) for vertical movement.

2.3.2 Overhead Assembly

The overhead assembly has the shape of a capital Greek Π and is attached to the three-axis positioner at the top center of its horizontal section. The two vertical arms of the overhead assembly straddle the FSWT test section. The bottom of one arm carries the receiving optics and photodetector assembly. The bottom of the other arm carries part of the transmitting optics. The laser is mounted approximately at the top center of the overhead assembly to place the weight of the laser as close to the center of mass of the overhead/three-axis positioner assembly as practical. The first part of the transmitting optics is also placed on top of the overhead assembly in order to minimize weight at the bottoms of the arms. This decreases the moment of inertia of the vertical arms and keeps the resonant frequencies high to maximize vibrational damping of the whole assembly.

The overhead assembly was made out of plywood because wood is fairly light, has a low thermal expansion coefficient, and has good damping properties. The crossbeam is made out of 3/4 inch thick plywood in the form of a square tube 13 inches on a side. The vertical arms are also 13 inches square, but use plywood 1/2 inch thick. The crossbeam also incorporates an internal reinforcing bracket made out of aluminum at the point where the crossbeam attaches to the three-axis positioner. The wood was assembled using waterproof epoxy and then the entire structure was sealed using three coats of polyurethane to seal out moisture in order to avoid the dimensional sensitivity of wood to humidity.

2.4 Laser Doppler Velocimeter System

No commercially available Laser Doppler Velocimeter (LDV) system was capable of generating the four focal volumes needed for measuring vorticity so it was necessary to design and fabricate the LDV system to the requisite specifications. The need for a high signal-to-noise ratio dictated the use of a dual beam forward scattering optical system. Four pairs of beams are generated from an Argon Ion laser by a set of cube beam splitters and diffraction gratings. Each pair of beams is used to measure the velocity at one of the four points, as shown in Figure 1.1. A quadrant detector is used to detect the light from the four focal volumes (one quadrant per focal volume). A pair of Bragg cells is used to shift the frequency of the beams used for the V velocity measurements, allowing measurement of the direction of the V

velocity as well as the magnitude. See Appendix B for more details on the laser, transmitting optics, and receiving optics. A phase locked loop frequency synthesizer, described in Appendix C, is used to generate the frequencies for the Bragg cells.

2.5 LDV Signal Processing Electronics

A block diagram of the LDV signal processing electronics is shown in Figure 2.9 and a photograph is shown in Figure 2.10. The output from each quadrant detector is amplified by a low noise amplifier. Since no standard photodiode amplifier provided a satisfactory signal-to-noise ratio, a low noise transimpedance amplifier was designed and built (see Appendix D.1). The signals are then high pass filtered to remove the pedestals from the Doppler bursts, using standard Krohn-Hite model 3202 variable filters. The two U channels are then fed into an analog multiplexor. A considerable amount of electronics is saved by sharing one low-pass filter, analog processor, and digital processor with both U channels. Likewise, one set of electronics is shared by both V channels. The low-pass filters are also Krohn-Hite model 3202's.

Figure 2.11 shows two photographs of the high- and low-pass filtered analog signals, showing the signal quality attainable (and necessary for vorticity measurements). The upper photograph shows individual traces of the u_1 (upper trace) and u_2 (lower trace) channels. The lower photograph shows individual traces of the u_1

(upper trace) and v_1 (lower trace) channels (note the significantly higher frequency of the v channel).

The high- and low-pass filtered signals are then sent to the analog signal processors. The main functions of the analog signal processors are to apply the analog validation tests to the incoming signal and convert the signal to a digital form for subsequent processing by the digital timing circuitry. The analog processor requires that the signal exceeds a certain level before it is accepted, and detects dropouts so that erroneous measurements are not made. The digital processor measures the elapsed time and number of cycles in the LDV burst. The digital processor also applies a cycle by cycle ratio test to the signal to provide an additional safeguard against erroneous measurements. The output of the digital processor is fed to a microcomputer controlled data acquisition system for subsequent recording and processing. The need to process four LDV channels with a data rate high compared to the large scale velocity fluctuations and provide extensive validation tests on the Doppler signal ruled out the use of commercial LDV processors. Additionally, experience with commercially available LDV processors suggests that the level of expected measurement accuracy per particle is of the order of 1-3% ; too high for the present application. The analog and digital processors were designed and fabricated and are described in greater detail in Appendices D.2 and D.3 respectively.

2.6 Free Stream Channel

In addition to the four main LDV channels, there is a fifth channel that monitors the free stream velocity. This channel is used to remove the effect of slow variations in the velocity of the FSWT during the course of a run, which may last several hours, by normalizing the four main channel velocities by the concurrent running average of the free stream channel velocity. The fifth channel uses an avalanche photodiode, a transimpedance amplifier, a high-pass filter, and a low-pass filter like the other channels. Since only the mean velocity of the fifth channel is needed, a phase locked loop is used to track the Doppler frequency for the fifth channel. The output frequency of the phase locked loop is measured by a programmable counter in the microcomputer based data acquisition system. This provides the mean frequency (proportional to mean velocity) at two second intervals for use in normalizing the measurements from the four main channels.

2.7 Data Acquisition

A data acquisition system, based on a Digital Equipment Corporation (DEC) LSI-11/23 microcomputer, was used to record the LDV data, control the experiment, and perform preliminary data processing. A photograph of the data acquisition system is shown in Figure 2.12. The DEC RT-11 operating system was used because it is a single user operating system optimized for real time use. RT-11 allows on-line program development, high speed double buffered I/O (one buffer can be

filled with new data while the other buffer is written to disk), and contiguous disk files.

The LDV digital processor is interfaced to a high speed (12 megabytes/sec) I/O bus called the device bus. The device bus, in turn, is interfaced to the data acquisition system by a bi-directional DMA interface (Peritek DMAL-11) that allows automatic setting of the LDV processor modes as well as regular data acquisition. See Appendix E for more details on the data acquisition system and the device bus.

An Andromeda PRTC-11 programmable real time clock card is used to measure the frequency of the phase locked loop utilized to monitor the free stream velocity component.

A high speed Winchester disk (80 megabytes unformatted storage capacity, 1.2 megabytes/second peak transfer rate) was used to record the data. A dual floppy disk drive was used to transfer the data from the LSI-11/23 to a PDP-11/44 based computer for subsequent data processing after the completion of a run.

The LSI-11/23 microcomputer has a graphics terminal (Televideo 950 with a Selanar graphics board) to allow display of the data in real time. This was used primarily to assure that everything was set up correctly, as final data processing was done on the PDP-11/44. A four color plotter (Hewlett Packard HP9872) connected to the LSI-11/23 by an

IEEE-488 interface allowed generation of hard copy plots during the course of the run for additional monitoring purposes.

CHAPTER 3

MEAN PROFILE MEASUREMENTS

Data were acquired for several different velocities and for both laminar and turbulent initial boundary layers on the high speed side of the splitter plate. For a turbulent boundary layer on the high speed side, the flow was tripped using a trip wire located 8.2 cm upstream of the trailing edge of the splitter plate on the high velocity side. The boundary layer on the low speed side was laminar for all the measurements. Data were acquired for the following runs (Runs 1 through 6, in order):

1. U_1 = 41 cm/sec, laminar boundary layer, broad velocity defect on low speed side,
2. U_1 = 40 cm/sec, laminar boundary layer, shear layer insert modified to reduce velocity defect on low speed side for this and all subsequent runs,
3. U_1 = 40 cm/sec, laminar boundary layer, cover placed on top of free surface water tunnel for this and all subsequent runs,
4. U_1 = 42 cm/sec, turbulent boundary layer, 1.19 mm (3/64") diameter trip wire,
5. U_1 = 71 cm/sec, laminar boundary layer,

and,

6. U_1 = 71 cm/sec, turbulent boundary layer, 0.79 mm (1/32") diameter trip wire.

U_1 is the free stream velocity on the high speed side of the shear layer and U_2 is the free stream velocity on the low speed side of the shear layer. The larger diameter trip wire was necessary at the lower velocity (U_1 = 40 cm/sec) in order to ensure reliable tripping of the high speed boundary layer. See Appendix F for details on the data processing algorithms.

The data for the six runs can be presented in tabular form as shown below.

Run #	U_1 cm/sec	U_2 cm/sec	θ_1 cm	x_o cm	$d\theta/dx$	Re_{δ_ω} x=99cm
1	41.4	20.0	.073	-3.3	.0172	17,900
2	39.9	19.2	.073	-37.5	.0096	13,500
3	39.9	19.4	.073	-30.1	.0100	13,100
4	42.2	20.3	.150	-27.2	.0093	12,700
5	70.5	35.6	.056	-14.0	.0116	22,000
6	71.4	36.2	.107	-11.3	.0106	21,000

The momentum thickness of the high speed side boundary layer is θ_1 , x_o is the x-coordinate of the virtual origin, and Re_{δ_ω} is the Reynolds number based on the vorticity thickness, δ_ω. The growth rate of the

integral thickness, $d\theta/dx$, is based on the data at $x = 30$ or 33 cm and $x = 99$ cm.

3.1 Growth of Shear Layer

An integral thickness was used for comparing the growth rate of the shear layers. Computing the integral thickness was complicated by the fact that $\bar{u}$ dips below U_2 over part of the shear layer profile for the x positions located a short distance downstream of the splitter plate trailing edge (see Figures 3.3 through 3.8). The initial shear layer profile at the trailing edge of the splitter plate can be considered to be a superposition of an ideal shear layer profile and a wake from the splitter plate. A velocity profile downstream of the splitter plate trailing edge is considered to have a wake component if the minimum $\bar{u}$ velocity, U_m, is less than the low speed free stream velocity, U_2. The integral thickness, θ, is given by the following integral

$$\theta = \int_{y_m}^{\infty} \left[\frac{1}{4} - \left(\frac{\bar{u} - U_{cm}}{\Delta U_m} \right)^2 \right] dy = \int_{y_m}^{\infty} \left(\frac{U_1 - \bar{u}}{\Delta U_m} \right) \left(\frac{\bar{u} - U_m}{\Delta U_m} \right) dy , \quad (3.1)$$

where y_m is the y location for which $\bar{u} = U_m$, $\Delta U_m = U_1 - U_m$, and $U_{cm} = (U_1 + U_m)/2$. There are two limiting cases for this integral thickness equation. The first case is when the wake component goes to zero, giving $U_m \to U_2$, $U_{cm} \to U_c$, $\Delta U_m \to \Delta U$, and $y_m \to -\infty$. This gives the integral thickness equation for the conventional shear layer, defined by Winant & Browand (1974). The second case is when $U_m \to 0$ and

$\Delta U_m \rightarrow U_1$, giving the well known momentum thickness equation for the boundary layer.

Figure 3.1 shows the integral thickness as a function of distance downstream of the splitter plate for the 4 runs at $U_1 = 40$ cm/sec. Note that Runs 2 & 3 differ only in that a cover was placed on top of the free surface water tunnel in contact with the water to eliminate the effect of free surface waves for Runs 3 on up. These data indicate that the cover had a fairly small effect. The non-tripped cases take longer to reach similarity, but, once similarity is reached, grow at the same rate as the tripped case. Figure 3.2 shows the results for the case of $U_1 = 71$ cm/sec. Again, the tripped case reaches similarity sooner than the non-tripped case. Note also that the flow reaches similarity sooner for $U_1 = 71$ cm/sec than for $U_1 = 40$ cm/sec.

Figures 3.3 through 3.8 show the $\overline{u}$ velocity profiles a short distance downstream of the splitter plate for the 6 runs. Note that the profile for Run 1 is 2.79 cm downstream of the splitter plate while the profiles for the other runs are 1.93 cm downstream of the splitter plate. The wake component is still visible for all these figures. The wake component for Run 1 is partially filled in due to the larger measurement distance used for Run 1 (2.79 cm vs. 1.93 cm). Run 1 shows a broad (3 cm) velocity defect of approximately 5 cm/sec on the low speed side. This velocity defect was reduced by approximately 1/2 in both width and amplitude, as shown in Runs 2 through 6, by modifying

the insert as described in Appendix A. The wake component has completely disappeared from the $\overline{u}$ velocity profile at x = 15 cm downstream of the splitter plate and does not reappear farther downstream for Runs 2 through 6. The $\overline{u}$ velocity profile for Run 1 has a wake component at x = 2.79 cm, x = 15 cm, and x = 30 cm but not at x = 61 cm or x = 99 cm.

The rest of the thesis will concentrate on the results from Run 6 because Run 6 exhibits a linear growth profile and space and time constraints preclude showing the results of all the runs.

3.2 $\overline{u}$ Profile Measurements

Figure 3.9 shows a $\overline{u}$ velocity profile (U_1 = 40 cm/sec, tripped boundary layer) plotted in similarity coordinates. The circles represent the measuring point closest to the high speed side (u_1 channel) and the squares represent the measuring point closest to the low speed side (u_2 channel). The solid curve plotted through the points was obtained by applying a non-linear least squares fit to the data. The parametric form used is

$$u = B_5 \tanh\left[B_2 y_t + B_3 y_t^{3.2} \right] + B_6 + u_w , \quad y_t < 0 \qquad (3.2a)$$

$$u = B_5 \tanh\left[B_2 y_t + B_4 y_t^{3.2} \right] + B_6 + u_w , \quad y_t > 0 \qquad (3.2b)$$

$$\text{where} \quad u_w = B_{10} \exp\left[-\left((y_h + B_8)/B_9\right)^2 \right] , \qquad (3.2c)$$

$$y_t = y_h + B_1 \quad , \tag{3.2d}$$

$$y_h = y + B_7 \quad \text{for } u_1 \quad , \tag{3.2e}$$

$$y_h = y - B_7 \quad \text{for } u_2 \quad , \tag{3.2f}$$

and tanh is the hyperbolic tangent. B_1 through B_{10} are the adjustable parameters used by the non-linear least squares fit routine. The wake component, u_w, was only used for the first three x locations for Run 1 and for the first x location (1.93 cm) for Runs 2 through 6, as the rest of the $\overline{u}$ data did not show a wake component. Note that the y separation between the u_1 and u_2 measuring points is $h = 2\,B_7$ and is determined to high accuracy from the non-linear least squares fit. The separation between v_1 and v_2 is the same as the separation between u_1 and u_2 to within a few percent as ensured by the grating that splits the two v channels and the grating that splits the two u channels both of which are scribed from the same master grating. The grating used in these experiments (150 lines/inch) gives a value for h of 1.9 mm.

Figure 3.10 shows the root mean square (RMS) u velocity fluctuations for the same conditions as Figure 3.9. Again, the circles represent the u_1 channel and the squares represent the u_2 channel. The maximum RMS fluctuation is about 0.15 of ΔU. The error bars are derived by splitting the record into 8 equal time intervals and computing the RMS for each interval. See Appendix F.3 for additional details on computing the error bars. If the error bar is smaller than the symbol size, the error bar was not plotted. The error bar

computations were also carried out for Figure 3.9, but the error bars were always smaller than the symbol size for this case.

3.3 $\overline{v}$ Profile Measurements

Figure 3.11 shows the $\overline{v}$ velocity profile (same conditions as Figure 3.9) plotted in similarity coordinates. The squares represent the v_1 channel measuring points and the circles represent the v_2 channel measuring points. The solid curve is derived from the curve fitted to the $\overline{u}$ velocity profile (equation 3.2) and the time averaged continuity equation using the assumption of similarity. The similarity parameter is

$$\eta = \frac{y - y_o}{x - x_o} \quad , \tag{3.3}$$

where x_o, y_o is the virtual origin, as determined from the data. The points at $x = 30$ or 33 cm and $x = 99$ cm are used to determine the virtual origin (see Figure 3.1). The virtual origin for Run 6 is $x_o = -11.3$ cm, $y_o = 0.76$ cm. The time averaged continuity equation in similarity coordinates (assuming two-dimensionality) is

$$-\eta \frac{d\overline{u}}{d\eta} + \frac{d\overline{v}}{d\eta} = 0 \quad , \quad \text{or} \quad \frac{d\overline{v}}{d\eta} = \eta \frac{d\overline{u}}{d\eta} \quad . \tag{3.4}$$

Integrating the continuity equation over η gives

$$\overline{v} = \int_{-\infty}^{\eta} \eta \frac{d\overline{u}}{d\eta} \, d\eta + V_2 \quad , \tag{3.5}$$

where V_2 is the boundary condition as $\eta \to -\infty$ ($\bar{v} \to V_2$ as $\eta \to -\infty$). The integral of the continuity equation fixes the velocity difference,

$$V_1 - V_2 = \int_{-\infty}^{\infty} \eta \frac{d\bar{u}}{d\eta} d\eta \quad , \tag{3.5a}$$

but not the value of V_2. The value of V_2 is determined by the requirement that the Reynolds stress integral approach zero as $\eta \to \infty$ (see section 3.5 on the Reynolds stress). Once the value of V_2 is known, the value of V_1 follows from equation 3.5a.

The V axis of the LDV system differed from the true V axis by about half a degree (~ 0.01 radian). Consequently, it was necessary to apply a rotation to the measured V channel data in order to get the best fit between the measured V channel data and the solid line derived from the $\bar{u}$ profile and the continuity equation.

$$v_{corr} = v\cos\phi + u\sin\phi \approx v + u\phi \tag{3.6}$$

In this equation, ϕ was obtained using a least squares fit between the measured data and the curve derived from the $\bar{u}$ profile.

The error bars in Figure 3.11 are computed as described in Appendix F.3. This computation only accounts for the finite sample error (error due to a finite measurement time interval). For the $\bar{v}$ velocity data, there is another source of error caused by the

relatively low optical quality of the lucite walls used in the tunnel. This source of error was reduced as much as practical (see Appendix B.2), but could not be completely eliminated. The residual error causes some of the data points to miss the curve by more than the computed error bar size.

Figure 3.12 shows the RMS v velocity fluctuations. Note that the RMS v velocity fluctuations are about 40% less than the RMS u velocity fluctuations at this location.

3.4 Vorticity Profile Measurements

Figures 4.18 through 4.22 show the mean vorticity profiles for different x locations for Run 6. The circles represent the measured data, with error bars plotted if the error bar size is greater than the symbol size. The solid line was derived from equations 1.1 and 3.2 with the help of similarity. The squares, representing the rotational component of vorticity, will be explained in section 4.3. Expressing equation 1.1 in similarity coordinates and time averaging gives

$$-\overline{\omega_z} = \frac{\partial \bar{u}}{\partial y} - \frac{\partial \bar{v}}{\partial x} = \frac{1}{x - x_o}\left[\frac{d\bar{u}}{d\eta} - \eta\frac{d\bar{v}}{d\eta}\right] . \qquad (3.7)$$

Multiplying by $x - x_o$ and eliminating $\bar{v}$ by using the continuity equation (3.4) gives

$$-\overline{\omega_z}(x - x_o) = (1 + \eta^2)\frac{d\bar{u}}{d\eta} = \frac{d\bar{u}}{d\eta} . \qquad (3.8)$$

The η^2 term can be ignored since $\eta < .06$ over the region of interest.

The error caused by the relatively low optical quality of the lucite walls also appears in these data, causing some of the free stream data points to vary slightly from the zero value. See Chapter 3.3 and Appendix F.3 for more details.

3.5 Reynolds Stress Profile Measurements

Figures 3.13 through 3.16 show the Reynolds stress profiles for different distances downstream of the splitter plate for Run 6. The Reynolds stress is $-\overline{u'v'}$, where $u' = u - \bar{u}$ and $v' = v - \bar{v}$. The Reynolds stress is normalized by $100/\Delta U^2$ for these figures. The solid curve is obtained by integrating the time averaged momentum equation (assuming similarity). The time averaged (2-dimensional) momentum equations in similarity coordinates are

$$\text{x)} \quad -\eta\frac{d}{d\eta}\left(\bar{u}^2 + \overline{u'^2}\right) + \frac{d}{d\eta}\left(\bar{u}\bar{v} + \overline{u'v'}\right) = \eta\frac{d}{d\eta}\left(\frac{p}{\rho}\right) \qquad (3.9a)$$

$$\text{y)} \quad -\eta\frac{d}{d\eta}\left(\bar{u}\bar{v} + \overline{u'v'}\right) + \frac{d}{d\eta}\left(\bar{v}^2 + \overline{v'^2}\right) = -\frac{d}{d\eta}\left(\frac{p}{\rho}\right) . \qquad (3.9b)$$

Combining equations 3.9a and 3.9b and eliminating the p/ρ terms gives

$$\eta\frac{d}{d\eta}\left[\bar{u}^2 - \bar{v}^2 + \overline{u'^2} - \overline{v'^2}\right] = \left(1 - \eta^2\right)\frac{d}{d\eta}\left[\bar{u}\bar{v} + \overline{u'v'}\right] . \qquad (3.10)$$

Rearranging terms, we have

$$(1-\eta^2)\frac{d}{d\eta}\overline{u'v'} =$$

$$(\eta^2-1)\frac{d}{d\eta}\overline{u}\,\overline{v} + \eta\frac{d}{d\eta}(\overline{u}^2 - \overline{v}^2) + \eta\frac{d}{d\eta}(\overline{u'^2} - \overline{v'^2}) \quad (3.11)$$

$$\frac{d}{d\eta}\overline{u}\,\overline{v} = \overline{u}\frac{d\overline{v}}{d\eta} + \overline{v}\frac{d\overline{u}}{d\eta} \quad (3.11a)$$

$$\eta\frac{d}{d\eta}(\overline{u}^2 - \overline{v}^2) = 2\eta\overline{u}\frac{d\overline{u}}{d\eta} - 2\eta\overline{v}\frac{d\overline{v}}{d\eta} \; . \quad (3.11b)$$

Using the continuity equation to replace $\frac{d\overline{v}}{d\eta}$ by $\eta\frac{d\overline{u}}{d\eta}$ and combining terms gives

$$(1-\eta^2)\frac{d}{d\eta}\overline{u'v'} = (1+\eta^2)(\eta\overline{u} - \overline{v})\frac{d\overline{u}}{d\eta} + \eta\frac{d}{d\eta}[\overline{u'^2} - \overline{v'^2}] \; . \quad (3.12)$$

Dividing by $(1-\eta^2)$ and integrating over η then yields

$$\overline{u'v'} = \int_{-\infty}^{\eta}\frac{1+\eta^2}{1-\eta^2}(\eta\overline{u} - \overline{v})\frac{d\overline{u}}{d\eta}\,d\eta$$

$$+ \int_{-\infty}^{\eta}\frac{\eta}{1-\eta^2}\frac{d}{d\eta}[\overline{u'^2} - \overline{v'^2}]\,d\eta + C \; . \quad (3.13)$$

The constant C can be determined by noting that $\overline{u'v'} \to 0$ as $\eta \to -\infty$. When integrating equation 3.13, $\overline{v}$ is obtained from equation 3.5. The boundary condition for equation 3.5, V_2, is adjusted to satisfy the boundary condition for equation 3.13, $\overline{u'v'} \to 0$ as $\eta \to +\infty$. The contribution to $\overline{u'v'}$ by the $[\overline{u'^2} - \overline{v'^2}]$ term in equation 3.13 can be seen to be less than 1% of the total and was not included in the calculation of the solid line in Figures 3.13 through 3.16.

For Figure 3.13, the shear layer is not fully developed, and the measured Reynolds stress is somewhat low compared to the calculated Reynolds stress. For Figures 3.14 through 3.16 the agreement between the measured and calculated Reynolds stress is quite good except that one point in Figure 3.16 appears to be anomalously high.

CHAPTER 4

VORTICITY MEASUREMENTS

4.1 Measurements of Vorticity vs. Time

Figures 4.1 through 4.3 show plots of the four filtered velocity components (u_1, u_2, v_1, and v_2) and the vorticity ($-\omega_z$) as a function of time, for x = 76.2 cm downstream of the splitter plate. The data in Figure 4.1 were recorded on the low speed edge of the shear layer ($\eta = -.0464$), the data in Figure 4.2 were recorded slightly closer to the centerline ($\eta = -.0319$), and the data in Figure 4.3 were recorded near the centerline ($\eta = -.0087$). For the upper pair of lines, the solid line is the time trace of u_1 while the line consisting of dashes and dots represents u_2. For the middle pair of lines, the dotted line represents v_1 and the dashed line represents v_2. For the lower pair of lines, the solid line represents the computed $-\omega_z$ and the straight dashed line is $-\omega_{zo}$, the mean vorticity at the centerline of the shear layer. The following features can be seen in the data:

1. The peak-to-peak fluctuation amplitude of the instantaneous vorticity is many times the mean vorticity.
2. There are intervals of zero vorticity (irrotational flow) even during times when the four velocity components are fluctuating.

3. There are significant negative excursions in the instantaneous vorticity, $-\omega_z$ (many excursions last several times as long as the transit time through the measurement geometry).

The first observation can also be inferred from the fact that the RMS vorticity is 1.2 to 2.8 times the mean vorticity (the ratio increasing as one goes downstream). See Figures 4.7 through 4.11 for RMS vorticity data and Figures 4.18 through 4.22 for mean vorticity data. At first glance, the existence of negative excursions in $-\omega_z$ may seem rather surprising. The mean vorticity, $-\overline{\omega_z}$, is greater than zero in the fully developed portion of the shear layer, but as can be seen in Figure 4.12, in the initial portion of the shear layer, $-\overline{\omega_z}$ is less than zero on the low speed side due to the low speed boundary layer shed from the splitter plate. The low speed boundary layer can give rise to "cells" of negative vorticity that can persist for some distance into the shear layer. In other words, the flow downstream of the splitter plate can be viewed as the "superposition" of a pure wake and pure shear (see Chapter 3.1). The wake part contributes vorticity of both signs, which, from the study of wake flows, one could argue should persist for large distances downstream. In addition, there may be production of negative vorticity in the shear layer proper after the flow becomes three-dimensional.

Figures 4.4 through 4.6 show time traces of the vorticity, $-\omega_z$, and the product, $-u'v'$, for the same locations as the data in Figures 4.1 through 4.3 respectively. The upper solid line represents $-\omega_z$, the straight dashed line is $-\omega_{zo}$, and the lower solid line represents $-u'v'$. The following features can be seen in these data:

1. The vorticity data are characterized by much higher frequencies than the $-u'v'$ data.
2. There are significant excursions in $-u'v'$, even when $-\omega_z$ is nearly zero, and vice versa.
3. There is no obvious simple relationship between the vorticity data and the $-u'v'$ data.

4.2 Vorticity Histograms

The vorticity vs. time data were processed to generate histograms of the vorticity. The bin size of the histograms was chosen to be small compared to the measurement resolution of the vorticity data. Figure 4.13 shows a vorticity histogram for the low speed side free stream at $x = 76.2$ cm downstream of the splitter plate. The width of the free stream histogram is a consequence of the finite resolution of the LDV measurement process. In order to reduce the effects of noise, the histograms were digitally filtered using a Gaussian filter envelope in a manner similar to the digital filtering of the velocity vs. time traces. The histograms were filtered using a filter width one-half the width of the unfiltered free stream histogram. A filter width of

one-half the width of the free stream data was chosen as a compromise between resolution and noise. The filtering process decreases the amplitude and increases the width of the free stream histogram by a factor of 1.12, as shown in Figure 4.14. Note that the histogram has a very nearly Gaussian profile and is centered about zero.

Figure 4.15 shows a filtered vorticity histogram on the low speed side part way into the shear layer, and is from the same record as the data shown in Figure 4.2 (Figure 4.2 shows only a small portion of the data; the record is about 20 seconds long). Note that the filter width is one-half the width of the unfiltered free stream histogram. Here, we see a large Gaussian spike centered about zero that represents the irrotational component of the flow. We also see a broader, but lower amplitude, non-Gaussian distribution, not centered about zero, that represents the rotational (vortical) component of the flow. Figure 4.16 shows a vorticity histogram near the centerline of the shear layer (same record as for Figure 4.3). This is similar to Figure 4.15 except that the amplitude of the Gaussian spike (representing the irrotational flow) is much smaller, and the amplitude of the broader profile (representing the rotational flow) is much larger. Note that the width of the Gaussian spike representing the irrotational component of the flow remains relatively constant throughout the shear layer.

4.3 Intermittency

One item of interest is the intermittency factor, which is defined as the fraction of the time that the flow is turbulent. Most prior measurements of the intermittency factor (see Demetriades 1968, Wygnanski & Fiedler 1969, and Wygnanski & Fiedler 1970) used a time derivative of the velocity signal to establish the presence of turbulent flow. A typical derivative used is $(\partial^2 u'/\partial t^2)^2 + (\partial u'/\partial t)^2$ to minimize the contribution of low frequency fluctuations caused by potential flow. The differentiated signal is fed to a Schmidt trigger with a fixed threshold. It is often necessary to vary the threshold as the probe is moved across the flow.

Since it is now possible to measure instantaneous vorticity (as averaged over a small measurement volume), an independent method of measuring the intermittency is available. The non-turbulent flow (irrotational) has zero vorticity, while the turbulent flow is characterized by a non-zero, fluctuating component of vorticity. This suggests the use of the fraction of the time that the flow has non-zero vorticity as a measure of intermittency. In the case of the vorticity histograms shown (Figures 4.14 - 4.16) this means separating the narrow Gaussian representing the irrotational flow from the rest of the histogram. It is important to note that only $-\omega_z$ is measured here, while, strictly speaking, irrotational flow requires that $\omega_x^2 + \omega_y^2 + \omega_z^2 = 0$. This limitation is overcome, in part, by using only the excess probability of $-\omega_z = 0$ due to irrotational flow (see

Figure 4.17 and the next subsection).

4.3.1 Determining the Irrotational Component of the Flow

Since the narrow Gaussian representing the irrotational component of the flow has a sharp radius of curvature near the origin, it was decided to curve fit the second derivative of a Gaussian to the second derivative of the filtered vorticity histogram. This means that the curve representing the rotational component of the histogram (histogram minus the fitted Gaussian) will have a small second derivative in the vicinity of the origin, giving a smoothly varying curve. The second derivative of the filtered vorticity histogram was approximated by the method of finite differences. At first, the second derivative of the Gaussian was computed analytically. The curve representing the rotational component of the histogram was somewhat irregular in the vicinity of the origin, where the irrotational component (Gaussian) had been subtracted out. This irregularity was due to errors from estimating the second derivative of the histogram by the method of finite differences. Since the histogram consists of discrete points, it was not possible to compute the second derivative of the histogram analytically. The solution to this problem was to use the method of finite differences to estimate the second derivative of the Gaussian as well. Both the Gaussian and the histogram are evaluated at the same points so the errors resulting from the method of finite differences cancel to highest order. The result of the new procedure is a smooth curve for the rotational component of the vorticity in the vicinity of

the origin.

The results of the curve fit procedure are shown in Figure 4.17. The solid line represents the filtered vorticity histogram. The dashed line represents the Gaussian that was fitted to the histogram using the second finite differences. The ratio of the area under this curve to the total area of the histogram provides an estimate of the fraction of the time that the flow is irrotational. The filtering process decreases the amplitude and increases the width of the spike representing the irrotational component of the flow by the same amount, so that the area under the curve is not changed. The dotted line represents the histogram minus the Gaussian. The ratio of the area of this curve to the total area of the histogram is an estimate of the fraction of the time that the flow is vortical, and gives a measure of the intermittency.

Figure 4.21 shows the vorticity profile at $x = 76.2\,cm$ downstream of the splitter plate (fully developed shear layer). The circles represent the measured mean vorticity at each point. The solid line is the value of the vorticity computed from the mean U velocity profile using the continuity equation and assuming similarity. The squares represent the mean of the rotational component of the vorticity histogram (mean vorticity of the rotational fluid). The triangles represent the mean of the irrotational component of the vorticity histogram (mean vorticity of the irrotational fluid). Note that the

mean vorticity of the rotational fluid is nearly constant throughout the shear layer and is approximately equal to the the maximum of the mean vorticity in the layer. Likewise, the mean vorticity of the irrotational fluid is nearly zero throughout the shear layer, as would be expected if the measurements and the decomposition of the vorticity histogram were error-free.

Figure 4.26 shows the same vorticity profile normalized to unity. The circles and solid line are the same as in Figure 4.21. The pluses represent the intermittency obtained by dividing the area of the rotational component of the histogram by the total area of the histogram. It is interesting that the intermittency follows the normalized vorticity quite closely. This indicates that, for a fully developed shear layer, the variation in the mean vorticity is almost entirely due to the variation in the probability of observing turbulent flow and not due to a variation in the average vorticity in the turbulent portions of the flow.

4.3.2 Probability of Counter-rotating Flow

The histogram in Figure 4.17 shows that the instantaneous vorticity can have the opposite sign of the mean vorticity for a significant portion of the time. The rotational component of the vorticity histogram was integrated from $-\infty$ to 0 and normalized by the total area of the vorticity histogram to obtain the probability of flow counter-rotating to the predominant sense of rotation. Subtracting the

irrotational component from the histogram before integrating avoids including one-half the probability of irrotational flow in the probability of counter-rotating flow. The probability of counter-rotating flow is indicated in Figure 4.26 by the diamonds. The maximum probability of counter rotating flow is 0.30 and is observed at $(y-y_0)/(x-x_0) = -.02$. The total intermittency at this location is 0.96, so the probability of irrotational flow is estimated by this procedure to be 0.04 and the probability of flow rotating in the predominant sense of rotation is 0.66.

4.4 Variation of Intermittency with x

Figures 4.18 through 4.22 show the mean vorticity and the mean vorticity of the rotational fluid at x = 15 cm, 33 cm, 57 cm, 76 cm, and 99 cm downstream of the splitter plate, respectively. Figures 4.23 through 4.27 show the normalized mean vorticity, the probability of rotational flow (intermittency), and the probability of counter-rotating flow for the same x locations. At x = 15 cm (Figure 4.18), the mean vorticity of the rotational fluid (squares) is only slightly higher than the mean vorticity, and follows the mean vorticity fairly closely. As one goes farther downstream of the splitter plate, the curve representing the mean vorticity of the rotational fluid gradually flattens out, and becomes nearly independent of $\eta = (y-y_0)/(x-x_0)$ at x = 76 cm and 99 cm (Figures 4.21 and 4.22).

The first two x locations (Figures 4.23 and 4.24) show an excess in the intermittency (plus symbols). As one proceeds downstream, the excess intermittency gradually disappears, with the intermittency following the normalized mean vorticity very closely at x = 57 cm, 76 cm, and 99 cm (Figures 4.25 through 4.27). The variation of the mean vorticity of the rotational fluid and the excess intermittency at the first two x locations is due, at least in part, to vorticity from the high and low speed boundary layers and the resulting wake from the splitter plate. This effect is greatest on the low speed side, where approximately equal amounts of positive and negative vorticity can give rise to a large value of the intermittency and a nearly zero mean vorticity of the rotational fluid. The effect of the wake from the splitter plate is shown even more dramatically in the plots of the probability of counter-rotating flow (see Chapter 4.5).

The finite spatial and temporal resolution of the measurement process may be an additional contributing factor to the variation of the mean vorticity of the rotational fluid and the excess intermittency at the first two x locations. Since h ~ 2 mm (see Figure 1.1), the measurement averages the vorticity over a region on the order of 2 mm by 2 mm. The temporal resolution is equivalent to a spatial resolution on the order of 2 mm since the filter width is equal to the mean transit time through the measurement volume, i.e., $\tau_f = h/\overline{u}$. When the small scale is small compared to 2 mm, this will cause an excess in the measured intermittency because there will be times when the 2 mm

measurement volume will contain some vorticity whereas a smaller measurement volume would indicate irrotational fluid. Likewise, when the 2 mm measurement volume indicates rotational fluid, part of the fluid within the volume may actually be irrotational, giving a lower value for the mean vorticity of the rotational fluid. Doubling the filter width (approximately equivalent to increasing the length of the measurement volume to 4 mm) will cause slightly more irrotational fluid to be averaged with rotational fluid, and should give rise to an increase in the observed intermittency. Figures 4.28 through 4.32 represent the same set of data as Figures 4.23 through 4.27, except that the filter width has been increased by a factor of 2 to $\tau_f = 2h/\overline{u}$. At $x = 15$ cm (Figure 4.28) there was a slight increase in the intermittency, but for $x \geq 33$ cm (Figures 4.29 through 4.32), there was no significant change.

4.5 Variation of Counter-rotating Flow with x

Figures 4.23 through 4.27 show the probability of counter-rotating flow for $x = 15$ cm, 33 cm, 57 cm, 76 cm, and 99 cm, respectively. In Figure 4.23, the probability of counter-rotating flow reaches a peak of 0.29 on the low speed edge of the shear layer, while the maximum probability within the shear layer is only 0.22. This is caused by vortical fluid from the low speed boundary layer of the splitter plate (see Figure 4.12). As the shear layer develops, this counter-rotating fluid is gradually entrained within the shear layer, and the profile becomes symmetrical by $x = 57$ cm (Run 6, Figure 4.25). This can be

contrasted with the $\bar{u}$ profile, which becomes symmetrical by x = 15 cm for Runs 2 through 6 (see Chapter 3.1). The peak probability of counter-rotating flow within the shear layer gradually rises until it reaches a similarity value of 0.30 and remains at this level for the rest of the shear layer. Thus, it can be seen that the regions of counter-rotating flow persist throughout the shear layer even for the last x location (99 cm, Figure 4.27) measured.

Referring back to the initial velocity profile shown in Figure 4.12, it can be seen that the initial ratio of probabilities of fluid rotating with the predominant sense of rotation to fluid rotating against the predominant sense of rotation is approximately the same as the velocity ratio, $U_1/U_2 \approx 2.0$. The current data (Figures 4.23 through 4.27) suggest that the regions of counter-rotating flow do not decay significantly, or, at least, the decay is balanced by some sort of production term. The implications of this conclusion required a check to see if the regions of counter-rotating flow are not an artifact of the measurement process.

It is possible for a small vortex just outside the measurement geometry to give a measurement of opposite sign to the vorticity of the vortex. A simulation was undertaken to estimate the magnitude of this error (see Appendix F.5) and shows that the errors are quite small given the chosen filter width ($\tau_f = h/\bar{u}$) and the typical range of vortex sizes. The small residual error can be further reduced by

choosing the filter width to be $\tau_f = 2h/\bar{u}$. This will also reduce the LDV measurement error by a factor of $\sqrt{.5}$. Figures 4.28 through 4.32 represent the same set of data as Figures 4.23 through 4.27, except that the filter width was increased by a factor of 2 . The probability of counter-rotating flow was reduced from .30 - .31 to .28 - .30 for the last three x locations. The fact that increasing the filter width had such a small effect indicates that the majority of the negative excursions of vorticity extend over large spatial regions and are well above the measurement error. Increasing the filter width had a slightly larger effect for the first x locations, where the measured vorticity (positive and negative) has the largest amplitude. This indicates that the decrease in counter-rotating flow is due, in part, to the temporal averaging of legitimate vorticity fluctuations.

One major question remaining is whether this persistence of counter-rotating flow holds for other velocities and initial conditions. Figures 4.33 through 4.37 show results for runs 1 through 5, respectively (all for a velocity ratio of approximately 2 to 1). These figures show similar results and even show a slightly higher probability of counter-rotating flow for most of the runs (around .33 to .35). It cannot be determined from these data if the ratio of co-rotating flow to counter-rotating flow is approximately the same as the velocity ratio for other velocity ratios. Even though the intermittency and the probability of counter-rotating flow did not seem to be sensitive to the initial conditions, the growth rate was

sensitive to the initial conditions. Run 1 had a much higher growth rate than Runs 2 and 3 even though they had the same high speed boundary layer momentum thickness. Since Run 1 had a larger wake component (due to the increased low speed boundary layer momentum thickness), this suggests that the width of the wake at the trailing edge of the splitter plate may be as important in determining the downstream behavior of the shear layer as the initial high speed boundary layer momentum thickness (see Chapter 3.1).

CHAPTER 5

SPATIAL VS. TIME DERIVATIVES OF V

Most prior attempts to measure the vorticity have used hot wire probes (see Chapter 1.2). The term that gives the greatest difficulty is the $-\partial v/\partial x$ term in equation 1.1. The approximation of finite differences gives

$$-\frac{\partial v}{\partial x} \approx \frac{v_2 - v_1}{h} \quad . \tag{5.1}$$

The method of finite differences cannot be used with hot wires because the wake of the upstream probe interferes with the flow as seen by the downstream probe. Most hot wire measurements approximate the $-\partial v/\partial x$ term by using the Taylor hypothesis (Taylor 1938) which states that the temporal variation of the flow at a stationary point can be considered to be due to the convection of a "frozen" spatial pattern past that point with a mean velocity, $\bar{u}$. Use of the "frozen" convection approximation gives

$$\frac{\partial v}{\partial t} + \bar{u}\frac{\partial v}{\partial x} \approx 0 \quad , \tag{5.2a}$$

or

$$-\frac{\partial v}{\partial x} \approx \frac{\partial v}{\bar{u}\partial t} \quad . \tag{5.2b}$$

Other approximations used by researchers are

$$-\frac{\partial v}{\partial x} \approx \frac{\partial v}{u \partial t} \tag{5.2c}$$

and

$$-\frac{\partial v}{\partial x} \approx \frac{\partial v}{U_c \partial t} \quad , \tag{5.2d}$$

where $u = (u_1 + u_2)/2$ and $U_c = (U_1 + U_2)/2$ (convection velocity of large structures). U_c has been used for mixing layers where $U_2 = 0$ in order to avoid singularities when u or $\overline{u} = 0$.

5.1 Derivatives of v vs. time

For the first time, we have the ability to estimate the accuracy of the approximation in equation 5.2b by comparing $\partial v/\overline{u}\partial x$ with $(v_2 - v_1)/h$ from equation 5.1. We do not have the value of v at the center of the measurement geometry (see Figure 1.1) so it was necessary to generate v from v_1 and v_2. Rather than taking $v = (v_1 + v_2)/2$, the following equation was used:

$$v(t) = \frac{1}{2}\left[v_1\left(t + \frac{\tau}{2} \right) + v_2\left(t - \frac{\tau}{2} \right) \right] \quad , \tag{5.3}$$

where τ is the transit time based on the mean u velocity, $\tau = h/\overline{u}$.

Figure 5.1 plots the spatial and temporal approximations as a function of time. The approximation of finite differences, $(v_2 - v_1)/h$ (equation 5.1), is shown by the upper solid line. The "frozen" convection approximation, $\partial v/\overline{u}\partial x$ (equation 5.2b), is shown by

the dashed line. These two lines appear fairly similar and have the same main features, but there are regions where the two lines are significantly different, especially when the signal is rapidly fluctuating. The lower solid line shows the difference, $(v_2 - v_1)/h - \partial v/\bar{u}\partial x$, for better visualization.

Figure 5.2 is the same as Figure 5.1 except that the dashed line uses the approximation $\partial v/u\partial x$ (equation 5.2c). Again, the lower solid line shows the difference, $(v_2 - v_1)/h - \partial v/u\partial t$, for better visualization. The data for Figures 5.1 and 5.2 are very similar, meaning that the effect of using $\bar{u}$ or u is small compared to other error terms in the "frozen" convection approximation for a 2 to 1 shear layer.

5.2 Time Derivative Accuracy

A quantitative measure of the accuracy of using $\partial v/u\partial t$ in place of $-\partial v/\partial x$ can be derived by computing the root mean square (RMS) of $(v_2 - v_1)/h - \partial v/u\partial t$ normalized by the RMS of $(v_2 - v_1)/h$. This is plotted as a function of $\eta = (y-y_0)/(x-x_0)$ in Figure 5.3 (shown by the squares). If the two signals were completely uncorrelated, the normalized RMS would be equal to 1.414 (upper plot limit). If the two signals were completely correlated, the normalized RMS would be equal to 0 (lower plot limit). The circles are similar, except that they show the RMS of $(v_2 - v_1)/h - \partial v/\bar{u}\partial t$ normalized by the RMS of $(v_2 - v_1)/h$. This shows that the difference in using u or $\bar{u}$ in the

"frozen" convection approximation is negligible for a 2 to 1 shear layer.

The circles in Figure 5.4 are the same as the circles in Figure 5.3. The diamonds show the result when U_c is used (equation 5.2d). Using the convection velocity of the large scale structures, U_c, gives significantly poorer results, especially in the outer regions of the shear layer (away from the centerline).

5.3 Optimum U Velocity for Scaling

Instead of using $\overline{u}$ or U_c in the "frozen" convection approximation (equations 5.2b and 5.2d, respectively), it is possible to make U a variable, and find the fixed value of U as a function of y that gives the best fit to $(v_2 - v_1)/h$ (equation 5.1). The resulting value of U is called U_{opt} (note that U_{opt} is not a function of time). The root mean square (RMS) of $(v_2 - v_1)/h - \partial v/U_{opt}\partial t$ normalized by the RMS of $(v_2 - v_1)/h$ is indicated in Figure 5.4 by the triangles. For most of the points, the mean velocity ($\overline{u}$, indicated by the circles) works just as well as the optimum velocity, U_{opt}.

Perhaps of greater interest is a plot of U_{opt}, shown in Figure 5.5. The circles indicate the measured $\overline{u_1}$, while the squares indicate the measured $\overline{u_2}$. The solid line is a curve (hyperbolic tangent) fitted to the measured data points using a nonlinear least squares fit. The corresponding values of U_{opt} are indicated by the triangles. The

optimum velocity follows the mean velocity fairly closely, but has a slightly lower slope in the central region of the shear layer. Note that U_{opt} is a weighted measure of the average velocity of the structures (small and large). This means that the weighted average velocity of the structures is slightly less than the mean velocity, $\bar{u}$, on the high speed side of the shear layer and slightly greater than the mean velocity on the low speed side of the shear layer.

A particularly interesting feature is that U_{opt} approaches $U_c = (U_1 + U_2)/2$ just outside of the shear layer, then returns to $\bar{u}$ farther away from the shear layer. This effect can be explained by noting that the shear layer is composed of small scale structures that essentially move with an average velocity equal to the local mean, $\bar{u}$, and large scale structures that move with an average velocity equal to U_c. In the central region of the shear layer, the small scale structures have somewhat smaller amplitudes and much higher spatial and temporal frequencies than the large scale structures. Consequently, the small scale structures contribute the dominant portion of the $\partial v/\partial x$ and $\partial v/\partial t$ terms, causing U_{opt} to be weighted towards the velocity of the small scale structures. The large scale structures still contribute a small portion of the $\partial v/\partial x$ and $\partial v/\partial t$ terms, causing the slope of U_{opt} to be slightly lower than the slope of $\bar{u}$ in the central region of the shear layer. As one moves outside the shear layer, the induced velocities due to the small scale structures decay very rapidly. Since the induced velocities of the large scale structures

decay more slowly, the induced velocities of the large scale structures become the dominant term just outside the shear layer. This causes U_{opt} to bend towards the large scale convection velocity, U_c, in this region. As one continues to move farther from the shear layer, the induced velocities of the large scale structures continue to decay, leaving the free stream turbulence as the dominant term in the velocity derivatives. The free stream turbulence convects with a velocity very nearly equal to $\overline{u}$, so that, far away from the shear layer, U_{opt} approaches $\overline{u}$ once again.

These results are quite different from the conclusions of Zaman and Hussain (1981), who concluded that U_c was the optimum velocity to use in the temporal approximation (equation 5.2d). Zaman and Hussain, however, used phase-averaged data from a forced flow. Phase averaging reconstructs the large scale structures as a function of space and time but averages out the small scale fluctuations. The phase-averaged data of Zaman and Hussain indicate that the large scale convection velocity, U_c, is the best velocity to use for the large scale data, which is consistent with the results presented here. The phase-averaged data, however, fail to take into account that the small scale structures dominate the magnitude of the spatial and temporal derivatives when the flow is turbulent.

CHAPTER 6

CONCLUSIONS

A new flow diagnostic tool, an instantaneous vorticity meter, based on the Laser Doppler Velocimeter (LDV), has been built and successfully demonstrated. The vorticity meter measures the velocity at the four corners of a right angle diamond and estimates the circulation of the flow enclosed by the diamond. The utility of the instrument is further enhanced by the instantaneous u, v, and -u'v' data provided along with the instantaneous spanwise component (Z component) of vorticity.

The LDV vorticity meter was used to study what is perhaps the best understood shear flow, the two-dimensional shear layer. Despite the intensive prior research on the two-dimensional shear layer, the instantaneous vorticity data have revealed several new items that are crucial to a better understanding of the two-dimensional shear layer.

A summary of the results is presented below.

1. Use of the Laser Doppler Velocimeter avoids the probe interference effects and calibration problems that plague the users of hot wires.

2. Interpolating between random LDV data points and digitally

filtering the data yields the continuous data necessary for further processing.

3. It is possible to achieve a LDV signal of sufficiently high quality so that the vorticity can be computed with adequate precision even though the vorticity is computed from the difference of 4 large numbers. Achieving a sufficiently good LDV signal is mainly a matter of careful design and choosing the proper components for the optical subsystem and LDV signal processing electronics.

4. A large initial low speed side velocity defect in the shear layer profile increases the growth rate of the shear layer. At the farthest downstream location measured, there was no reduction in the increased growth rate relative to the growth rate for a small initial low speed side velocity defect.

5. Tripping the high speed boundary layer decreases the distance to establish similarity in the shear layer. Once similarity is reached, the growth rate appears to be the same for the tripped and non-tripped cases.

6. Increasing the velocity also decreases the distance to reach similarity.

7. The $\overline{u}$, $\overline{v}$, $\overline{\omega_z}$, and Reynolds stress profiles were plotted and shown to agree quite well with the results predicted using the $\overline{u}$ profile and similarity. The normalized Reynolds stress

profile was found to peak at about 0.010 to 0.013 for most of the data.

8. Plotting the instantaneous vorticity as a function of time shows that there are long intervals of zero vorticity (irrotational flow) coupled with bursts of highly fluctuating vorticity. The bursts of highly fluctuating vorticity can have short intervals of zero vorticity and also have significant intervals of counter-rotating flow (vorticity opposite the prevailing sign). The highly fluctuating nature of the vorticity is further demonstrated by plots showing the RMS vorticity to be 2.0 to 2.5 times the mean vorticity.

9. An investigation of the vorticity histograms shows that the histogram is composed of two parts: a relatively narrow Gaussian shaped peak due to the irrotational flow; and a low, but broader base due to the turbulent part of the flow. It is possible to separate the two components of the vorticity histogram by curve fitting a Gaussian profile to the irrotational peak of the histogram. The fractional area of the low, but broad base gives a measure of the time that the flow is rotational (turbulent or intermittent).

10. Plots of the intermittency and mean of the rotational (turbulent or intermittent) component of the vorticity histogram as a function of η show that, for a fully developed shear layer, the mean of the rotational component of the

histogram is nearly constant. The intermittency, on the other hand, follows the mean vorticity profile (normalized to unity) quite closely. This means that the variation in the mean vorticity is almost entirely due to the variation in the probability of observing turbulent flow and not due to a variation in the average vorticity in the turbulent portions of the flow.

11. Plots of the probability of $-\overline{\omega_z} < 0$ show that when the vorticity is not zero, there is a 1/3 probability that the flow is rotating opposite to the mean rotation (for a 2 to 1 shear layer). For the first downstream location, there is a considerable excess of counter-rotating flow on the low speed side of the shear layer. As one proceeds downstream, the counter-rotating fluid is entrained into the shear layer and becomes symmetrically distributed about the centerline. This counter-rotating flow persists to the farthest downstream location measured.

12. The initial velocity profile just after the splitter plate generates vorticity of both signs in the same ratio as the initial velocity ratio; that is, the probability of $-\overline{\omega_z} > 0$ divided by the probability of $-\overline{\omega_z} < 0$ is equal to U_1/U_2. This ratio is seen to remain constant even to the farthest downstream location measured for a two to one shear layer, demonstrating that the initial wake component of the shear

layer affects the behavior of the entire shear layer. This may explain, in part, the observed sensitivity of the shear layer to the initial conditions. It is not known if the ratio of probabilities of co-rotating flow to counter-rotating flow is the same as the velocity ratio for velocity ratios other than 2 to 1.

13. Many other researchers use the "frozen" convection approximation $-\partial v/\partial x \approx \partial v/(U\partial t)$, where U can be any of several different velocities. To test the accuracy of this approximation, a comparison was made between the spatial and time derivatives of the v velocity component. The best agreement was obtained by using u or $\overline{u}$ for U, but even for these the agreement was only fair.

14. The value of U that gave the best agreement between the spatial and time derivatives in the "frozen" convection approximation, U_{opt}, was plotted as a function of η along with $\overline{u}$. The optimum velocity was found to follow the local mean velocity fairly closely in the center of the shear layer, to bend towards the convection velocity just outside of the shear layer, and to approach the local mean again far away from the shear layer. These results can be best interpreted by noting that the shear layer is composed of small structures that move at the local mean velocity, $\overline{u}$, and large structures that move at the convection velocity, U_c. The small scale structures

dominate the derivative terms within the shear layer, while the large scale structures dominate just outside the shear layer, and free stream turbulence dominates far away from the shear layer. Since both the large and small structures are simultaneously present and have different propagation velocities, any velocity chosen for U in the "frozen" convection approximation is, at best, a compromise between the propagation velocities of the small and large scale structures.

APPENDIX A

SHEAR LAYER INSERT

The insert contains a curved piece of lucite that accelerates the flow below the curved piece of lucite, and decelerates the flow above it (see Figures 2.5 and 2.6). A curved perforated plate and a screen placed in the upper part of the flow equalizes the pressure drop above and below the curved lucite piece. The perforated plate is placed near the beginning of the expansion, just before the place where the flow would normally separate. The screen is placed just before the exit of the insert to help smooth out the flow. A splitter plate with a trailing angle of 6.5 degrees is attached to the trailing edge of the curved piece of lucite. The resulting shear layer has a velocity ratio of between 2.0 to 1 and 2.1 to 1 (the velocity ratio decreases slightly as the velocity is increased). Both the screen and the perforated plate were chosen to have an open area greater than 57% in order to avoid instability (jet coalescense, Loehrke & Nagib 1972) The perforated plate uses a hexagonal hole pattern with a hole diameter of 3.97 mm (5/32") and a hole spacing of 4.76 mm (3/16") for an open area of 62%.

The initial shear layer insert performed quite well, but there was a rather large velocity defect on the low speed side with a width of approximately 3 cm and an amplitude of approximately 5 cm/sec (see

Figure 3.3). This is due to the effect of the boundary layer on the low speed side of the curved piece of lucite. Dye injection tests show that the flow remains attached on the low speed side throughout the range of velocities used in the experiment. Nevertheless, the unfavorable pressure gradient causes the boundary layer to grow rapidly on the low speed side, and the screen near the exit of the shear layer insert is insufficient to completely fill in the resulting velocity defect.

The velocity defect on the low speed side was minimized by slightly enlarging the bottom two rows of holes in the perforated plate. The results, after drilling out the bottom two rows of holes, are shown in Figures 3.4 through 3.8. Note that the data for run 1 (Figure 3.3) is for an x location of 2.79 cm after the splitter plate and that the wake from the splitter plate has completely filled in at this x location. The data for runs 2 through 6 (Figures 3.4 through 3.8) are for an x location of 1.93 cm after the splitter plate, so the wake from the splitter plate has not completely filled in for runs 2 through 5.

APPENDIX B

LDV OPTICAL SYSTEM

B.1 Conventional LDV Systems and Performance

Conventional LDV system accuracy in practice is 1% to 3%, i.e., in steady laminar flow $\delta u/u \approx .01 - .03$. This is the case for several reasons:

1. Most lasers are intensity modulated by modal or plasma noise.
2. Most commercially available LDV optical systems have an unnecessarily large number of components, which leads to wavefront and fringe fidelity degradation and also causes alignment difficulties.
3. Photomultiplier tubes have relatively low quantum efficiencies and most photodiode amplifiers have excessive current noise which results in a low signal-to-noise ratio (see Appendix D).
4. Conventional LDV processors do not have adequate particle validation criteria, giving a high rate of erroneous measurements (see Appendix D).

The present work required accuracies approximately one order of magnitude higher, a fact which dictated substantial improvements in all of the problem areas listed above.

B.2 The Laser

An important requirement was a source of laser light with high spectral and spatial mode purity and sufficient intensity to give a good signal-to-noise ratio. From previous experience, about 5 mW per pair of beams was considered to be sufficient for a good signal-to-noise ratio at the operating velocities of interest here. Since there are 4 pairs of beams, this comes out to 20 mW total power at the focal volumes. To allow for losses in the transmitting optics (including the low efficiency amplitude gratings used) about 200 mW laser power was considered desirable. This power level dictated a low power argon ion laser.

The frequency spacing between longitudinal modes in a laser is $f = c/2\ell$ and is typically several hundred MHz for commercial lasers. This frequency is well above the Doppler frequencies of interest, but there are normally more than 2 longitudinal modes oscillating simultaneously. The frequency spacing between successive modes typically varies by 10-100 KHz. The resulting beat frequency between successive modes has been observed to amplitude modulate the output of He-Ne lasers, and causes interference with the desired Doppler signal. Consequently, a laser with an oven stabilized etalon was chosen.

The laser used was a Lexel model 85 argon ion laser with a line selecting prism and a temperature stabilized etalon. The laser was operated single line (514.5 nm), single mode, and produced a maximum of

300 mW under these conditions. At lower powers (less than 50 mW) some noise due to plasma oscillations was observed. Fortunately, the amplitude of this noise decreased rapidly with increasing laser power, and was not observed at the 200 mW operating power. The laser was operated in the constant light mode (output stabilized by using feedback from a photodiode) to minimize low frequency amplitude fluctuations.

B.3 LDV Transmitting Optics

The primary goal of the transmitting optical system was to generate the necessary 4 pairs of beams (2 for the U velocity and 2 for the V velocity) with as few optical components as practical in order to simplify alignment and minimize degradation of optical beam quality and coherence.

The first portion of the transmitting optics is located at the top of the overhead assembly and is enclosed in a lucite dust cover (see Figure B.3). The laser beam first passes through a long focal length collimating lens (1 meter focal length). The incoming beam is then split into 4 beams by a pair of cube beam splitters (see Figure B.1). The beam splitters are oriented so that the partially reflecting hypotenuse faces are parallel to and slightly offset from the incoming (horizontal) laser beam. The hypotenuse of one beam splitter is rotated +45 degrees from the vertical about an axis parallel to the axis of the laser beam. The hypotenuse of the other beam splitter is

rotated -45 degrees from the vertical about the same axis. The polarization of the incoming laser beam is vertical so the beam splitters are also oriented 45 degrees with respect to the polarization vector. This configuration produces 4 parallel beams situated at the 4 corners of a right angle diamond. Each beam of the vertical pair (to be used for the V velocity measurement) passes through a Bragg cell to shift its frequency. One Bragg cell generates a frequency shift of 40 MHz while the other Bragg cell generates a frequency shift of 40 MHz + Δf . Δf is typically on the order of a few hundred KHz. This allows measuring the direction as well as the magnitude of the V velocity. The 4 beams then pass through a set of 1 degree wedge prisms to allow fine adjustment of the orientation of the beams. The wedge prisms are also set to deflect the 4 beams up by approximately 1 degree. This upward deflection is removed by the next component, a large mirror, that reflects the beams downward to the bottom of the arm (see Figure B.1) This upward bias was added to all the beams because it is very difficult to adjust a pair of wedge prisms to give a deflection that is small compared to the deflection of one prism (one degree).

The rest of the transmitting optics is located at the bottom of the overhead arm (see Figures B.2 and B.3). This provides sufficient distance to allow masking out the undesired orders from the Bragg cells. The horizontal pair of beams passes through a horizontal set of Ronchi rulings (an amplitude transmission grating which was approximately 150 lines per inch in this experiment), and the vertical

pair of beams passes through a vertical set of otherwise identical Ronchi rulings. The beams are then reflected by a second mirror towards the test section perpendicular to the tunnel walls. Just before reaching the focusing lens, the zero, second, and higher order diffraction beams from the Ronchi rulings are masked out, leaving the desired first order beams. This generates two horizontal pairs of beams, each pair slightly divergent in the vertical direction, and gives rise to the two U velocity measuring locations separated by a vertical distance of approximately 2 mm as dictated by the Ronchi ruling line spacing. Likewise, the two vertical pairs of beams are slightly divergent in the horizontal direction, giving rise to the two V velocity measuring locations separated by the same distance. Finally, the beams pass through a corrected achromat lens and come to a focus in the mid-span of the test section. A corrected achromat was used to reduce spherical aberration (only the 514.5 nm line was used).

The laser was mounted parallel to the top of the overhead assembly so the polarization vector was perpendicular to the top of the overhead assembly. The cube beam splitters, however, are 45 degrees with respect to the top of the overhead assembly, so that the reflected beam undergoes a rotation of the polarization vector. The two vertical beams wound up with vertical polarization vectors. The horizontal beams wound up with polarization vectors 45 degrees from vertical and 90 degrees with respect to each other. In order to avoid signal degradation, a mica half-wave plate was placed in one of the horizontal

beams to rotate the polarization vector of that beam parallel to the first beam.

In analyzing the LDV data, a small amplitude vibration of around 35Hz was noted. The corresponding amplitude was around 10 μm. This frequency was too high to be in the main overhead structure. The transmitting optics were mounted on two aluminum plates, and the two mirrors were mounted near the edges of the plates. The small amplitude vibrations in the plates were being amplified by the mirrors because the angle of the reflected beams change by twice the change in the angle of the mirror, and because the small angular displacement was magnified by the relatively long distances involved. The upper plate of 1/2 inch thick aluminum overhangs the end of the horizontal crossbeam by about 7 inches. A pair of aluminum reinforcing braces was added as shown in Figure 2.4. The lower plate of 3/8 inch thick aluminum was replaced by two hollow aluminum tubes 1/8 inch thick and 2 inches square. These changes decreased the moment of inertia, thereby raising the resonant frequencies, and eliminated the vibration problem by increasing the effective damping.

One last problem had to do with the relatively low quality of the lucite windows available in the tunnel test section. The windows are 4.5 inches thick, and date from around 1950, and have their share of scratches and bulges. This resulted in a small scatter in the mean V velocity measurements (around 0.5%). Lucite has an index of refraction

of 1.49 while water has an index of refraction of 1.33. Consequently, the lucite/air interface is approximately 3 times as critical as the lucite/water interface. Problems at the lucite/air interface were minimized by placing a strip of 1/8 inch thick photographic quality plate glass over the lucite at each x measuring location, and filling the gap with an index matching fluid (light machine oil was used). Each strip of plate glass was long enough to accommodate the full Y travel of the three-axis positioner. This reduced the scatter in the V velocity data by about a factor of 2.

B.4 LDV Receiving Optics

The arrangement for the receiving optics is shown in Figure B.4. A photograph is shown in Figure B.5 (note that the direction of the light is from right to left in Figure B.5). The scattered light from the four focal volumes is collected by a pair of back to back achromats. Again, achromats are used to reduce spherical aberration. The direct beams are blocked by beam stops. The first lens is used to collect the spherically expanding scattered light and collimate it. The second lens takes the collimated light and focuses it back down. At the focal plane a mask is used to block most of the stray light scattered from the walls and from parts of the flow away from the focal volumes. A small biconvex lens then refocuses the scattered light onto the surface of a quadrant detector (manufactured by Centronic). The quadrant detector is a round chip of silicon that has been scribed into four 90 degree segments, each segment forming an independent photodiode

with its own output. Each segment receives the light from one focal volume (see Figure 1.1). Finally, the quadrant detector is housed in a shielded enclosure in close proximity to four transimpedance amplifiers, one amplifier for each output of the quadrant detector.

APPENDIX C

BRAGG CELL ELECTRONICS

C.1 Phase Locked Loop Frequency Synthesizer

The required frequency shift used for the V channels of the Laser Doppler Velocimeter was in the range of 100 KHz to 600 KHz depending on the flow velocity. The bias frequency was chosen so that the lowest V channel frequency was about 1.5 times the highest U channel frequency. This enabled removal of the residual crosstalk between the U and V channels (on the order of 1%) by electronic filtering. By nearly balancing the Bragg cell frequencies, a higher bias frequency was avoided since this would reduce the signal-to-noise ratio (the amplifier noise increases with frequency above 300 KHz) and would reduce the dynamic range of the V channel frequency.

The two Bragg cells (IntraAction Corp. model # ADM-40) for the V channels are optimized to operate around 40 MHz. The net bias frequency is the difference of the two Bragg cell frequencies. One Bragg cell was driven at a fixed frequency of 40 MHz by a crystal oscillator. The second Bragg cell was driven at a frequency of 40 MHz + Δf, where Δf is the net bias frequency. A phase locked loop frequency synthesizer was built that has two inputs, 40 MHz from the crystal oscillator and Δf from an external signal generator, and one output at 40 MHz + Δf. Any drift in the 40 MHz signal appears on both

Bragg cell signals, and consequently cancels out when the scattered light from each of the two beams heterodynes on the detector. A Hewlett Packard 3325A Frequency Synthesizer/Function Generator was used to produce the Δf signal, which, as a consequence, was known to a high degree of accuracy. (The HP 3325A has digitally programmable frequencies and an oven controlled crystal timebase.)

A diagram of the phase locked loop frequency synthesizer is shown in Figure C.1. A Voltage Controlled Oscillator (VCO) is used to generate a signal of frequency f_{out}. This signal and the 40 MHz reference signal are fed into a digital mixer. The output of the digital mixer is the difference signal, f_{out} - 40 MHz. The output of the digital mixer and the Δf signal from the HP 3325A frequency synthesizer are fed into a phase comparator. The error output of the phase comparator is filtered by a low-pass filter, and then used to control the frequency of the VCO, closing the loop. This forces the two signals at the inputs of the phase comparator to be of the same frequency, f_{out} - 40 MHz = Δf, or f_{out} = 40 MHz + Δf.

Finally, the two output signals (40 MHz and 40 MHz + Δf) are fed to a pair of Electronic Navigation Industries (ENI) Model 300L broadband RF power amplifiers and amplified to a power level of 2 watts each to drive the Bragg cells.

APPENDIX D

LDV SIGNAL PROCESSING ELECTRONICS

D.1 Low Noise Transimpedance Amplifiers

A silicon quadrant detector (Centronic model QD 50-2) was used to detect the scattered light from the 4 focal volumes, using one quadrant per focal volume (see Figure 1.1). The quadrant detector has a very high quantum efficiency of nearly 70% at 514.5 nm. The disadvantage of the quadrant detector utilized is that there is no amplification in the detector, and, consequently, the first stage of amplification must be very low noise in order to avoid a system limited by amplifier noise rather than shot noise.

The total input noise current, as a function of frequency, is given by the following equation for both amplifier circuits shown in Figure D.1.

$$i_t^2 = 2q_e[I_L + I_S] + i_a^2 + e_a^2[1/R_L^2 + (\omega C)^2] + 4kT/R_L \qquad (D.1)$$

i_t is the total noise current in Amps/$\sqrt{Hz}$. The first term on the right-hand side is the square of the shot noise (in Amps/$\sqrt{Hz}$), where q_e is the electronic charge, I_L is the leakage current of the photodiode, and I_S is the photoelectrically induced signal current. i_a is the

amplifier input noise current (in Amps/$\sqrt{Hz}$). e_a is the amplifier equivalent noise voltage (noise voltage at amplifier output with input shorted to ground divided by amplifier gain) in Volts/$\sqrt{Hz}$. The factor multiplying the e_a squared term represents the reciprocal of the input impedance squared, where R_L is the load resistance in ohms, ω is the frequency in radians/seconds, and C is the total input capacitance (photodiode + amplifier + stray capacitance). Finally, the $4kT/R_L$ term is the square of the Johnson noise current (in Amps/$\sqrt{Hz}$) of the load resistor, where k is the Boltzmann's constant, T is the absolute temperature, and R_L is the load resistance in ohms (the dynamic resistance of the photodetector is assumed to be much greater than R_L).

The first amplifier circuit shown in Figure D.1 is a conventional amplifier circuit while the second circuit is called a transimpedance amplifier (note that for a transimpedance amplifier, the gain must be negative). The two circuits give identical signal-to-noise ratios for the same value of R_L but the transimpedance configuration gives a much wider bandwidth. The bandwidth of the conventional amplifier is $f = 1/2\pi R_L C$ while the bandwidth of the transimpedance amplifier is $f = |G|/2\pi R_L C$ (-3db bandwidth). In the actual amplifier used, R_L is 1 megohm and the input capacitance is approximately 40 picofarads (most of the input capacitance is the capacitance of the photodiode). The corresponding bandwidth is approximately 4KHz for the conventional amplifier. For the transimpedance amplifier used, the measured bandwidth was 1.5MHz, an increase of nearly 400 times.

The contribution to the total noise current due to the photodiode leakage current is .057 picoamps/$\sqrt{Hz}$ for I_L = 10 nanoamperes. The amplifier used a field effect transistor (FET) at the input so the input noise current of the amplifier was negligible. The measured input noise voltage of the amplifier is 1.5 nanovolts/$\sqrt{Hz}$. Below $f = 1/2\pi R_L C$ (4 KHz) the equivalent noise current is (dividing e_a by R_L) $\approx$ .0015 picoamps/$\sqrt{Hz}$. Above $f = 1/2\pi R_L C$ the equivalent noise current is $\approx e_a 2\pi f C$ or .00038 f picoamps/$\sqrt{Hz}$ where f is the frequency in KHz. At 1 MHz this becomes .38 picoamps/$\sqrt{Hz}$. Finally, the Johnson noise current due to R_L is .13 picoamps/$\sqrt{Hz}$. In the absence of any illumination on the photodiode, the dominant term is the Johnson noise current due to R_L up to a frequency of about 350 KHz. Above 350 KHz, the $e_a 2\pi f C$ term is the dominant term.

The actual range of frequencies used in the experiment was from 20 KHz to 600 KHz. The intensity of the Doppler signal was generally high enough so that the $\sqrt{2eI_S}$ noise term (where I_S is the photocurrent due to scattered light) was the dominant term (typically 2 to 3 times the total of all the other noise terms). Consequently, the amplifier was not the limiting factor in the overall signal-to-noise ratio. It should be noted that the resulting signal-to-noise ratio was also better than what could be achieved by a photomultiplier tube detector since the quantum efficiency of the photodiode at the laser wavelength (70%) is significantly better than the quantum efficiency of standard photomultiplier tubes (normally between 12% and 20%).

D.2 Analog Processor Subsystem

The analog processor takes the filtered LDV signal, applies a set of analog validation tests to the signal, and converts the signal to a digital form for the digital processor. The analog processor can handle two independent LDV signals simultaneously, and by multiplexing upstream of the analog processor, 4 LDV signals can be accommodated (see Figure 2.9).

The analog tests must detect signal dropouts and multiple zero crossings due to high frequency noise. This is accomplished by the use of a 3-level crossing scheme (see Figure D.2). There is a positive level of amplitude $+V_L$ and a symmetric negative level of amplitude $-V_L$, where the voltage V_L can be adjusted according to the signal strength and desired data rate. The third level, for the present measurements, was set to zero volts (zero crossing level). The zero crossing output signal (digital) is generated from the zero crossings of the analog input signal and is of opposite polarity. Note that the negative slope of the analog input signal (positive slope of the zero crossing signal) is used for timing purposes. In addition, a valid data output signal (digital) is generated along with the zero crossing output signal. The analog signal must first cross the negative level, then cross the positive level before asserting the valid data signal at the next negative zero crossing of the analog input signal. If the analog signal fails to cross these two levels, the valid data signal is negated at the next negative zero crossing transition. Note that the

digital processor considers the first cycle preceding the assertion of the valid data output signal to be valid, and the first cycle preceding the negation of the valid data output signal to be invalid. Consequently, the valid signal is the portion of the analog signal burst that crosses all the level crossings between the first and last negative zero crossings.

A small amount of hysteresis (adjusted to 5% of V_L) prevents multiple zero crossings at low signal frequencies by small amounts of high frequency noise present on the signal. Noise less than 5% of V_L will be ignored, while noise in excess of this value will cause the valid data signal to go low.

Finally, the analog processor implements a large particle rejection capability. If the signal crosses the level $+V_{max} \gg +V_L$, then a large particle rejection signal is generated. This feature is valuable for measurements in air, but was not necessary in this experiment because of the seed particle size uniformity. Particle lag was not a problem with the 3μm Al_2O_3 particles used to seed the flow.

D.3 Digital Processor Subsystem

The digital processor receives the digital LDV and valid data signals from the analog processor. The digital processor measures the period and number of cycles in each LDV burst, applies a zero crossing time interval ratio test validation scheme to the signal, and sends the validated results to the data acquisition computer.

The digital processor contains two independent channels and is capable of simultaneous 2 channel measurements. For this experiment, however, the 4 LDV signals arise from 4 independent focal volumes. In the present experiments, the seed density was adjusted so that the probability of an acceptable scattering particle in a measuring volume was on the order of 5% to 10%. Consequently, since the probability of 4 different particles being present in 4 different focal volumes is very small, the data rate must be sufficiently high to permit the time history in each of the four velocity channels to be reconstructed with sufficient accuracy and time resolution. Since simultaneity is not required, it is possible to multiplex each processor channel between two LDV signals within the constraint of a sufficiently high data rate. To help achieve this goal, an adaptive multiplexing scheme was used. After a processor channel has completed a measurement, it switches to the other LDV channel. The processor then waits for the next 3 zero crossings. If the processor has not started processing a valid burst by then, it switches back to the first LDV channel and again waits for the next 3 zero crossings. In the absence of any valid signal, the

processor switches back and forth between the two LDV channels, seeking a valid burst. A test was carried out comparing the multiplexed and non-multiplexed data rates. The multiplexed data rate for one channel was found to be 62% of the non-multiplexed data rate for the same channel. The combined data rate for both channels of a multiplexed pair was 124% the data rate for a single non-multiplexed channel, giving an increase in net data rate of approximately 24% due to the adaptive multiplexing algorithm. Since there were two processors and each multiplexed between two signals, the total data rate for all 4 channels was approximately 62% of the data rate that would have been achieved at the same threshold settings using 4 simultaneous processors. Building 4 simultaneous processors would have increased the cost and construction time of the processing electronics considerably.

The processor measures the absolute time of each zero crossing (t_n) and computes the elapsed time $\tau_n = t_n - t_{n-1}$. The processor then applies a ratio test criterion on the elapsed time intervals (τ_n) on a cycle by cycle basis. This can be done for Doppler frequencies up to 12.5 MHz. For Doppler frequencies above 12.5 MHz, which, however, were not encountered in the present experiments, pre-scalers permit the application of the ratio test every other cycle, or every third cycle, etc.

The ratio test criterion is $|\tau_n - \tau_{n-1}| \leq \varepsilon\tau_n$, where ε is equal to 2^{-m}, and where m is an integer that can be selected to be between 1 and 8. For most of the data, m was set to either 3 or 4, giving a value of ε of 12.5% or 6.25%. If the ratio test fails on the n^{th} zero crossing, the $(n-1)^{th}$ zero crossing is considered by the processor to be the last validated zero crossing.

The processor generates a cumulative validation signal that is the logical "and" of all the individual validation signals (analog data valid, ratio test valid, and not analog large particle). When the cumulative validation signal becomes false, or when the number of validated cycles, N, exceeds a preset number, N_{max}, then the measurement is terminated. If the number of validated cycles, N, is greater than or equal to N_{min} ($N_{min} < N_{max}$) then the validated timing and cycle data for the burst are written into a First In First Out (FIFO) buffer. If the number of validated cycles is less than N_{min}, then the measurement is discarded. In either case, the processor switches channels and starts looking for the next LDV signal. N_{min} sets the minimum number of validated cycles needed for a measurement, while N_{max} prevents the processor from staying on one channel for too long in the event of a long burst.

The information written in the FIFO buffer includes:

1. the starting time of the validated burst,

2. the ending time of the burst,

3. the number of cycles in the burst,

4. and the LDV channel number of the burst.

The ending time of the burst has a sufficient number of digits (25 binary digits) so that the probability of clock overflow between measurements is negligible under proper operating conditions. This also allows the reconstruction of the absolute time of each particle scattering event.

Finally, a Direct Memory Access (DMA) interface reads the measurements from the FIFO buffer and writes it to the memory of an LSI-11/23 minicomputer.

APPENDIX E

DATA ACQUISITION SYSTEM

The data acquisition system is based on a Digital Equipment Corporation (DEC) LSI-11/23 microcomputer. A photograph of the data acquisition system is shown in Figure 2.12. The DEC LSI-11/2 microcomputer was chosen after an extensive survey of the small computer systems available at the time (1978). The LSI-11/2 was chosen because of the excellent software and hardware available for it. When the LSI-11/23 became available, the system was upgraded by a simple swap of the cpu boards. Most importantly, a wide selection of I/O devices from DEC and other manufacturers are available for the LSI-11 bus. A block diagram of the data acquisition system is shown in Figure E.1.

E.1 Operating System

The DEC RT-11 operating system was chosen because it is a single user disk based operating system optimized for real time use. A large number of languages are available for RT-11 including Fortran, C, and Pascal. Most of the program development was done in Fortran, with a small amount of assembly language used to interface to the non-standard I/O devices on the system.

RT-11 allows high speed double buffered I/O (one buffer can be filled with new data while the other buffer is written to disk), and contiguous disk files. This allowed the continuous recording of up to 120,000 points/record with each data point consisting of 4 words (2 bytes/word).

E.2 Unibus

A bus converter from Able Computer Technology was added to generate the Unibus from the LSI-11 bus. Having the Unibus available increases the number of I/O options while maintaining software compatibility with devices on the LSI-11 bus. In addition, the Unibus has a significantly higher bandwidth than the LSI-11 Bus. Currently, the Winchester disk controller and the memory are placed on the Unibus.

E.3 Device Bus

The LSI-11 bus has a relatively low bandwidth of 1.83 Megabytes/second. When the LDV digital processor was designed, I decided to interface it to an I/O bus of my own design called the Device Bus. The Device Bus has a bandwidth of 12 Megabytes/second and is optimized for I/O devices.

The central controller for the Device Bus performs interrupt arbitration and performs centralized DMA control for the Device Bus. When a slave device generates an interrupt, the controller services the

interrupt and performs any required DMA operations. Any DMA operations are to/from a second port on the controller, thus utilizing only one bus cycle per word transferred. In the case of the LDV processor, the controller reads the data from the LDV processor and writes it to the second port, which can be dual ported memory or another DMA interface. While the data transfer is proceeding, the controller can be arbitrating another interrupt request.

A high bandwidth was not necessary for my thesis research because the highest data rates encountered were on the order of 4000 points/second or 32,000 bytes/second. For my thesis research, the second port of the Device Bus controller was connected to a bi-directional DMA interface on the LSI-11 bus (Peritek DMAL-11). The Peritek DMA interface and the Device Bus controller also support a direct access mode from the LSI-11 bus to the Device Bus, allowing the LSI-11/23 cpu to manipulate the registers of devices on the Device Bus directly.

As additional LDV channels are added, or as the velocities are increased, the bandwidth of the LSI-11 bus will be exceeded. In addition, Mr. D. Kerns has designed and built a high speed A/D converter using a flash converter that operates up to 20 megasamples/sec. The A/D converter also interfaces to the Device Bus. In order to accommodate the higher bandwidths, it is planned to interface the Device Bus controller either to the Unibus or to a dual

ported memory. A Unibus DMA interface will allow a maximum transfer rate to memory of 4 megabytes/sec or a maximum transfer rate to disk of approximately 900 kilobytes/sec (limited by the speed of the disk).

E.4 IEEE-488 Bus

A Digital Equipment Corporation (DEC) IBV11-A generates the IEEE-488 bus from the LSI-11 bus. The IEEE-488 bus allows interfacing to a number of laboratory instruments such as programmable power supplies and function generators. The most frequently used IEEE-488 device is the HP-9872 four color plotter from Hewlett Packard. The three-axis positioner also has an IEEE-488 interface designed and built by Mr. R. Morrison, allowing direct computer control of the measurement location of the LDV optics.

E.5 Disk Drives

The data acquisition system currently has a Winchester disk drive and a dual floppy disk drive. The Winchester disk drive is a Control Data Corporation 9730-MMD (Mini-Module Drive) with an unformatted storage capacity of 80 megabytes (65 megabytes formatted). The peak transfer rate is 1.2 megabytes/second but formatting overhead and seek times limit the maximum average transfer rate to around 900 kilobytes/second. The disk controller is a Mini-Computer Technology SMC-11, and interfaces to the Unibus.

The dual 8 inch floppy disk drive is an AED6200-FD from Advanced Electronic Design. The dual floppy disk drive has a formatted capacity of 1.2 megabytes per drive (2.5 times the capacity of the DEC RX-02).

E.6 Other Peripherals

Other peripherals included on the data acquisition system are:

1. An Andromeda PRTC-11 programmable real time clock card,
2. A four line serial interface to a terminal and printer,
3. A Televideo 950 terminal with Selanar graphics board,
4. A Datasouth DS-180 dot matrix printer (180 cps.),
5. A Data Translation DT-2782 A/D converter (125 KHz),

and,

6. A Data Translation DT-3362 A/D converter (250 KHz).

Additional peripherals can easily be added as the need arises due to the multiple bus structure of the data acquisition system.

APPENDIX F

LDV DATA PROCESSING ALGORITHMS

F.1 Initial Processing of Raw Data

The raw data were recorded as a function of time for each of the 4 channels: u_1, u_2, v_1, and v_2. The data were recorded in real time using a high speed Winchester disk. Enough data were recorded at each (x,y) location to represent a minimum of approximately 50 large structures in the flow. After the completion of a run, the data were moved by floppy disk to a PDP-11/44 minicomputer running RSX-11M PLUS for data processing.

The first pass through the data involved:

1. calculating the absolute time of each Doppler burst,
2. calculating the elapsed time of each Doppler burst,
3. dividing the elapsed time by the number of cycles to get the frequency,
4. correcting by the Bragg cell bias frequency for v_1 and v_2,

and,

5. converting to velocity using the Doppler shift formula.

The Doppler shift formula is

$$V = \ell \nu_D \quad , \tag{F.1}$$

where V is the velocity, ℓ is the fringe spacing of the focal volume,

and ν_D is the Doppler frequency. The fringe spacing, ℓ, is given by

$$\ell = \frac{\lambda}{2 \sin\frac{\alpha}{2}} \quad , \tag{F.2}$$

where λ is the wavelength of the laser light and α is the angle between the beams.

F.2 Uniform Sampling and Filtering of the Data

The raw data are randomly sampled in time, but, for processing purposes, it is simpler to deal with velocity data at uniform time intervals. The second pass through the data computed the velocity at uniform time intervals as follows. The raw data were converted to a continuous velocity versus time function by using a straight line (linear interpolation) to represent the velocity between the discrete raw data sample times. The raw velocity was integrated from $(t_{n-1} + t_n)/2$ to $(t_n + t_{n+1})/2$ to get the uniformly sampled velocity for the n^{th} point, where $t_n = n\tau_s$ and τ_s is the time between the uniform samples.

After uniformly sampling the data in time, the data were filtered in time using a Gaussian filter profile. The filter width was chosen to be comparable to the resolution of the 4-point measurement geometry. Specifically, the full width of the filter profile at the 1/e points was chosen to be equal to the average transit time through the 4-point measurement geometry; i.e.,

$$\tau_f = \frac{h}{\bar{u}} = \frac{2h}{\bar{u}_1 + \bar{u}_2} , \qquad (F.3)$$

where τ_f is the filter width (equal to the average transit time) and $\bar{u}$ is the local mean velocity of the flow ($u = (u_1 + u_2)/2$).

F.3 Vorticity, Reynolds Stress, and Histograms

Finally, the vorticity, $-\omega_z$ (from equation 1.1) and the Reynolds stress, $-\overline{u'v'} = -\overline{(u_1'+u_2')(v_1'+v_2')/4}$, were computed from u_1, u_2, v_1, and v_2 (all as a function of time). Each run of data contains at least 50 large structures. For processing purposes, each run was split into 8 equal time intervals containing at least 6 large structures each. For each time interval, the histograms (probability density functions) of the 4 velocities, the vorticity, and $-u'v'$ were computed. For each time interval, the mean, the 2nd moment (mean square), the 3rd moment, and the 4th moment were computed from the histogram. Note that the 2nd through 4th moments are computed about the mean. The histogram and the first 4 moments for the entire run of data were computed by taking the mean of the results for the 8 individual time intervals

$$\bar{a} = \frac{1}{8} \sum_{i=1}^{8} a_i \quad . \qquad (F.4)$$

The standard deviation of the first 4 moments was also computed from the values of the moments for the 8 equal time intervals. The standard deviation of a moment is given by

$$s = \left[\frac{1}{7} \sum_{i=1}^{8} (a_i - \bar{a})^2 \right]^{1/2} \quad . \qquad (F.5)$$

Since we want the standard deviation of the mean of the 8 samples rather than the standard deviation of the 8 samples themselves, we must divide the standard deviation of the individual samples by the square root of the number of samples

$$s_m = s/\sqrt{8} \quad . \tag{F.6}$$

The standard deviation of the mean is given by s_m. This process was carried out to obtain the mean and standard deviation of the mean for the first 4 moments of the 4 velocities, the vorticity, and $-u'v'$. All error bars plotted in the figures are ± one standard deviation of the mean in hight.

F.4 Estimated LDV Error in Measuring Vorticity

Of paramount importance is the expected error in the measured vorticity data, and the trade-off of spatial (and temporal) resolution vs. measurement accuracy. From equation 1.1 we have

$$-\omega_z \approx \frac{u_1 - u_2}{h} - \frac{v_1 - v_2}{h} \quad . \tag{F.7}$$

Filtering the velocity data and using f to denote the filtered quantities gives

$$-\omega_{zf} \approx \frac{u_{1f} - u_{2f}}{h} - \frac{v_{1f} - v_{2f}}{h} \quad . \tag{F.8}$$

If we assume that the measurement errors are uncorrelated (a fairly good approximation since the 4 velocities are from individual focal volumes), then we obtain

$$(\delta\omega_{zf})^2 \approx \frac{1}{h^2}\left[\, 2(\delta u_f)^2 + 2(\delta v_f)^2 \,\right] \quad , \tag{F.9}$$

where $\delta\omega_{zf}$ is the estimated z component vorticity measurement error, δu_f is the u-component measurement error, and δv_f is the v-component measurement error. Equation F.9 can be further simplified by making the approximation $\delta u_f \approx \delta v_f$, giving

$$(\delta\omega_{zf})^2 \approx \frac{4}{h^2}(\delta u_f)^2 \quad \text{or} \quad \delta\omega_{zf} \approx \frac{2}{h}\delta u_f \quad . \tag{F.10}$$

At the shear layer centerline, we have $\overline{\omega_z} = \Delta U/\delta_\omega$, where δ_ω is the vorticity thickness (as opposed to $\delta\omega$ which is the error in vorticity). Dividing by $\overline{\omega_z}$ to get the relative error of the vorticity at the centerline gives

$$\frac{\delta\omega_{zf}}{\overline{\omega_z}} \approx 2\left(\frac{\delta_\omega}{h}\right)\left(\frac{\delta u_f}{\Delta U}\right) \quad . \tag{F.11}$$

The error in the filtered velocity can be estimated from the error in the raw velocity data, the average raw data rate, and the filter width

$$\delta u_f \approx \delta u\left(\frac{\tau}{\tau_f}\right)^{1/2} = \delta u\left(\frac{\overline{u}\,\tau}{h}\right)^{1/2} \quad , \tag{F.12}$$

where τ is the average time between raw data points, and $\tau_f = h/\overline{u}$ is the filter width. Substituting equation F.12 for δu_f in equation F.11 gives

$$\frac{\delta\omega_{zf}}{\overline{\omega_z}} \approx 2\left(\frac{\delta_\omega}{h}\right)^{3/2}\left(\frac{\delta u}{\Delta U}\right)\left(\frac{\overline{u}\,\tau}{\delta_\omega}\right)^{1/2} \quad . \tag{F.13}$$

Finally, $u \approx \overline{u} = U_c$ on the centerline and, for a 2 to 1 shear layer, $U_c = 1.5\,\Delta U$, giving

$$\frac{\delta\omega_{zf}}{\overline{\omega_z}} \approx 3\left(\frac{\delta_\omega}{h}\right)^{3/2}\left(\frac{\delta u}{u}\right)\left(\frac{U_c\tau}{\delta_\omega}\right)^{1/2} \quad . \tag{F.14}$$

The most important thing to notice is that the expected error is proportional to h to the -3/2 power, dictating a trade-off between accuracy and spatial resolution (temporal resolution is chosen to be equivalent to spatial resolution by the prior choice of $\tau_f = h/\overline{u}$).

A value of $\delta u/u$ in the range of 0.2% to 0.4% can be achieved with careful optics and signal processing. The value achieved is dictated by a compromise between $\delta u/u$ and the sampling rate, specifically, to minimize $\sqrt{\tau}\,\delta u/u$. At $U_1 = 70$ cm/sec, a realistic compromise is $\delta u/u \approx 0.3\%$ and $\tau = 0.7$ milliseconds. If we select a location approximately midway between the first and last x locations surveyed, we get $x - x_o \approx 50$ cm. The approximate vorticity thickness can be obtained by the following empirical formula

$$\frac{\delta_\omega}{x - x_o} \approx 0.18\left(\frac{1-r}{1+r}\right) \quad , \tag{F.15}$$

where $r = U_2/U_1 = 0.5$ is the velocity ratio. Substituting in the numbers gives $\delta_\omega \approx 3$ cm, and $(U_c\tau/\delta_\omega)^{1/2} \approx 0.11$. For this case, equation F.14 becomes

$$\frac{\delta\omega_{zf}}{\overline{\omega_z}} \approx 1.0\cdot10^{-3}\left(\frac{\delta_\omega}{h}\right)^{3/2} \quad . \tag{F.16}$$

The chosen value of the focal volume separation, h, is 1.9 mm which gives $\delta_\omega/h \approx 15.7$ and

$$\frac{\delta\omega_{zf}}{\overline{\omega_z}} \approx 0.063 \quad \text{or} \quad 6.3\% \quad . \tag{F.16a}$$

This shows that the selected focal volume separation is a good compromise between accuracy and spatial resolution. An estimate of the accuracy can be obtained from the RMS vorticity of the free stream in Figure 4.11 . Using $x = x_0 = 110\,cm$ and $\Delta U = 35\,cm/sec$ gives $\delta\omega_{zf} = 1.0\,sec^{-1}$ for the low speed side and $\delta\omega_{zf} = 1.7\,sec^{-1}$ for the high speed side.

F.5 Estimated Finite Difference Error in Measuring Vorticity

Another source of error arises from the use of the method of finite differences (see equation 1.1) to approximate the derivatives of $-\omega_z$. The velocity induced by a vortex is nonlinear, so if the core of a vortex is small compared to the spacing of the focal volumes, h, and very close to one of the focal volumes, the induced velocity in that focal volume is greater than the sum of the induced velocities in the other three focal volumes. If the vortex is adjacent to a focal volume, but just outside the measurement geometry, this will generate a vorticity measurement of the opposite sign of the vorticity within the vortex core.

In order to determine the magnitude of this problem, some computer simulations were carried out of a line vortex parallel to the z axis crossing a measurement volume. The vortex used in the calculations has a circular core of uniform vorticity ($-\omega_z = \omega_0$). The calculations were carried out for trajectories parallel to the x axis and for y values in increments of $0.1\,h$, where h is the spacing between focal

volumes. The vortex moves with a constant velocity, U. The results for a vortex with a core diameter of $d_o = 0.2\,h$ are shown in Figure F.1. To ease interpretation of the results, the horizontal axis has been converted from time to the x position of the vortex by dividing by U. Note that the measured vorticity will be $\omega_o\,(d_o/h)^2$ when the vortex is in the center of the core ($x = 0, y = 0$). As can be seen in the plot, the vorticity can overshoot and undershoot the central value by substantial amounts.

Since the raw data are filtered before computing the vorticity, the same filtering algorithms were applied to the simulated vortex results from Figure F.1. Figure F.2 shows the filtered vorticity profiles for the same vortex as Figure F.1 and for a filter width of $\tau_f = h/\bar{u}$. The filtered results show that all of the overshoot and most of the undershoot are removed by filtering. The results also show that the method of finite differences is fairly accurate in approximating the circulation within the measurement geometry. The areas of the five lower traces in Figure F.2 are nearly constant, the area of the trace at $y/h = 0.5$ (which cuts through the u_1 focal volume) is approximately half that, and the areas of the upper traces are nearly zero. Figure F.3 shows the filtered vorticity results for the same vortex as Figures F.1 and F.2, but using a filter width of $\tau_f = 2\,h/\bar{u}$. The longer filter width reduces the amount of undershoot even further.

Since many of the plots show vortices with core diameters comparable to or several times larger than the focal volume spacing, h, calculations were also carried out for vortex core diameters of $d_o = 0.5h$ and $d_o = 1.0h$. The results for $d_o = 0.5h$ are shown in Figures F.4 through F.6 and the results for $d_o = 1.0h$ are shown in Figures F.7 through F.9. All three vortices have the same circulation, so the smallest vortex has 25 times the peak vorticity as the largest vortex. As can be seen in Figures F.4 through F.9, the size of the undershoots are reduced considerably for the larger vortices.

In a normal flow, it would be unrealistic for the small vortices to have the same circulation as the larger vortices. If the vortex with $d_o = 0.2h$ has a vorticity of 2.5 times the vorticity of the vortex with $d_o = 1.0h$, then the smaller vortex will have only 1/10 th the circulation of the larger vortex and the results for Figures F.1 - F.3 will have to be reduced by a factor of 10 relative to the results of Figures F.7 - F.9. This makes the already fairly small errors present in Figure F.2 very small relative to the vorticity shown in Figure F.8. The end result is that the filter width chosen, $\tau_f = h/\bar{u}$, represents a good compromise between temporal resolution and vorticity measurement accuracy.

REFERENCES

BROWAND, F.K. & WEIDMAN, P.D. 1976 Large Scales in the Developing Mixing Layer. Journal of Fluid Mechanics 76, 127.

BROWN, G.L. & ROSHKO, A. 1971 The Effect of Density Difference on the Turbulent Mixing Layer. Turbulent Shear Flows, AGARD-CP-93, paper # 23.

BROWN, G.L. & ROSHKO, A. 1974 On Density Effects and Large Structures in Turbulent Mixing Layers. Journal of Fluid Mechanics 64, 775.

CORRSIN, S. & KISTLER, A.L. 1955 NACA Rep. 1244.

DEMETRIADES, A. 1968 Journal of Fluid Mechanics 34, 465.

DIMOTAKIS, P.E. & BROWN, G.L. 1976 The Mixing Layer at High Reynolds Number: Large-Structure Dynamics and Entrainment. Journal of Fluid Mechanics 78, 535.

DIMOTAKIS, P.E., DEBUSSY, F.D., and KOOCHESFAHANI, M.M. 1981 Particle Streak Velocity Field Measurements in a Two-Dimensional Mixing Layer. Physics of Fluids 24(6), 995.

DIMOTAKIS, P.E., BROADWELL, J.E., and HOWARD, R.D. 1983 Chemically Reacting Turbulent Jets, AIAA Paper 83-0474.

FALCO, R.E. 1974 Some Comments on Turbulent Boundary Layer Structure Inferred From the Moments of a Passive Contaminant. AIAA Paper No. 74-99.

FOSS, J.F. 1976 Accuracy and Uncertainty of Transverse Vorticity Measurements. APS Bulletin 21(10), EB8.

FOSS, J.F. 1979 Transverse Vorticity Measurements. Dynamic Flow Conference, Skovlunde, Denmark.

FOSS, J.F. 1981 Advanced Techniques for Vorticity Measurements. Seventh Biennial Symposium on Turbulence, University of Missouri at Rolla.

FRISH, M.B. & WEBB, W.W. 1981 Direct Measurement of Vorticity by

Optical Probe. Journal of Fluid Mechanics 107, 173.

HOLDEMAN, J.D. & FOSS, J.F. 1975 Journal of Fluids Engineering 97(1), 342.

KASTRINAKIS, E.G., ECKELMANN, H. and WILLMARTH, W.W. 1979 Review of Scientific Instruments 50, 759.

KONRAD, J.H. 1976 An Experimental Investigation of Mixing in Two-Dimensional Turbulent Shear Flows With Applications to Diffusion-Limited Chemical Reactions. SQUID Report CIT-8-PU.

KOOCHESFAHANI, M.M., CATHERASOO, C.J., DIMOTAKIS, P.E., GHARIB, M. and LANG, D.B. 1979 Two-Point LDV Measurements in a Plane Mixing Layer. AIAA Journal 17(12), 1347.

KOVASZNAY, L.S.G. 1954 Physical Measurements in Gas Dynamics and Combustion, Princeton University Press.

LOEHRKE, R.I. & NAGIB, H.M. 1972 Experiments on Management of Free-Stream Turbulence, AGARD Report No. 598.

McCORMAK, B.W., TANGLER, J.L., and SHERRIEB, H.E. 1968 Journal of Aircraft 5, 260.

ROSHKO, A. 1976 Structure of Turbulent Shear Flows: A New Look. AIAA paper 76-78. Also in AIAA Journal 14, 1348 and AIAA Journal 15, 768.

TAYLOR, G. I. 1938 The Spectrum of Turbulence. Proceedings of the Royal Society of London 164, Series A, 476.

TENNEKES, T. & LUMLEY, J.L. 1972 A First Course in Turbulence, MIT Press.

TOWNSEND, A.A. 1976 The Structure of Turbulent Shear Flow (2nd Ed.), Cambridge University Press.

VUKOSLAVĈEVIĆ & WALLACE, J.M. 1981 Review of Scientific Instruments 52, 869.

WARD, T.M. 1976 The Hydrodynamics Laboratory at the California Institute of Technology-1976. Transactions of the ASME, Dec. 1976, 740.

WIGELAND, R.A., AHMED, M., and NAGIB, H.M. 1978 Vorticity Measurements Using Calibrated Vane-Vorticity Indicators and Cross-Wires. AIAA Journal 16(12), 1229.

WILLMARTH, W.W., & BOGAR, T.J. 1977 Survey and New Measurements of Turbulent Structure Near the Wall. Physics of Fluids 20(10), part II, S9.

WINANT, C.D. & BROWAND, F.K. 1974 Vortex Pairing: the Mechanism of Turbulent Mixing Layer Growth at Moderate Reynolds Number. Journal of Fluid Mechanics 63, 237.

WYGNANSKI, I. & FIEDLER, H.E. 1969 Journal of Fluid Mechanics 38, 577.

WYGNANSKI, I. & FIEDLER, H.E. 1970 The Two-Dimensional Mixing Region. Journal of Fluid Mechanics 41, 327.

WYNGAARD, J.C. 1969 Journal Scientific Instruments, Ser. 2, 2, 983.

ZAMAN, K. B. M. Q. & HUSSAIN, A. K. M. F. 1981 Taylor Hypothesis and Large-Scale Coherent Structures. Journal of Fluid Mechanics 112, 379.

BEAM GEOMETRY

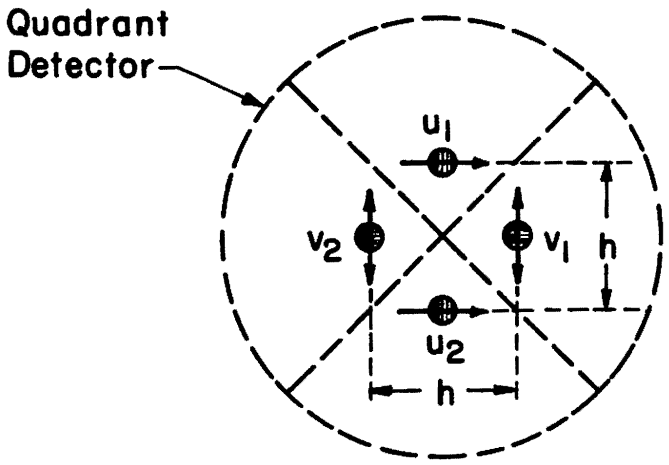

Each Quadrant Detector Element Receives
The Scattered Light From One Focal Volume.

For The Vorticity We Have:

$$-\omega_z = \frac{\partial u}{\partial y} - \frac{\partial v}{\partial x}$$

$$\simeq \left(\frac{u_1 - u_2}{h}\right) - \left(\frac{v_1 - v_2}{h}\right)$$

Where $1\,mm \lesssim h \lesssim 4\,mm$

Note : v — Channels Are Bragg-Cell Shifted.

Figure 1.1 Beam Geometry

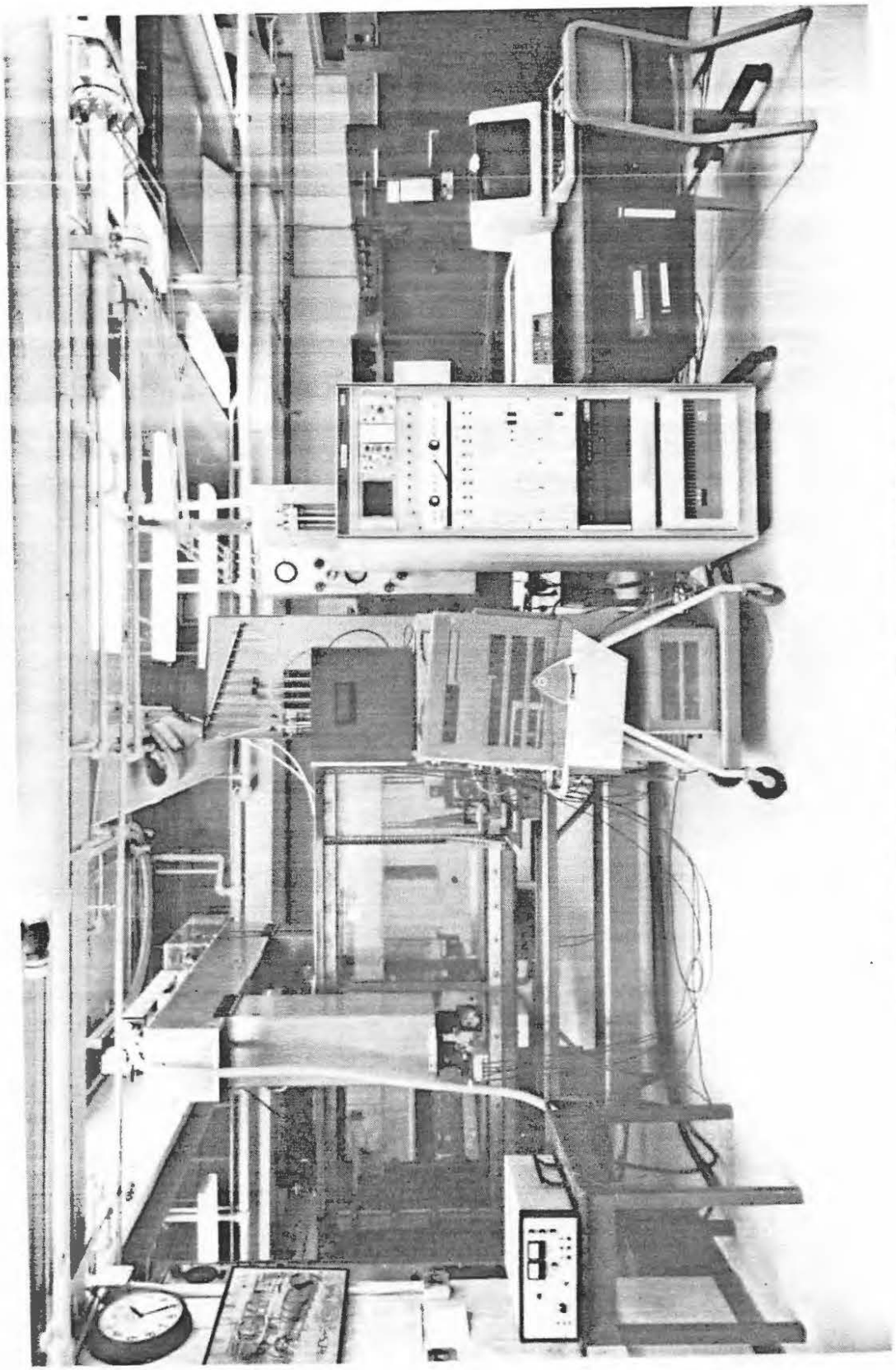

Figure 2.1 Overview of Experimental Setup

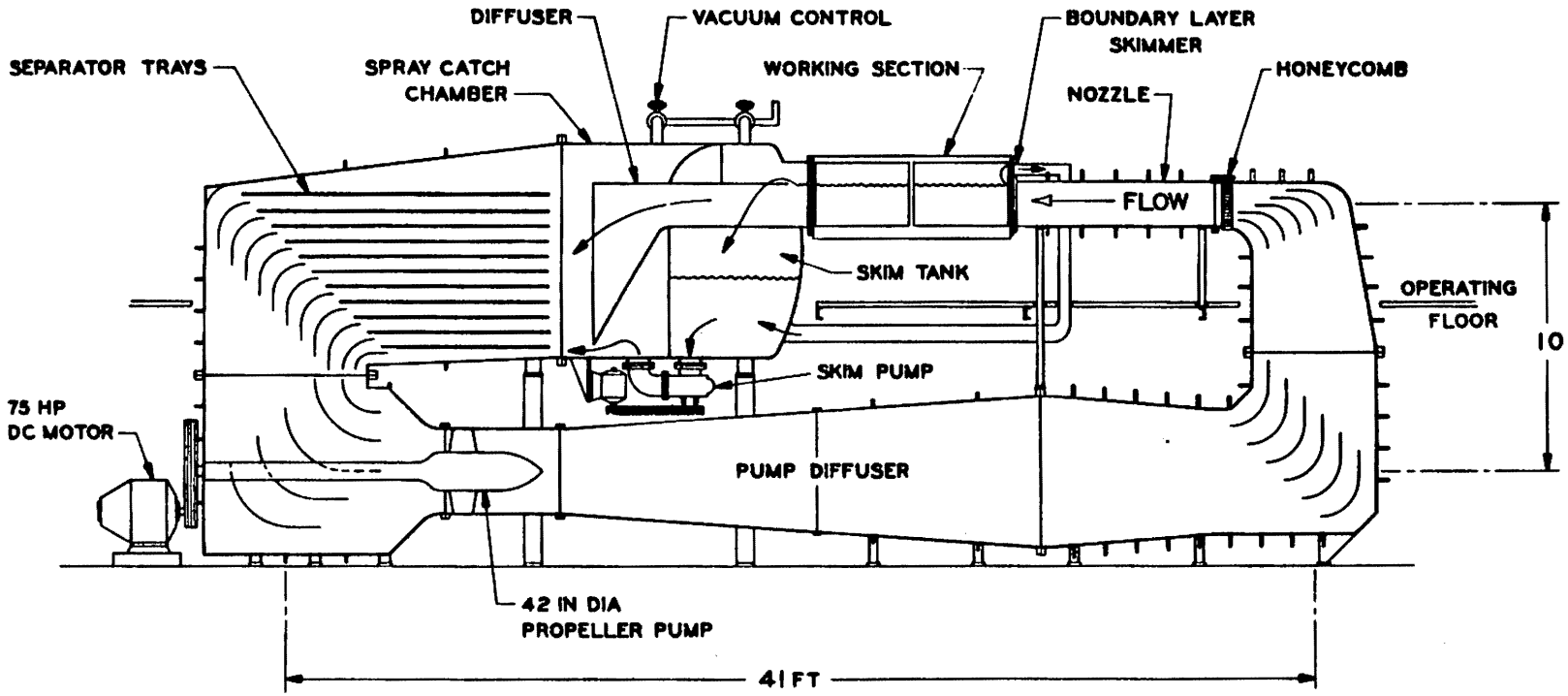

Figure 2.2 Diagram of Free Surface Water Tunnel (FSWT)

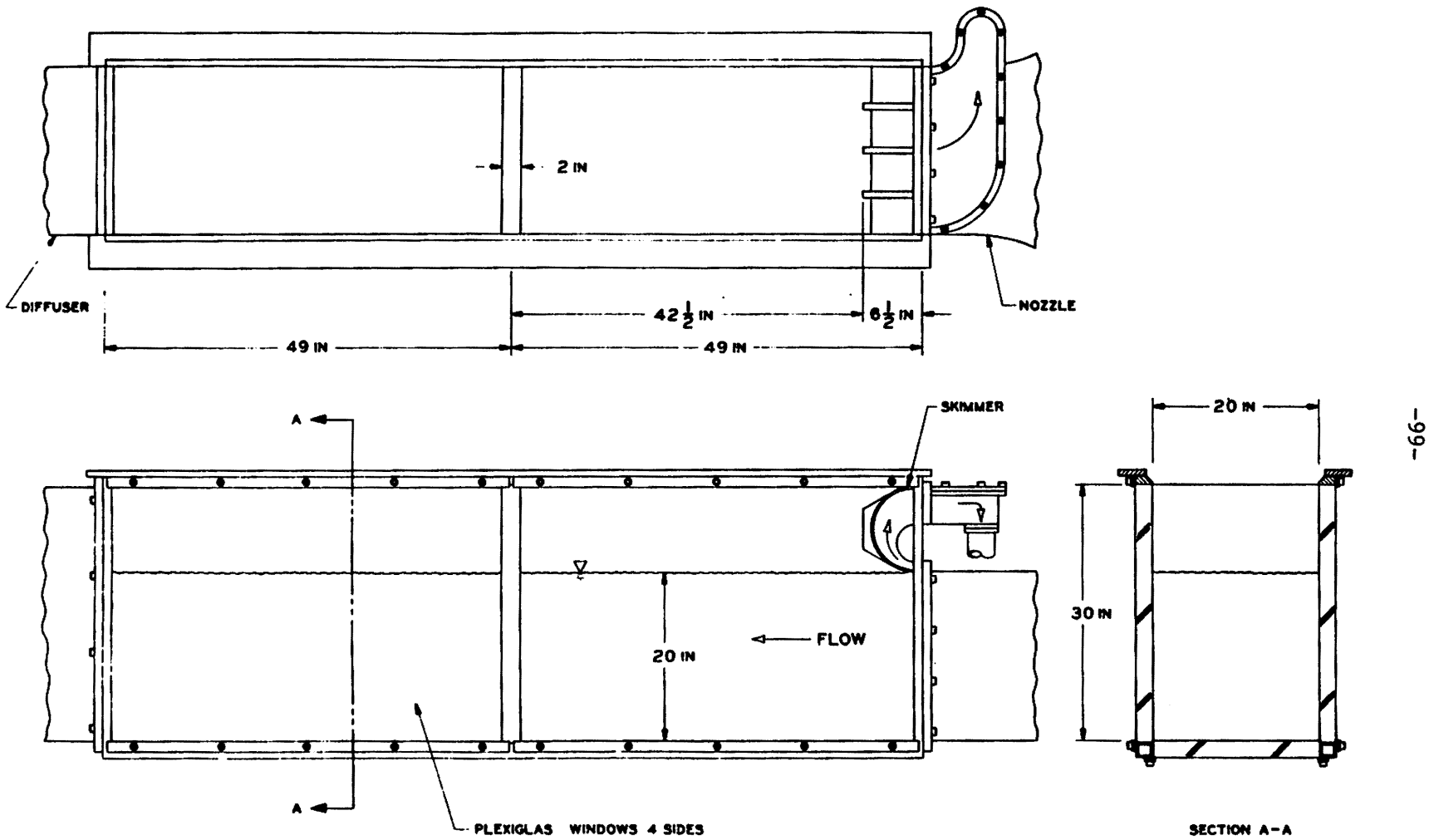

Figure 2.3 Diagram of FSWT Test Section

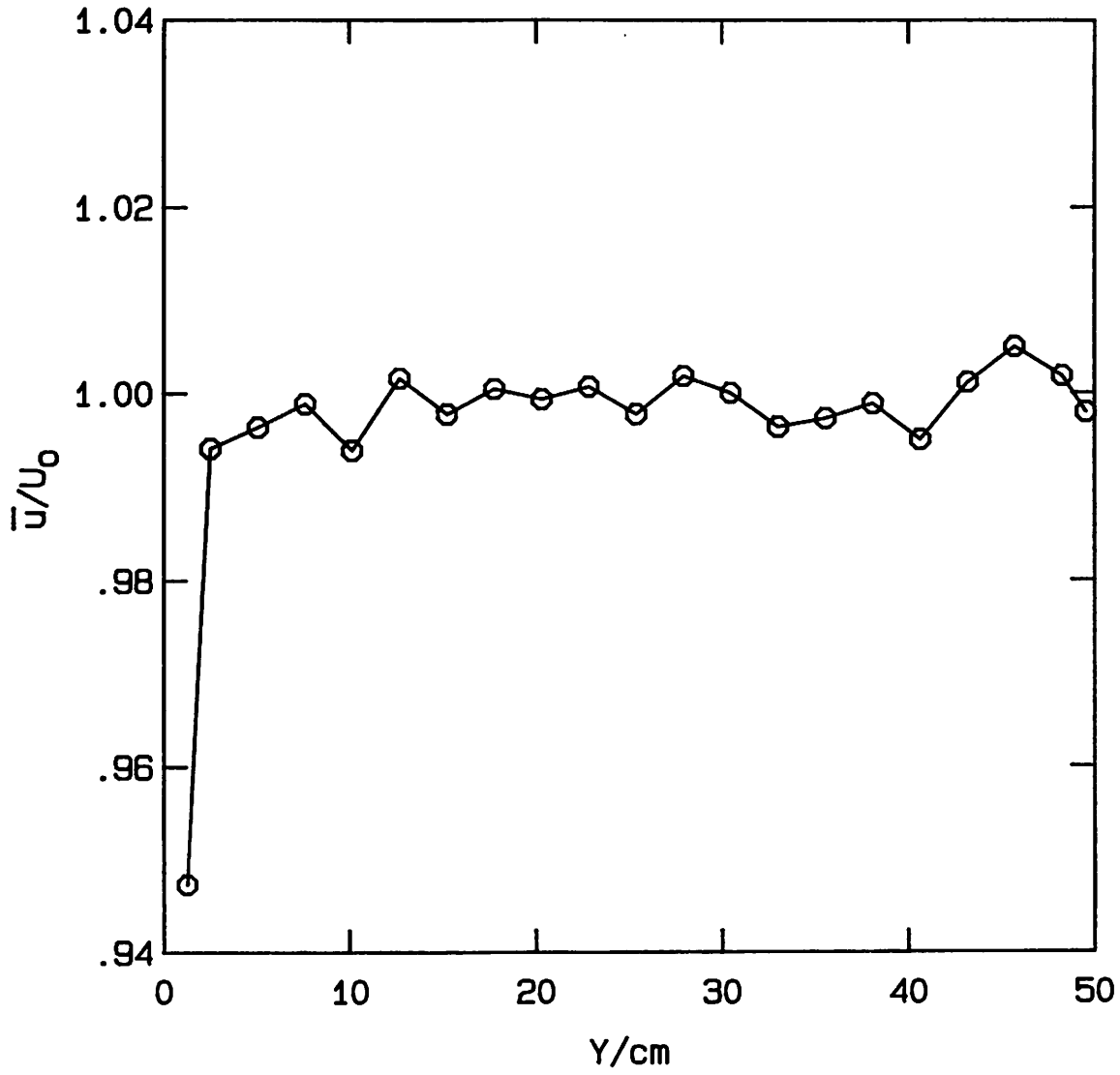

Figure 2.4 Velocity Profile of FSWT Test Section, U = 3.05 m/sec

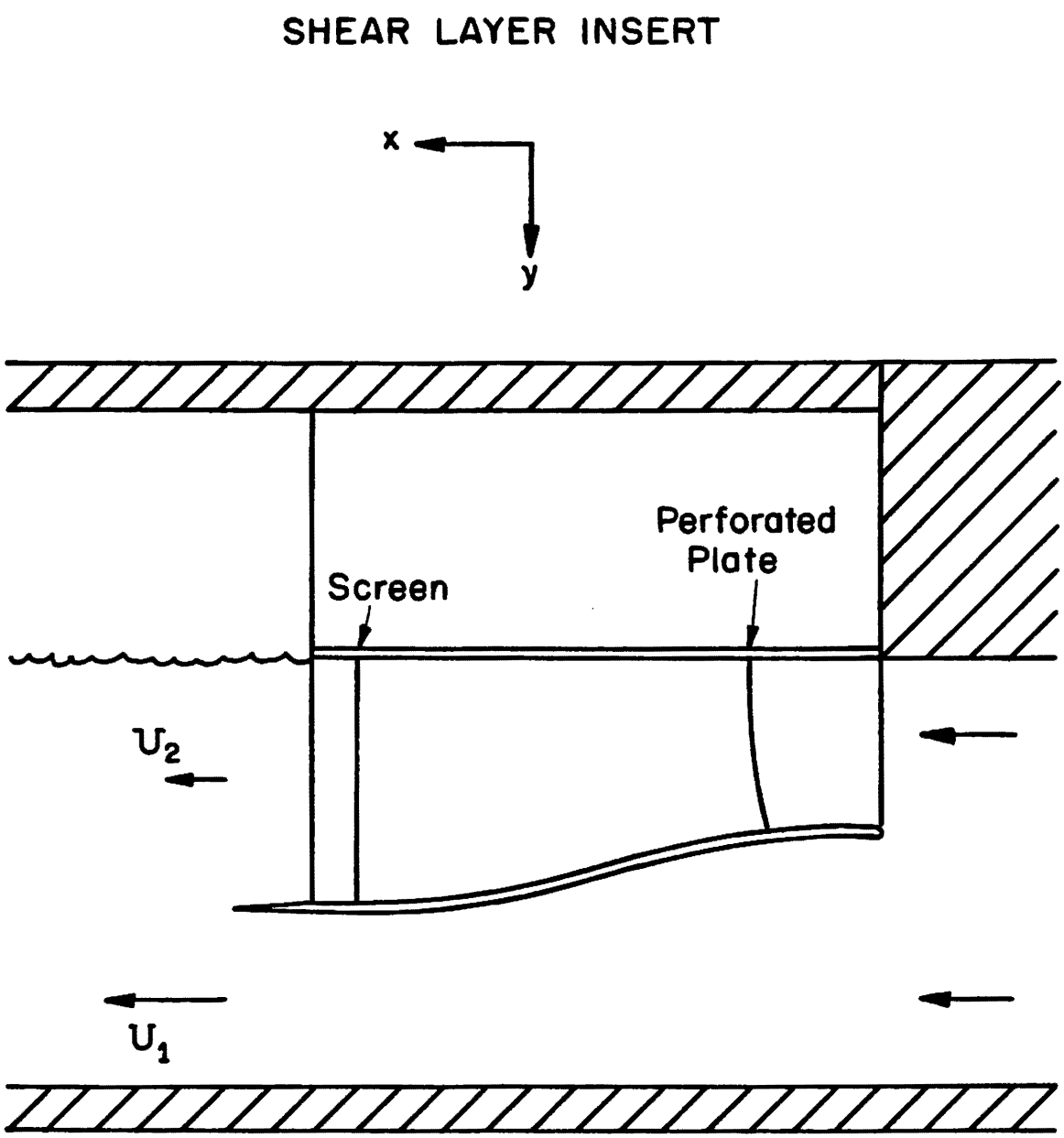

Figure 2.5 Diagram of Shear Layer Insert

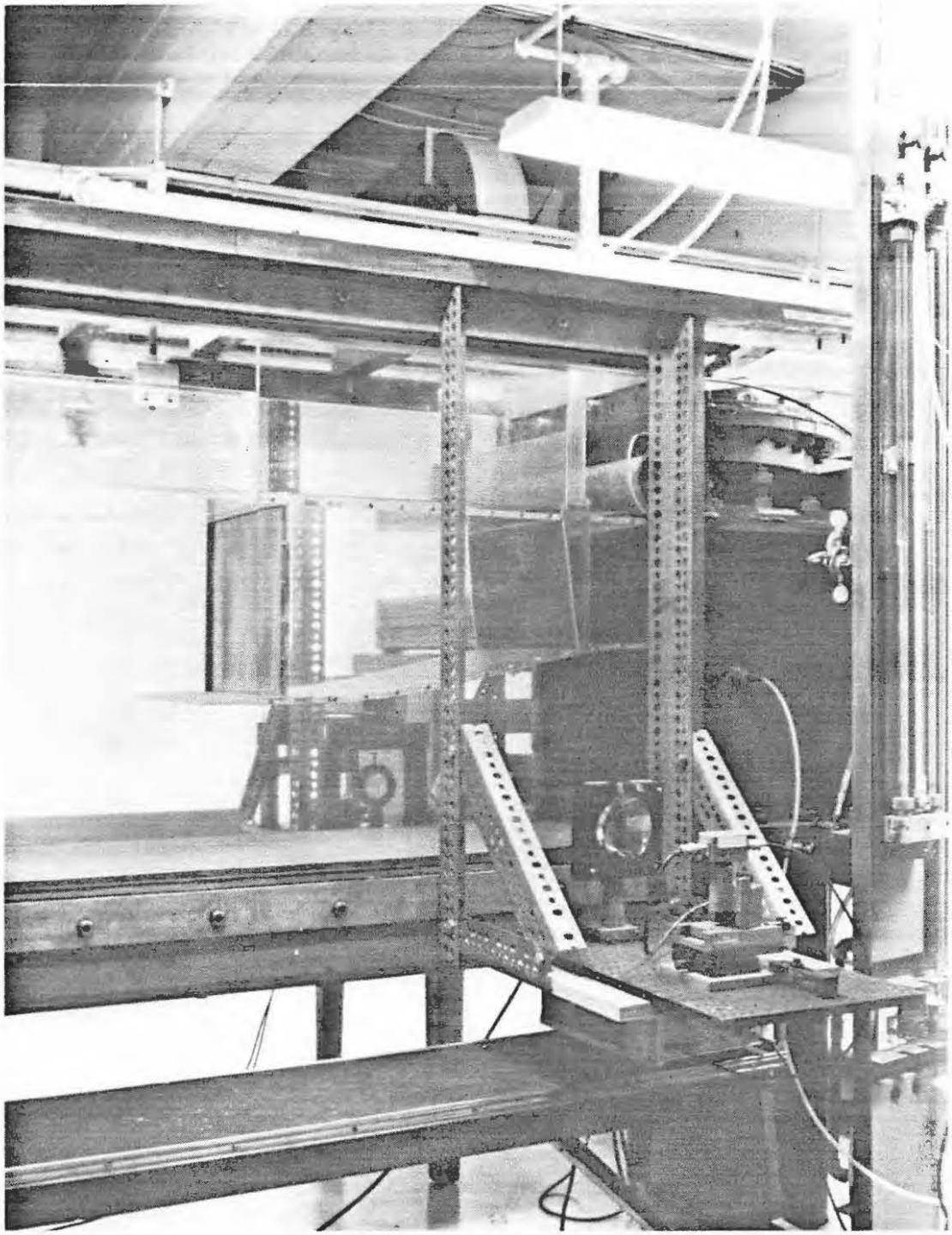

Figure 2.6 Photo of Shear Layer Insert

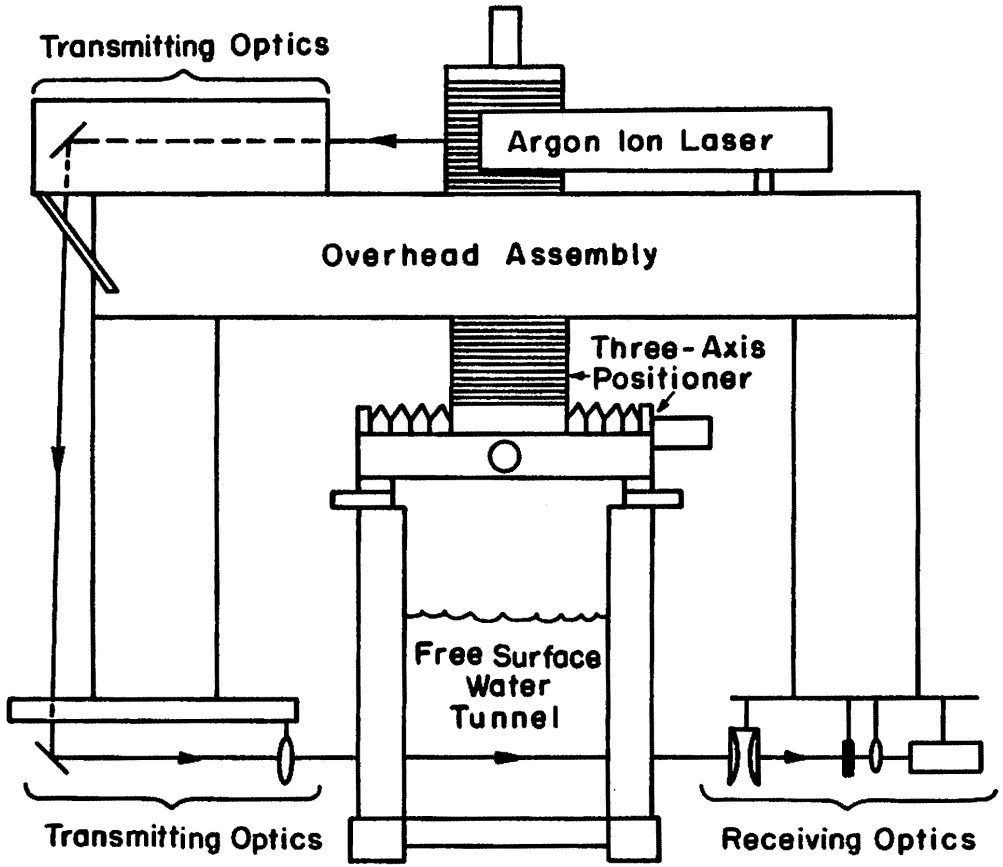

Figure 2.7 Diagram of Overhead Assembly

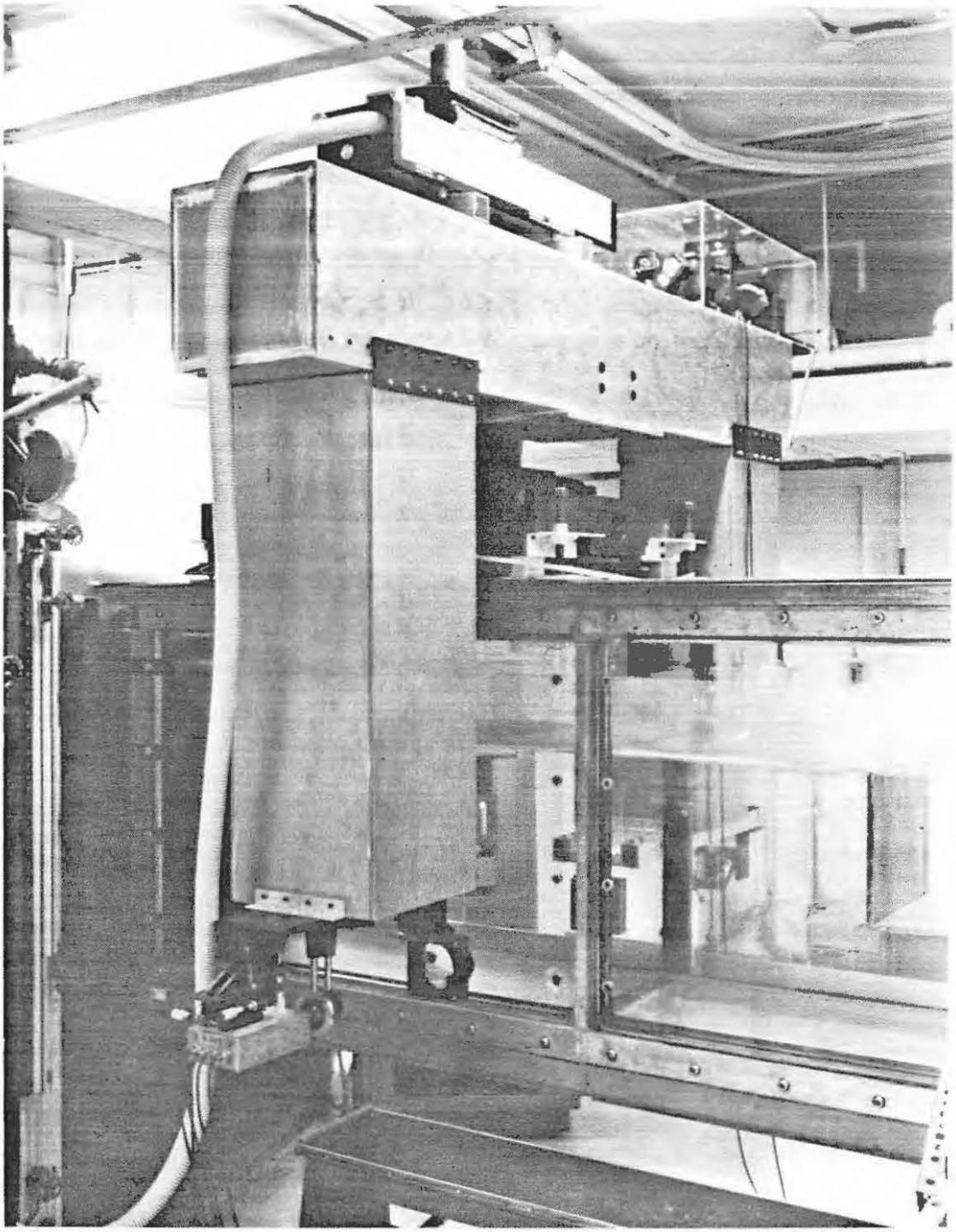

Figure 2.8 Photo of Overhead Assembly

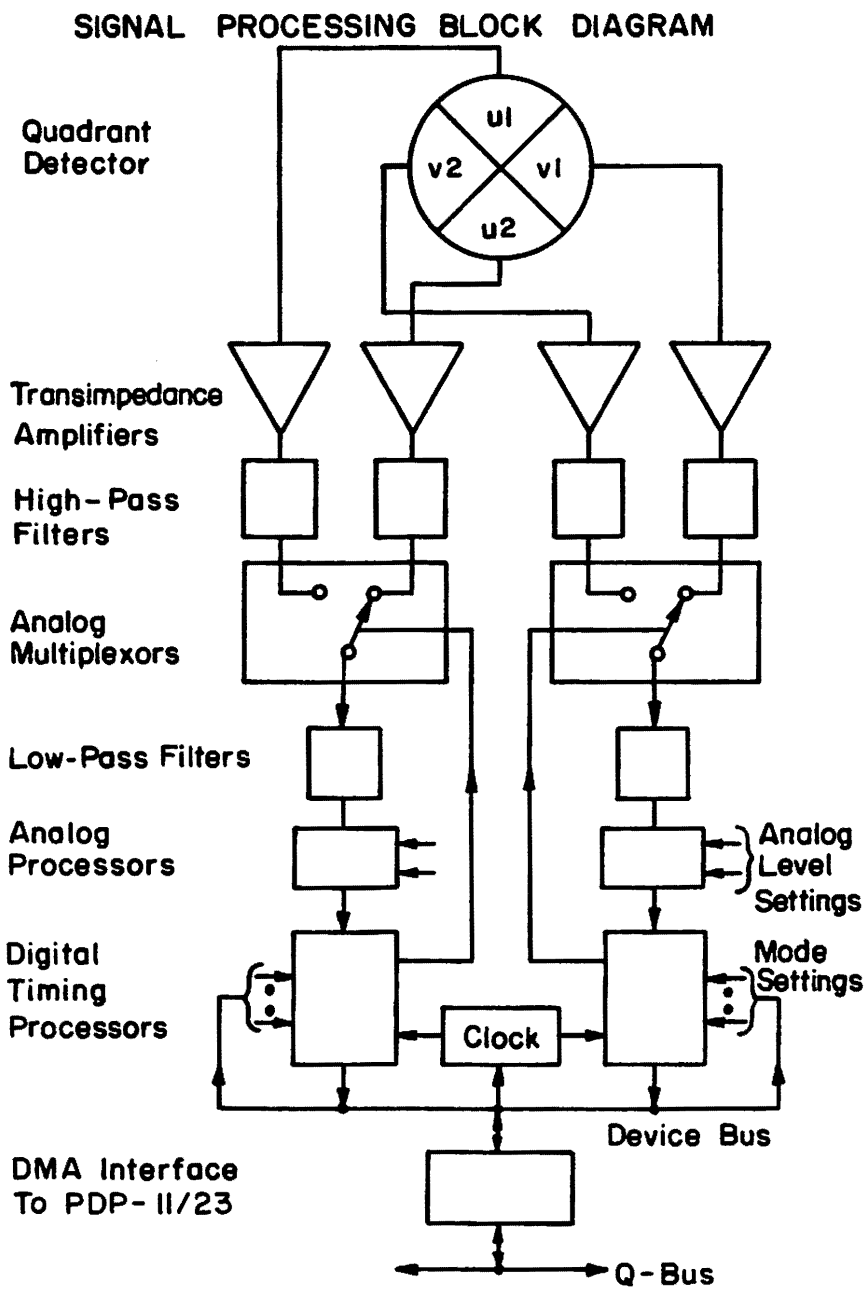

Figure 2.9 Signal Processing Block Diagram

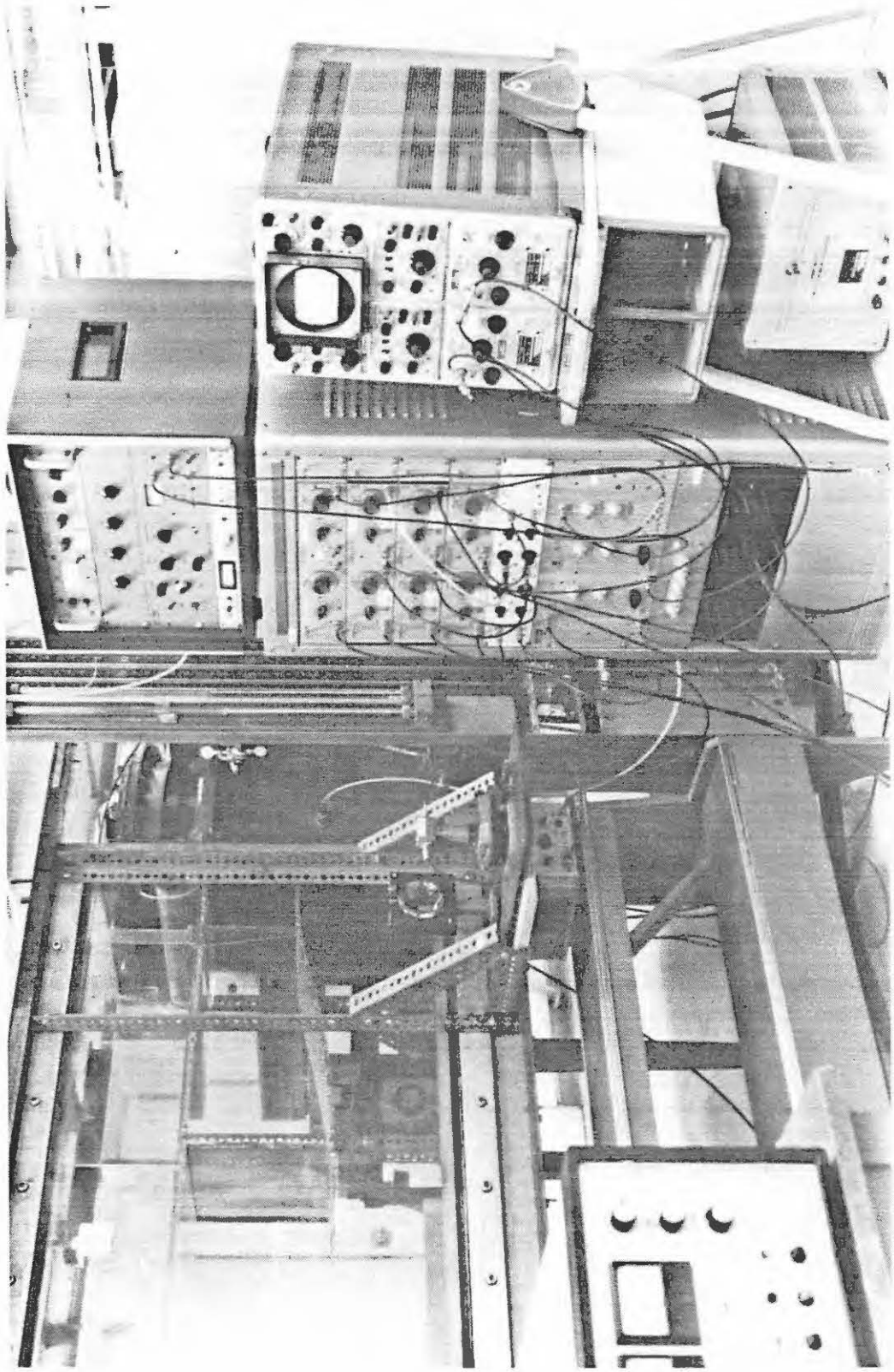

Figure 2.10 Photo of Signal Processing Electronics

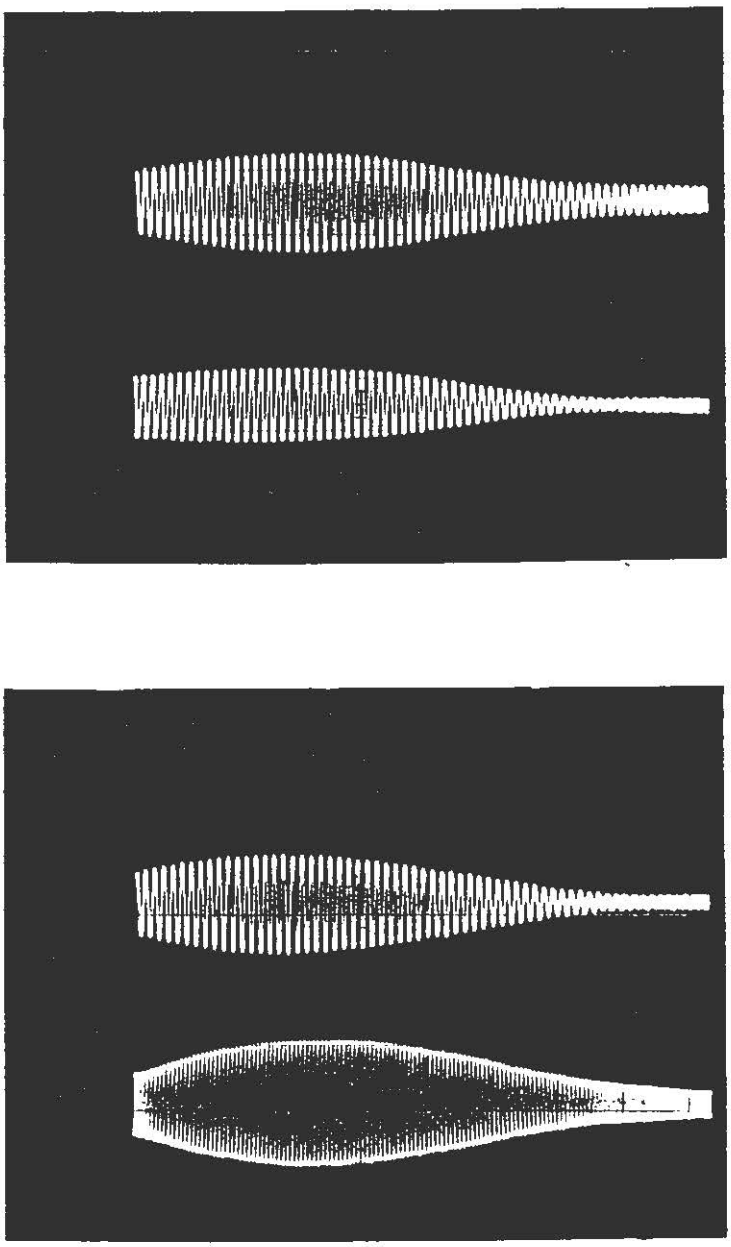

Figure 2.11 Discrete LDV Signal Traces

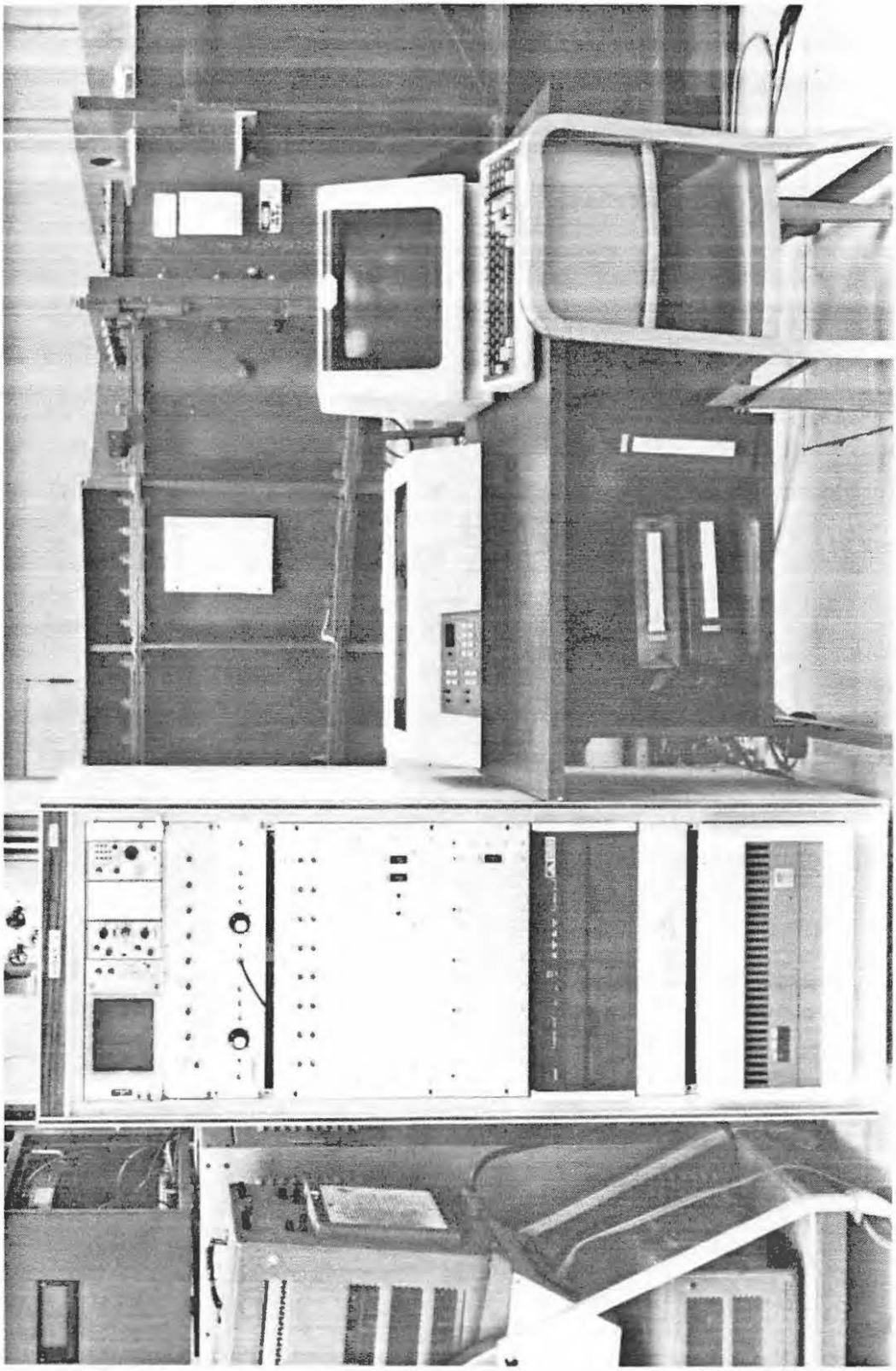

Figure 2.12 Photo of Data Acquisition System

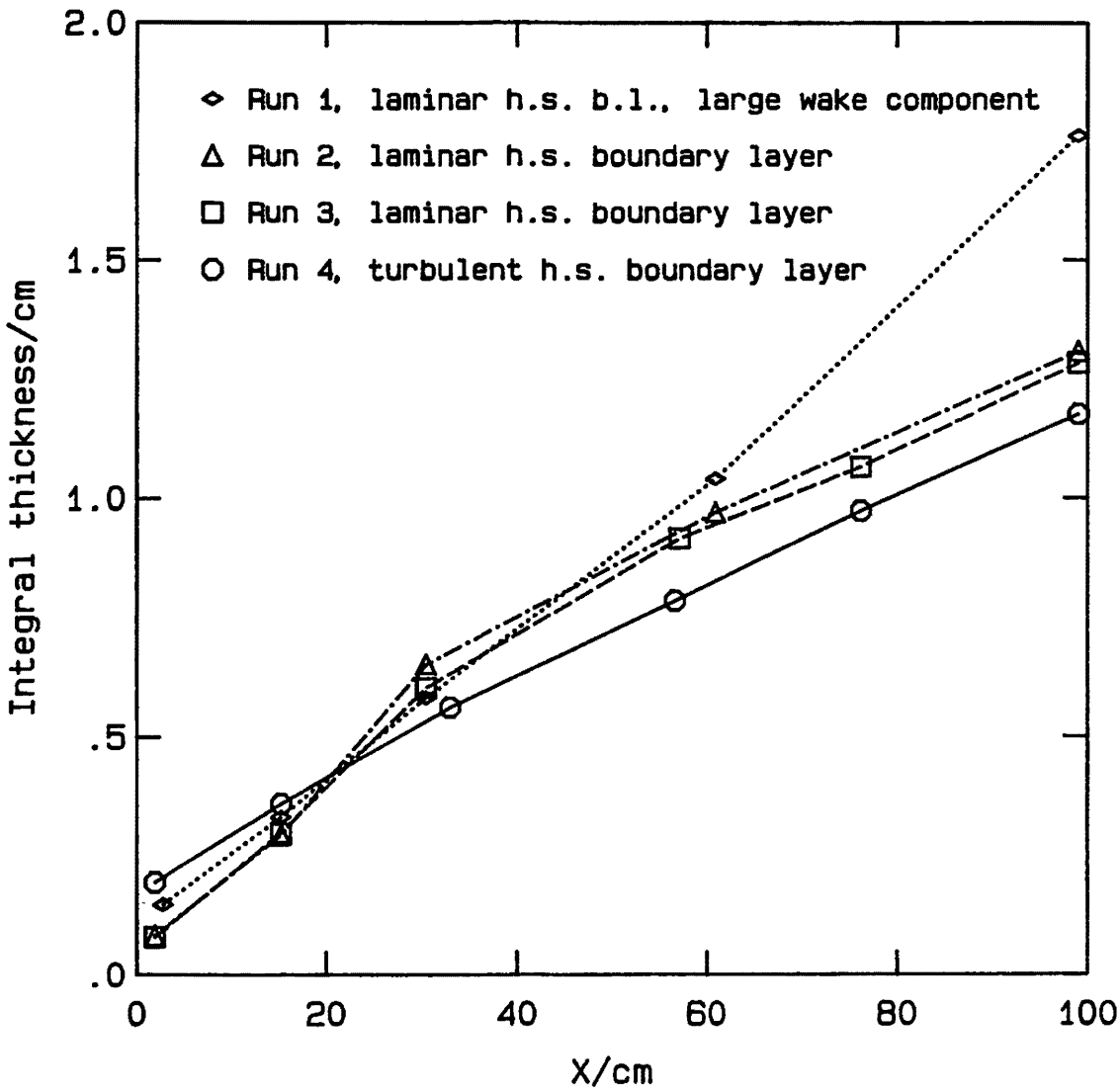

Figure 3.1 Integral Thickness for U_1 = 40 cm/sec

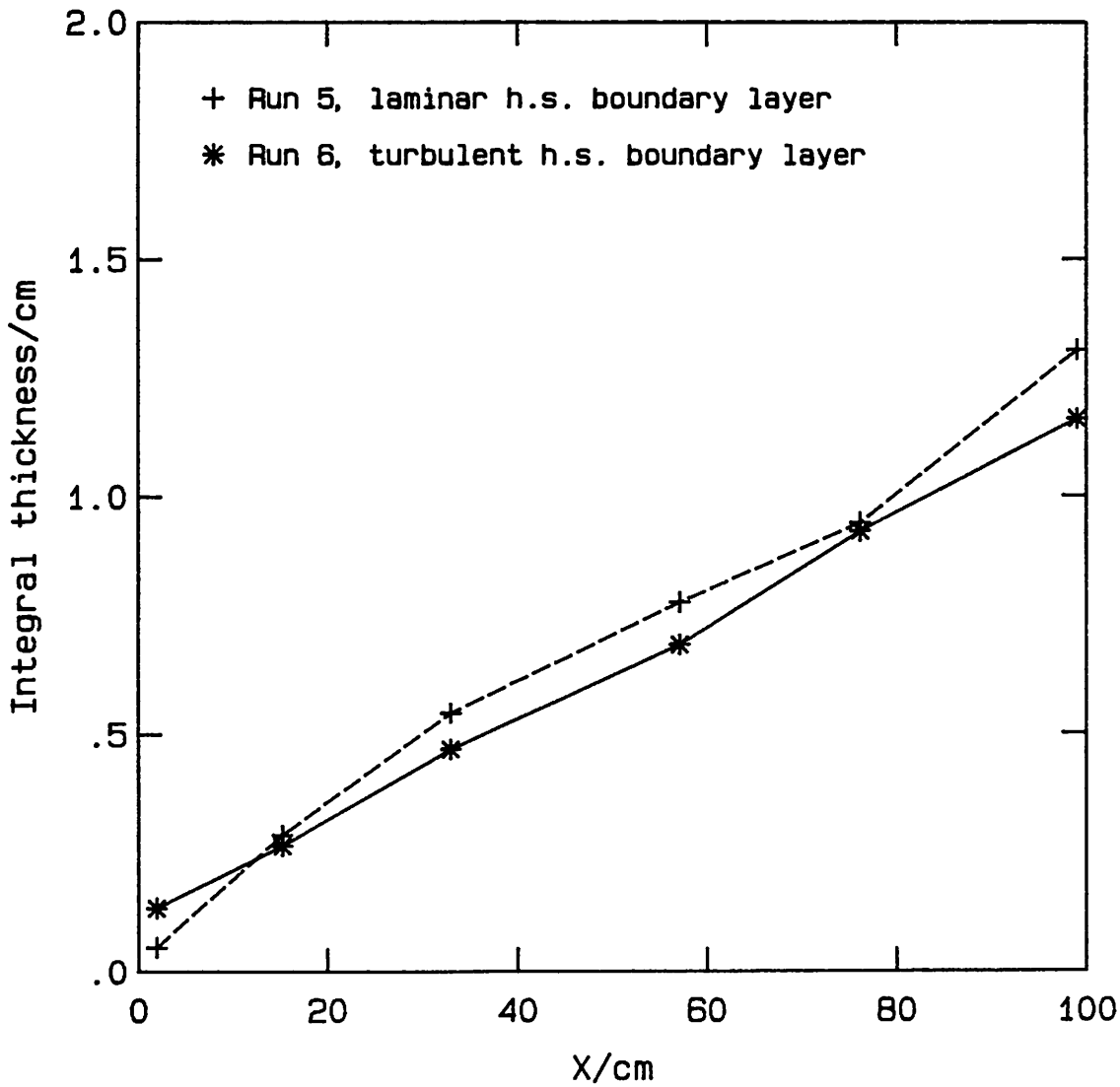

Figure 3.2 Integral Thickness for U_1 = 71 cm/sec

Run 1 U_1 = 41 cm/sec $\tau_f = h/\bar{u}$

File 1 x = 2.79 cm $x-x_0$ = 6.11 cm

θ = 0.147 cm

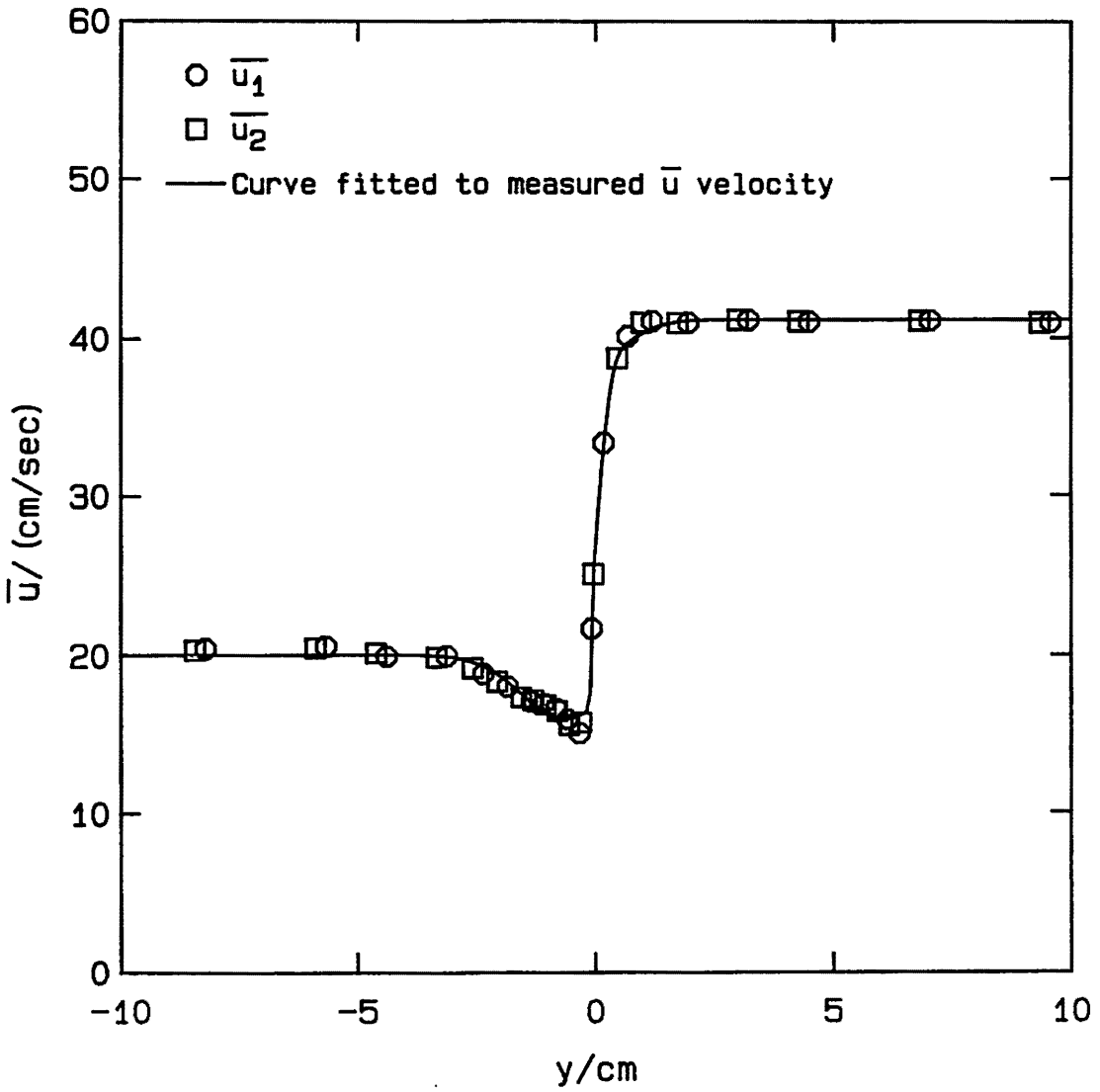

Figure 3.3 Initial $\bar{u}$ Profile for Run 1

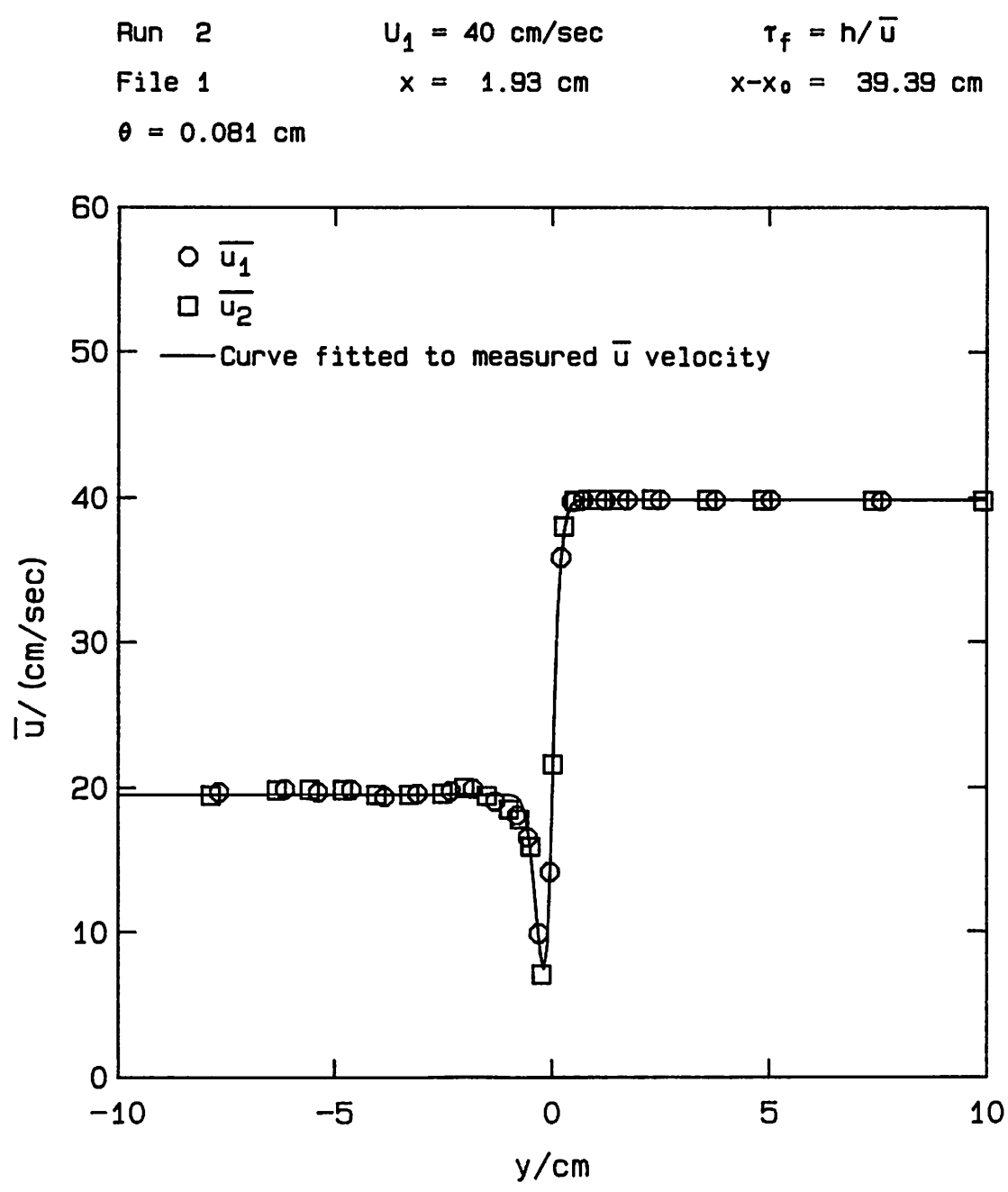

Figure 3.4 Initial $\bar{u}$ Profile for Run 2

Run 3 U_1 = 40 cm/sec $\tau_f = h/\bar{u}$

File 1 x = 1.93 cm $x-x_0$ = 32.06 cm

θ = 0.078 cm

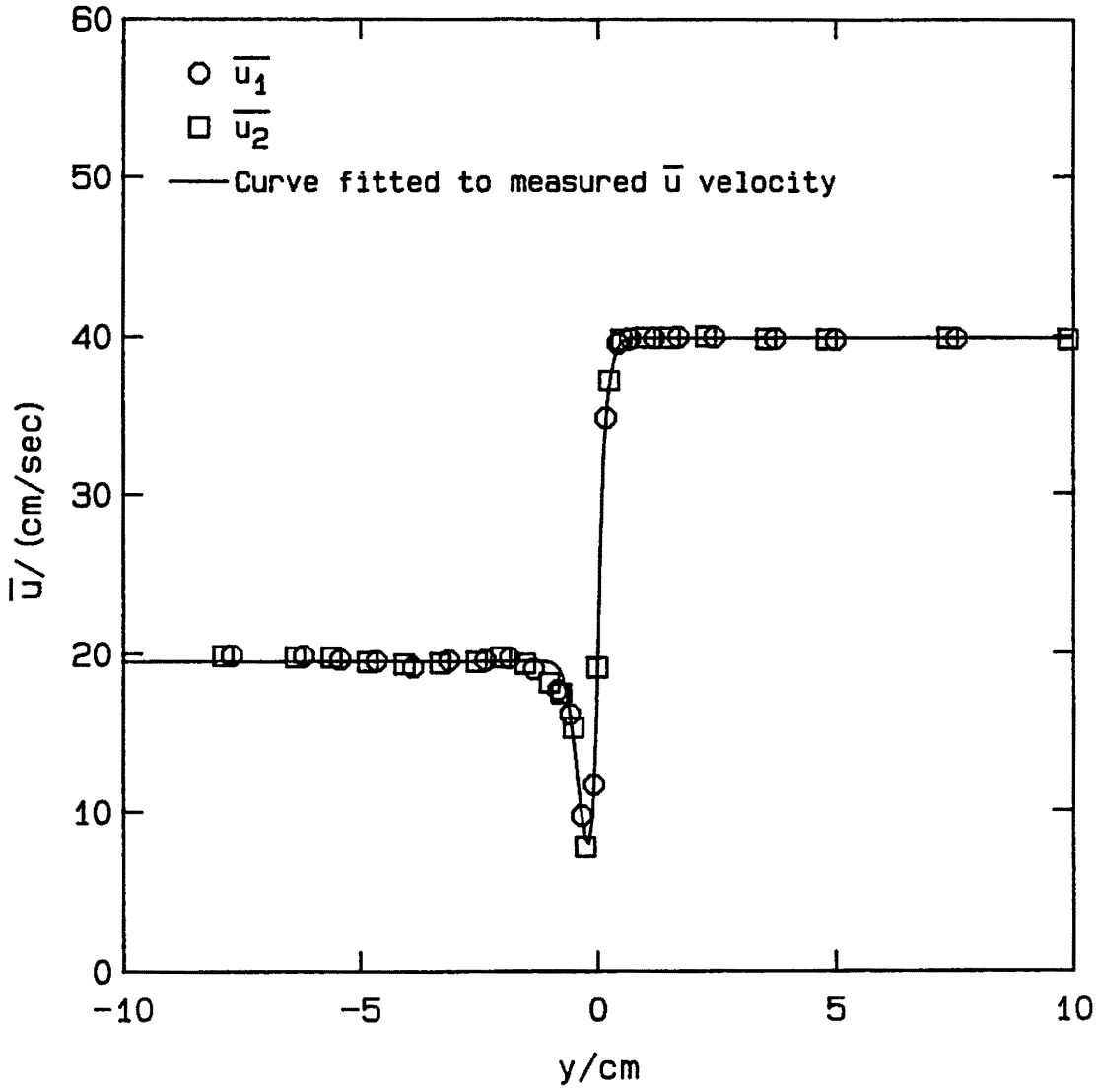

Figure 3.5 Initial $\bar{u}$ Profile for Run 3

Run 4 U_1 = 42 cm/sec $\tau_f = h/\bar{u}$

File 1 x = 1.93 cm $x-x_0$ = 29.15 cm

θ = 0.193 cm

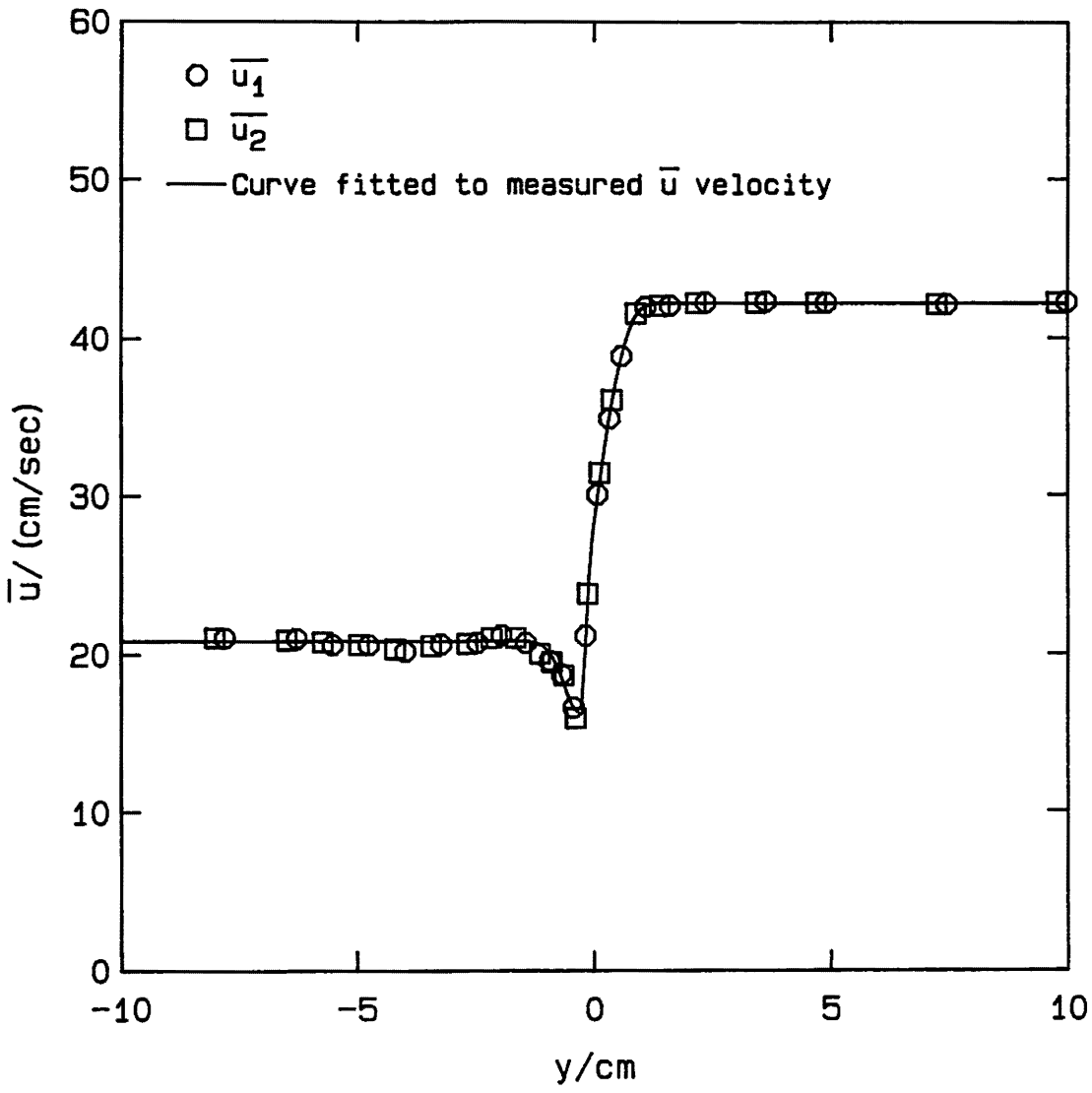

Figure 3.6 Initial $\bar{u}$ Profile for Run 4

Run 5 U_1 = 71 cm/sec $\tau_f = h/\bar{u}$

File 1 x = 1.93 cm $x-x_o$ = 15.90 cm

θ = 0.051 cm

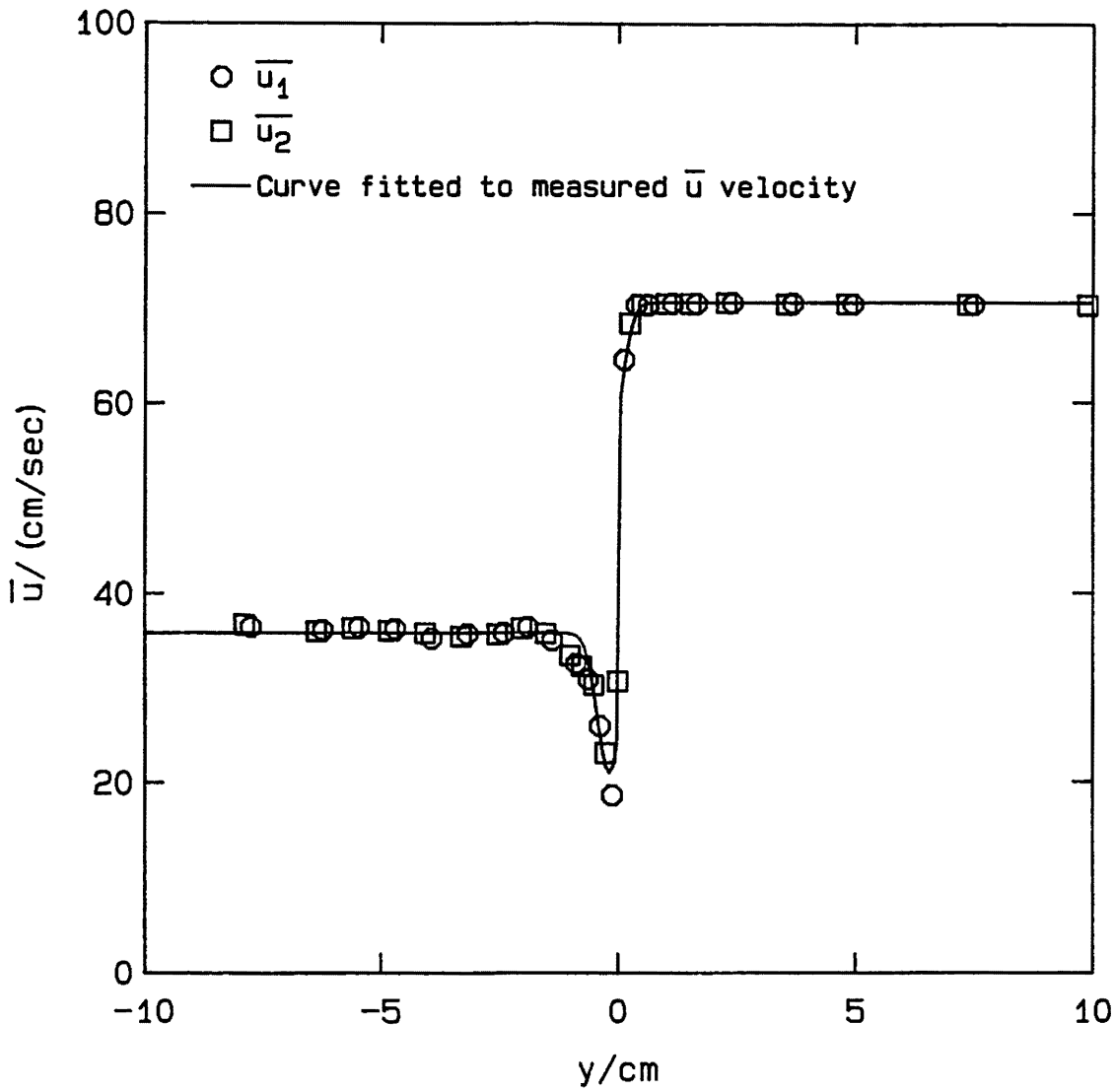

Figure 3.7 Initial $\bar{u}$ Profile for Run 5

Run 6 U_1 = 71 cm/sec $\tau_f = h/\bar{u}$

File 1 x = 1.93 cm $x-x_0$ = 13.27 cm

θ = 0.134 cm

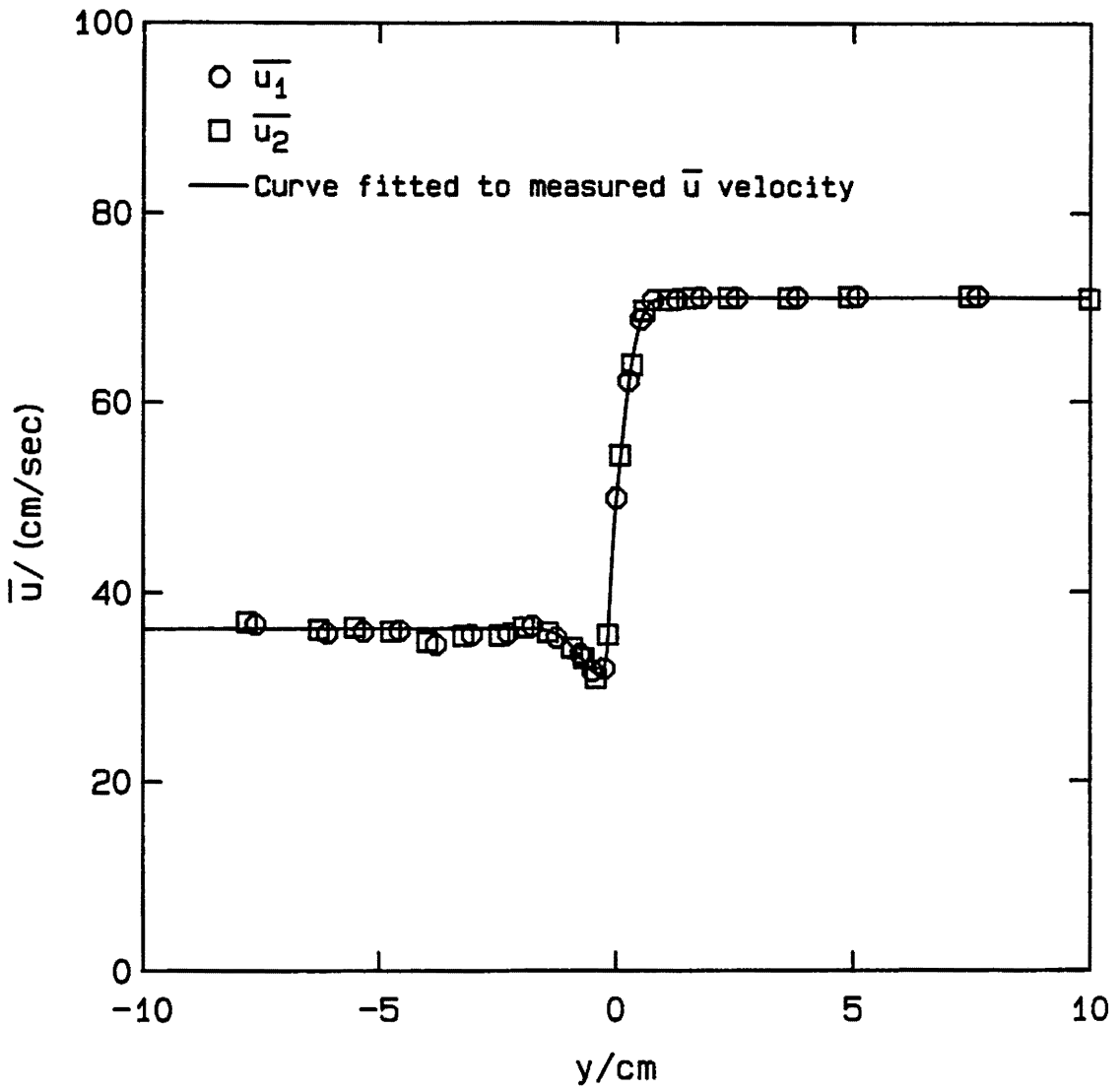

Figure 3.8 Initial $\bar{u}$ Profile for Run 6

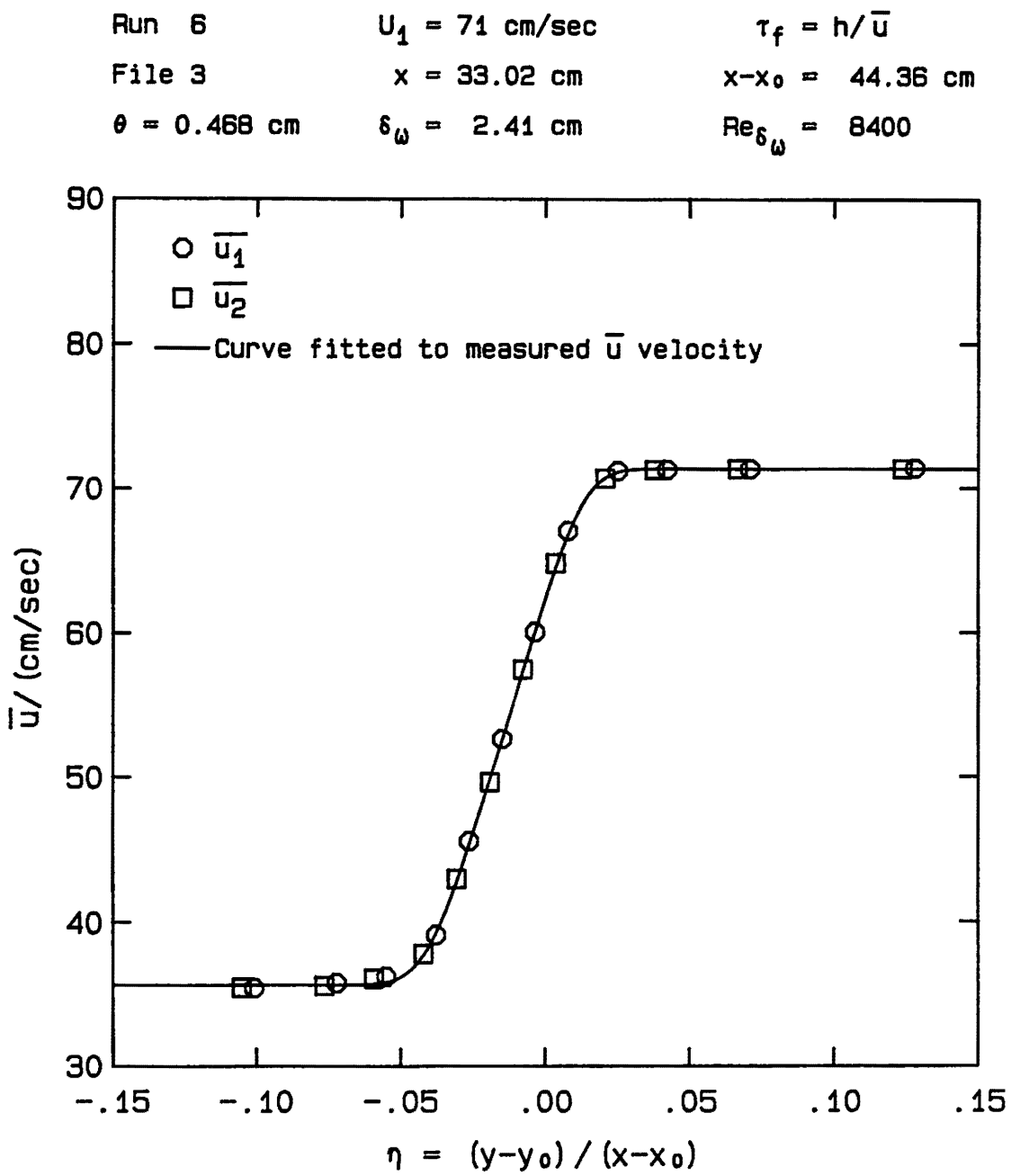

Figure 3.9 $\bar{u}$ Profile at x = 33 cm

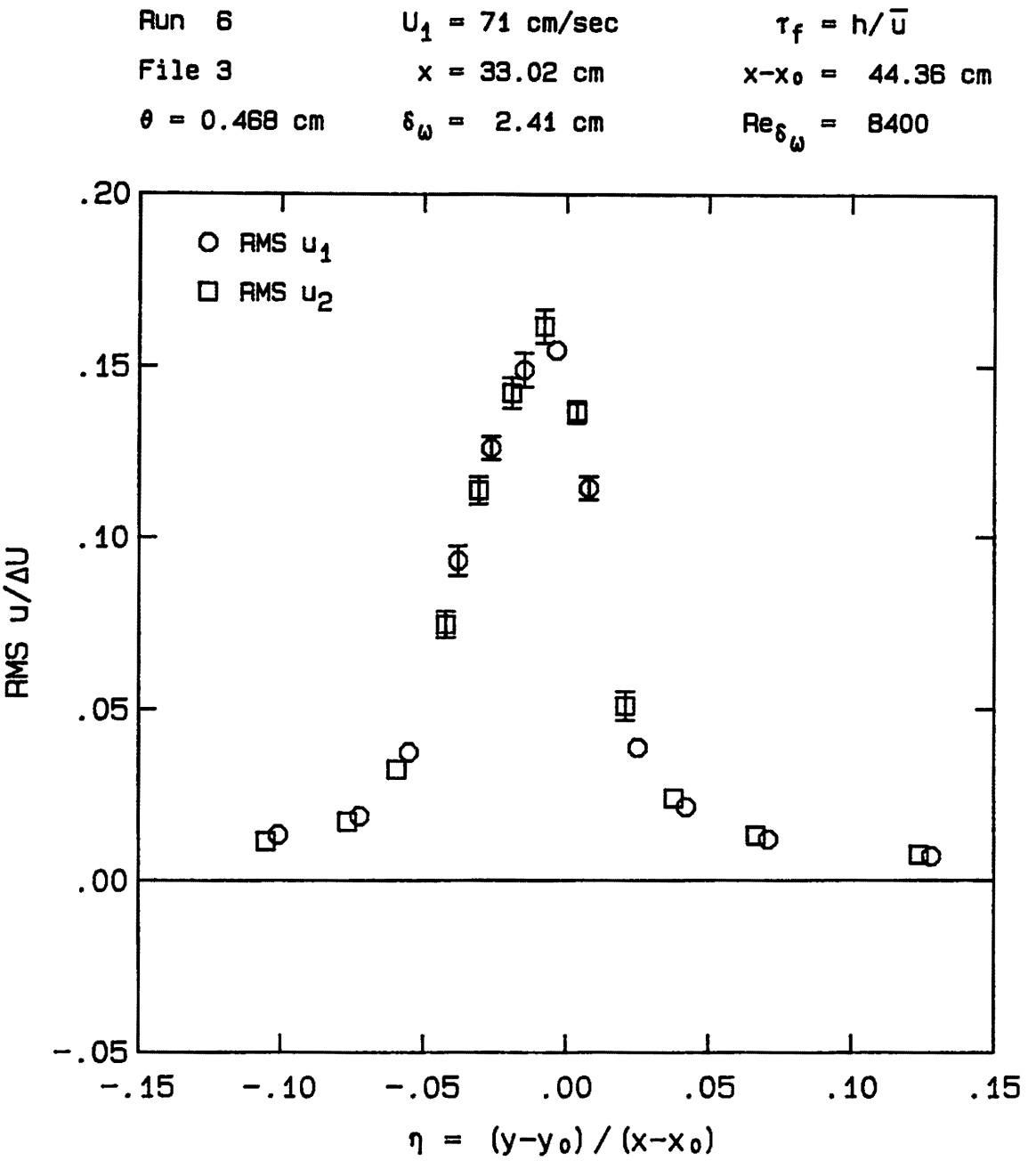

Figure 3.10 RMS u Profile at x = 33 cm

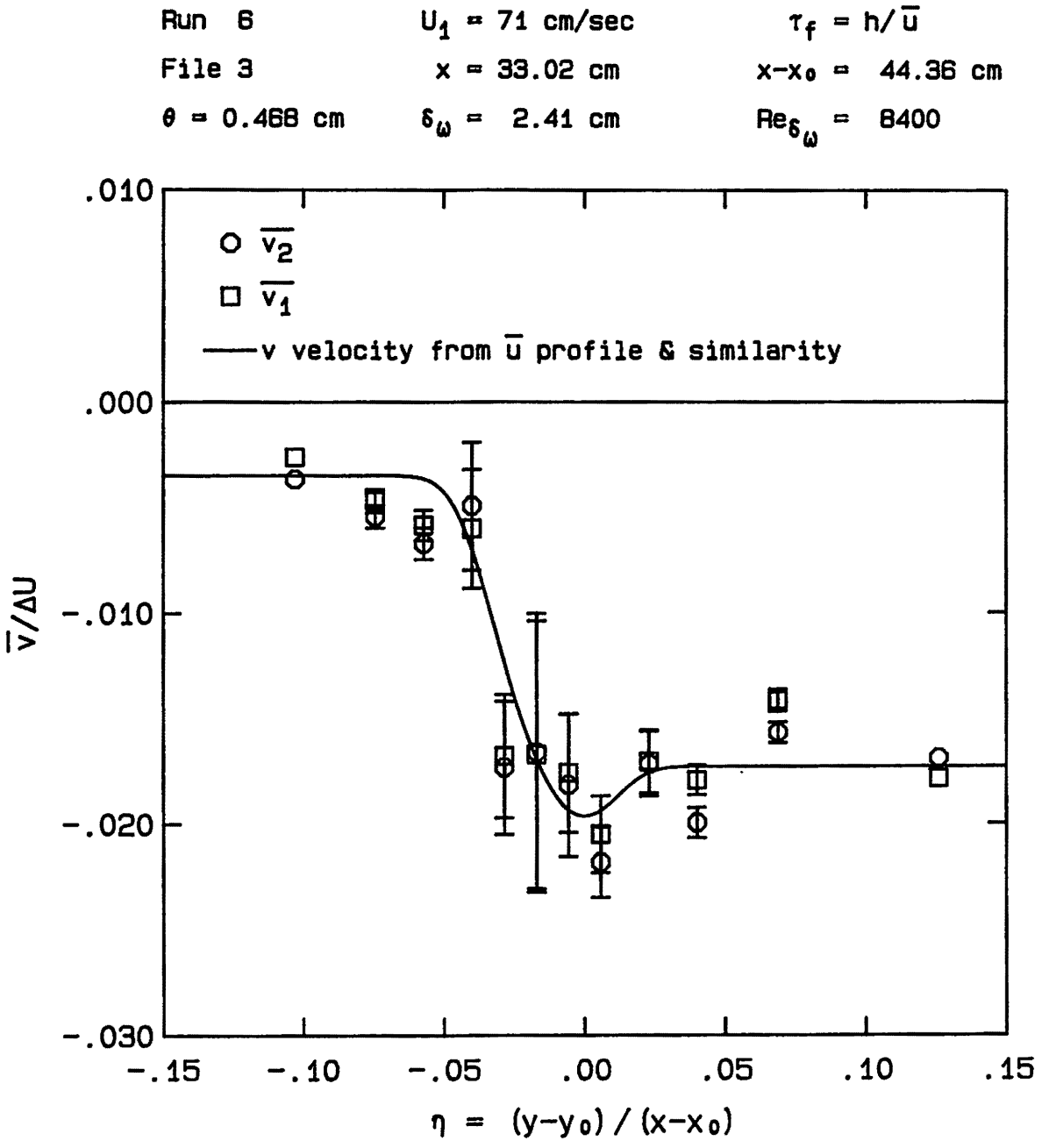

Figure 3.11 $\bar{v}$ Profile at x = 33 cm

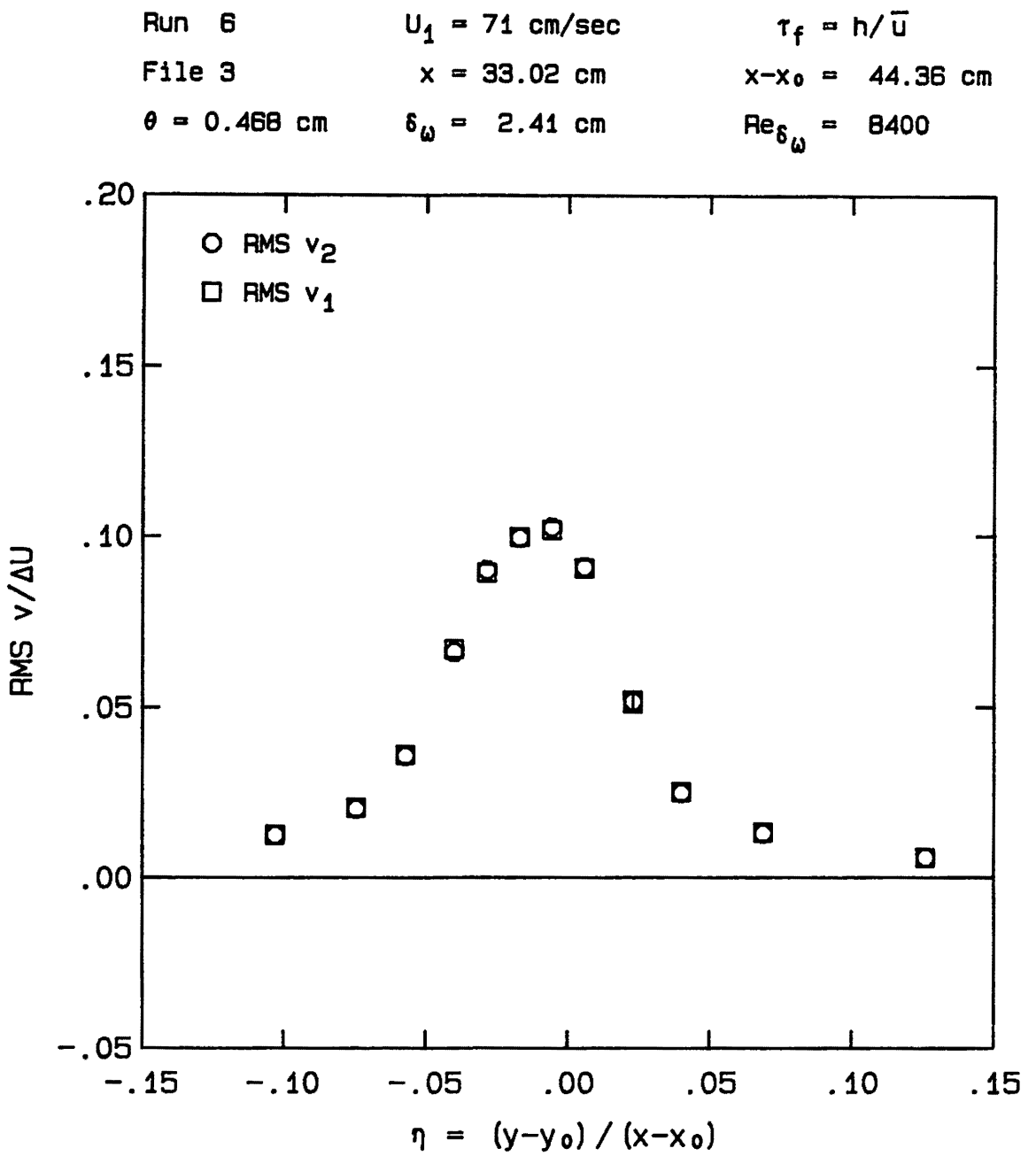

Figure 3.12 RMS v Profile at x = 33 cm

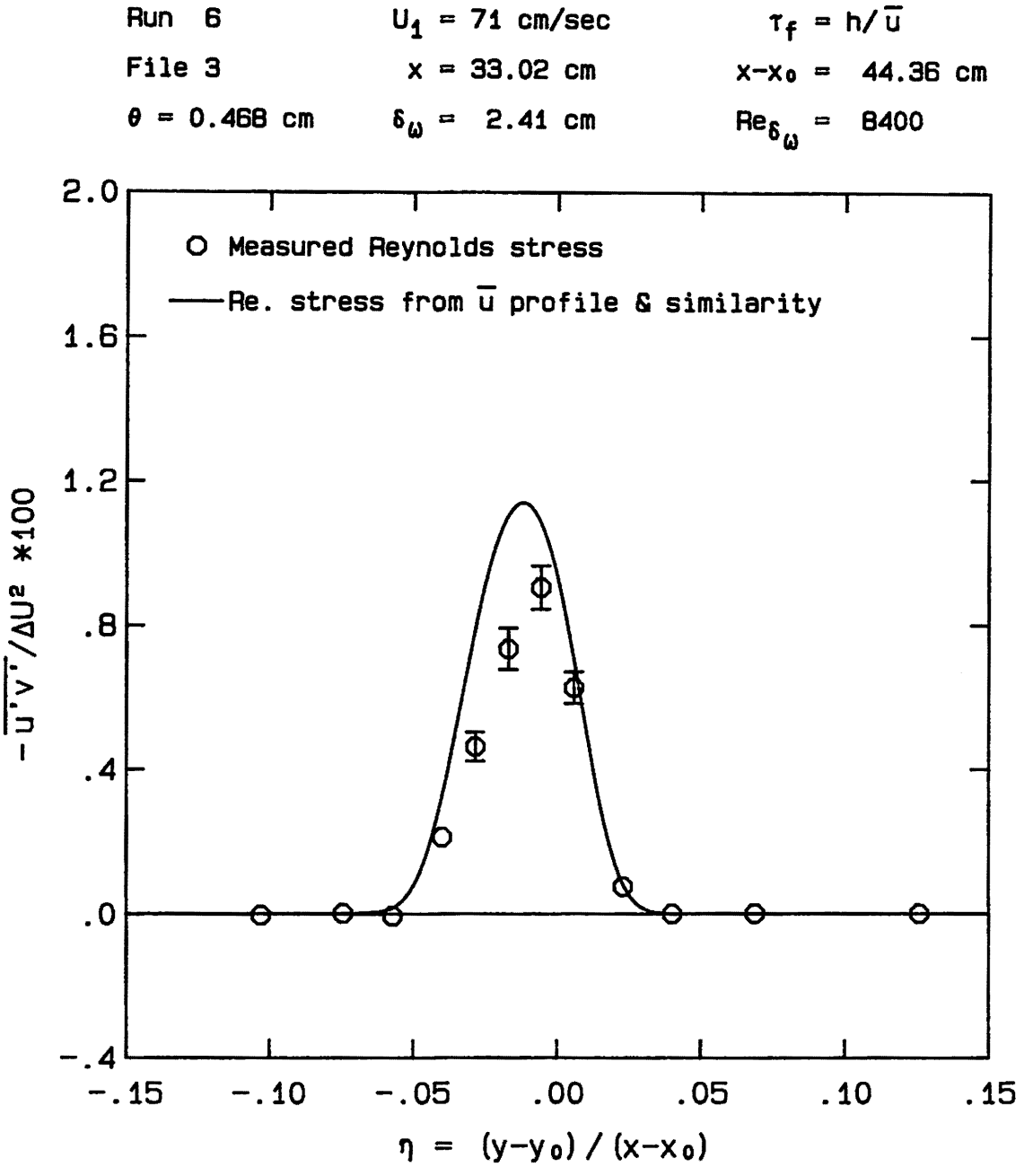

Figure 3.13 Reynolds Stress Profile at x = 33 cm

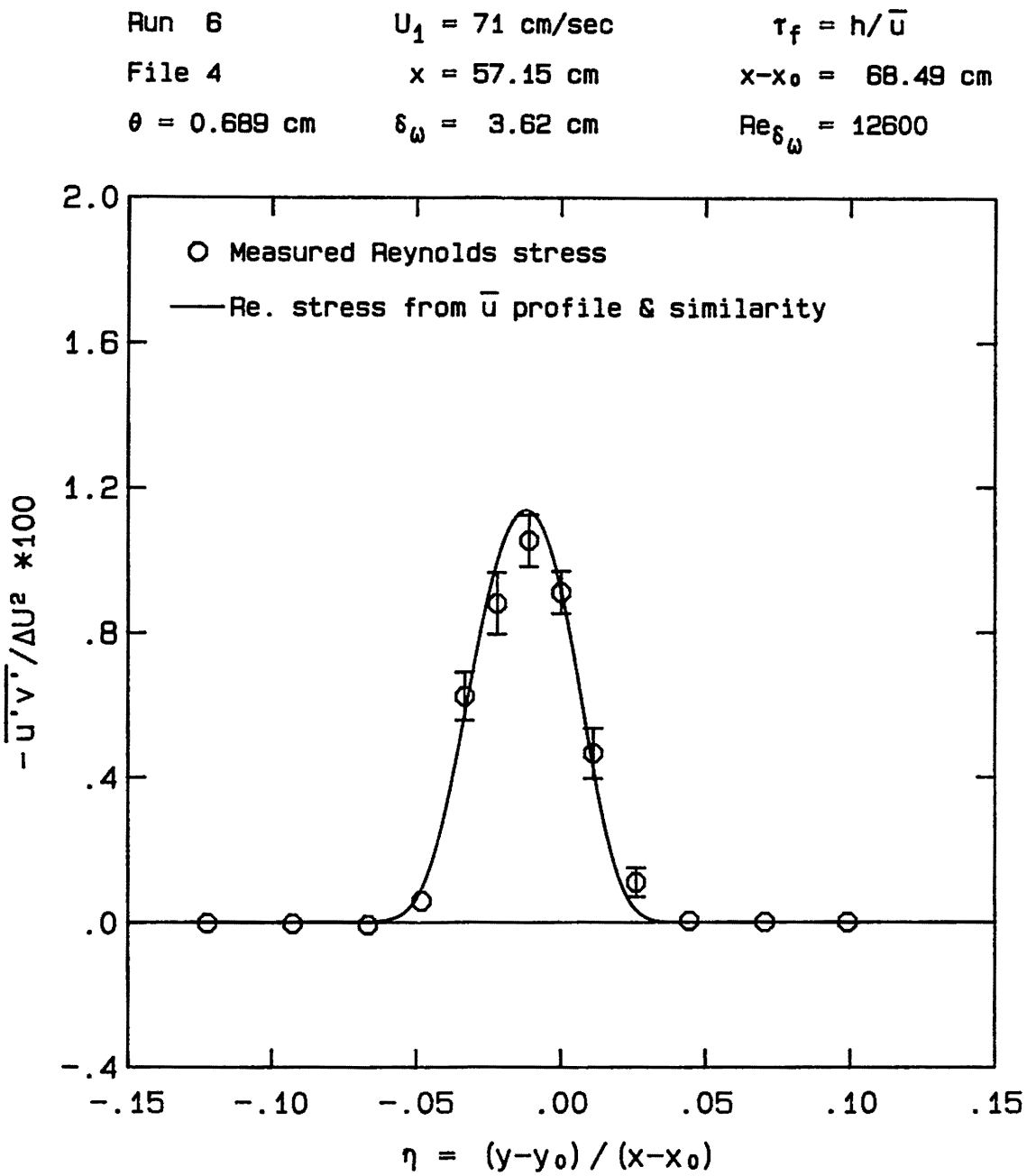

Figure 3.14 Reynolds Stress Profile at x = 57 cm

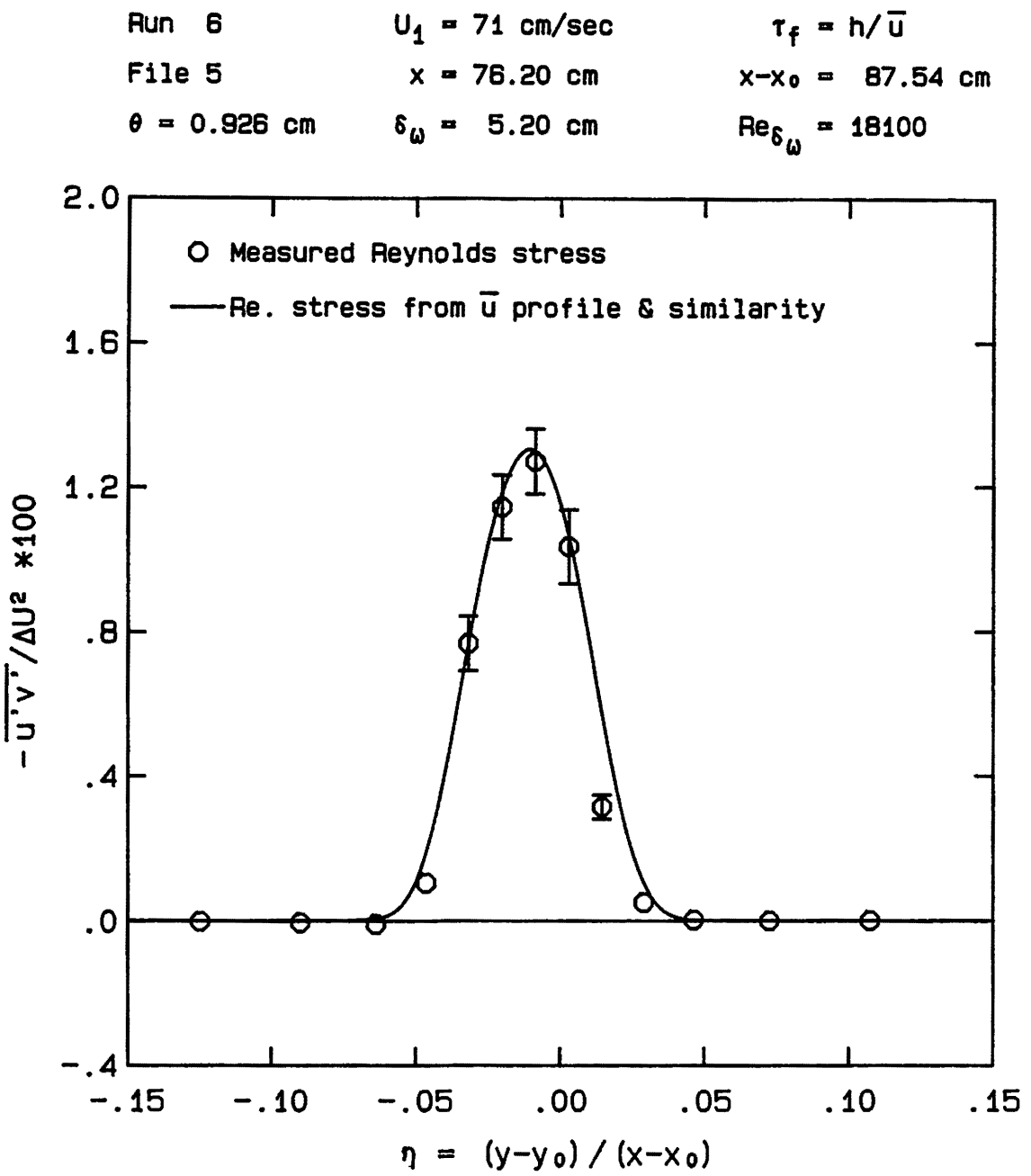

Figure 3.15 Reynolds Stress Profile at x = 76 cm

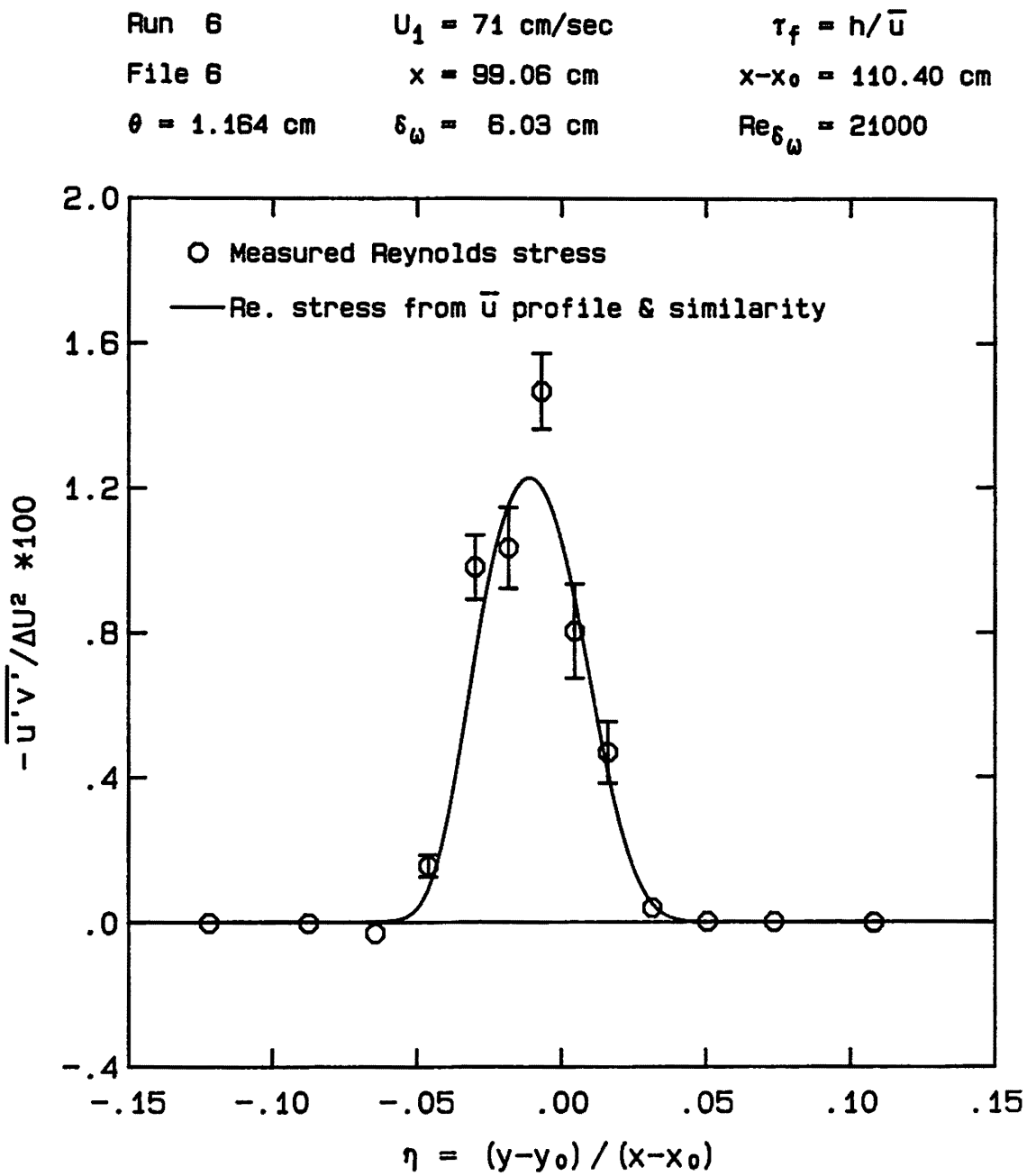

Figure 3.16 Reynolds Stress Profile at x = 99 cm

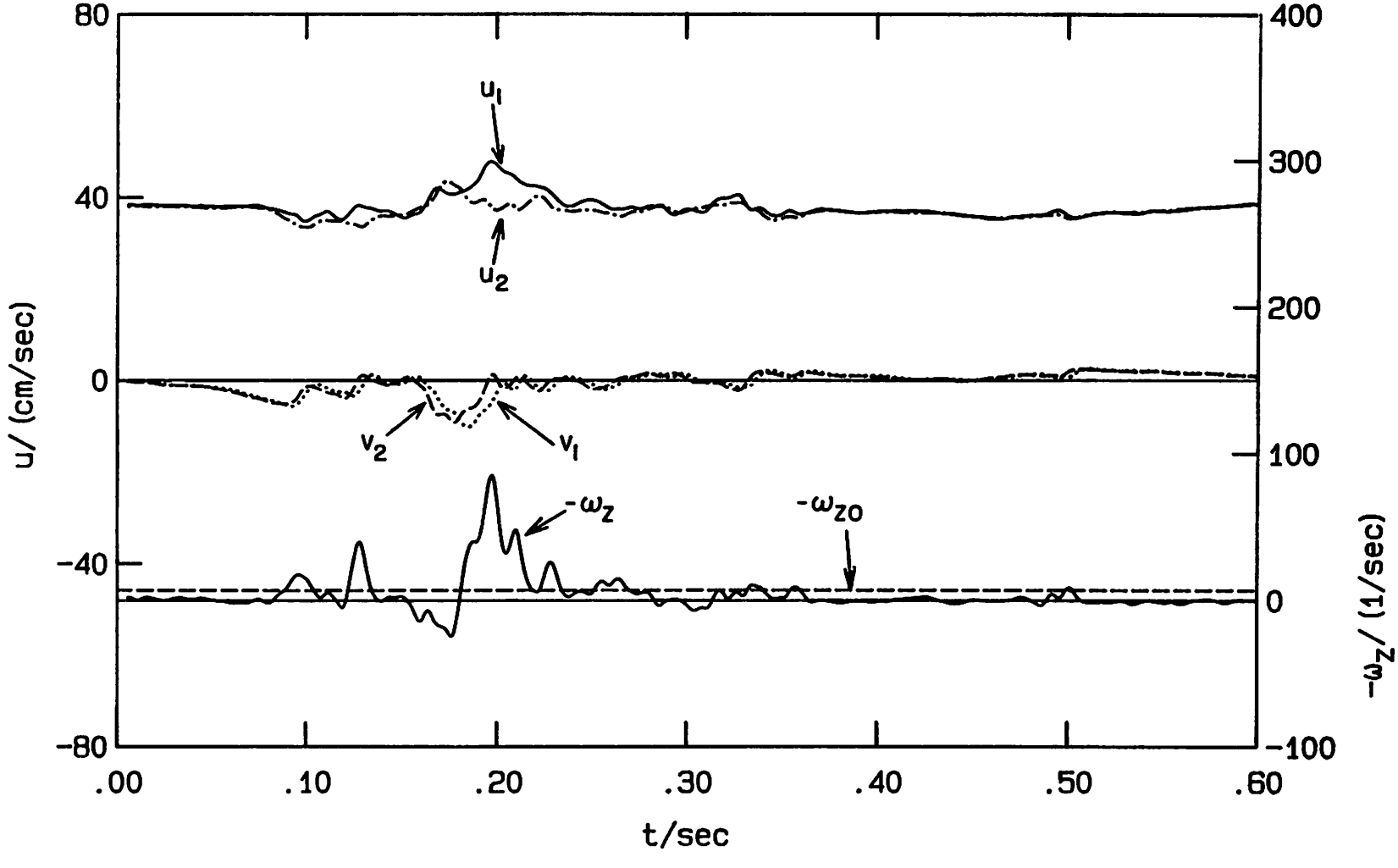

Figure 4.1a Velocity and Vorticity vs. Time, $\eta = -.0464$

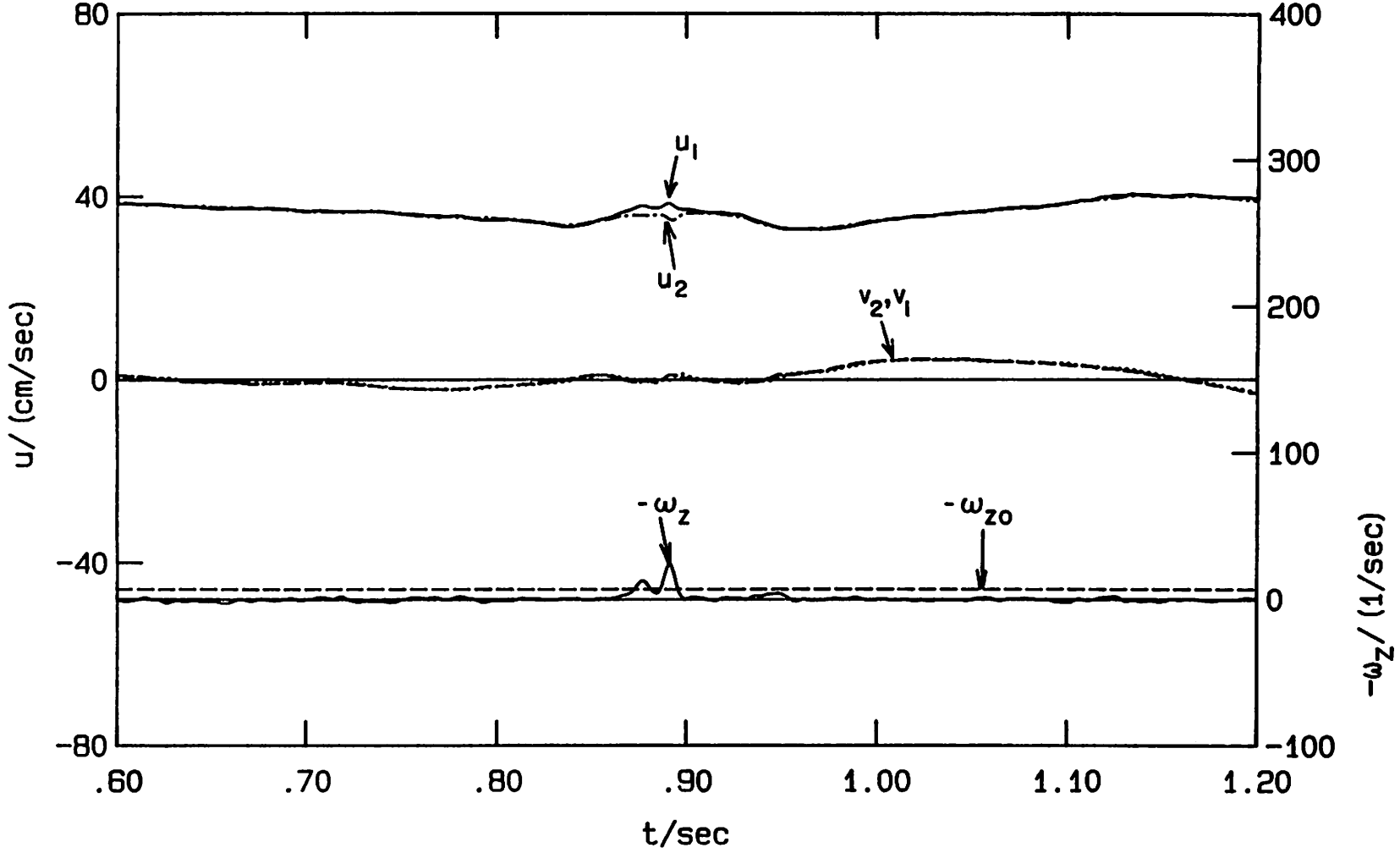

Figure 4.1b Velocity and Vorticity vs. Time, $\eta = -.0464$

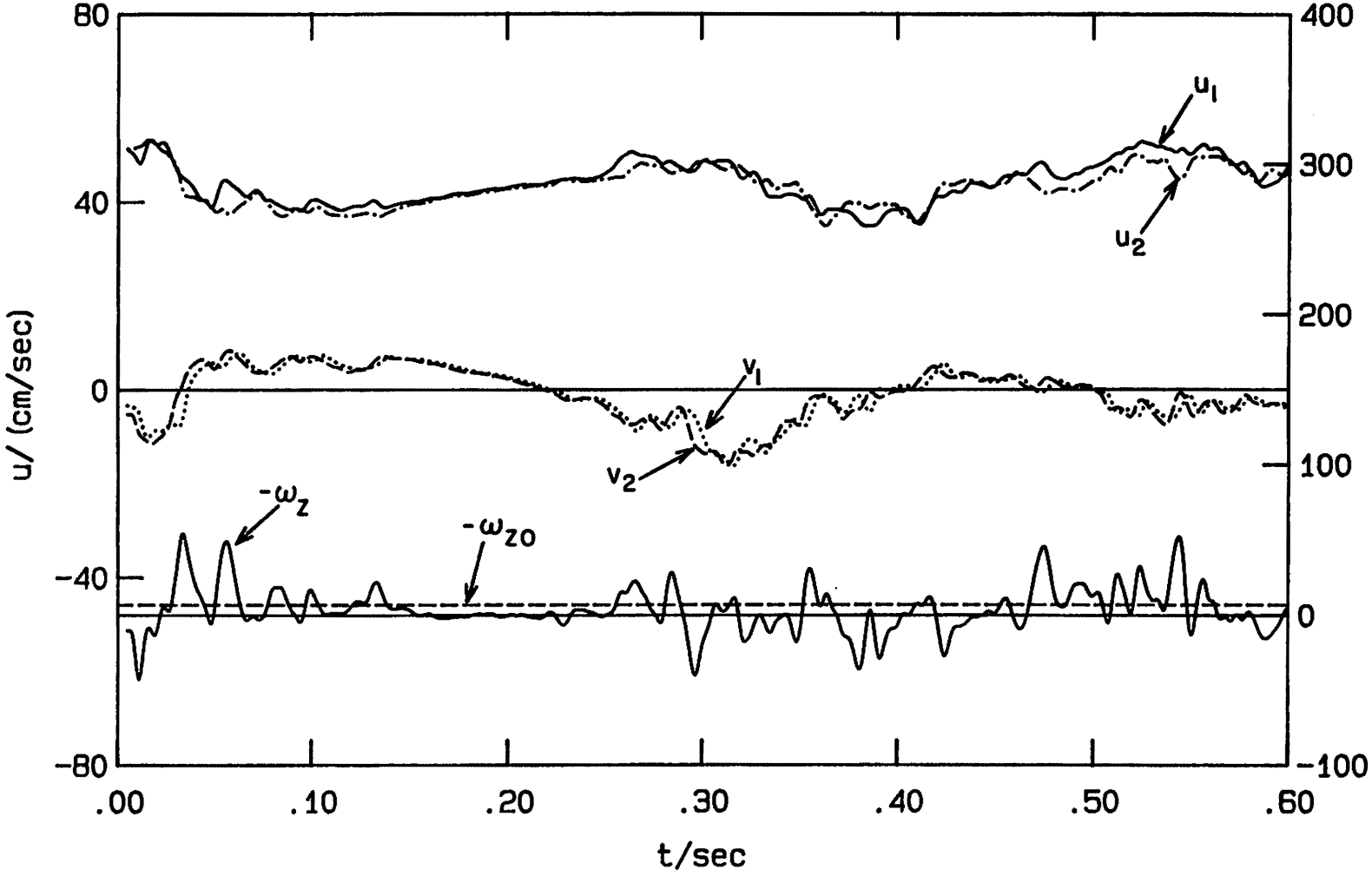

Figure 4.2a Velocity and Vorticity vs. Time, $\eta = -.0319$

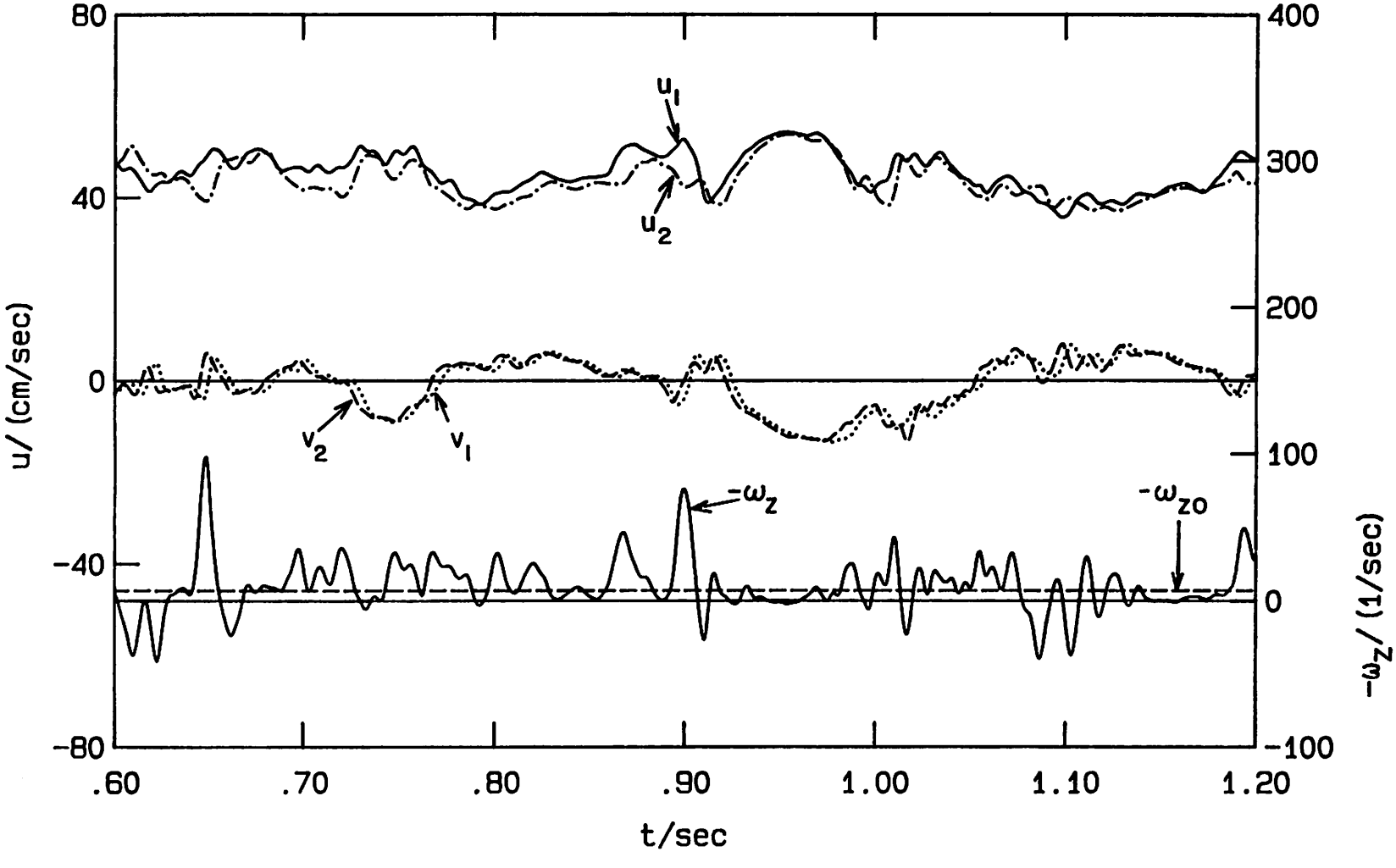

Figure 4.2b Velocity and Vorticity vs. Time, $\eta = -.0319$

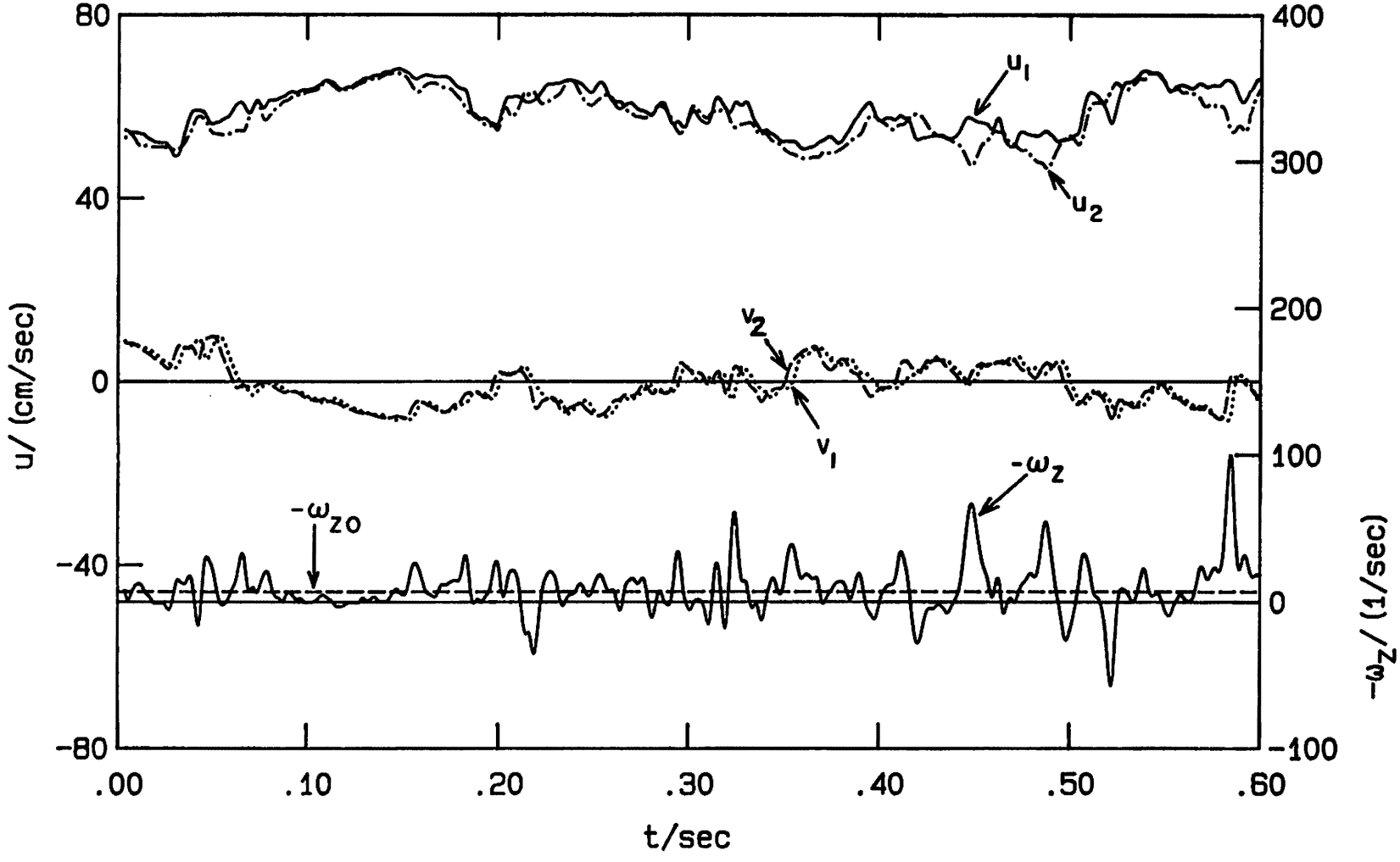

Figure 4.3a Velocity and Vorticity vs. Time, $\eta = -.0087$

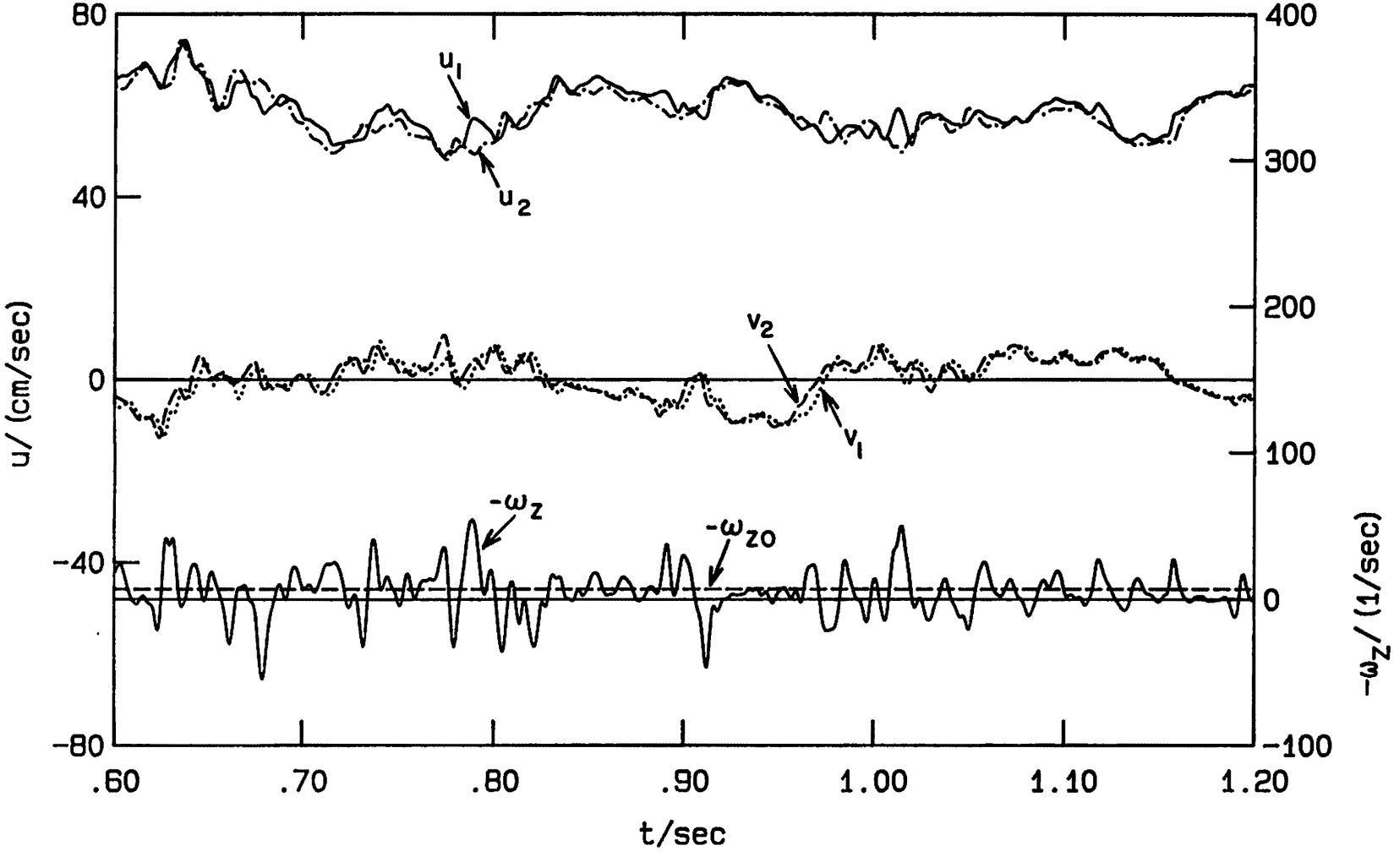

Figure 4.3b Velocity and Vorticity vs. Time, $\eta = -.0087$

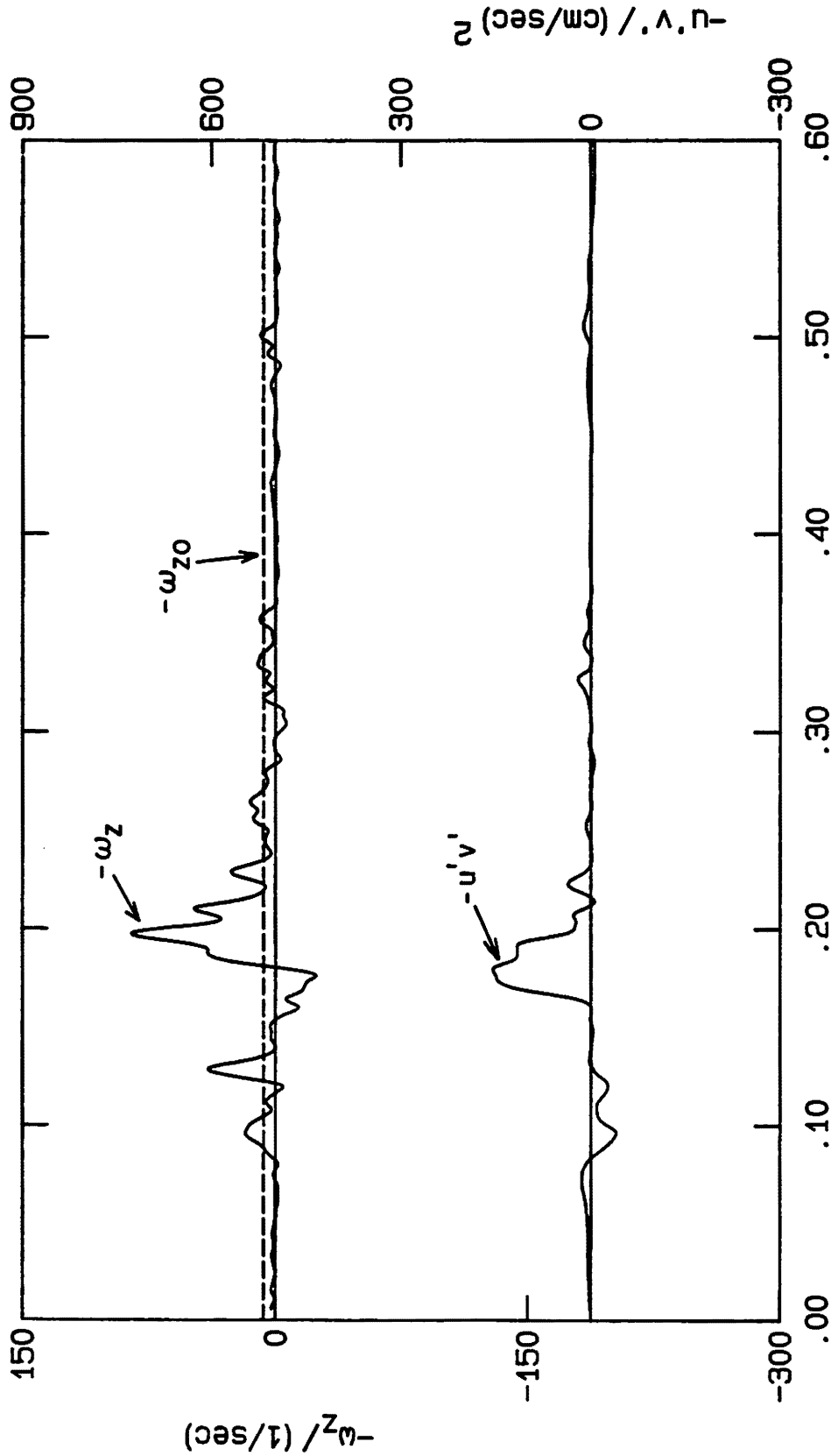

Figure 4.4 Vorticity and -u'v' vs. Time, $\eta = -.0464$

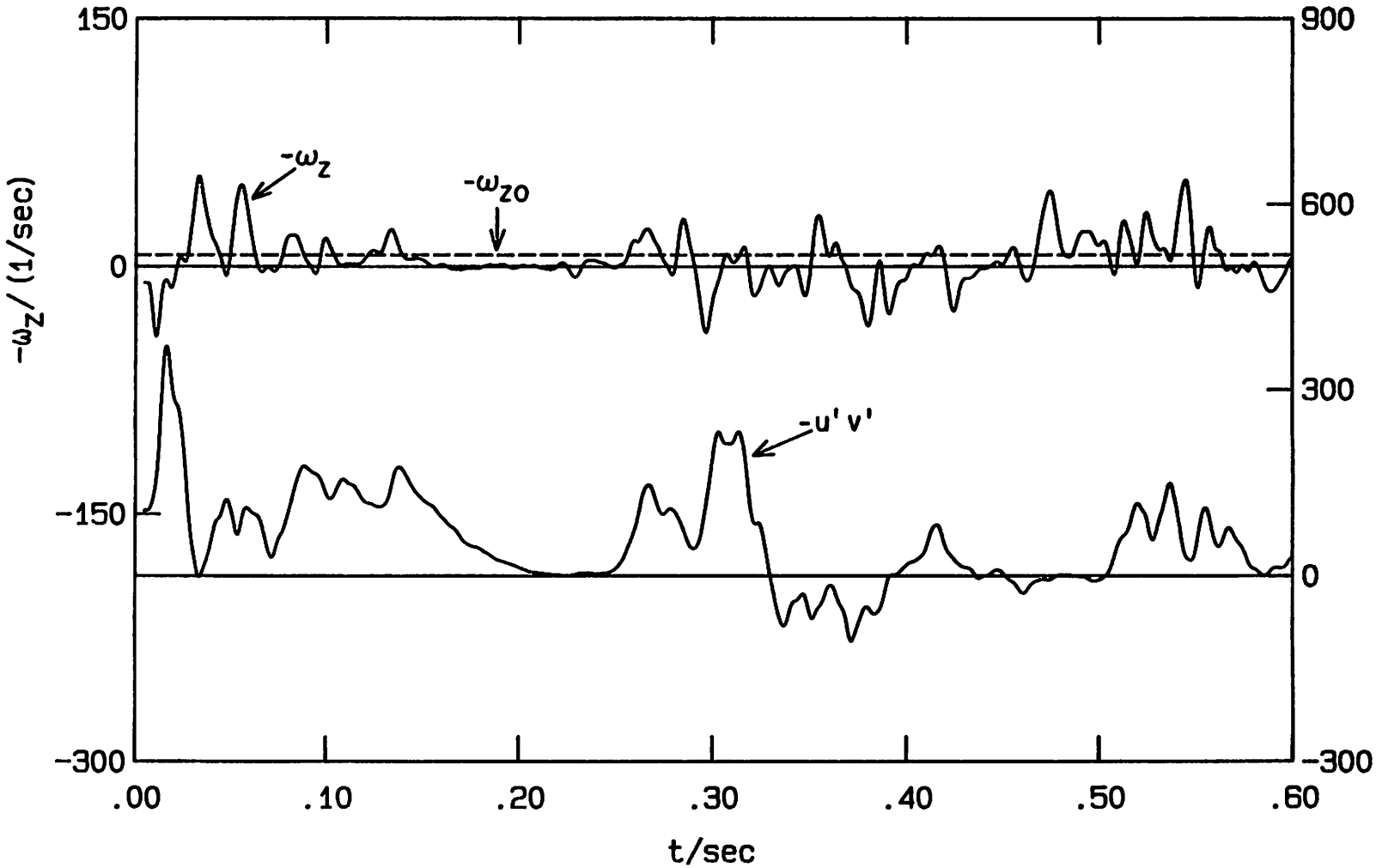

Figure 4.5 Vorticity and -u'v' vs. Time, $\eta = -.0319$

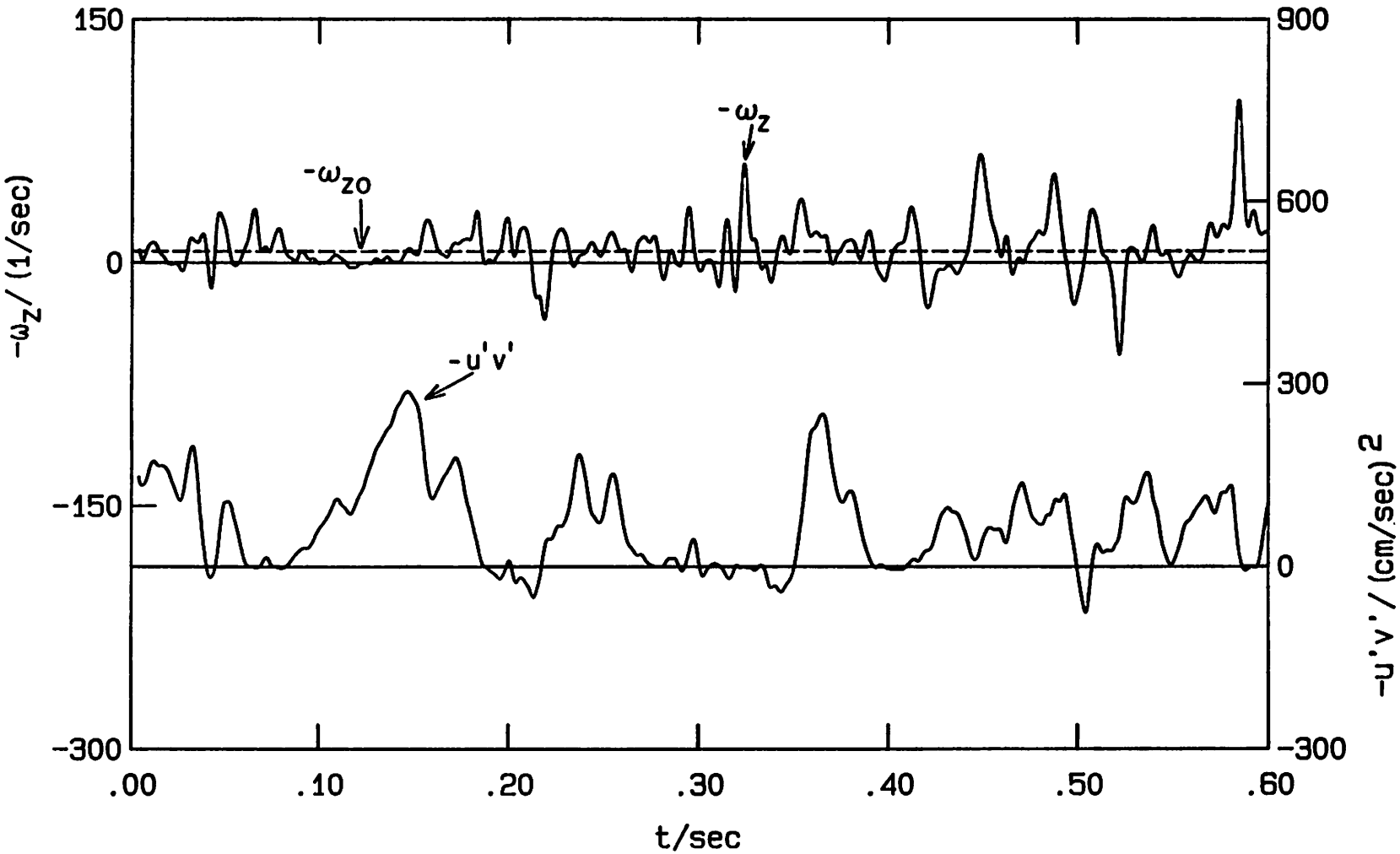

Figure 4.6 Vorticity and -u'v' vs. Time, η = -.0087

Run 6 U_1 = 71 cm/sec $\tau_f = h/\bar{u}$

File 2 x = 15.24 cm $x-x_o$ = 26.58 cm

θ = 0.264 cm δ_ω = 1.41 cm Re_{δ_ω} = 4900

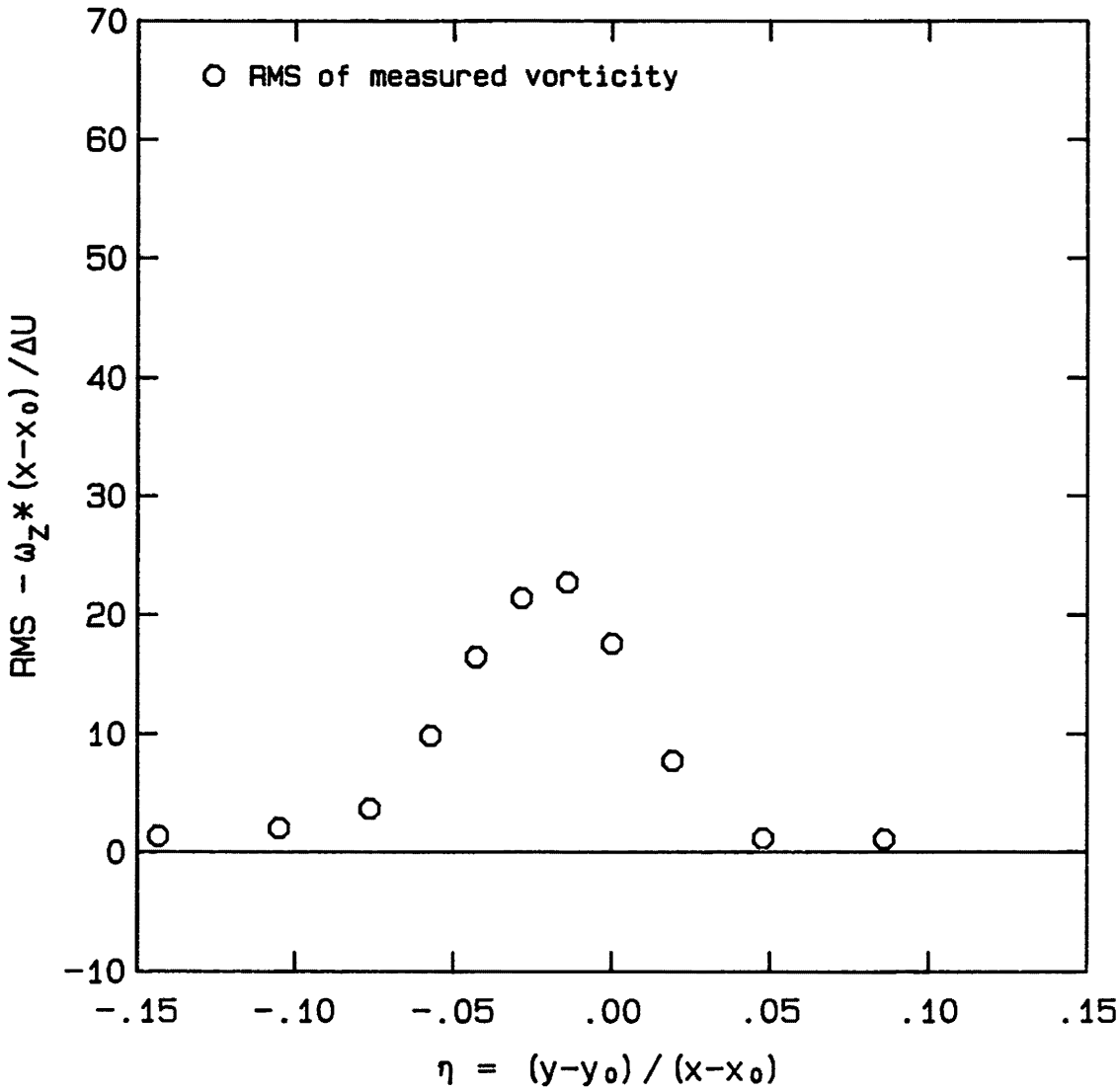

Figure 4.7 RMS of Measured Vorticity, x = 15 cm

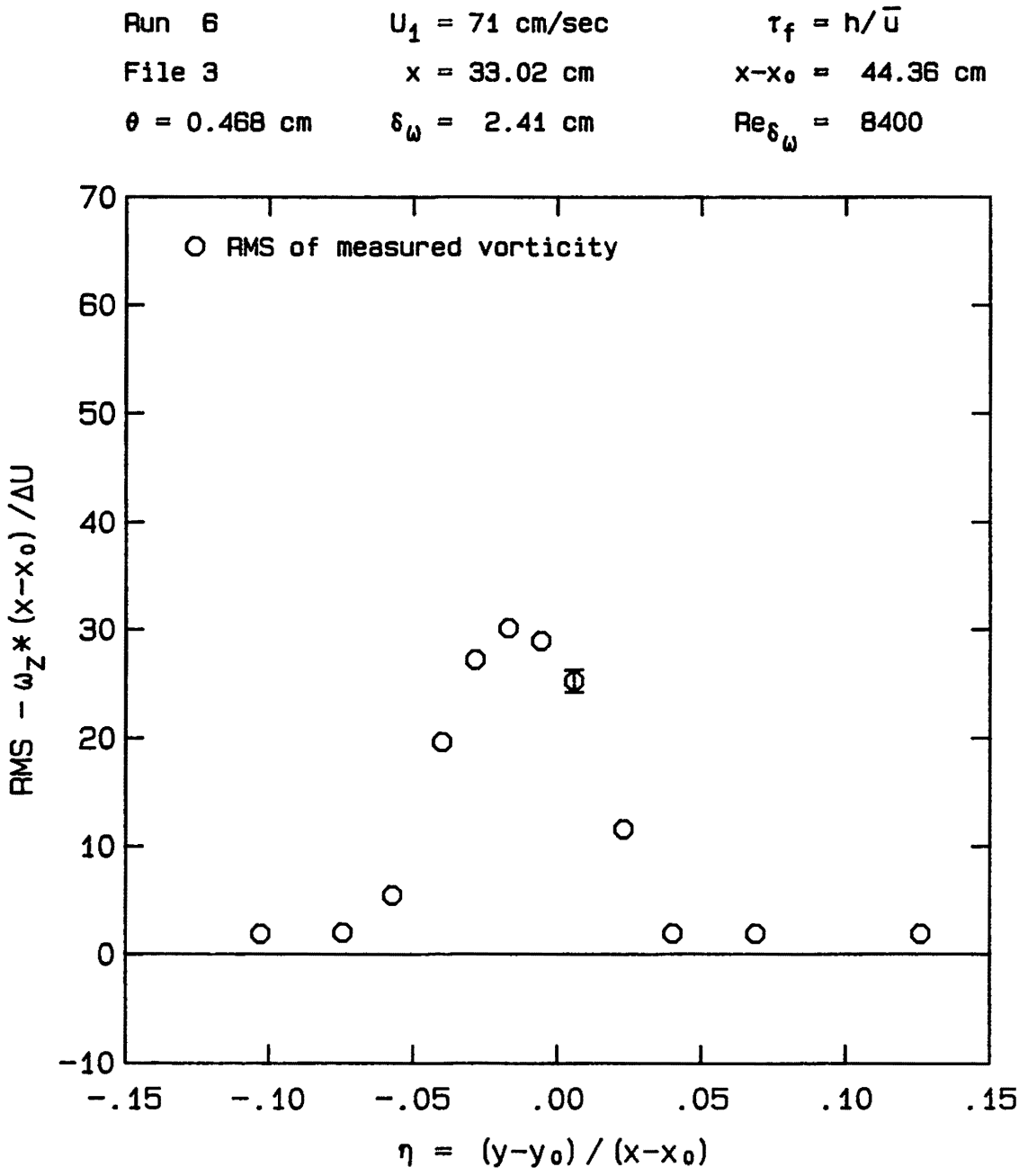

Figure 4.8 RMS of Measured Vorticity, x = 33 cm

Run 6 U_1 = 71 cm/sec $\tau_f = h/\bar{u}$

File 4 x = 57.15 cm $x-x_0$ = 68.49 cm

θ = 0.689 cm δ_ω = 3.62 cm Re_{δ_ω} = 12600

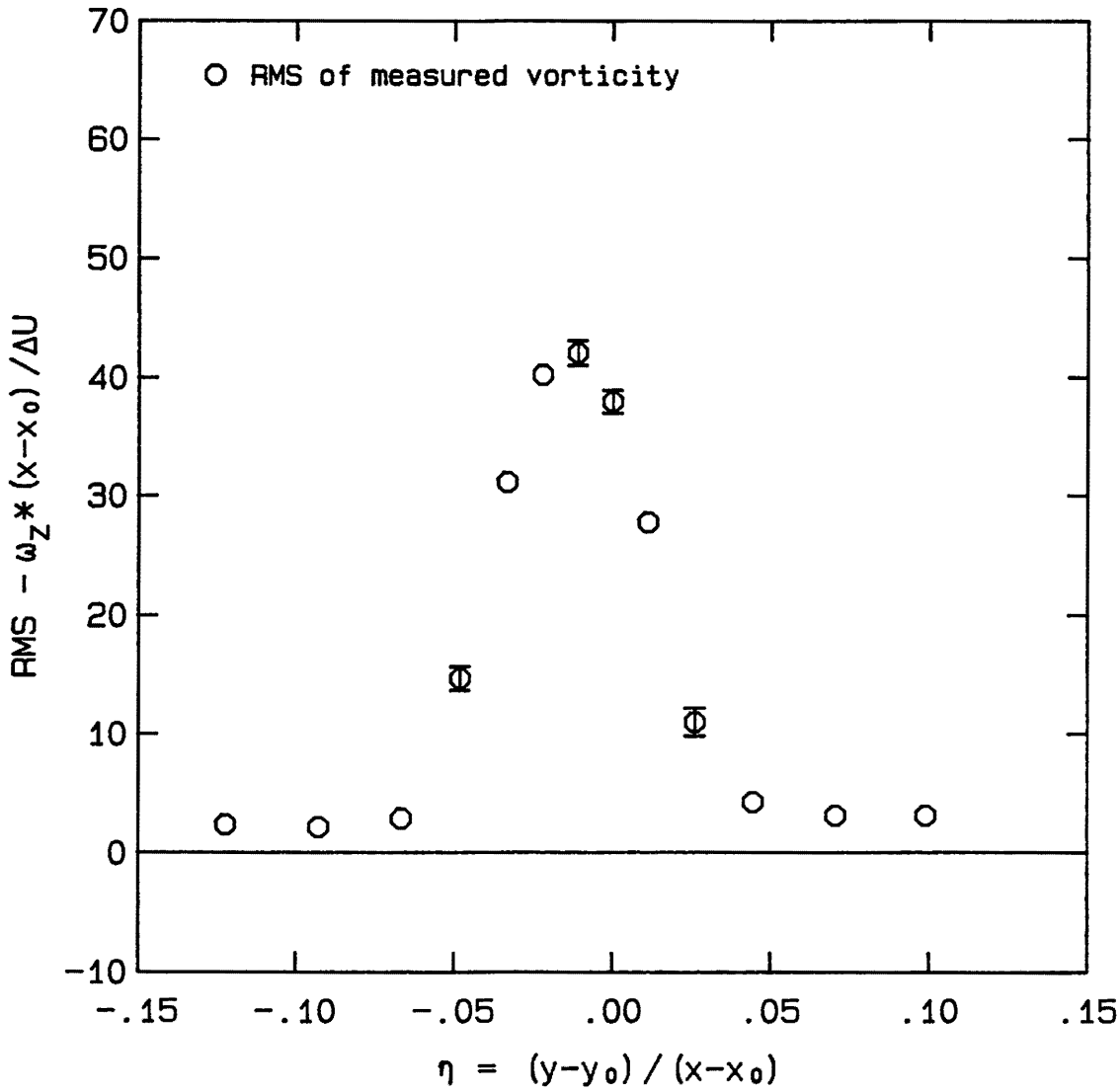

Figure 4.9 RMS of Measured Vorticity, x = 57 cm

Run 6 U_1 = 71 cm/sec $\tau_f = h/\bar{u}$

File 5 x = 76.20 cm $x-x_o$ = 87.54 cm

θ = 0.926 cm δ_ω = 5.20 cm Re_{δ_ω} = 18100

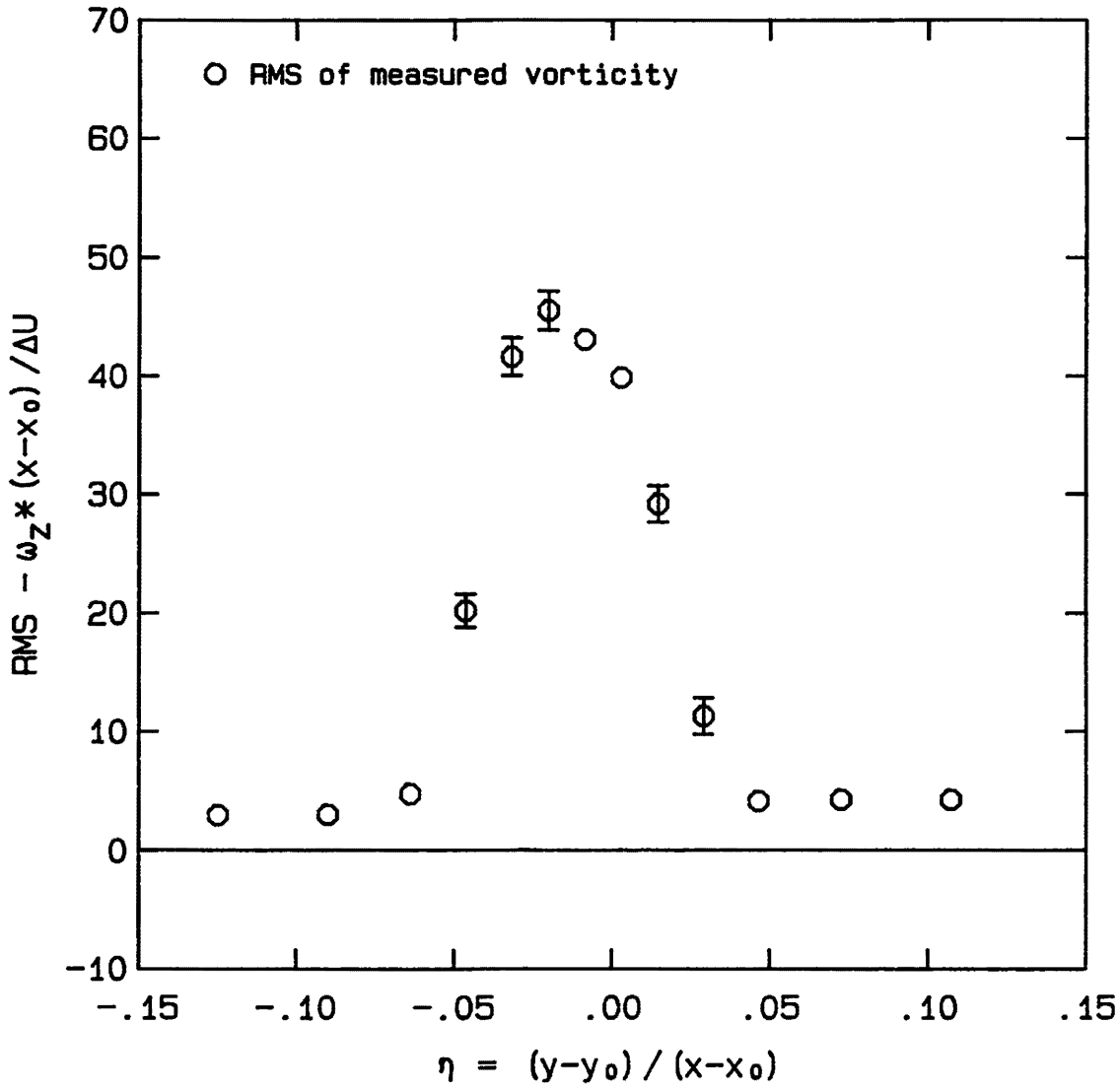

Figure 4.10 RMS of Measured Vorticity, x = 76 cm

Run 6 U_1 = 71 cm/sec $\tau_f = h/\bar{u}$

File 6 x = 99.06 cm $x-x_0$ = 110.40 cm

θ = 1.164 cm δ_ω = 6.03 cm Re_{δ_ω} = 21000

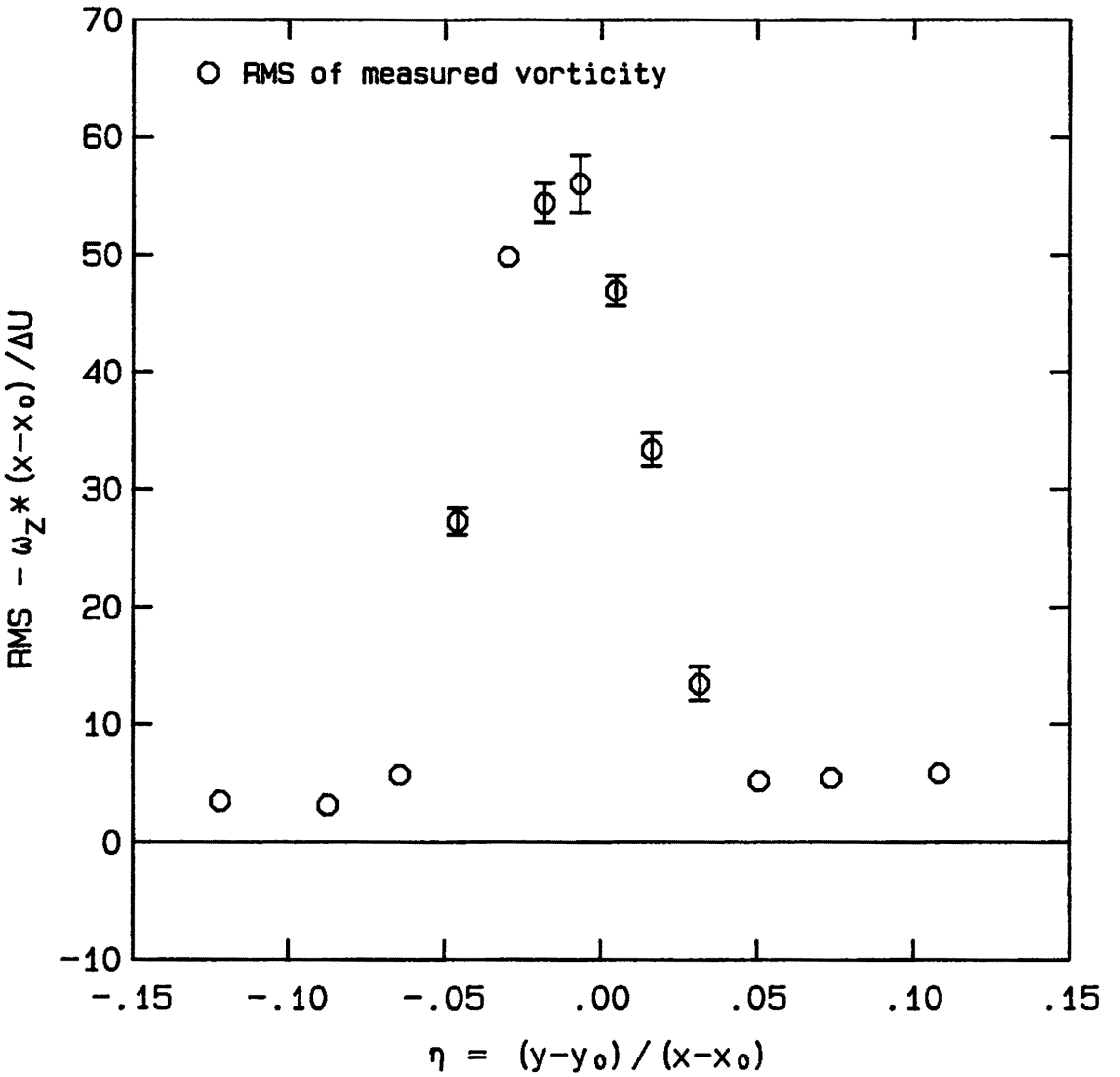

Figure 4.11 RMS of Measured Vorticity, x = 99 cm

INITIAL REGION OF SHEAR LAYER SHOWING
BOUNDARY LAYERS

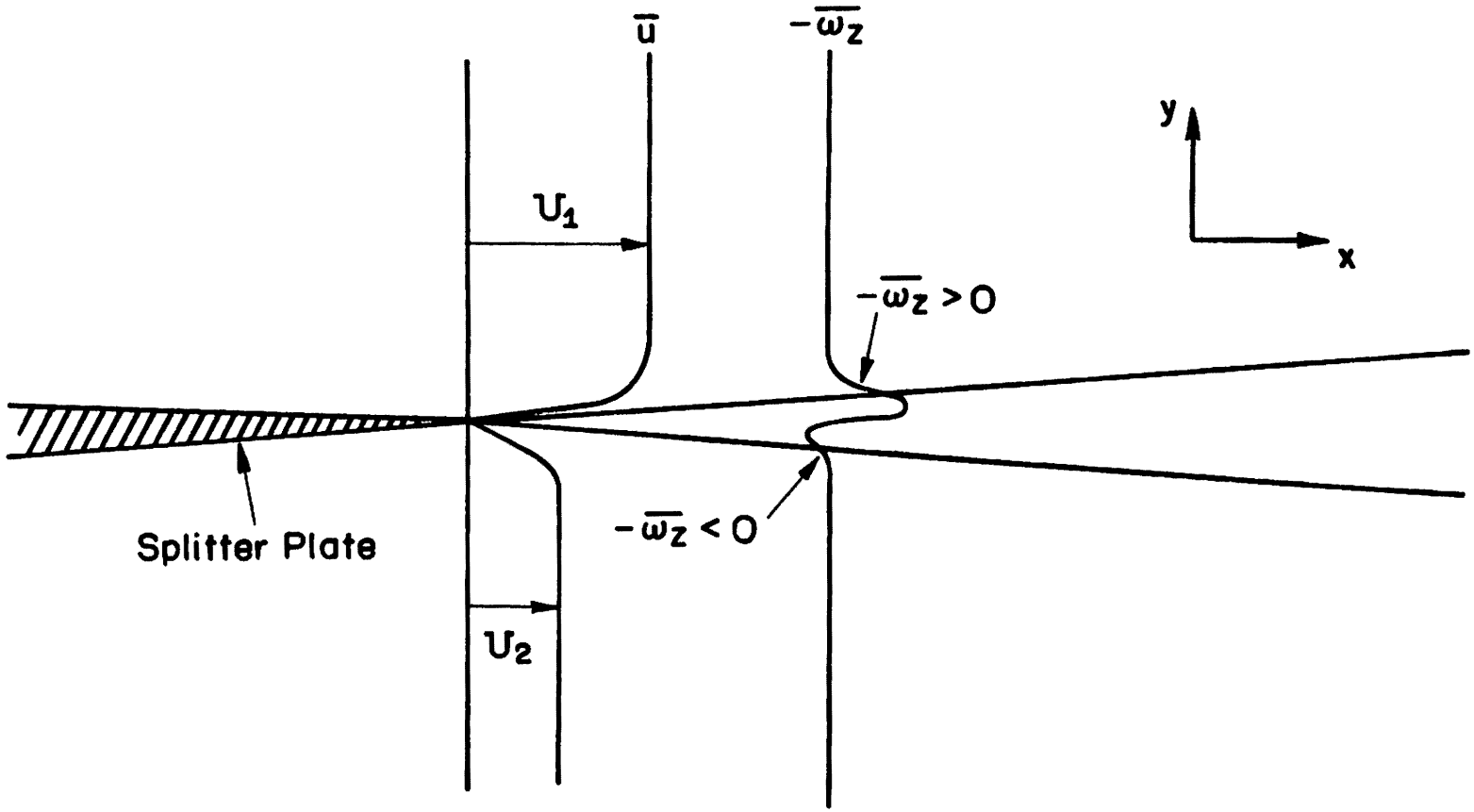

Figure 4.12 Initial Region of Shear Layer

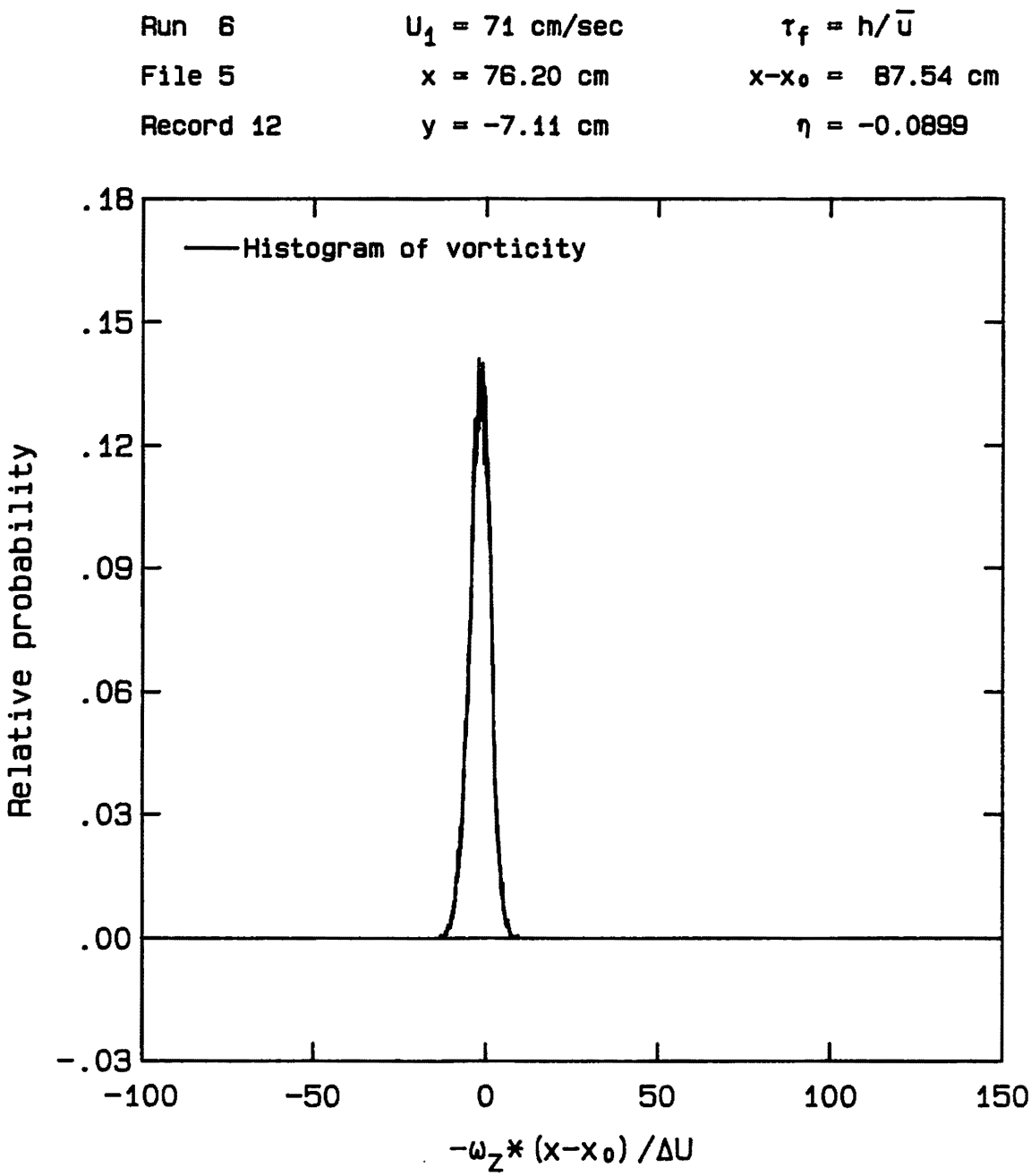

Figure 4.13 Unfiltered Vorticity Histogram, Low Speed Free Stream

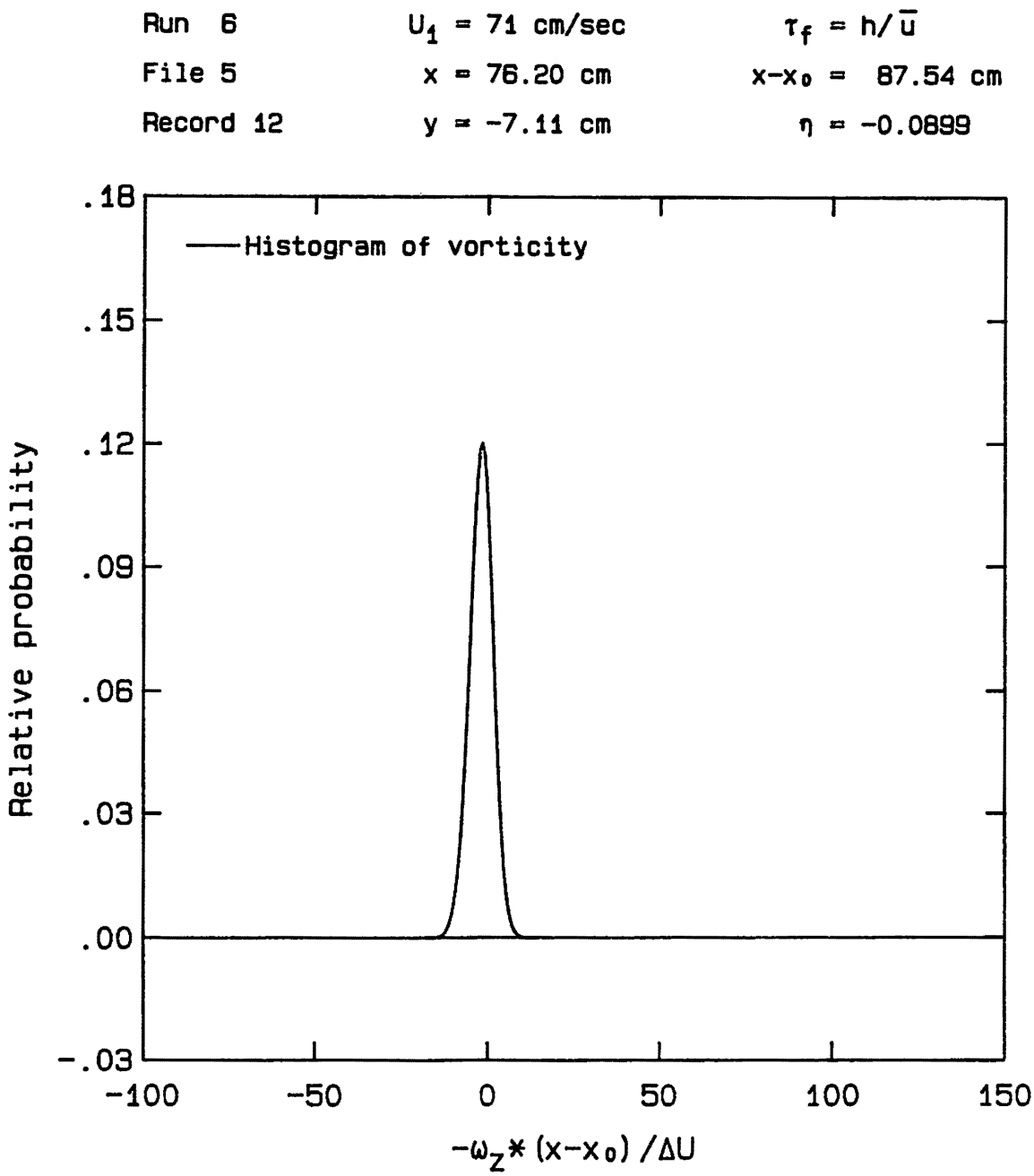

Figure 4.14 Filtered Vorticity Histogram, Low Speed Free Stream

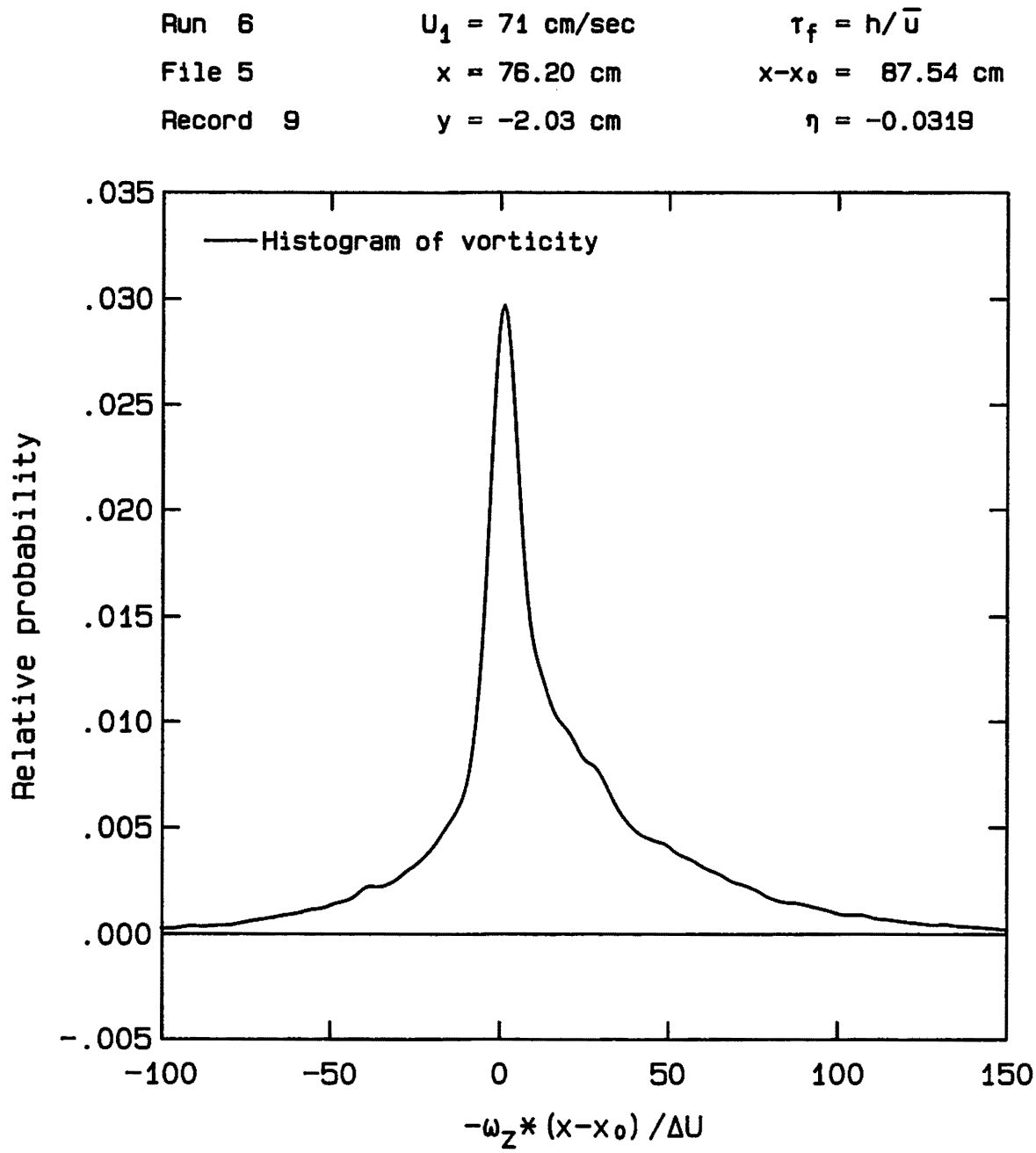

Figure 4.15 Filtered Vorticity Histogram, Slightly Below Centerline

Run 6 U_1 = 71 cm/sec $\tau_f = h/\bar{u}$

File 5 x = 76.20 cm $x-x_0$ = 87.54 cm

Record 7 y = 0.00 cm η = -0.0087

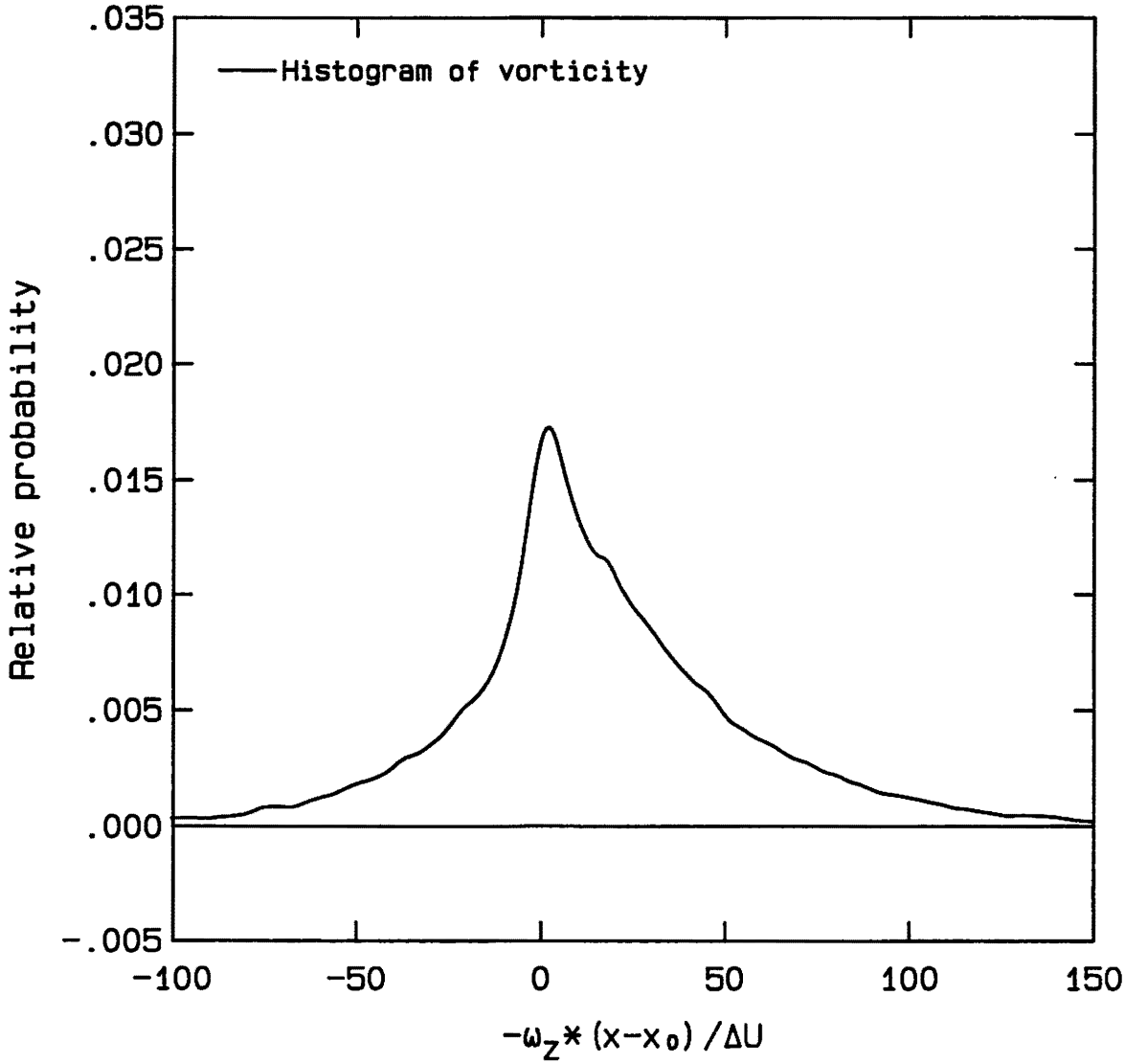

Figure 4.16 Filtered Vorticity Histogram, Near Centerline

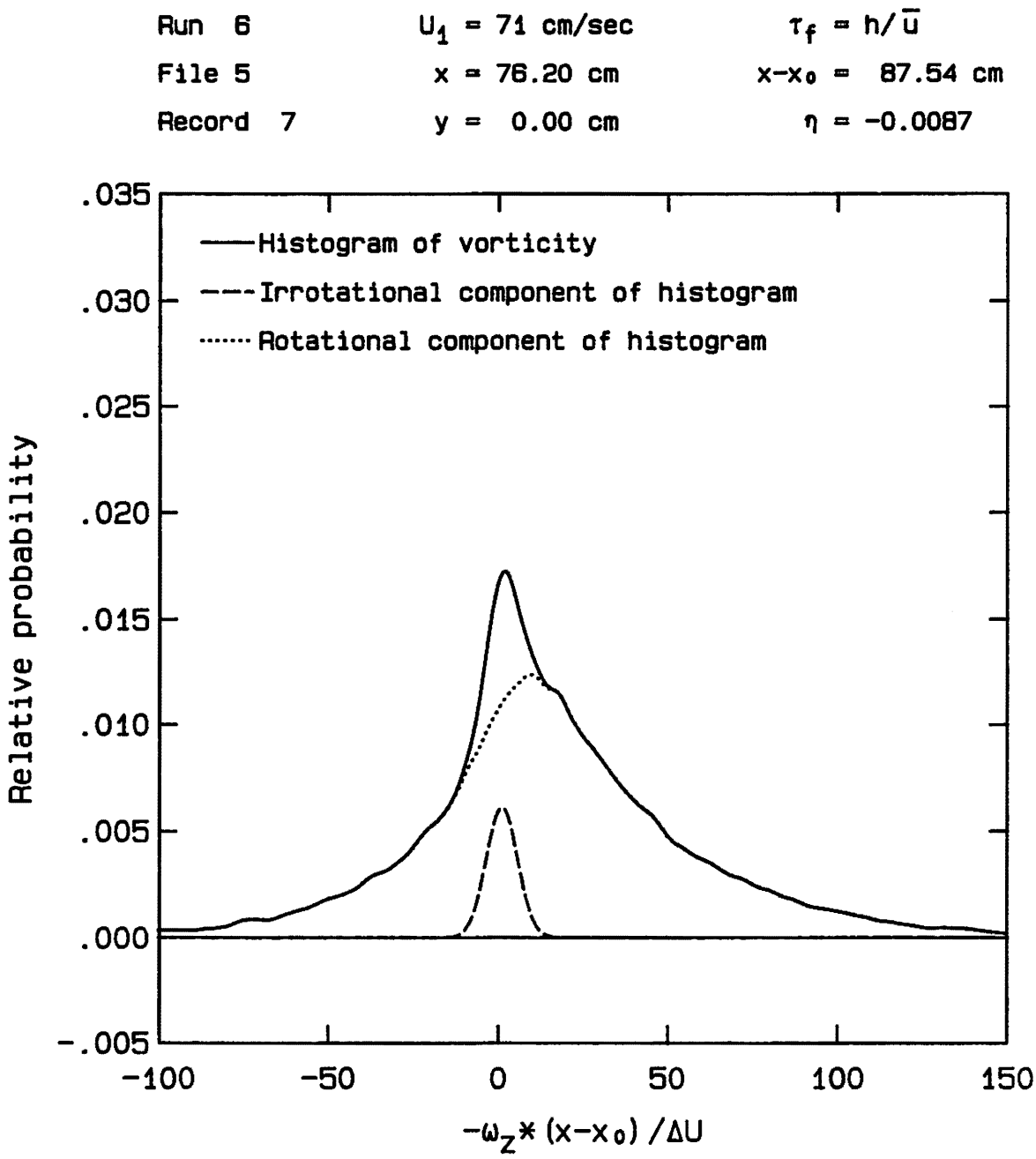

Figure 4.17 Filtered Vorticity Histogram Showing Gaussian Curve Fit, Near Centerline

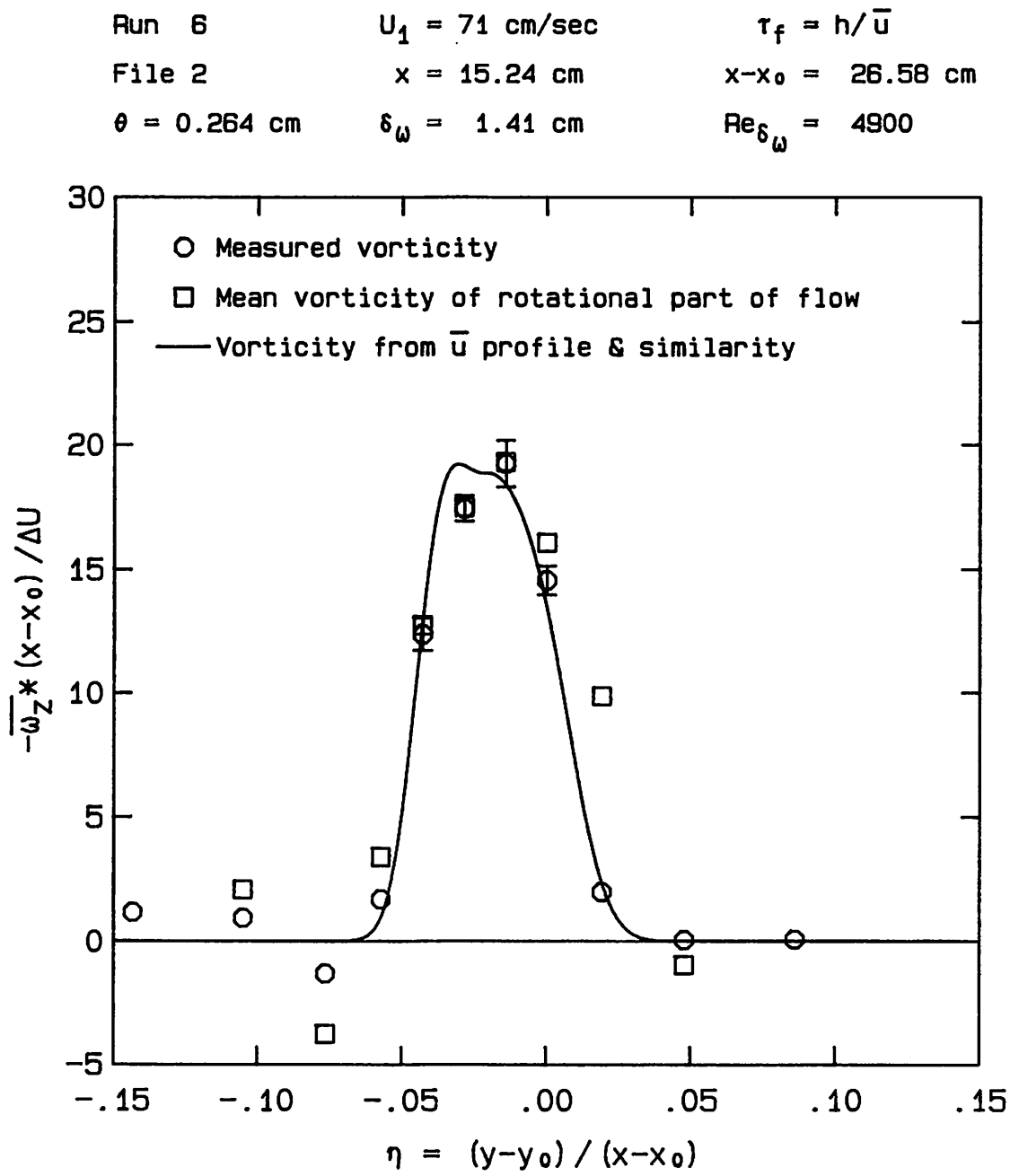

Figure 4.18 Vorticity Profile Showing Mean of Rotational Part of Flow, x = 15 cm

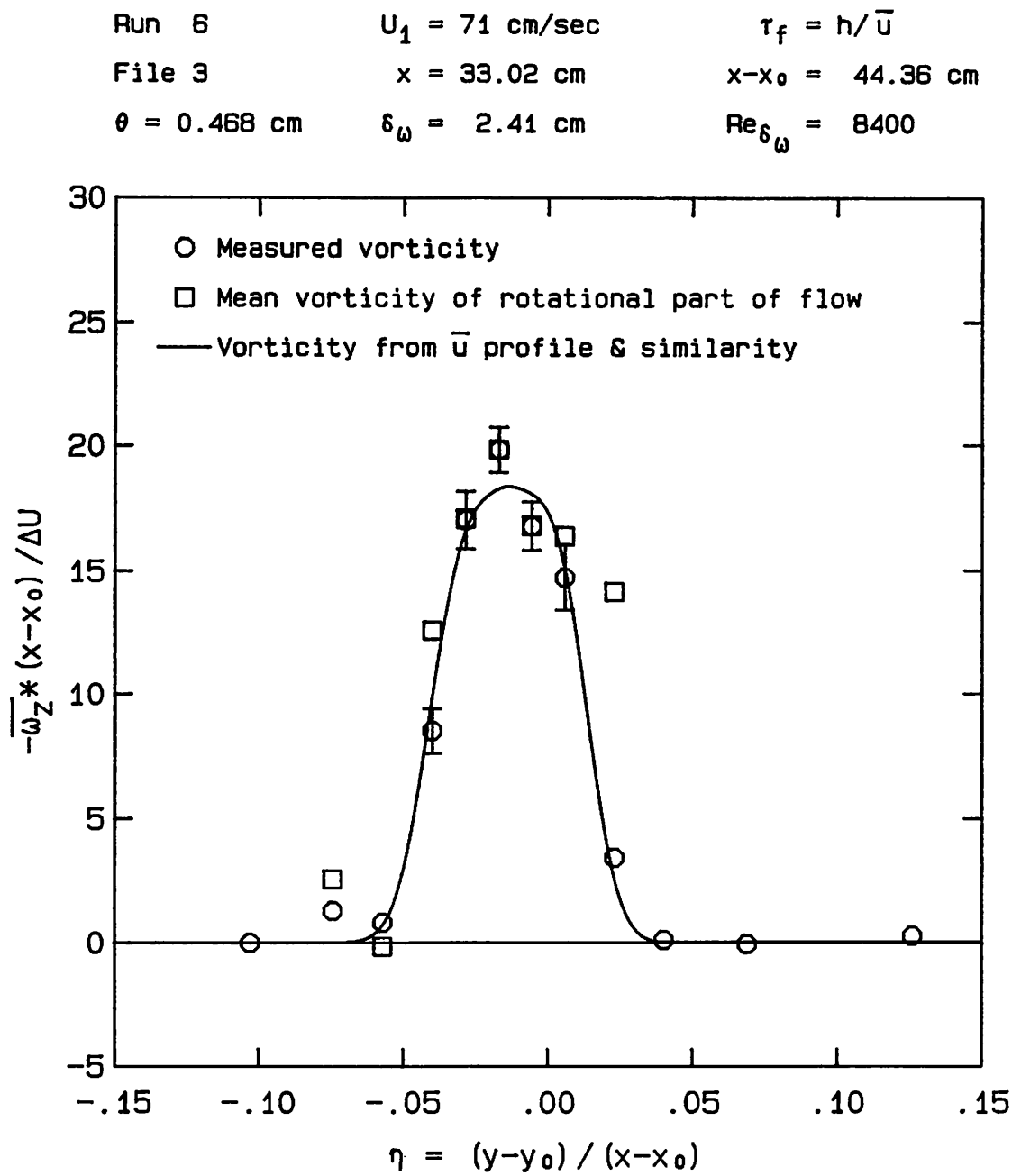

Figure 4.19 Vorticity Profile Showing Mean of Rotational Part of Flow, x = 33 cm

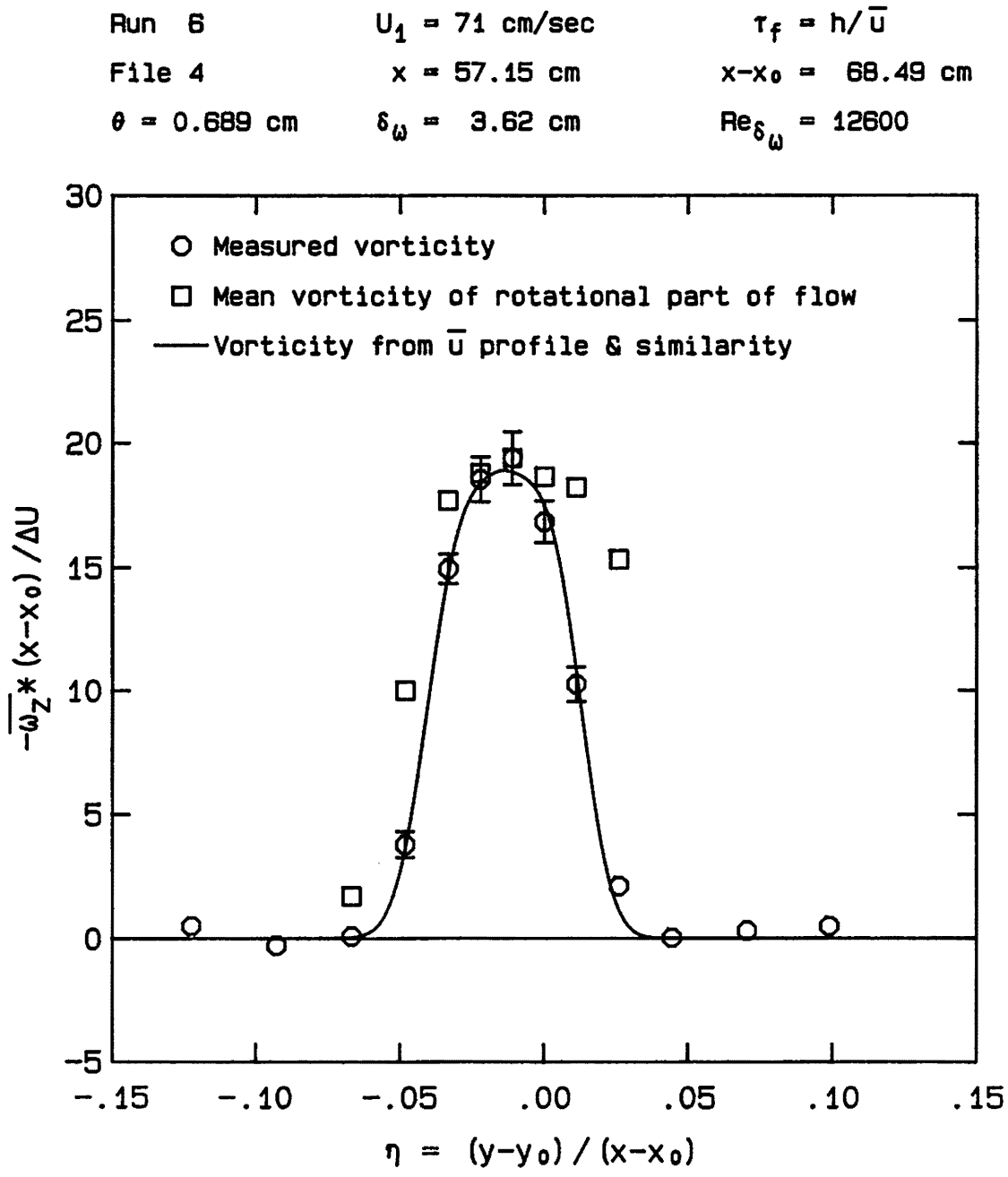

Figure 4.20 Vorticity Profile Showing Mean of Rotational Part of Flow, x = 57 cm

Run 6 U_1 = 71 cm/sec $\tau_f = h/\bar{u}$

File 5 x = 76.20 cm $x-x_o$ = 87.54 cm

θ = 0.926 cm δ_ω = 5.20 cm Re_{δ_ω} = 18100

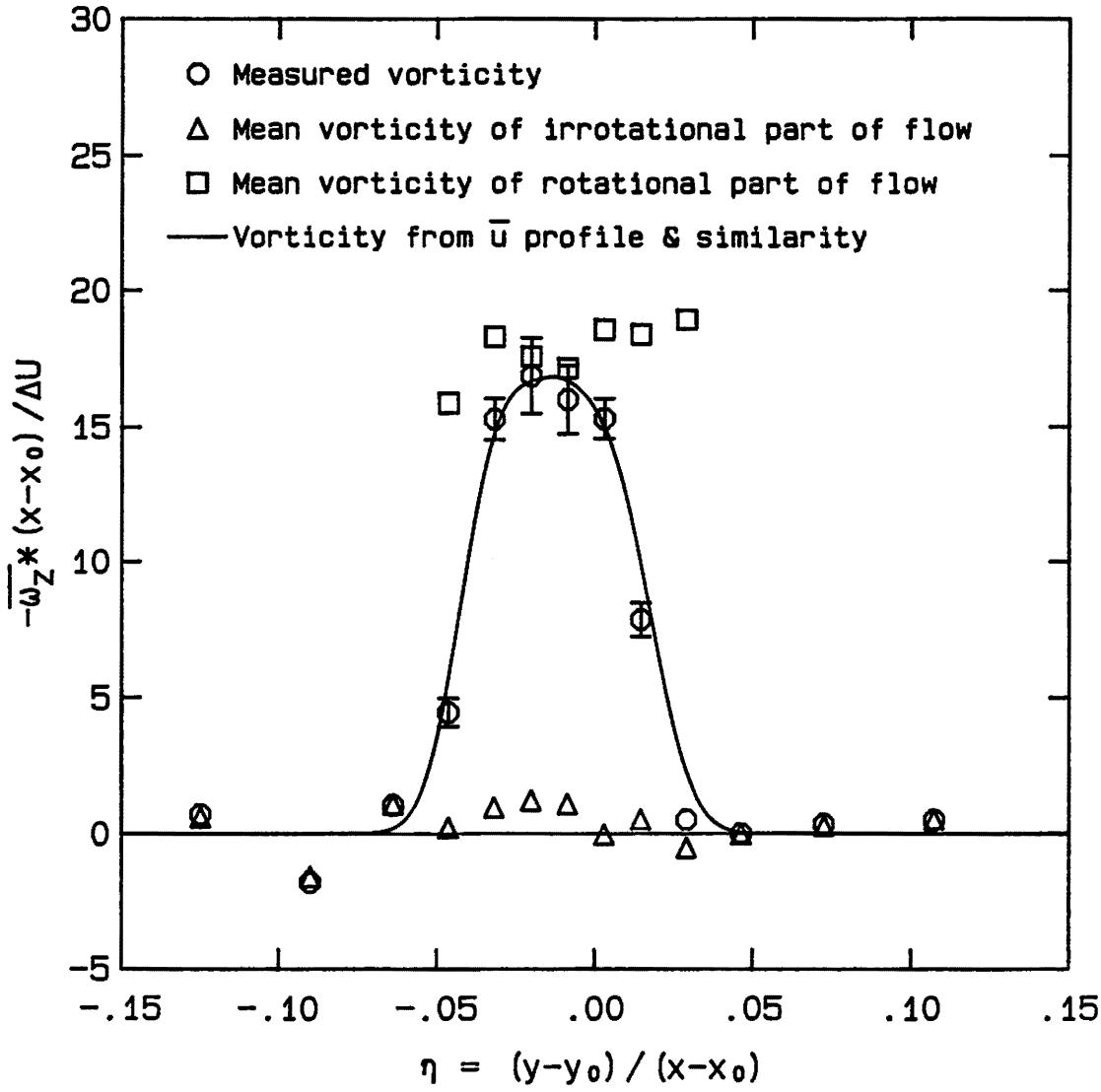

Figure 4.21 Vorticity Profile Showing Mean of Rotational Part of Flow, x = 76 cm

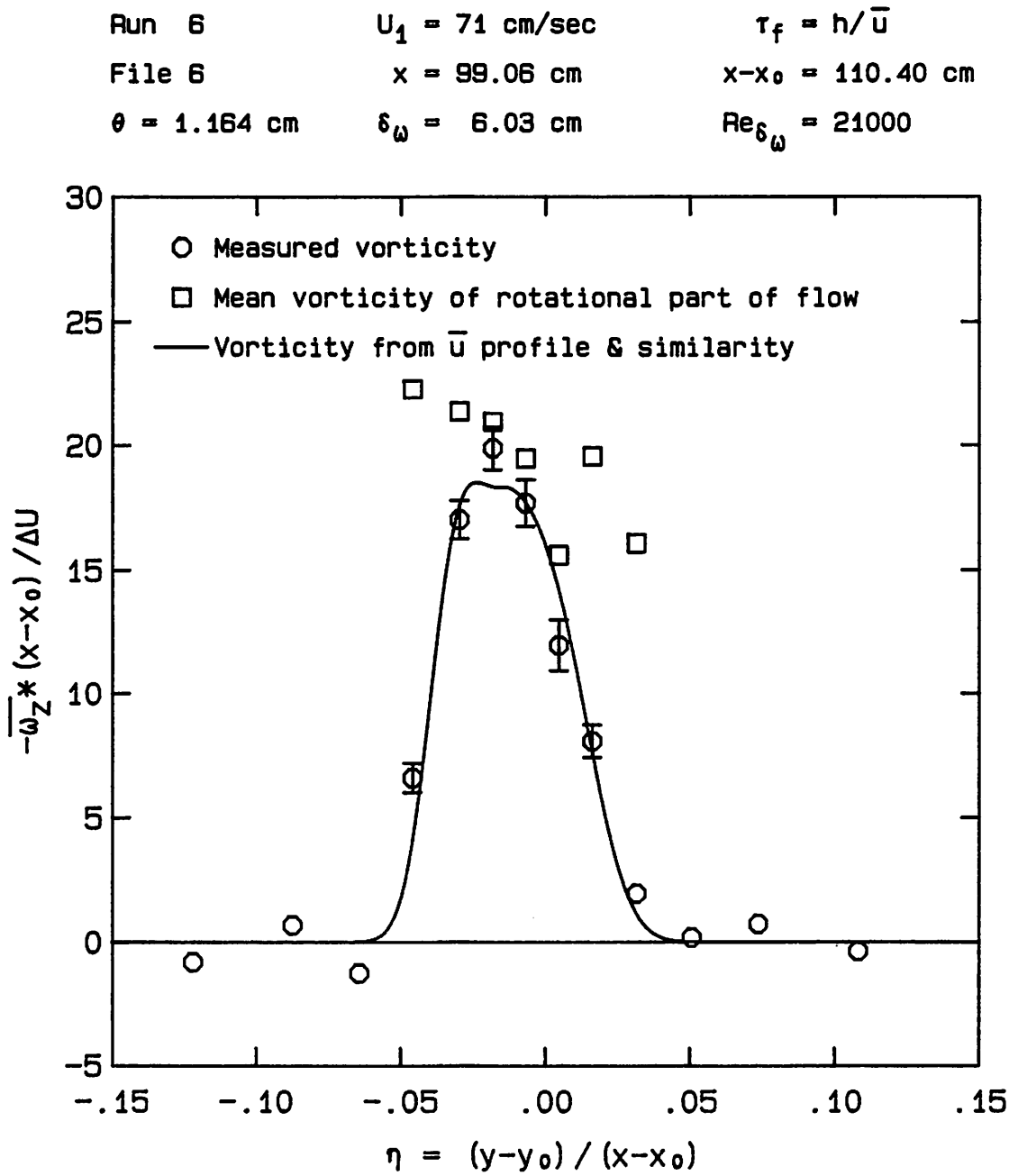

Figure 4.22 Vorticity Profile Showing Mean of Rotational Part of Flow, x = 99 cm

Run 6 U_1 = 71 cm/sec $\tau_f = h/\bar{u}$

File 2 x = 15.24 cm $x-x_o$ = 26.58 cm

θ = 0.264 cm δ_ω = 1.41 cm Re_{δ_ω} = 4900

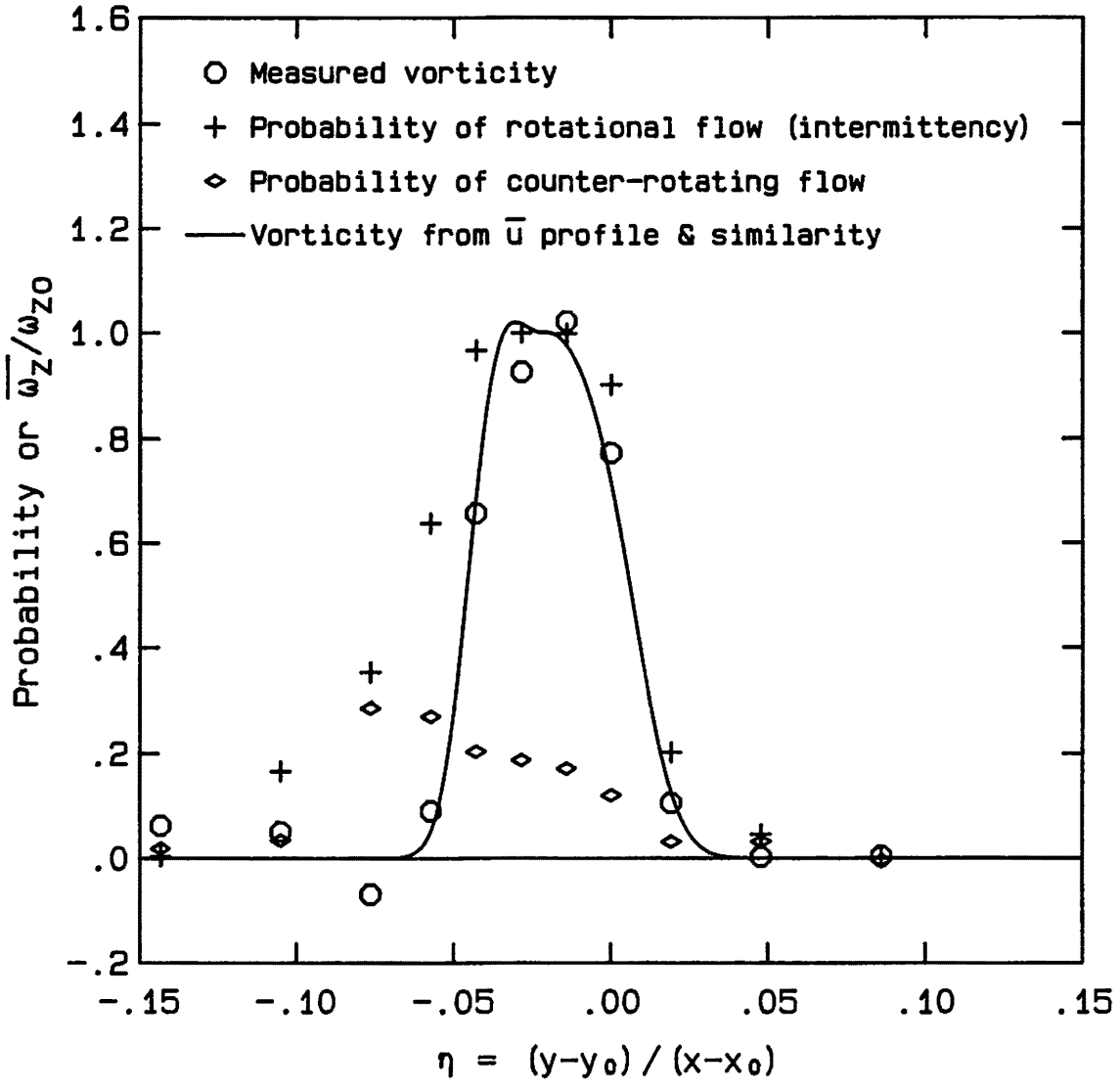

Figure 4.23 Vorticity Profile Showing Intermittency and Counter-rotating Flow, x = 15 cm

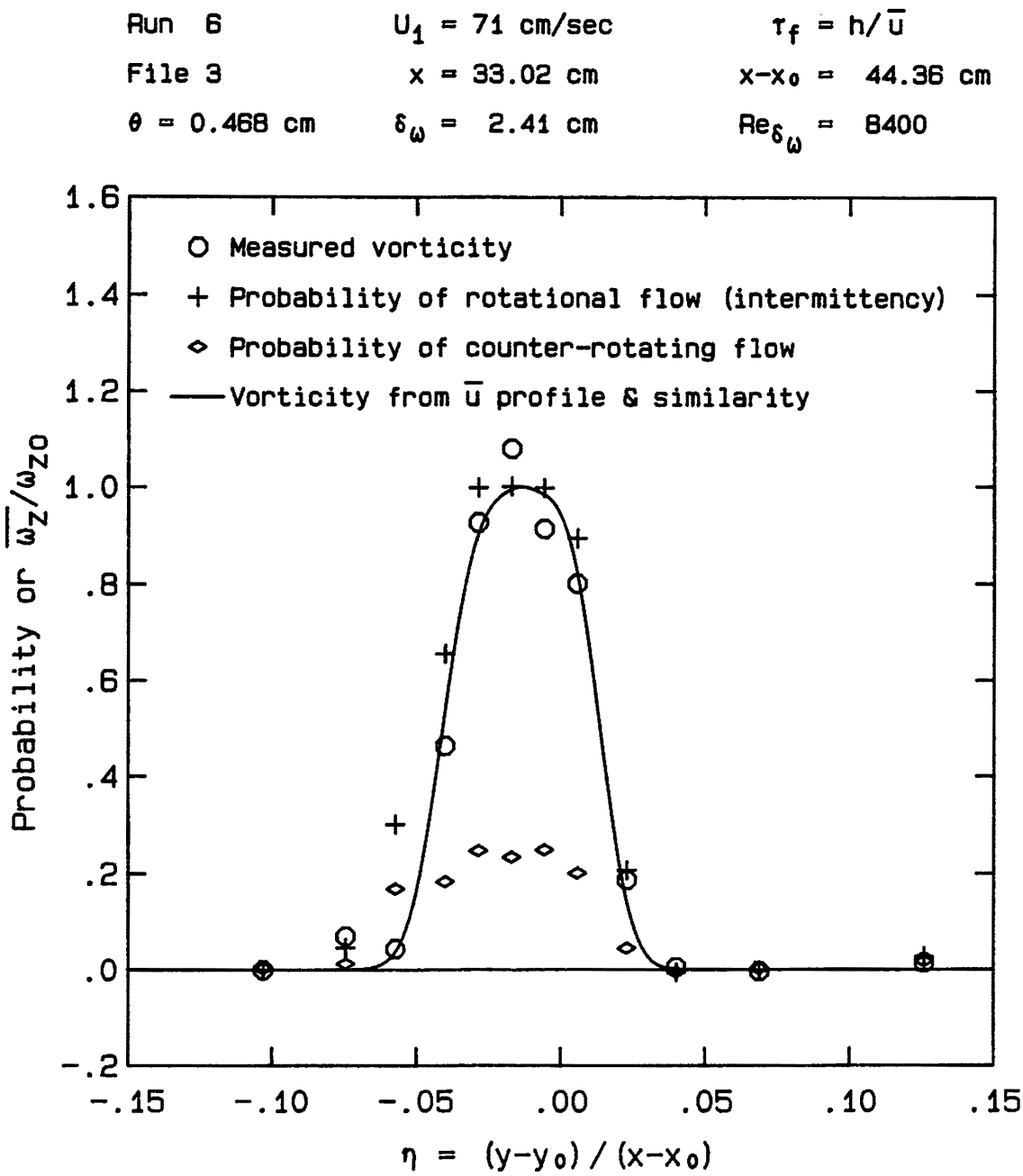

Figure 4.24 Vorticity Profile Showing Intermittency and Counter-rotating Flow, x = 33 cm

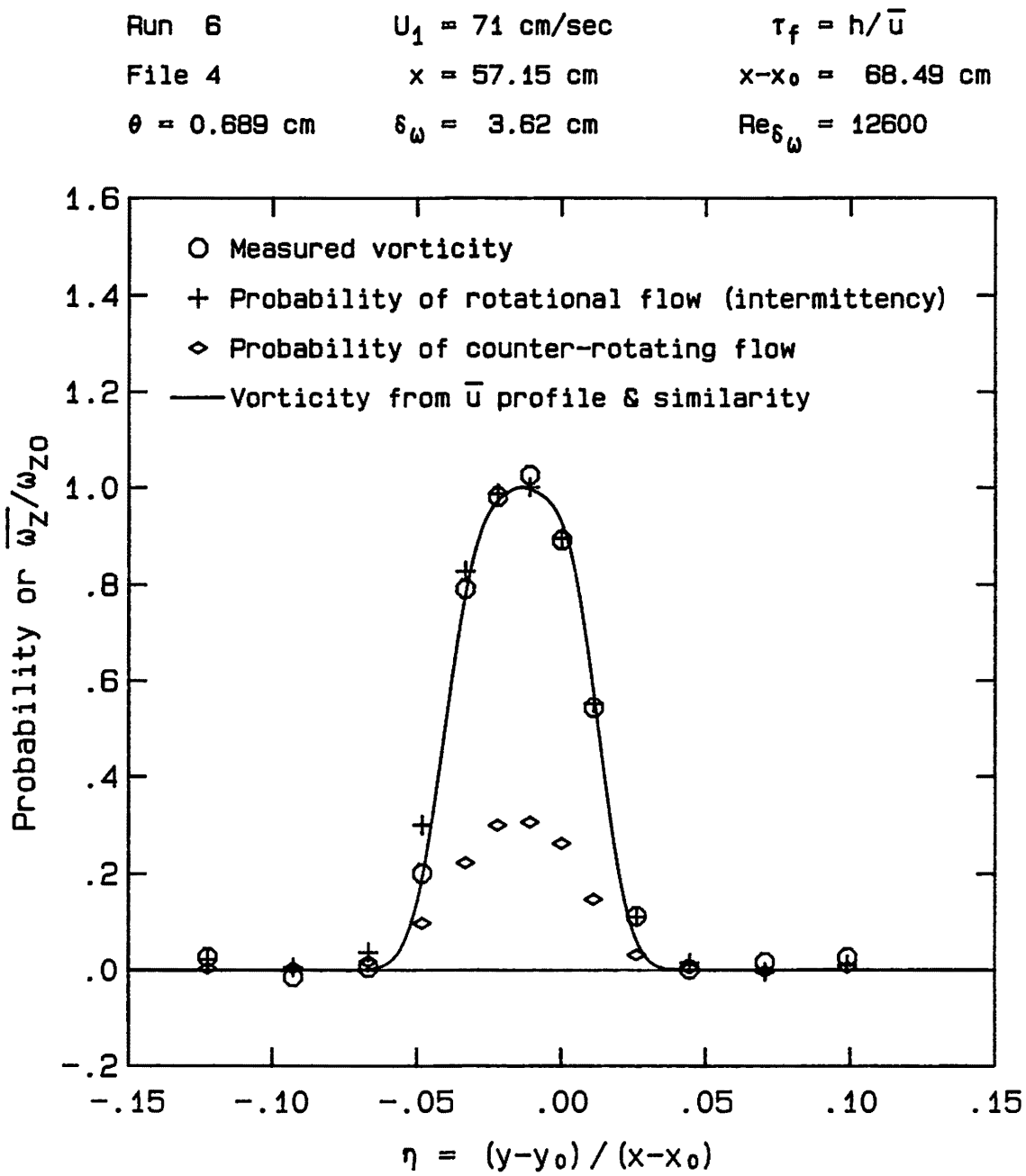

Figure 4.25 Vorticity Profile Showing Intermittency and Counter-rotating Flow, x = 57 cm

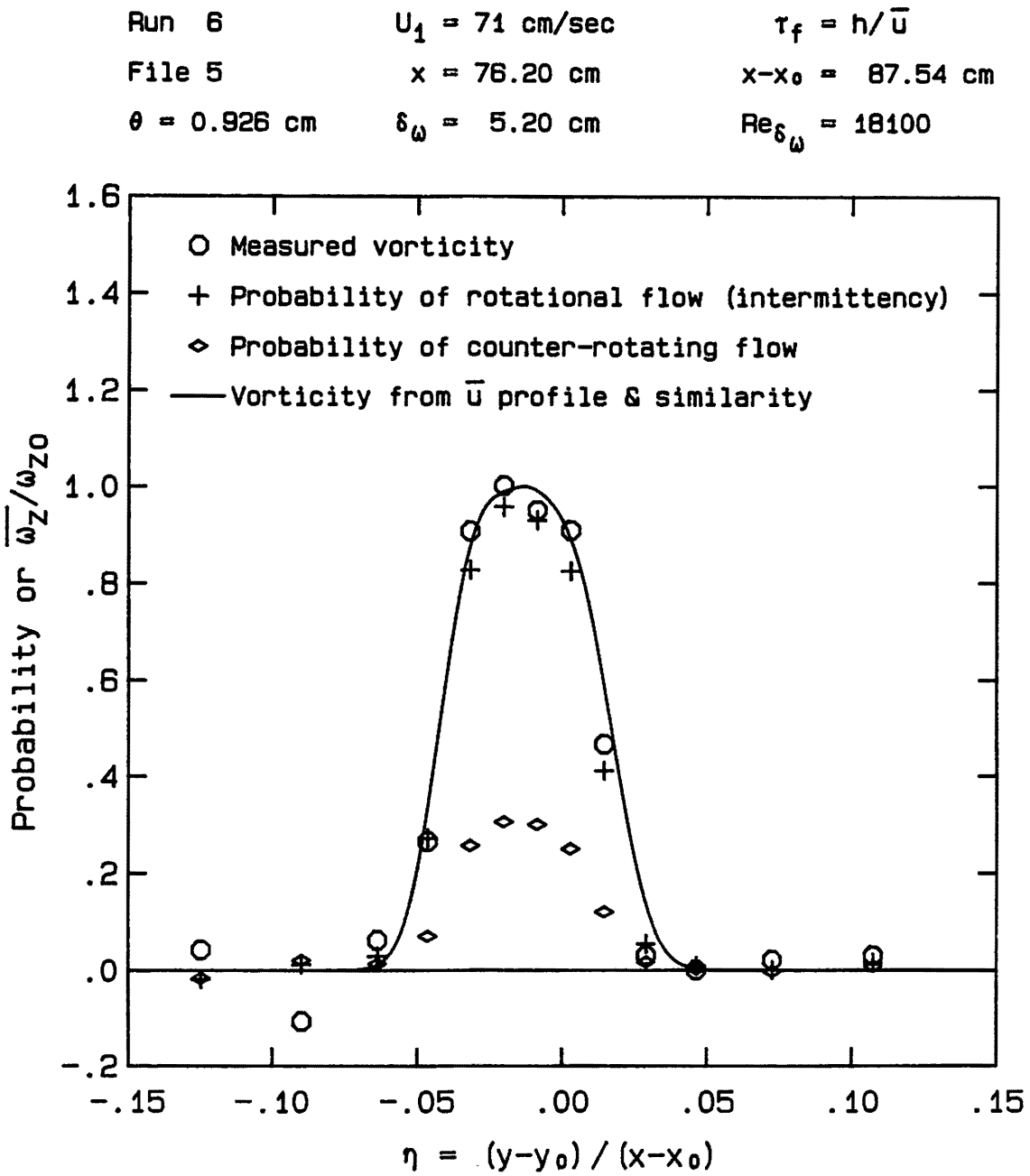

Figure 4.26 Vorticity Profile Showing Intermittency and Counter-rotating Flow, x = 76 cm

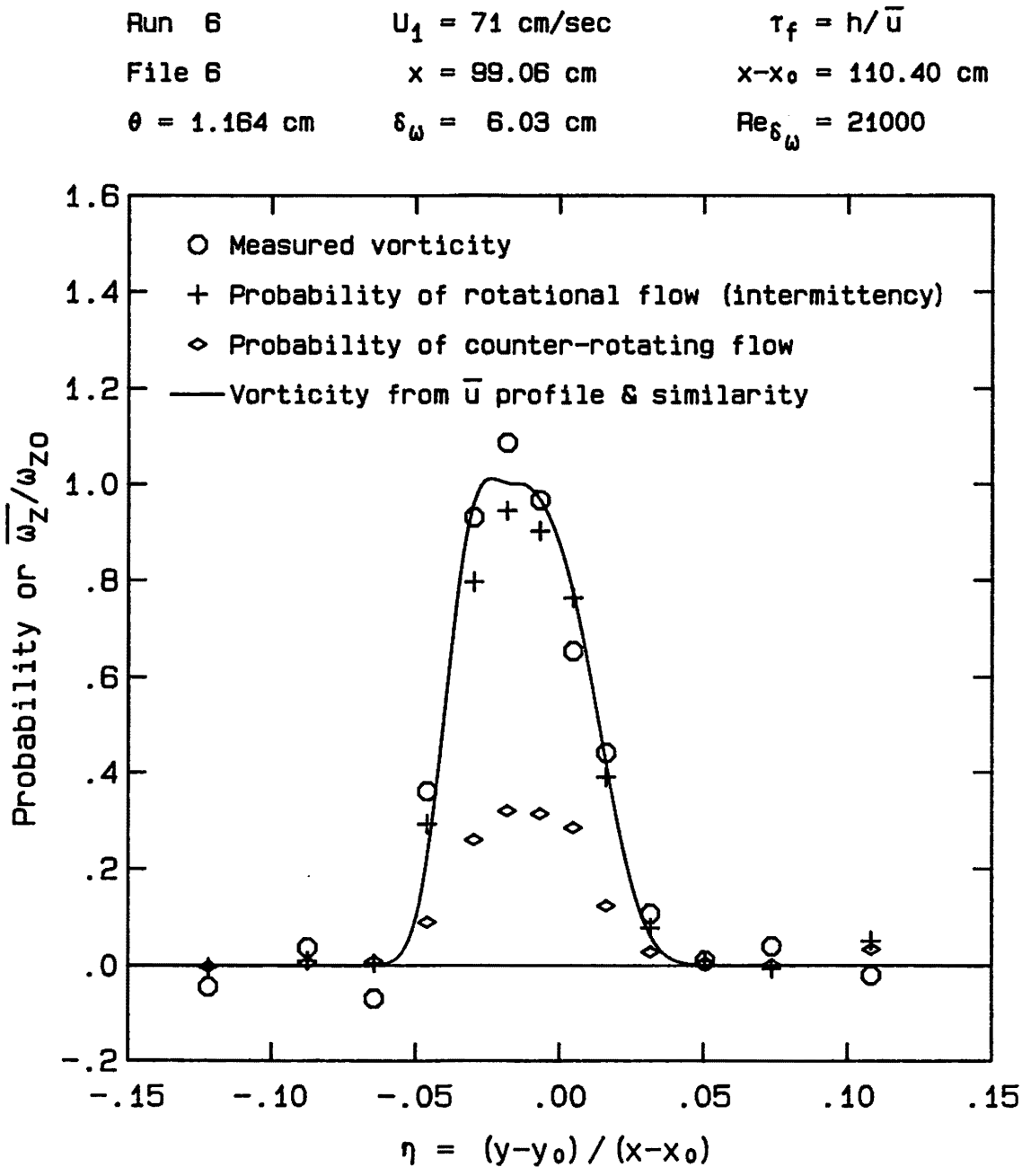

Figure 4.27 Vorticity Profile Showing Intermittency and Counter-rotating Flow, x = 99 cm

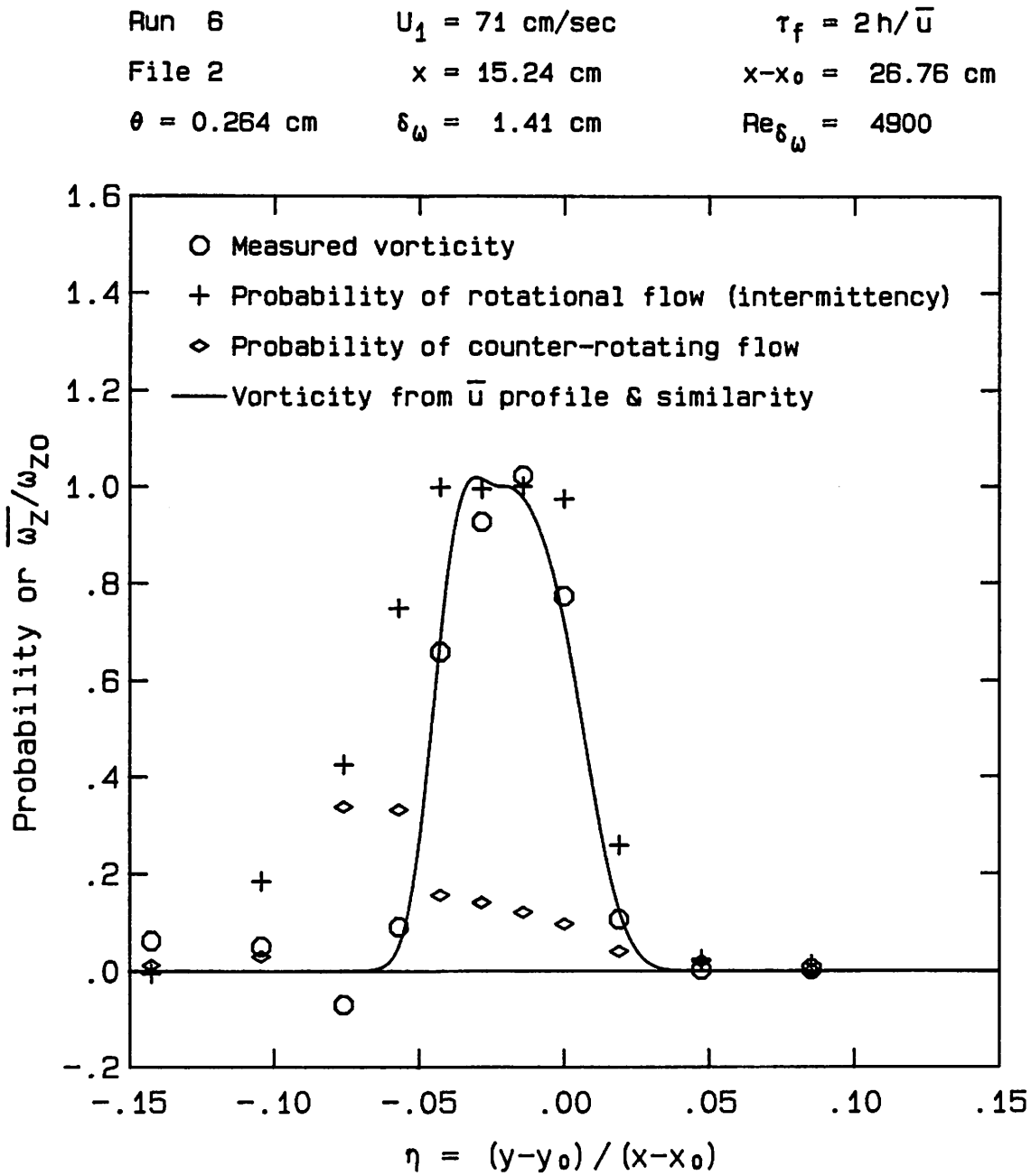

Figure 4.28 Intermittency and Counter-rotating Flow for Filter Width = $2h/\bar{u}$, x = 15 cm

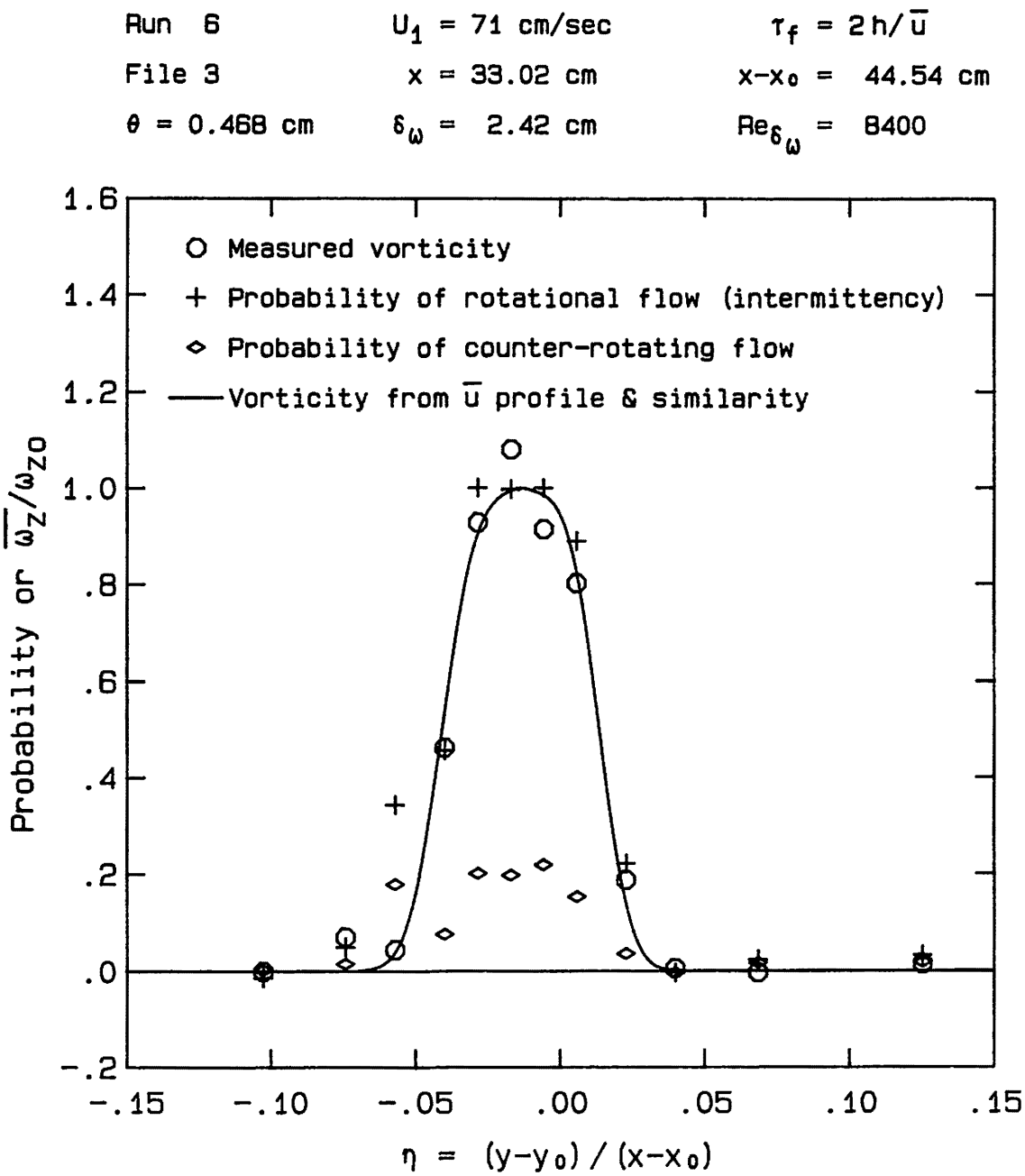

Figure 4.29 Intermittency and Counter-rotating Flow for Filter Width = $2h/\bar{u}$, x = 33 cm

Run 6 U_1 = 71 cm/sec $\tau_f = 2h/\bar{u}$

File 4 x = 57.15 cm $x-x_o$ = 68.67 cm

θ = 0.688 cm δ_ω = 3.62 cm Re_{δ_ω} = 12600

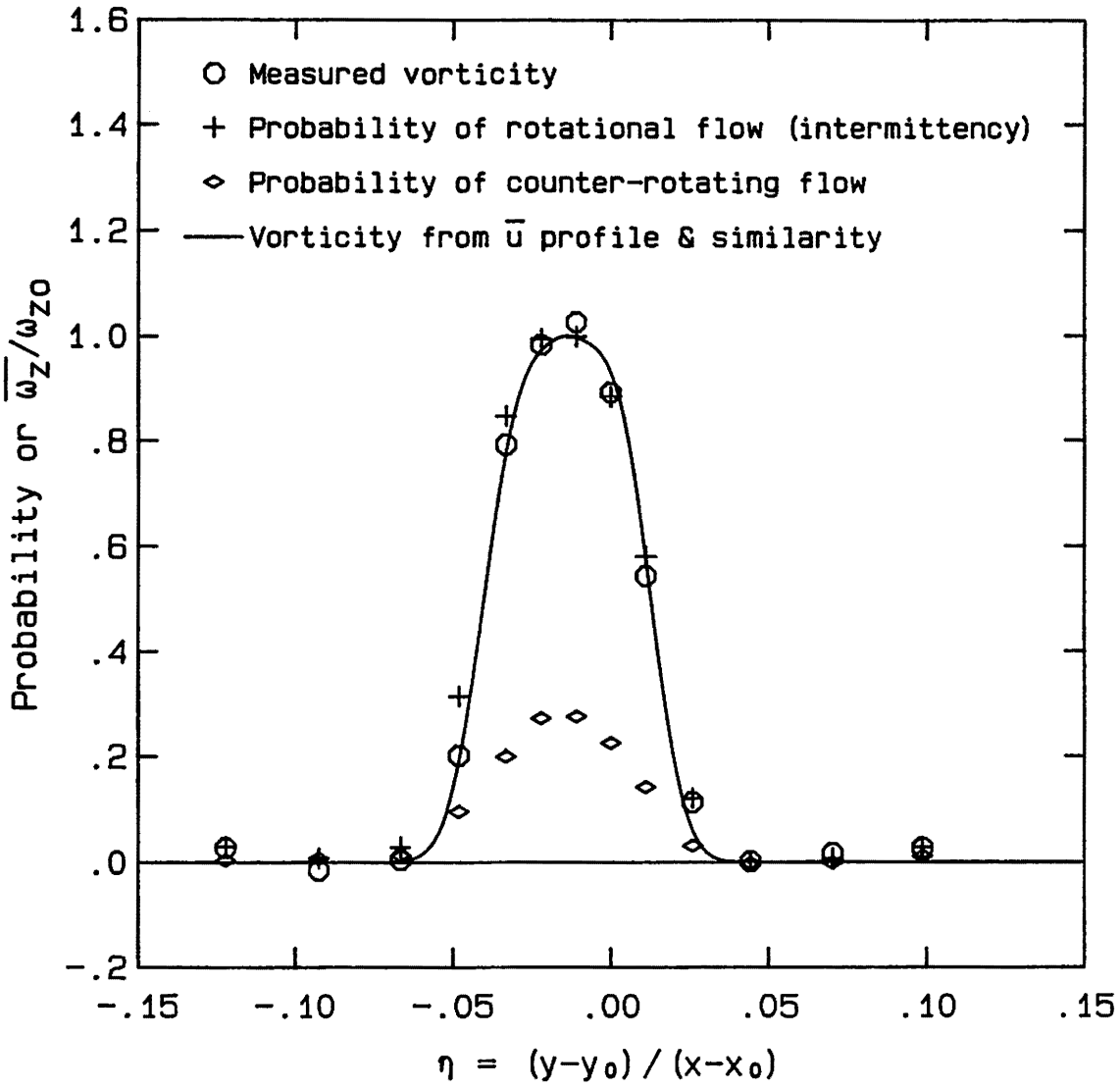

Figure 4.30 Intermittency and Counter-rotating Flow for Filter Width = $2h/\bar{u}$, x = 57 cm

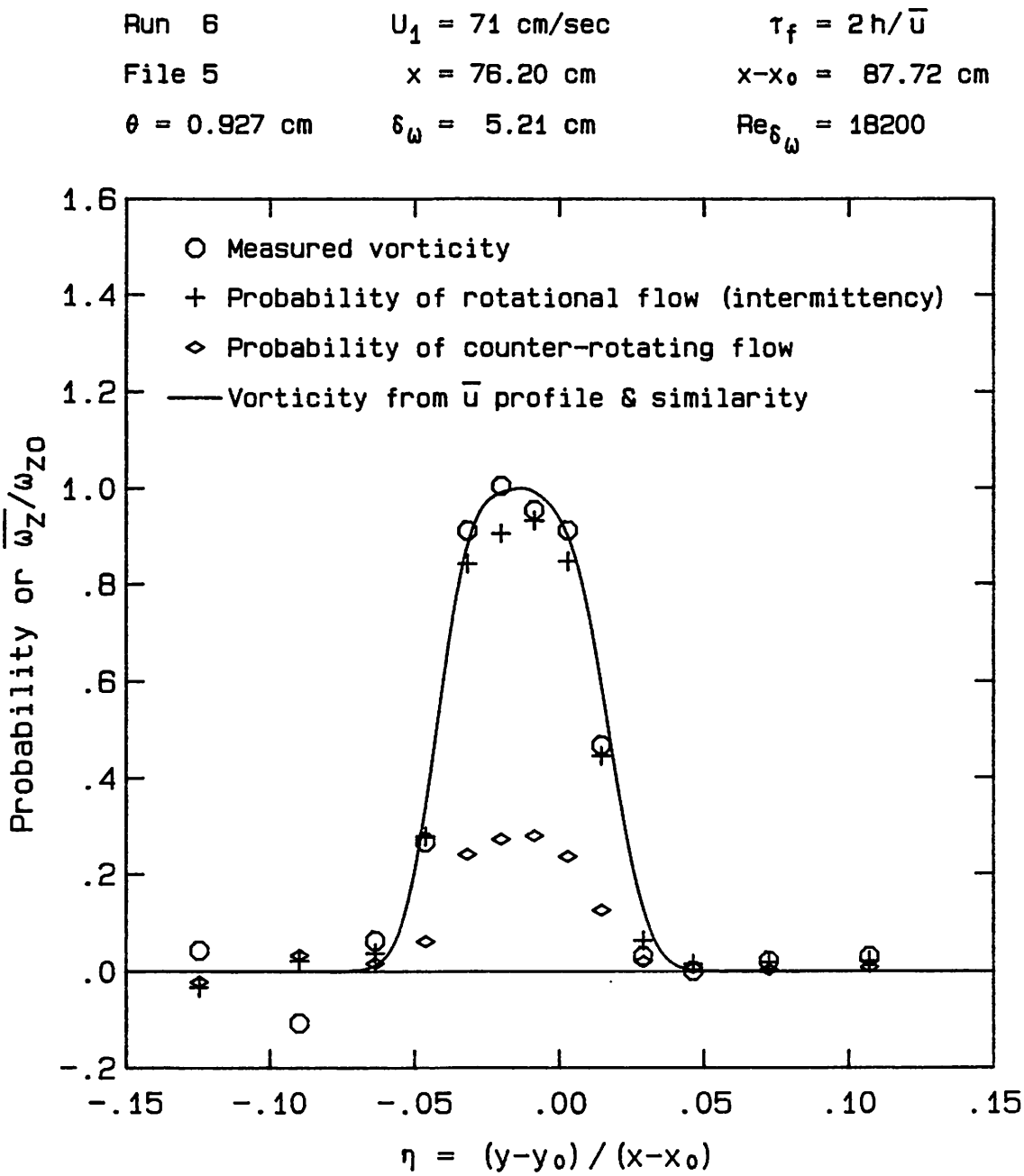

Figure 4.31 Intermittency and Counter-rotating Flow for Filter Width = $2h/\bar{u}$, x = 76 cm

Run 6 U_1 = 71 cm/sec $\tau_f = 2h/\bar{u}$

File 6 x = 99.06 cm $x-x_o$ = 110.58 cm

θ = 1.161 cm δ_ω = 6.02 cm Re_{δ_ω} = 21000

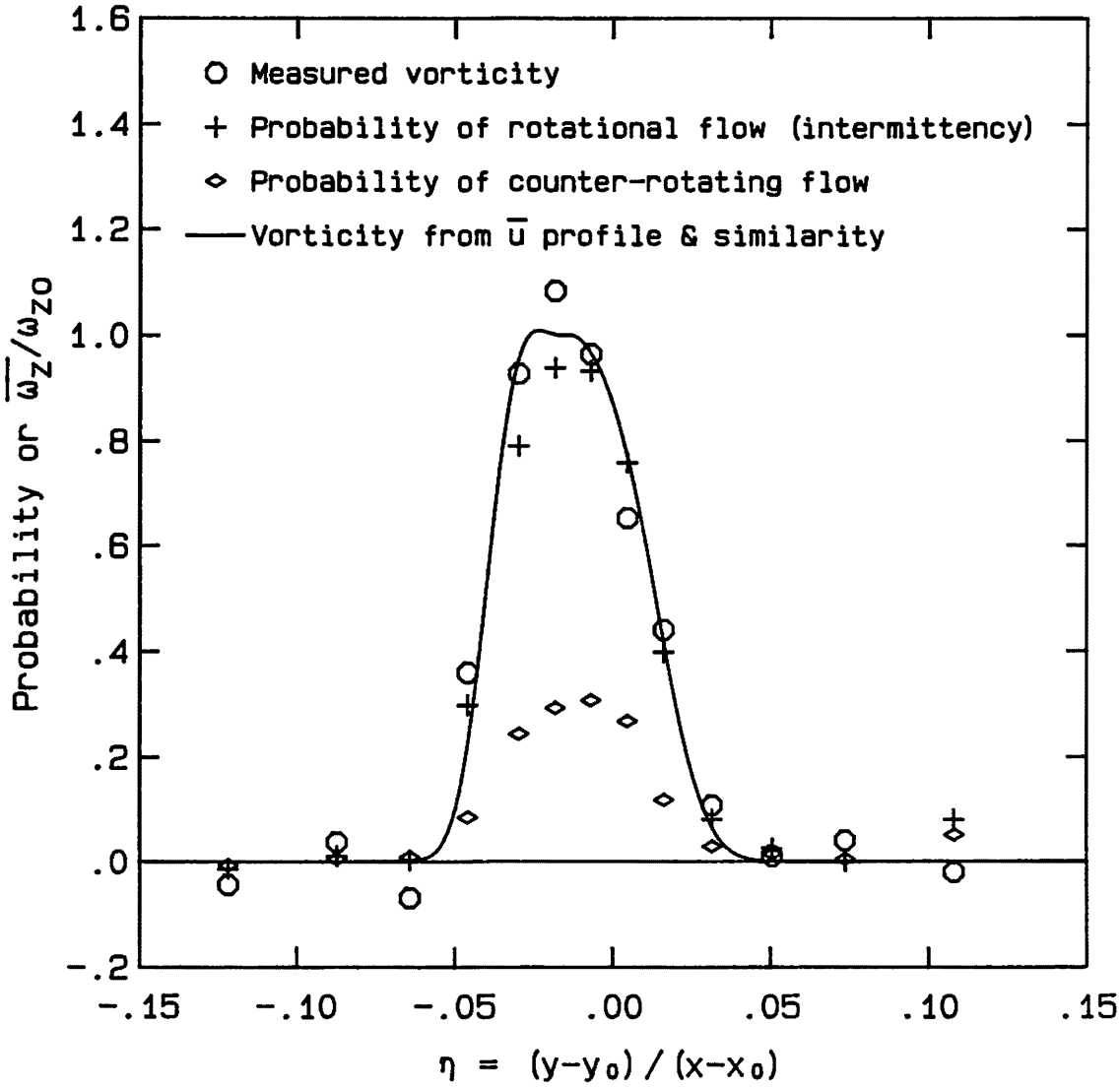

Figure 4.32 Intermittency and Counter-rotating Flow for Filter Width = $2h/\bar{u}$, x = 99 cm

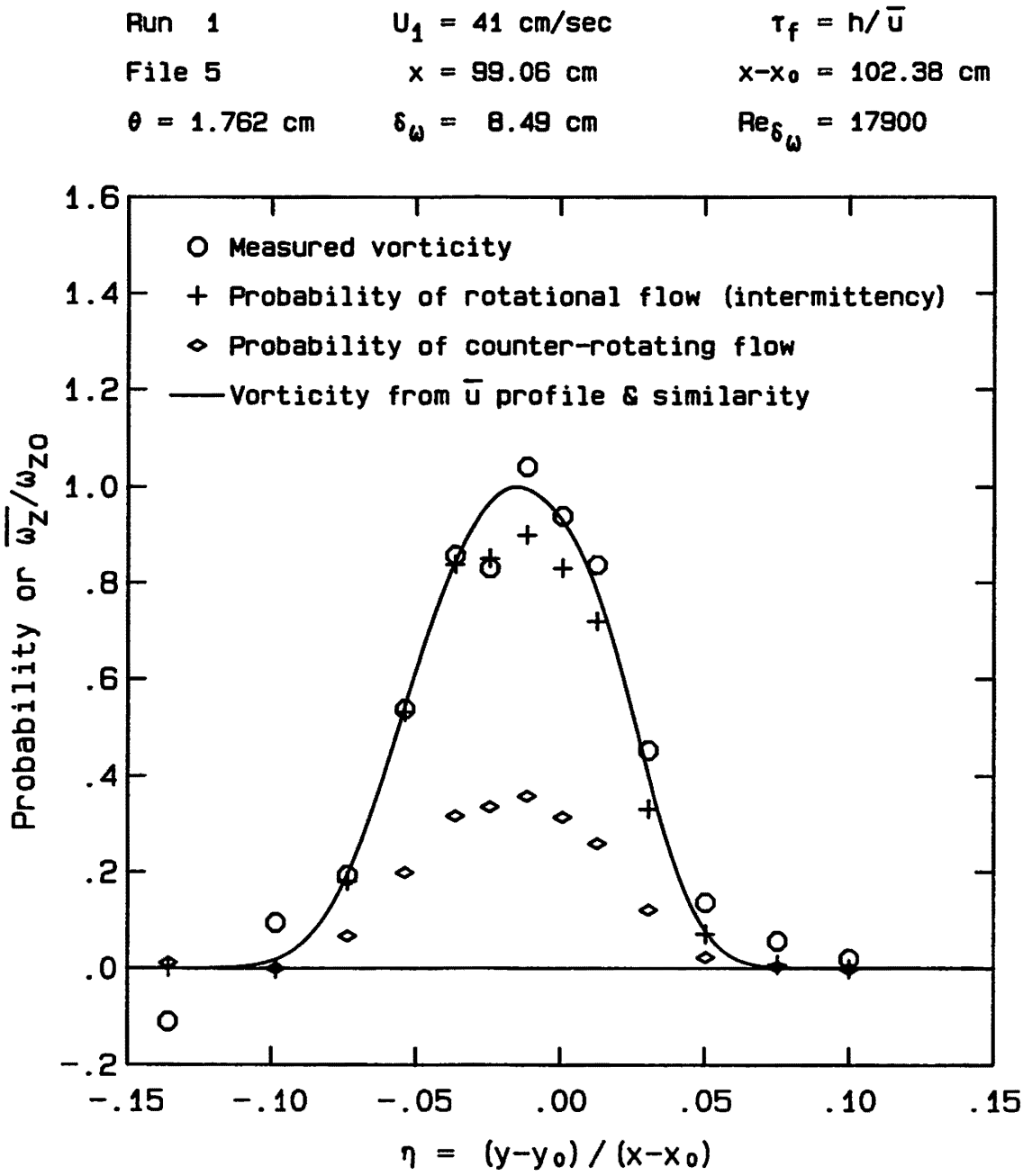

Figure 4.33 Vorticity Profile Showing Intermittency and Counter-rotating Flow, Run 1, x = 99 cm

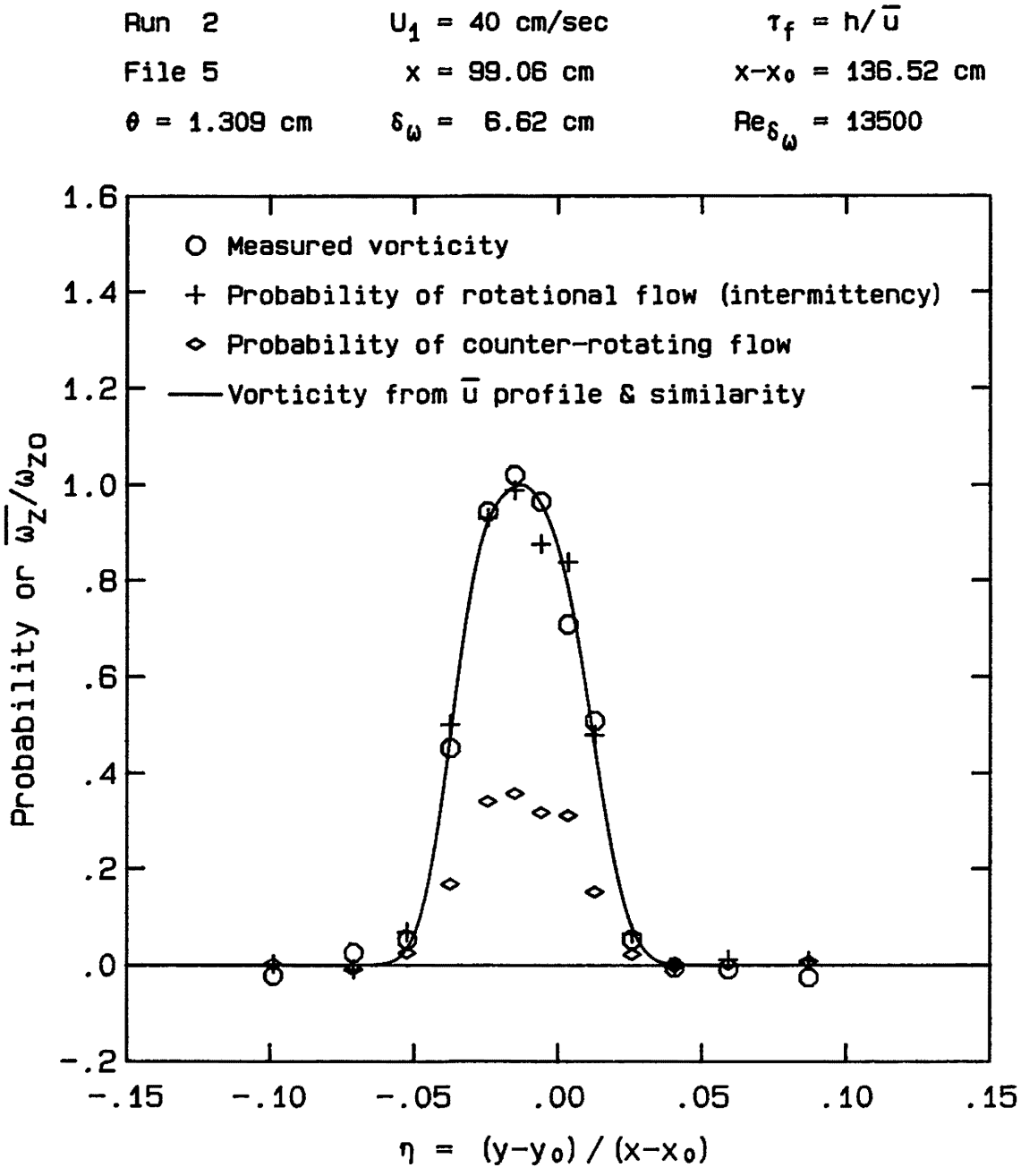

Figure 4.34 Vorticity Profile Showing Intermittency and Counter-rotating Flow, Run 2, x = 99 cm

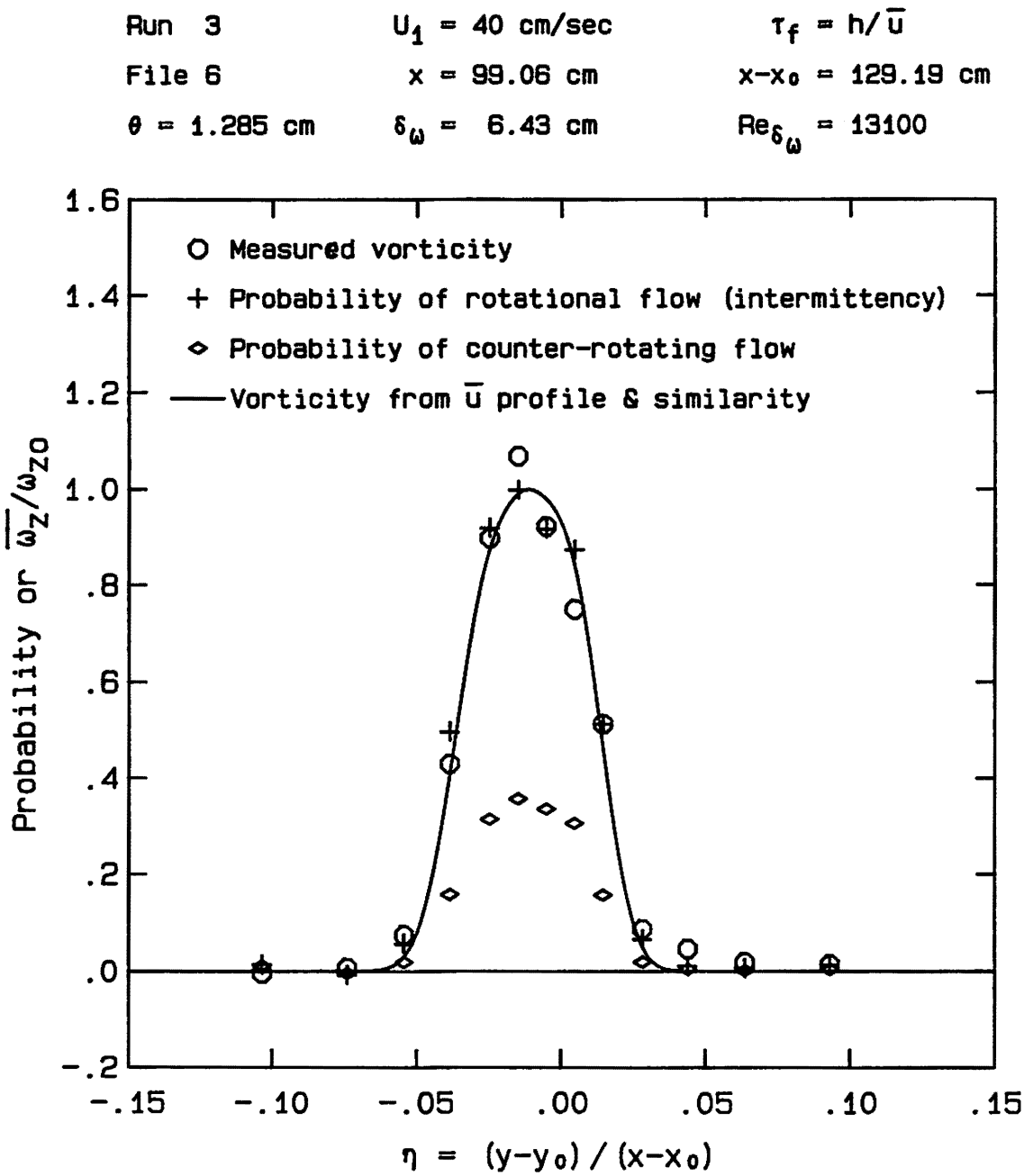

Figure 4.35 Vorticity Profile Showing Intermittency and Counter-rotating Flow, Run 3, x = 99 cm

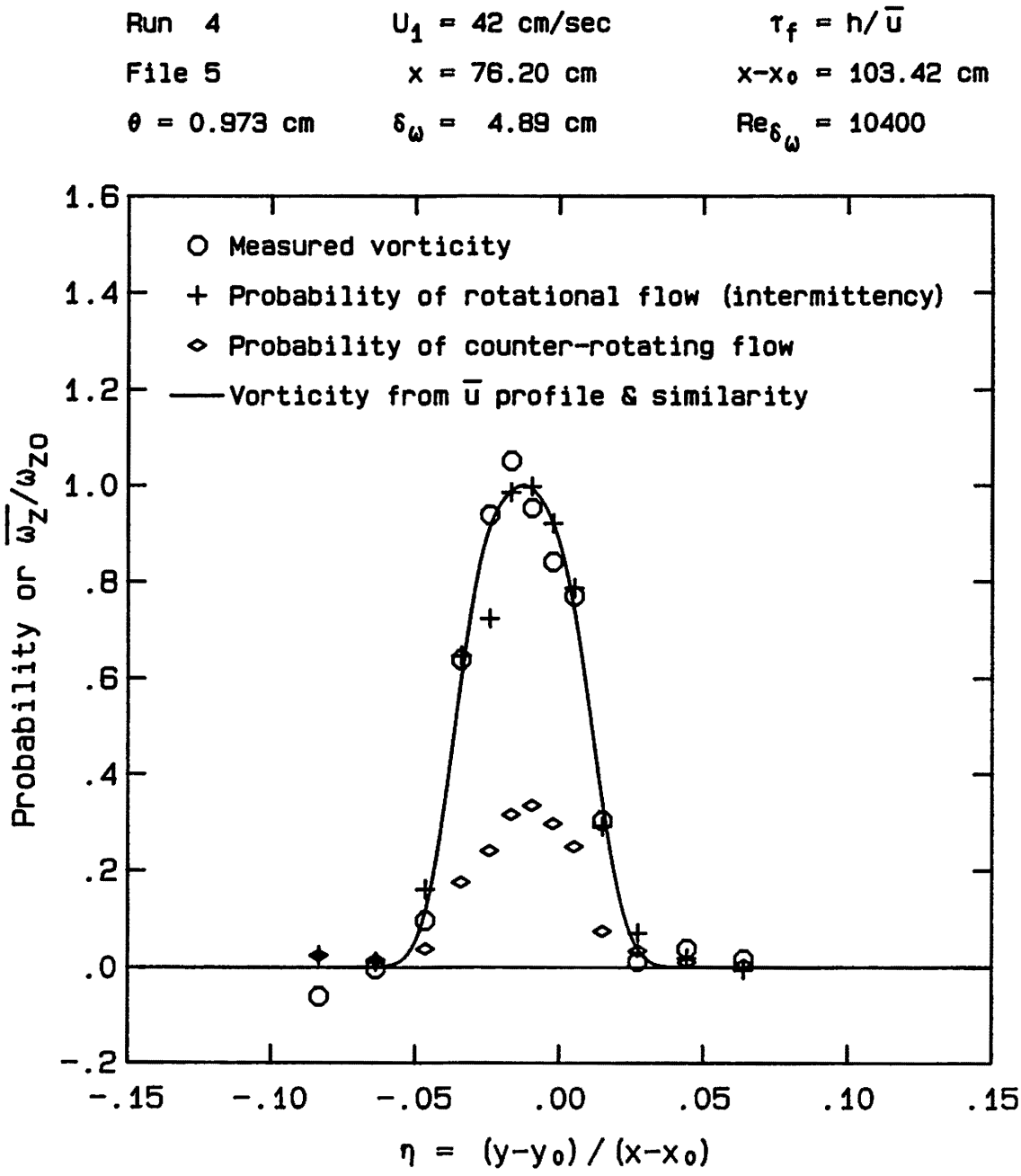

Figure 4.36 Vorticity Profile Showing Intermittency and Counter-rotating Flow, Run 4, x = 76 cm

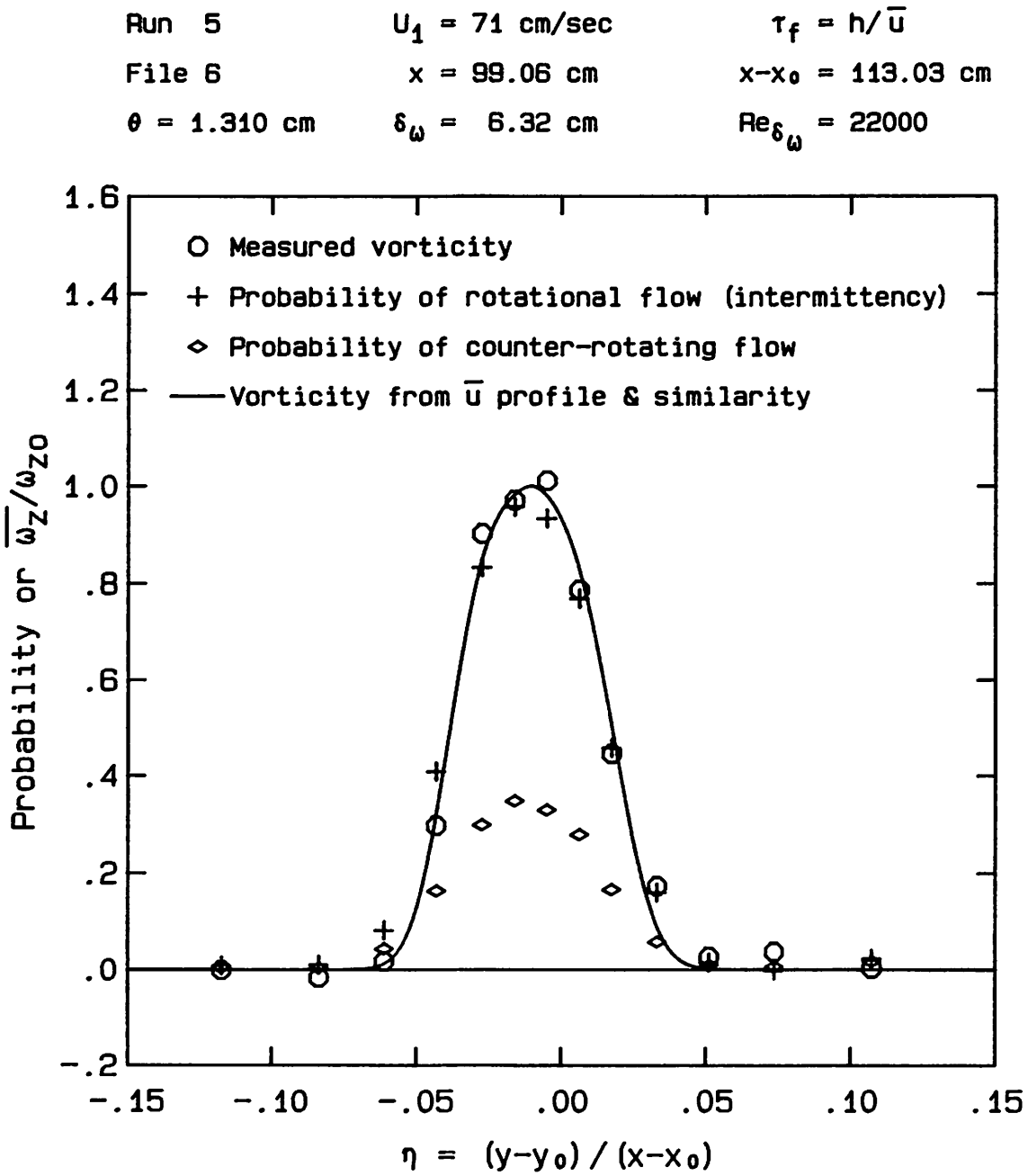

Figure 4.37 Vorticity Profile Showing Intermittency and Counter-rotating Flow, Run 5, x = 99 cm

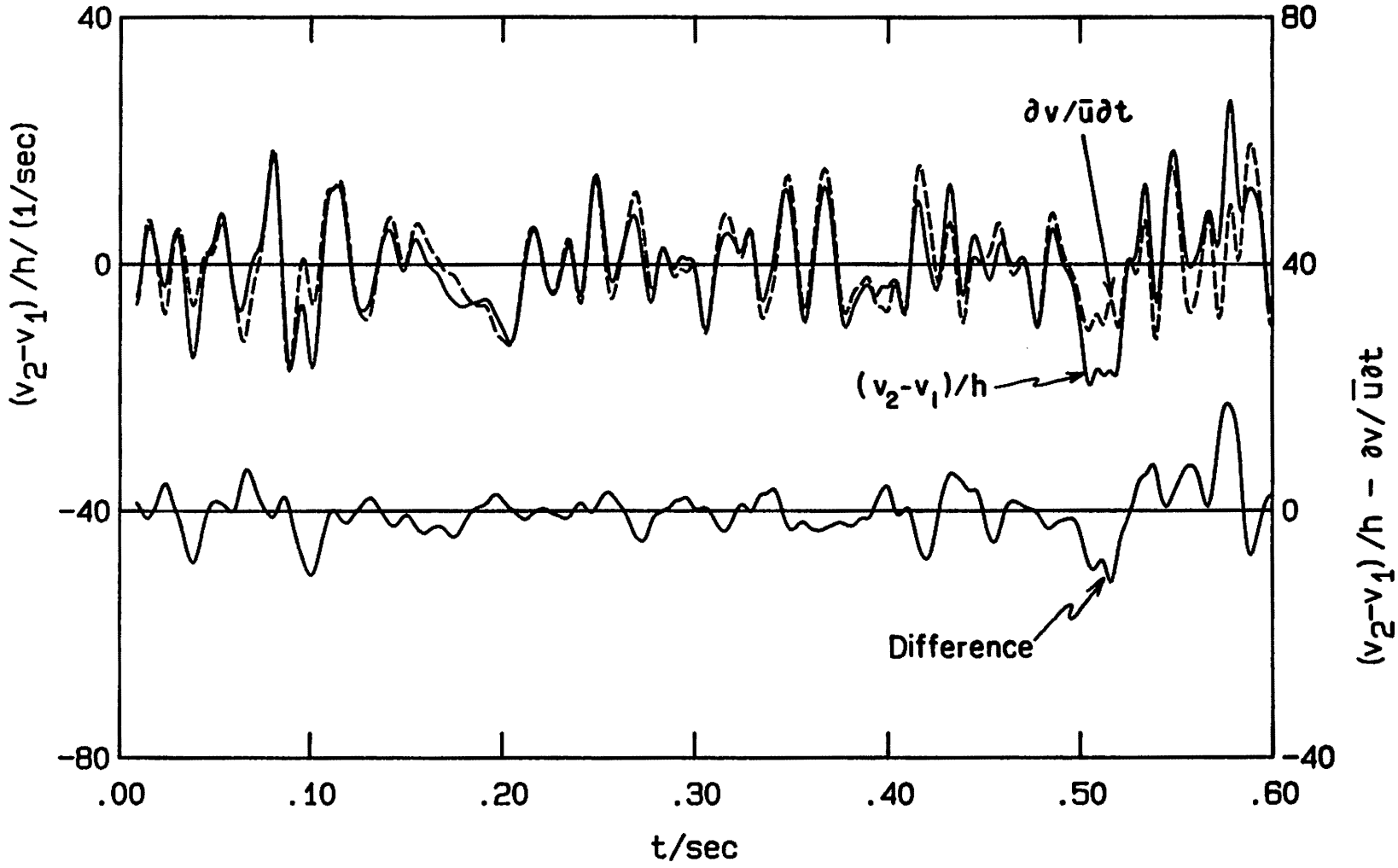

Figure 5.1a $(v_2-v_1)/h$ and $\partial v/\bar{u}\partial t$ vs. Time, x = 57 cm, η = -.022

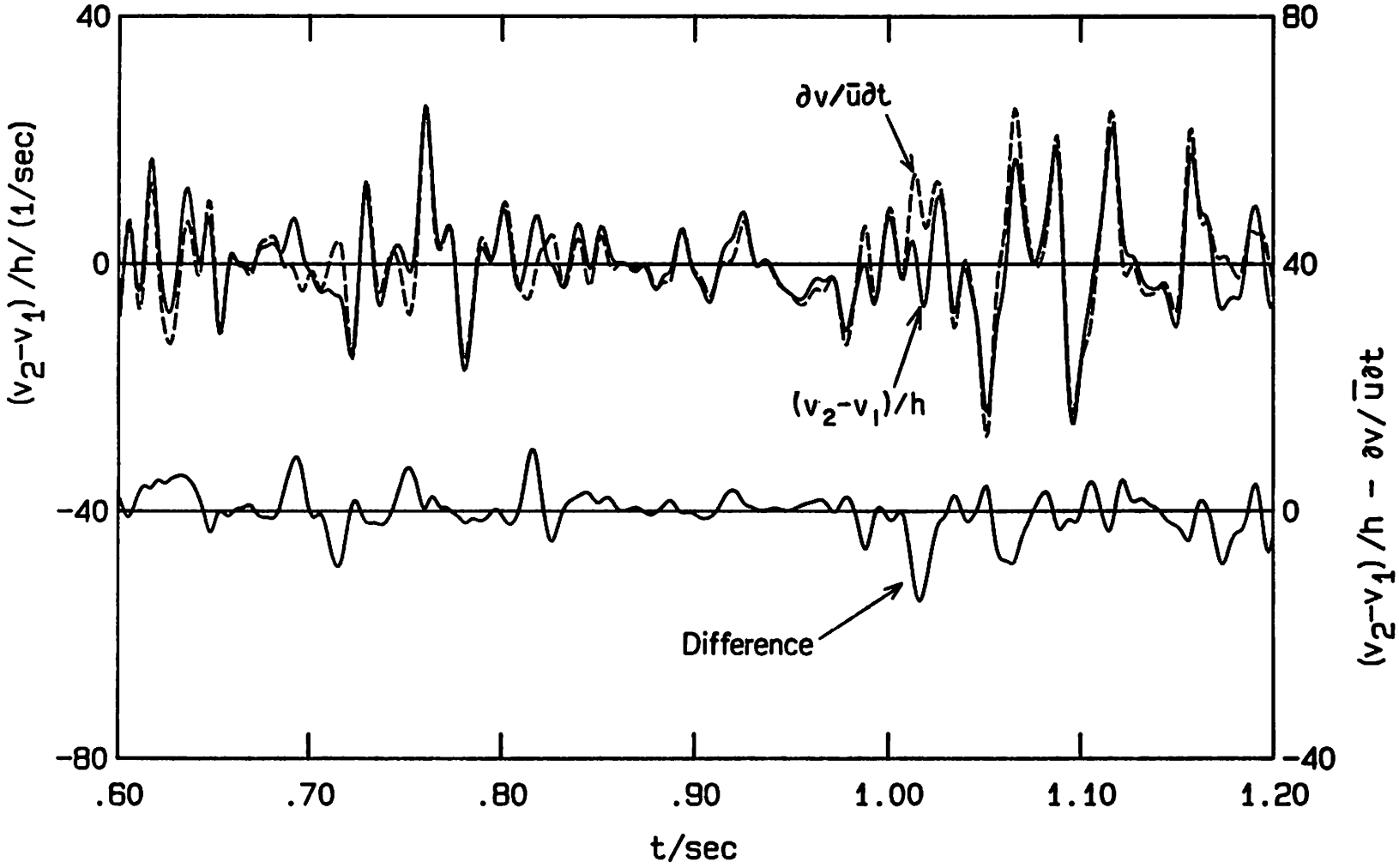

Figure 5.1b $(v_2-v_1)/h$ and $\partial v/\bar{u}\partial t$ vs. Time, x = 57 cm, η = -.022

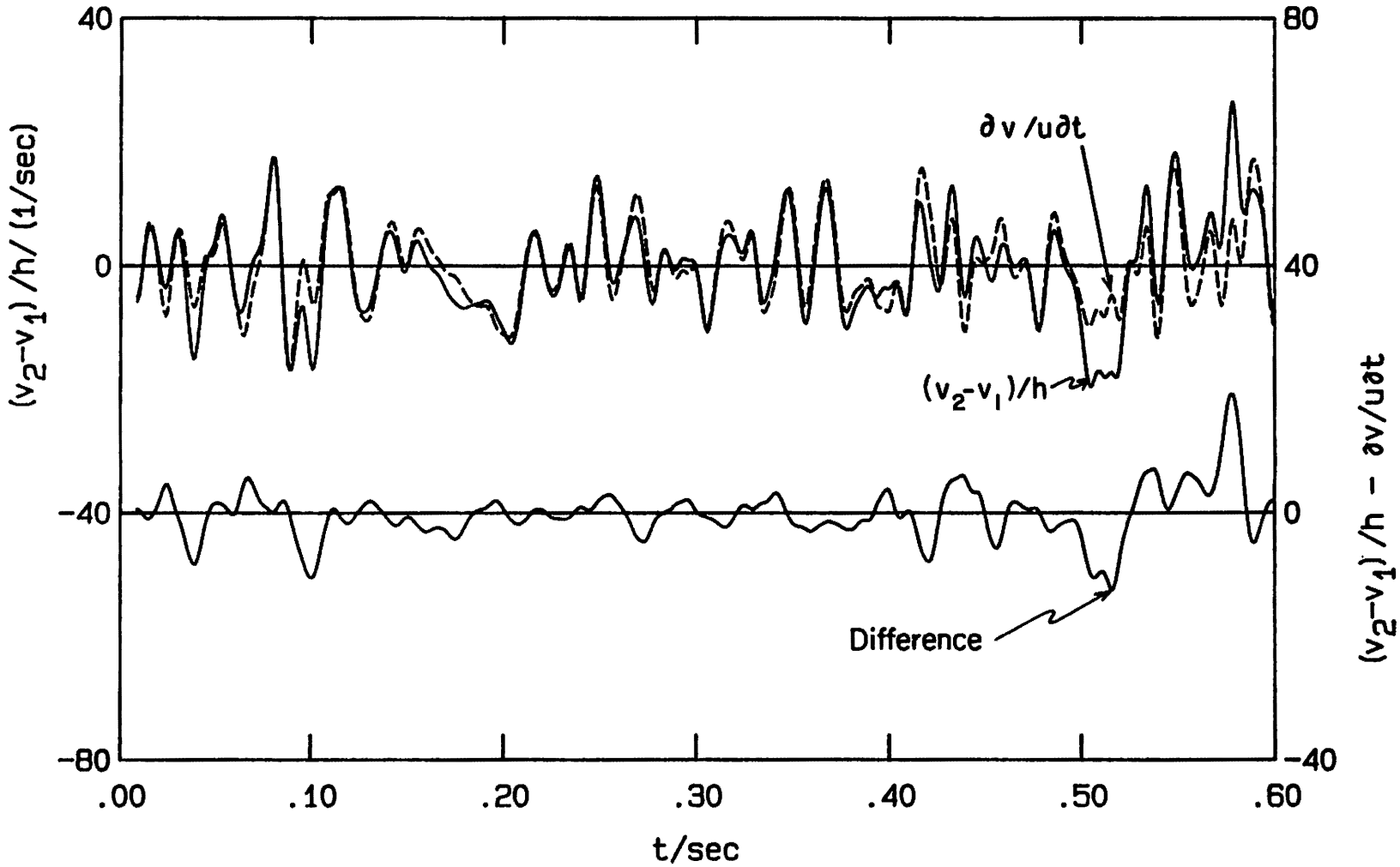

Figure 5.2a $(v_2-v_1)/h$ and $\partial v/u\partial t$ vs. Time, x = 57 cm, η = -.022

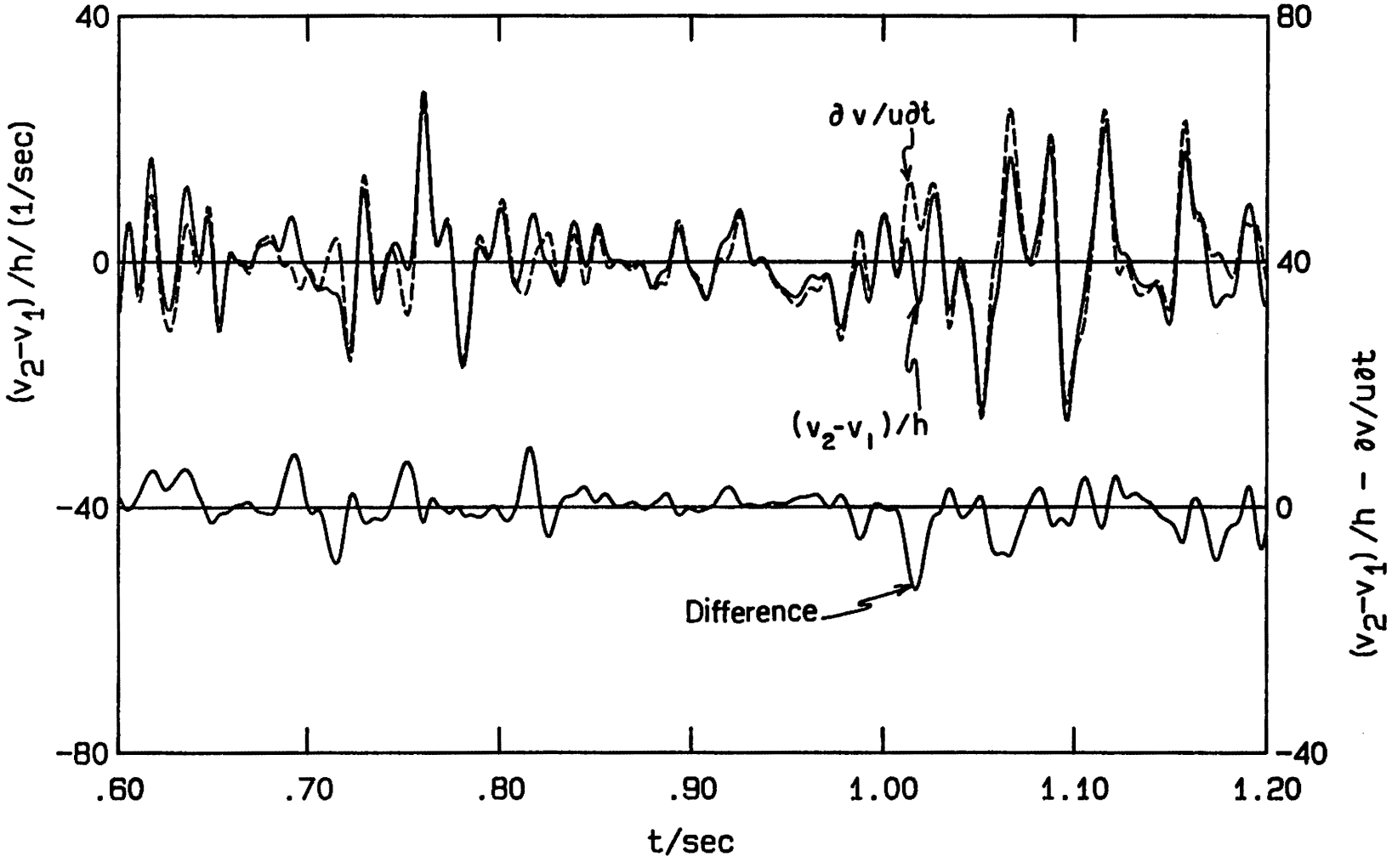

Figure 5.2b $(v_2-v_1)/h$ and $\partial v/u\partial t$ vs. Time, x = 57 cm, η = -.022

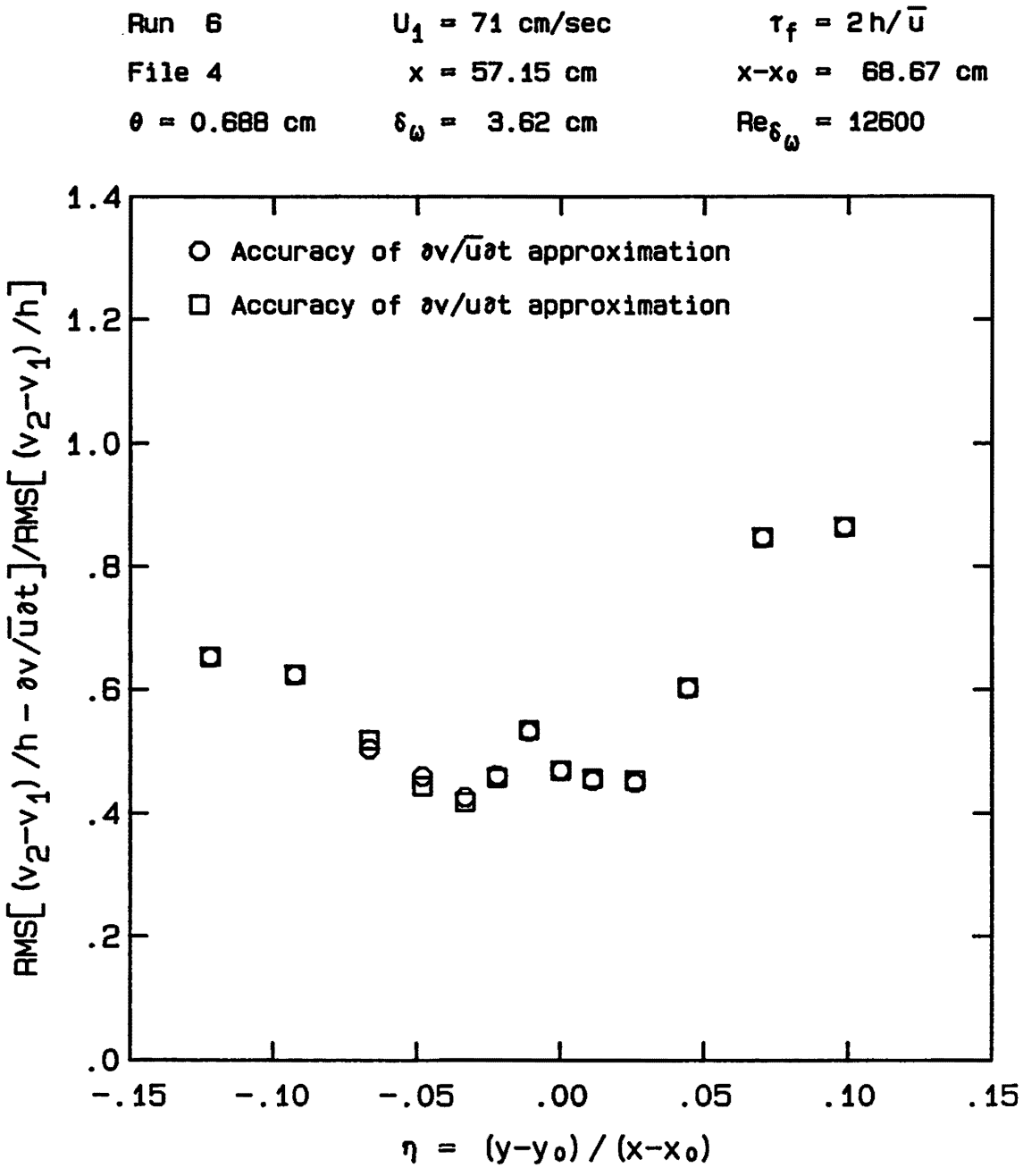

Figure 5.3 Accuracy of $\partial v/u\partial t$ and $\partial v/\bar{u}\partial t$ vs. η

Run 6 U_1 = 71 cm/sec $\tau_f = 2h/\bar{u}$

File 4 x = 57.15 cm $x-x_o$ = 68.67 cm

θ = 0.688 cm δ_ω = 3.62 cm Re_{δ_ω} = 12600

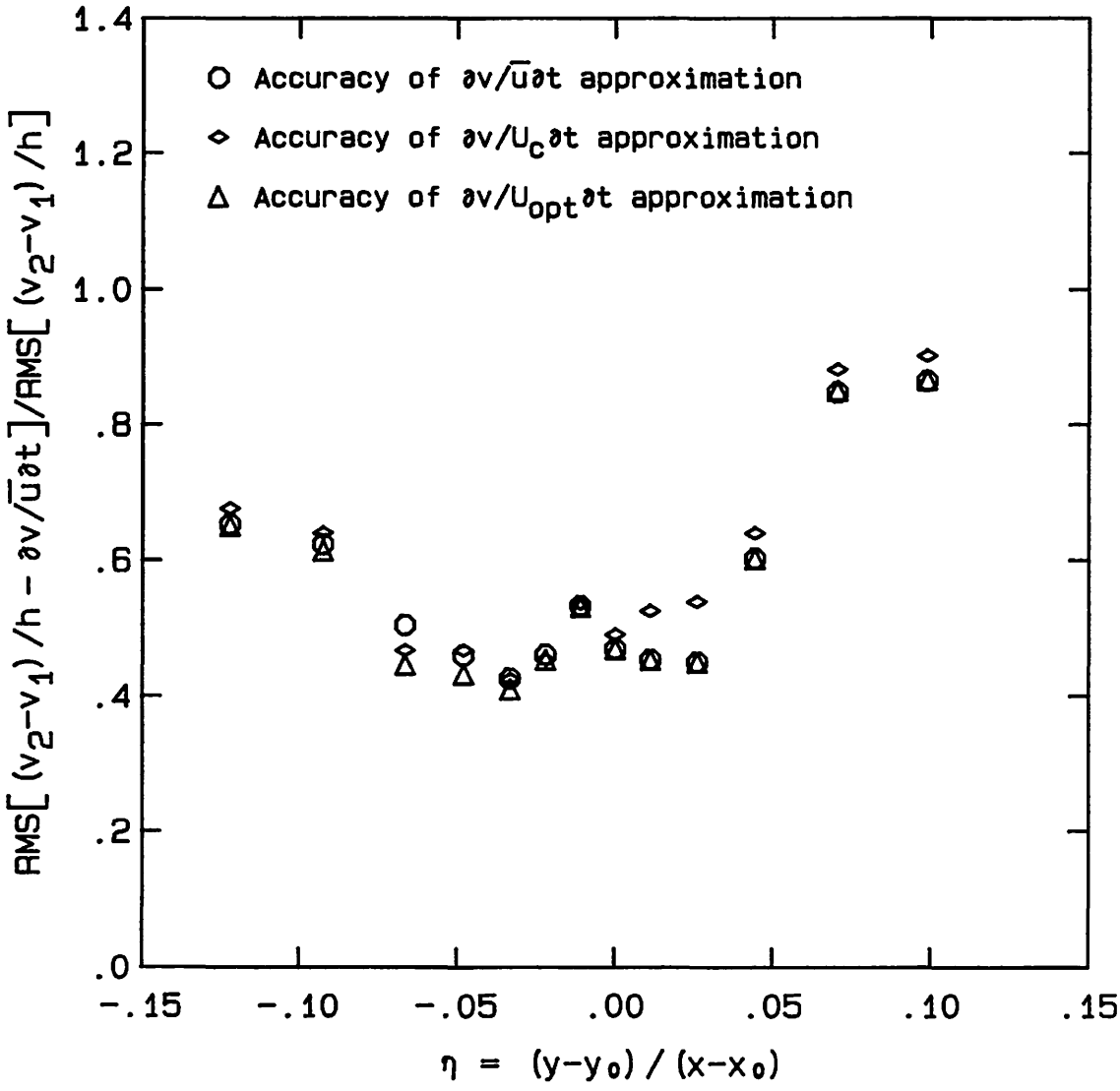

Figure 5.4 Accuracy of $\partial v/\bar{u}\partial t$, $\partial v/U_c\partial t$, and $\partial v/U_{opt}\partial t$ approximations vs. η

Run 6 U_1 = 71 cm/sec $\tau_f = 2h/\bar{u}$

File 4 x = 57.15 cm $x-x_0$ = 68.67 cm

θ = 0.688 cm δ_ω = 3.62 cm Re_{δ_ω} = 12600

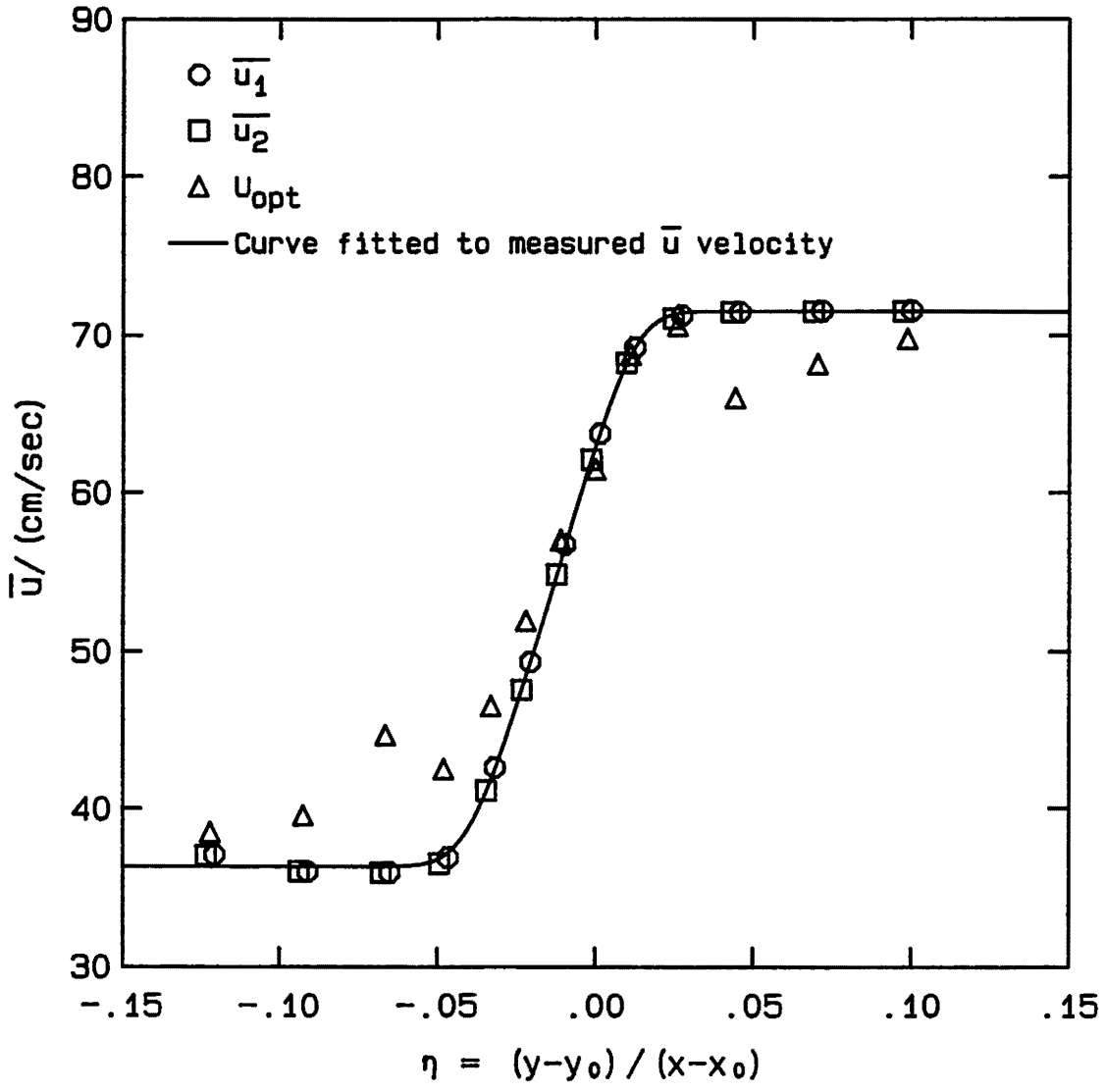

Figure 5.5 Plot of U_{opt} vs. η

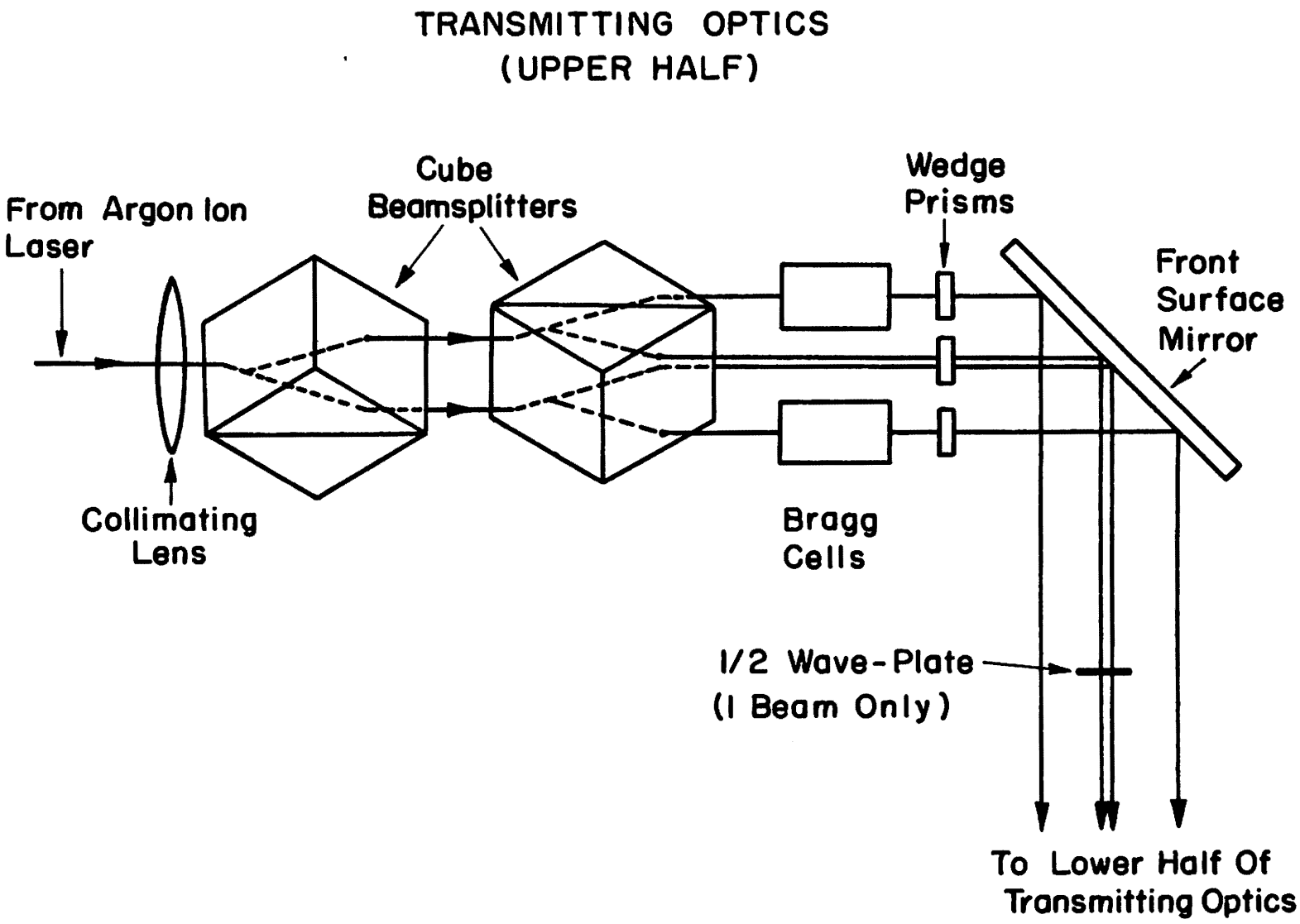

Figure B.1 Diagram of Transmitting Optics, Upper Half

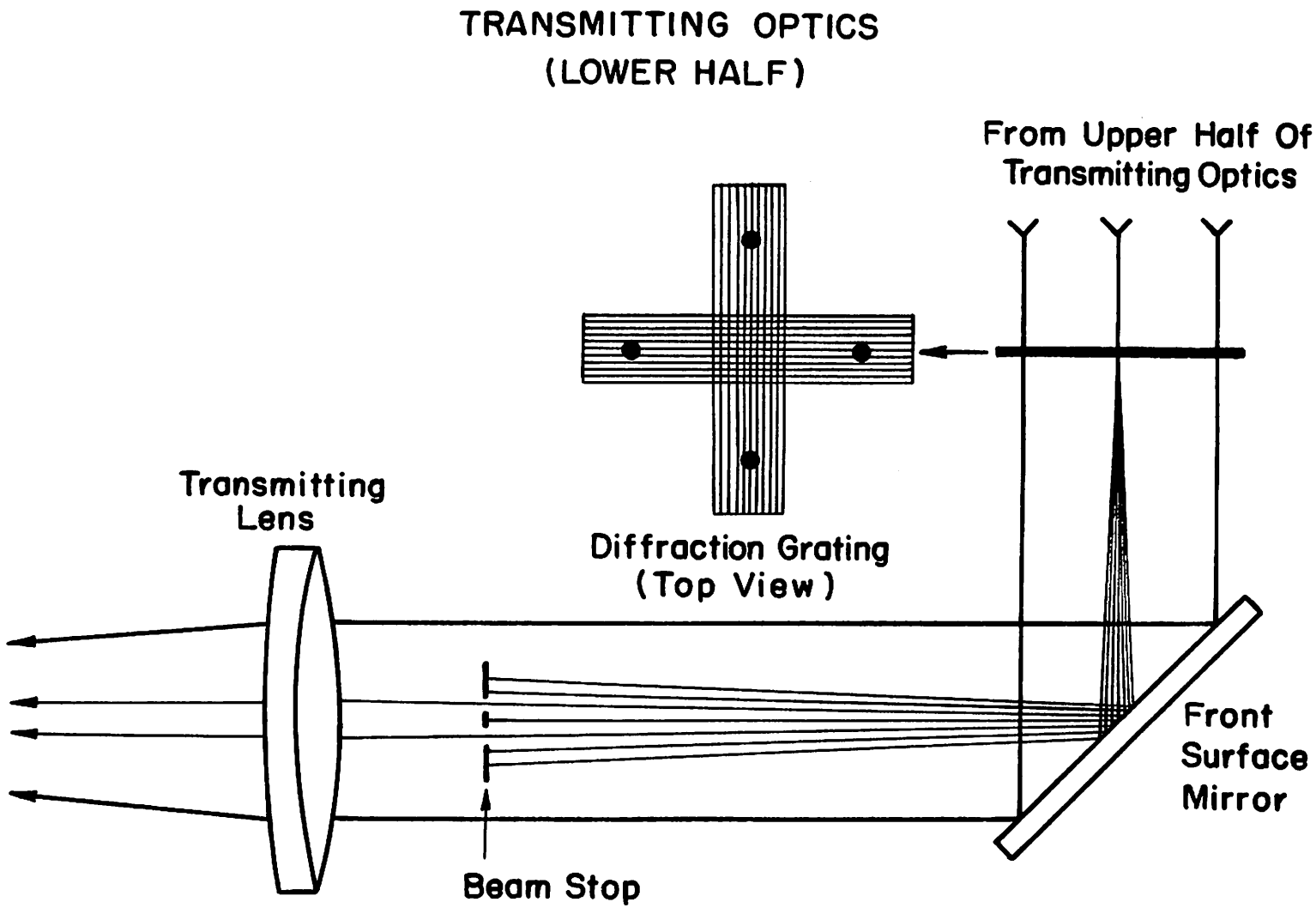

Figure B.2 Diagram of Transmitting Optics, Lower Half

Figure B.3 Photo of Transmitting Optics

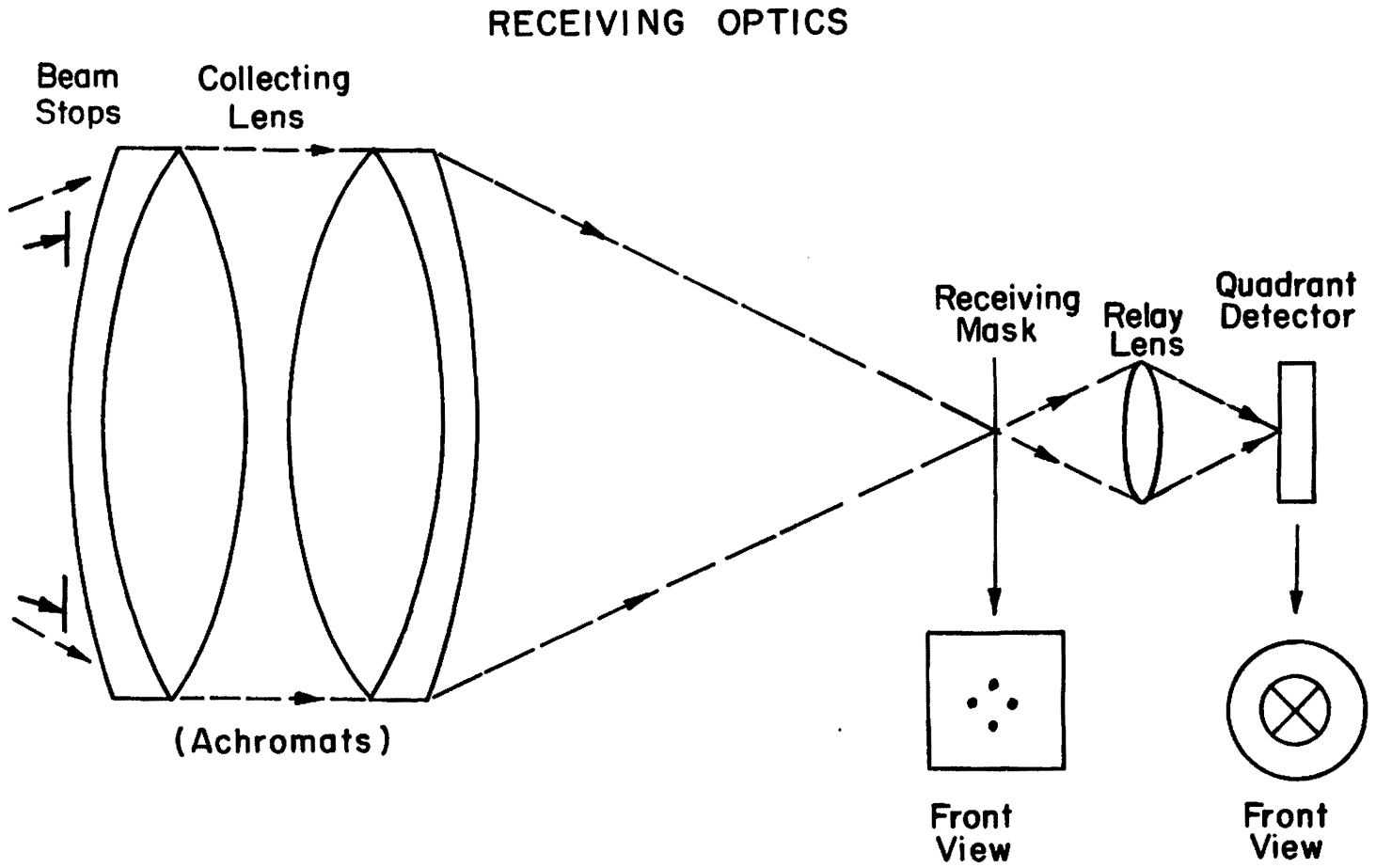

Figure B.4 Diagram of Receiving Optics

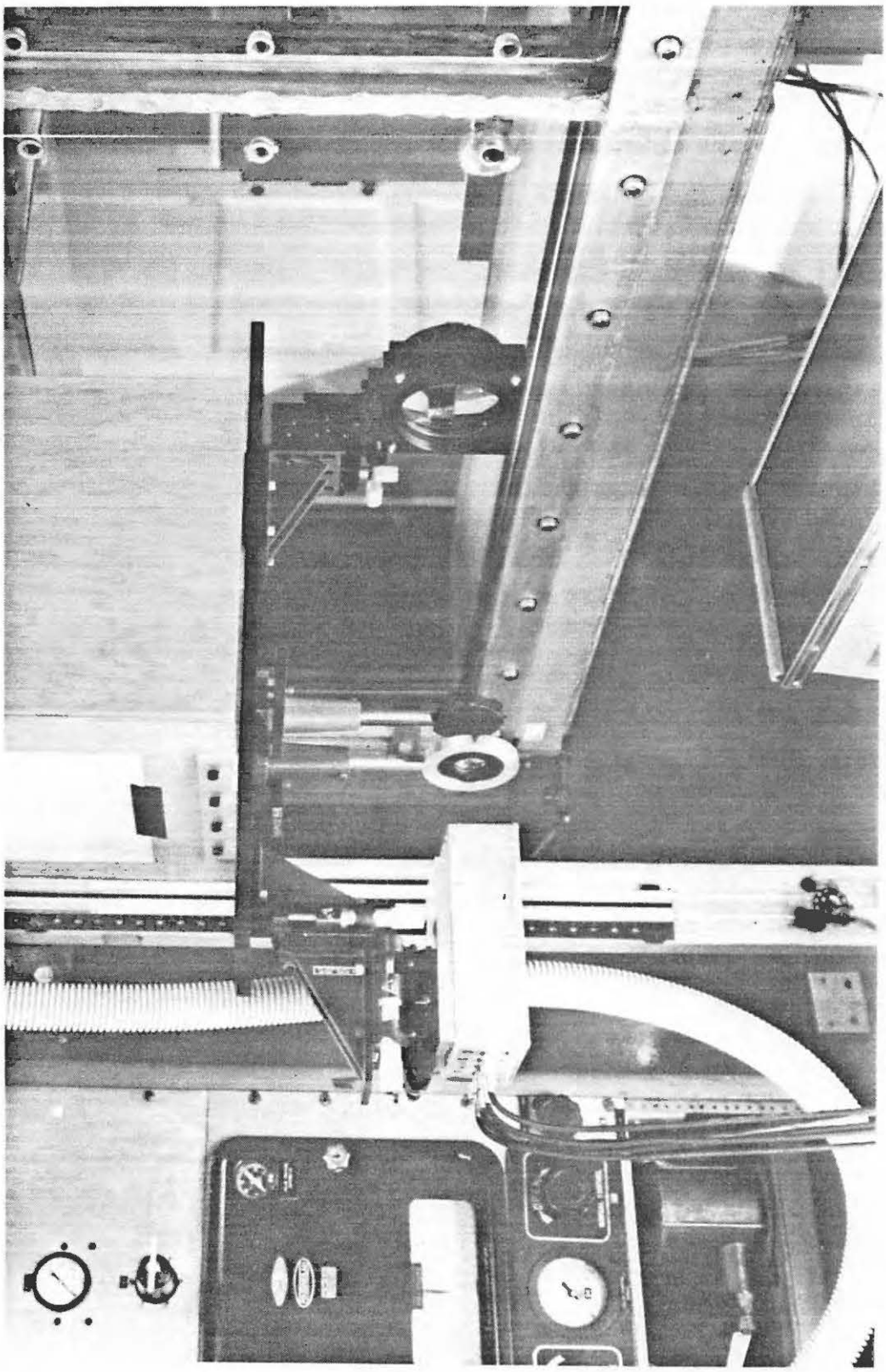

Figure B.5 Photo of Receiving Optics

PHASE LOCKED LOOP FREQUENCY SYNTHESIZER

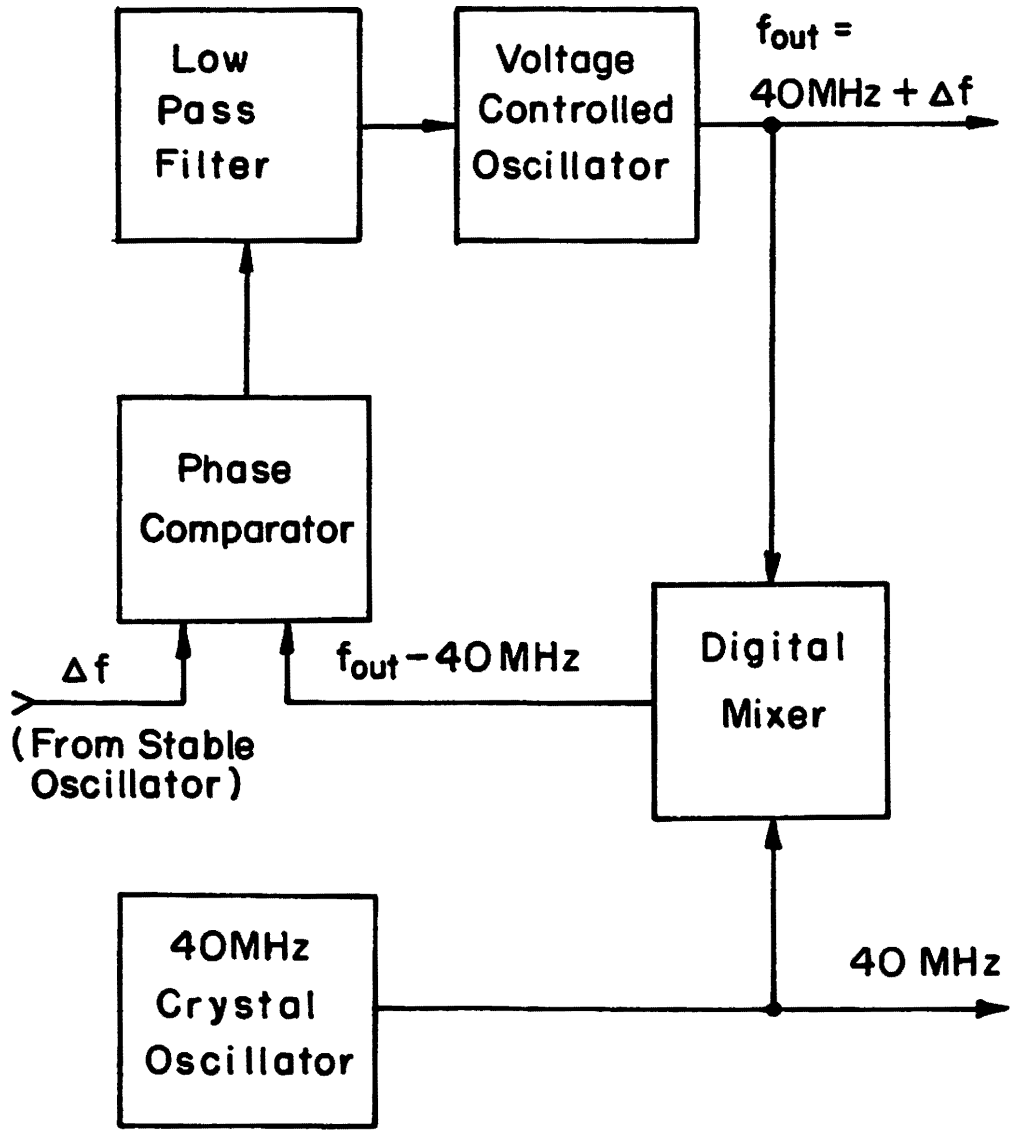

Figure C.1 Phase Locked Loop Block Diagram

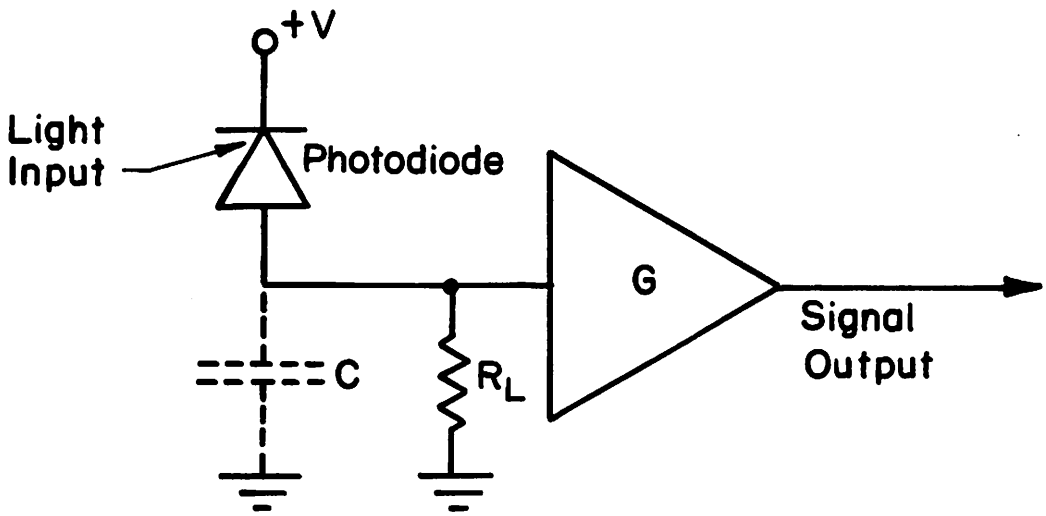

Conventional Amplifier

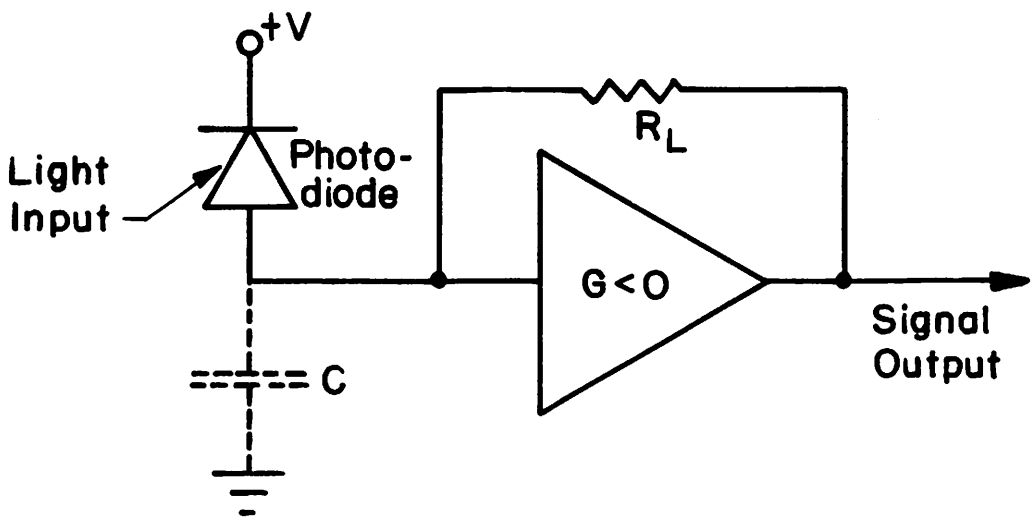

Transimpedance Amplifier

PHOTODIODE AMPLIFIERS

Figure D.1 Photodiode Amplifiers

ANALOG PROCESSOR
LEVEL CROSSING TEST

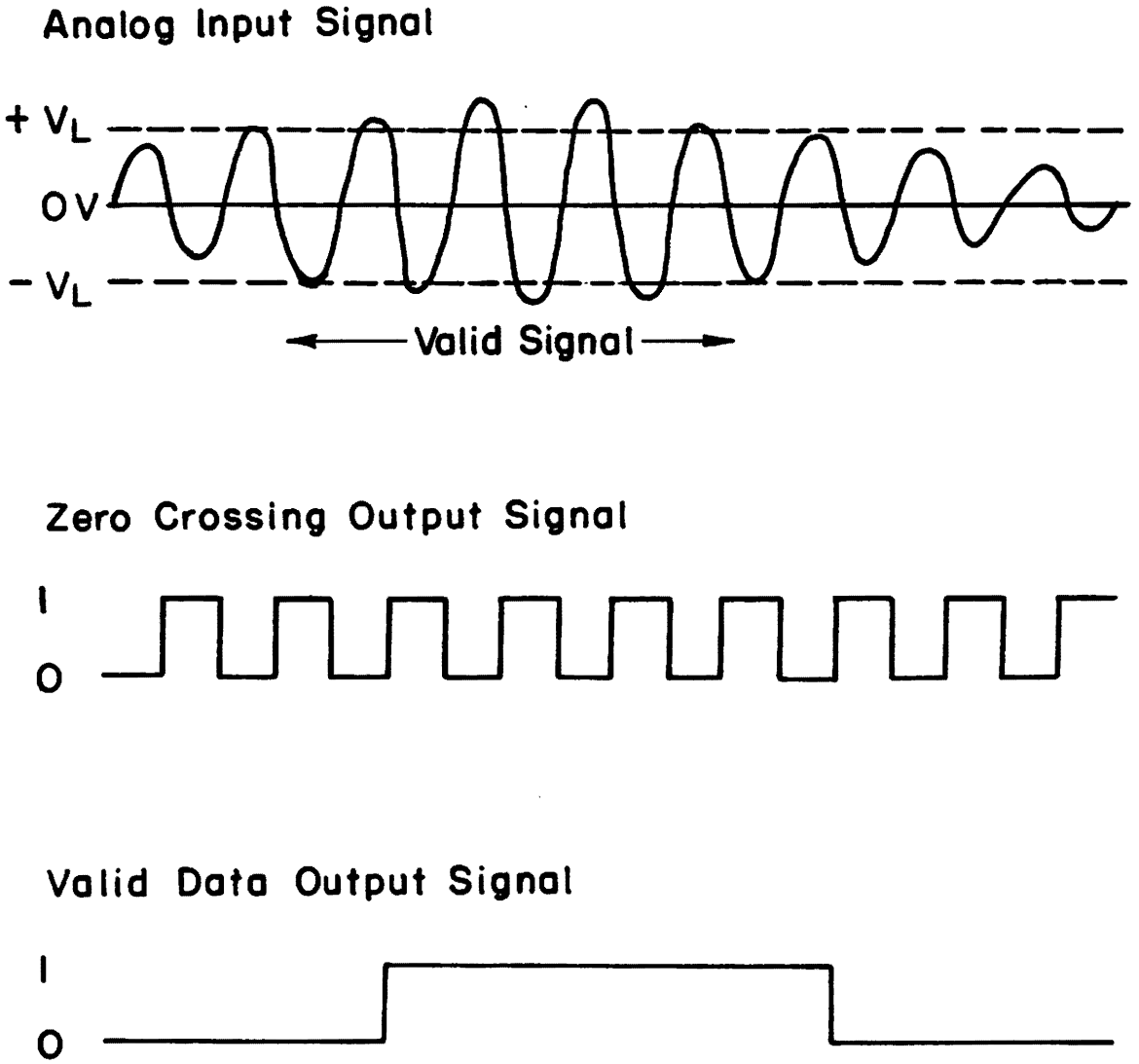

Figure D.2 Analog Processor Level Crossing Test

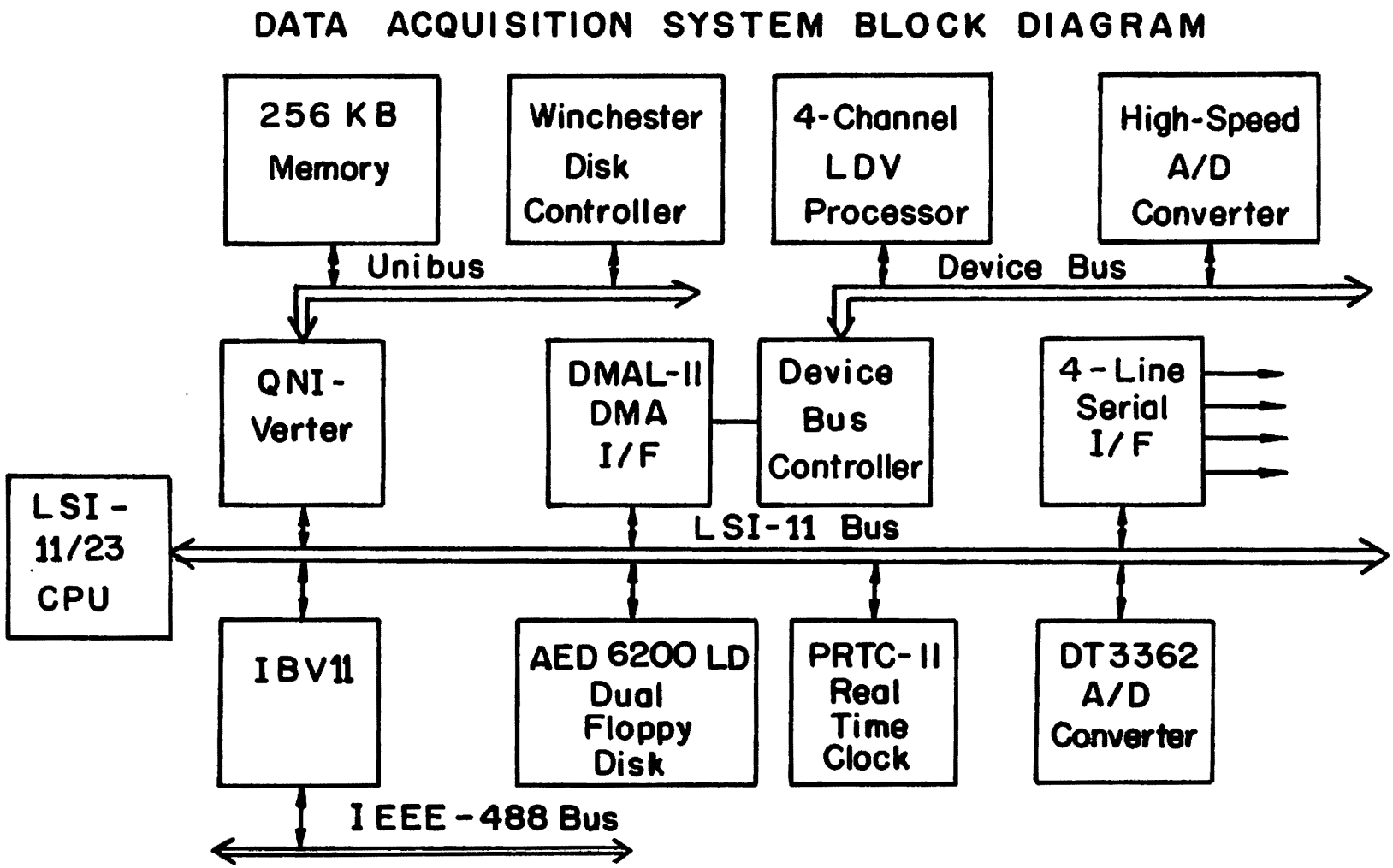

Figure E.1 Data Acquisition System Block Diagram

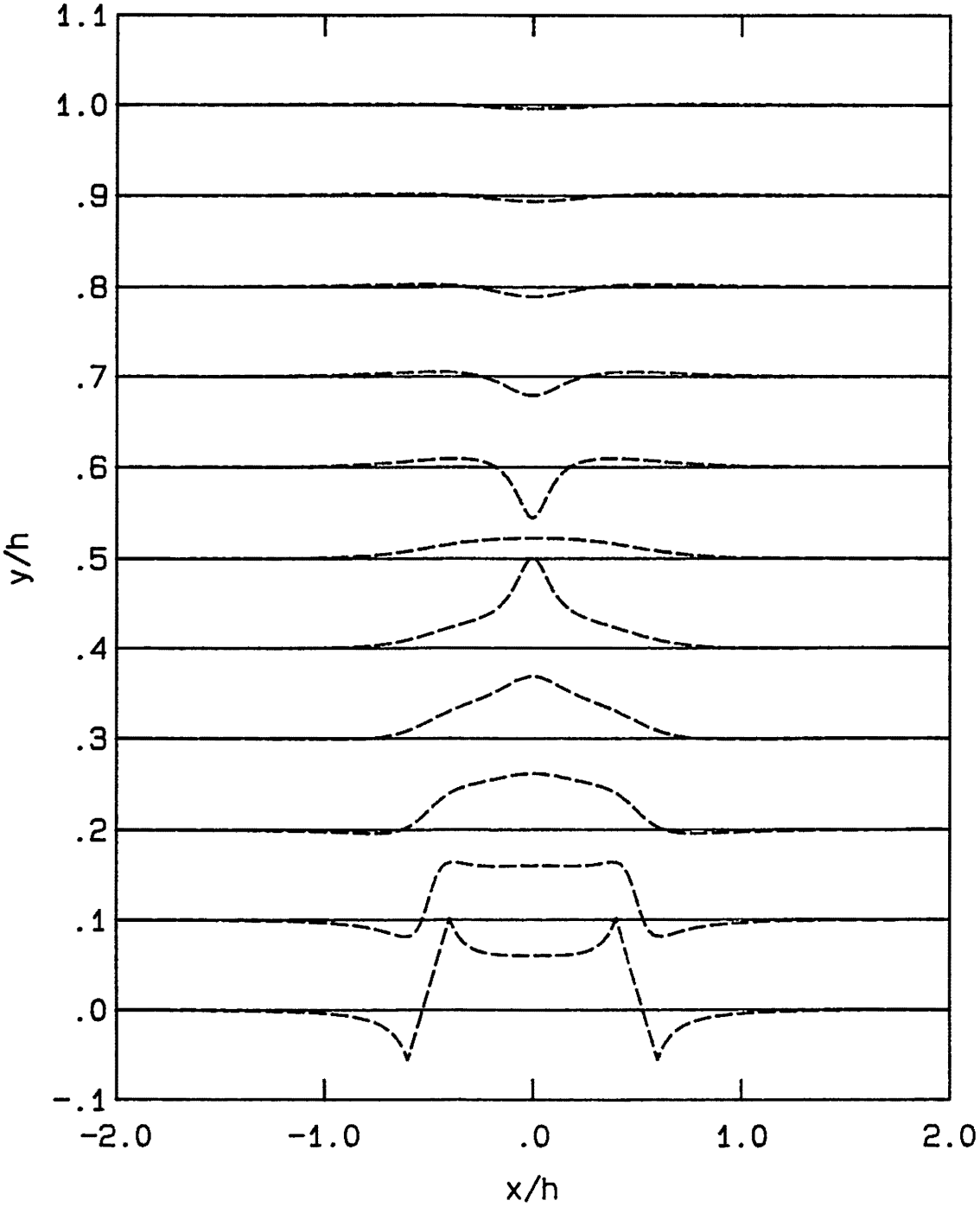

Figure F.1 Vortex Simulation, Unfiltered, $d_0 = 0.2h$

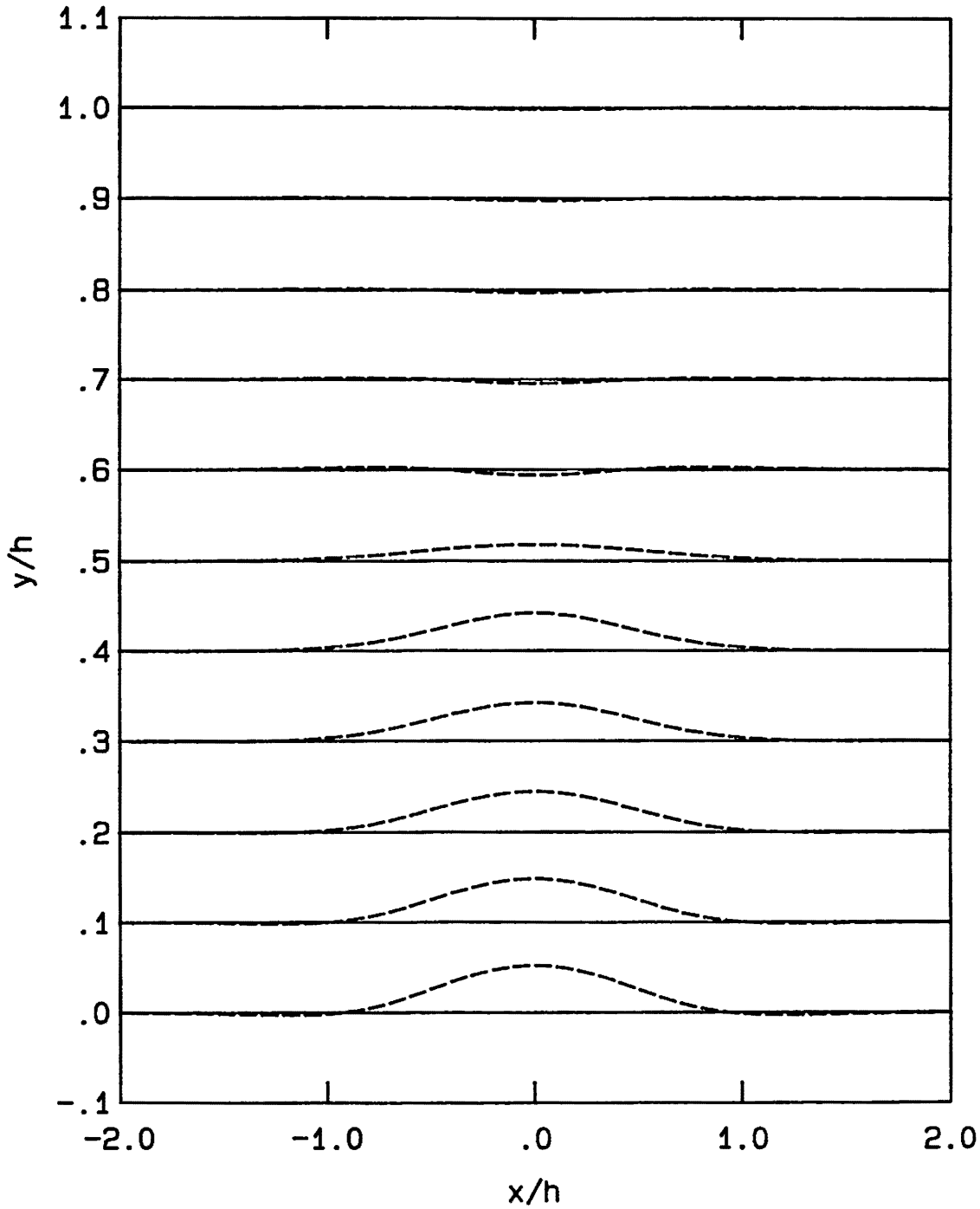

Figure F.2 Vortex Simulation, $\tau_f = h/\bar{u}$, $d_o = 0.2h$

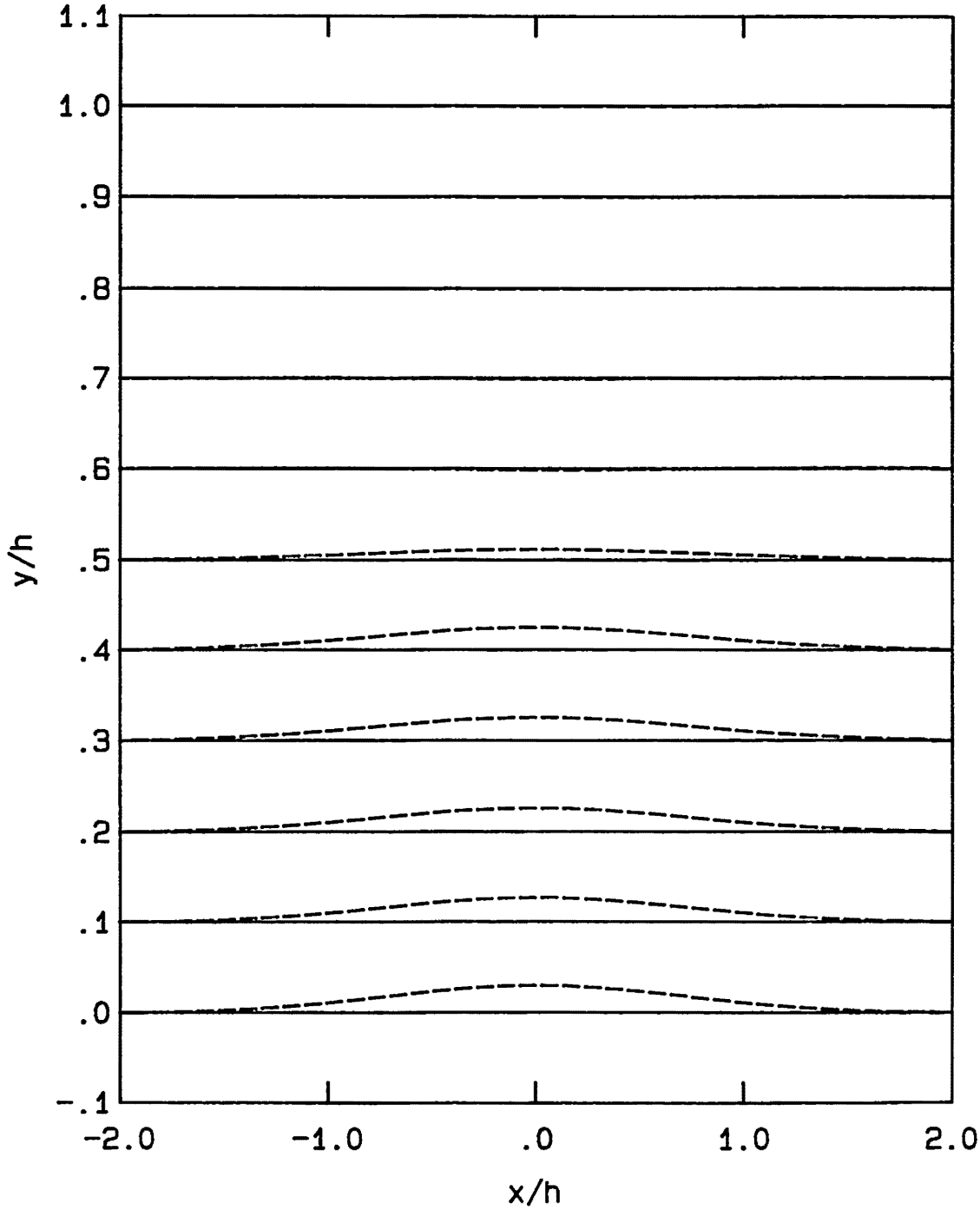

Figure F.3 Vortex Simulation, $\tau_f = 2h/\bar{u}$, $d_o = 0.2h$

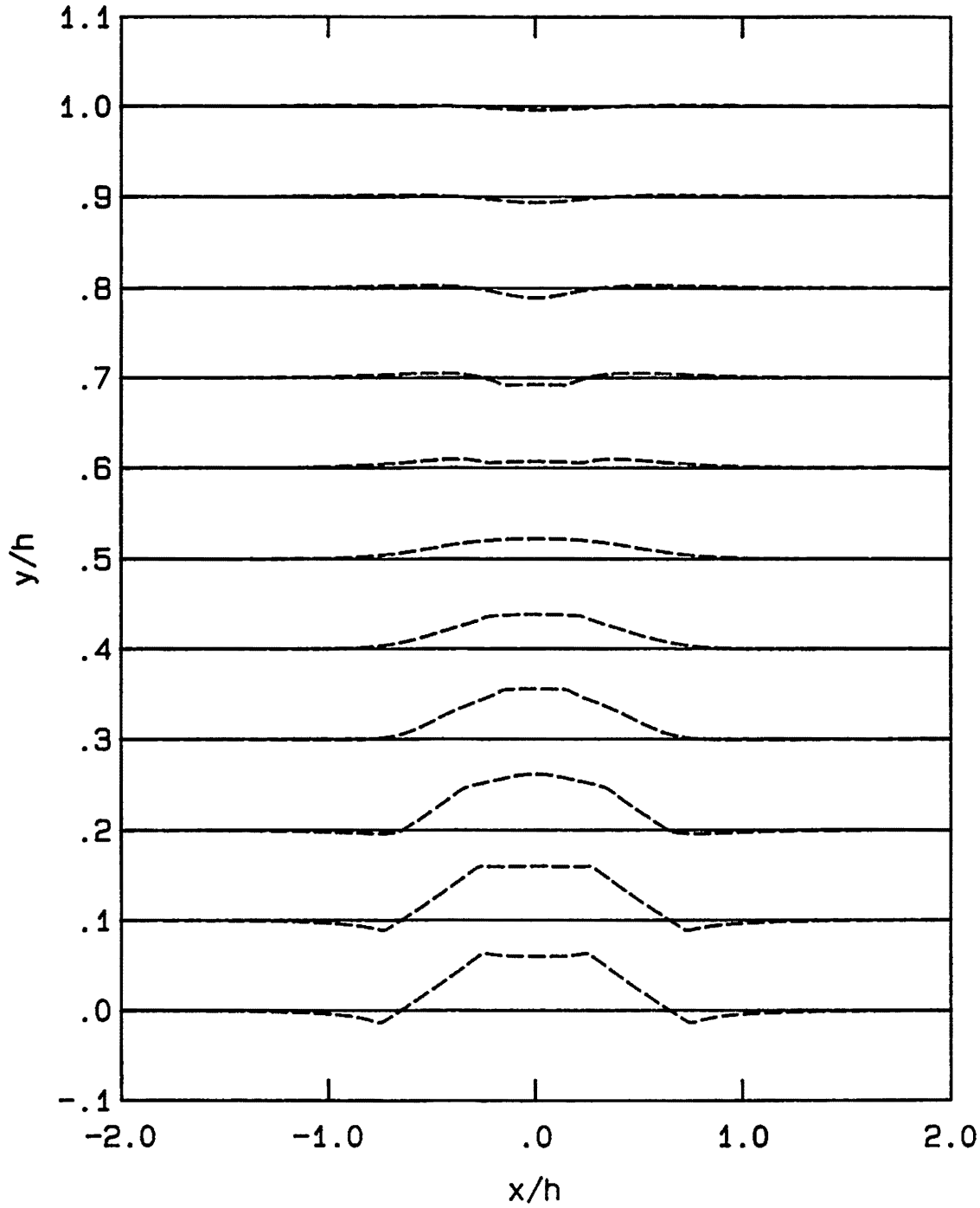

Figure F.4 Vortex Simulation, Unfiltered, $d_0 = 0.5h$

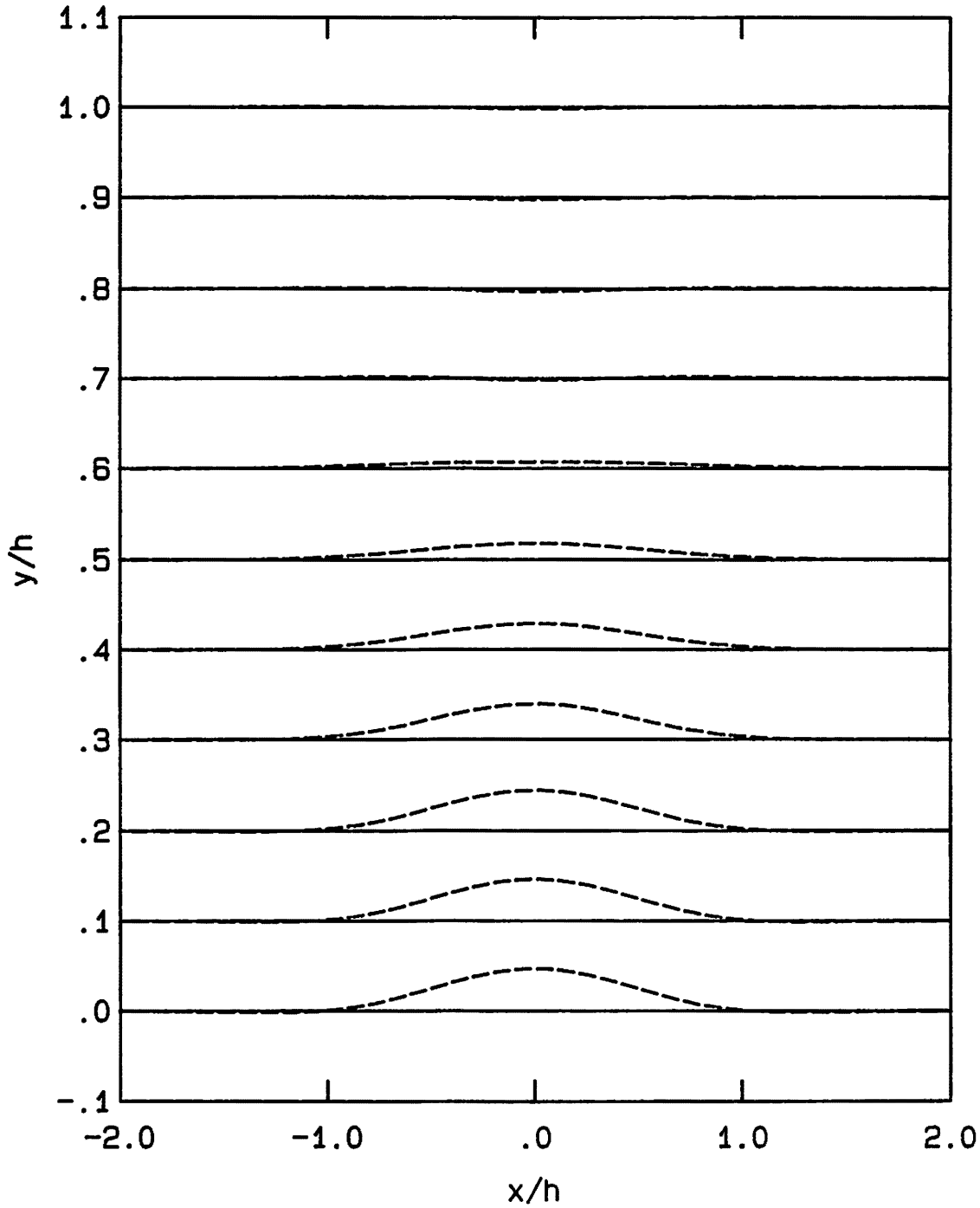

Figure F.5 Vortex Simulation, $\tau_f = h/\bar{u}$, $d_o = 0.5h$

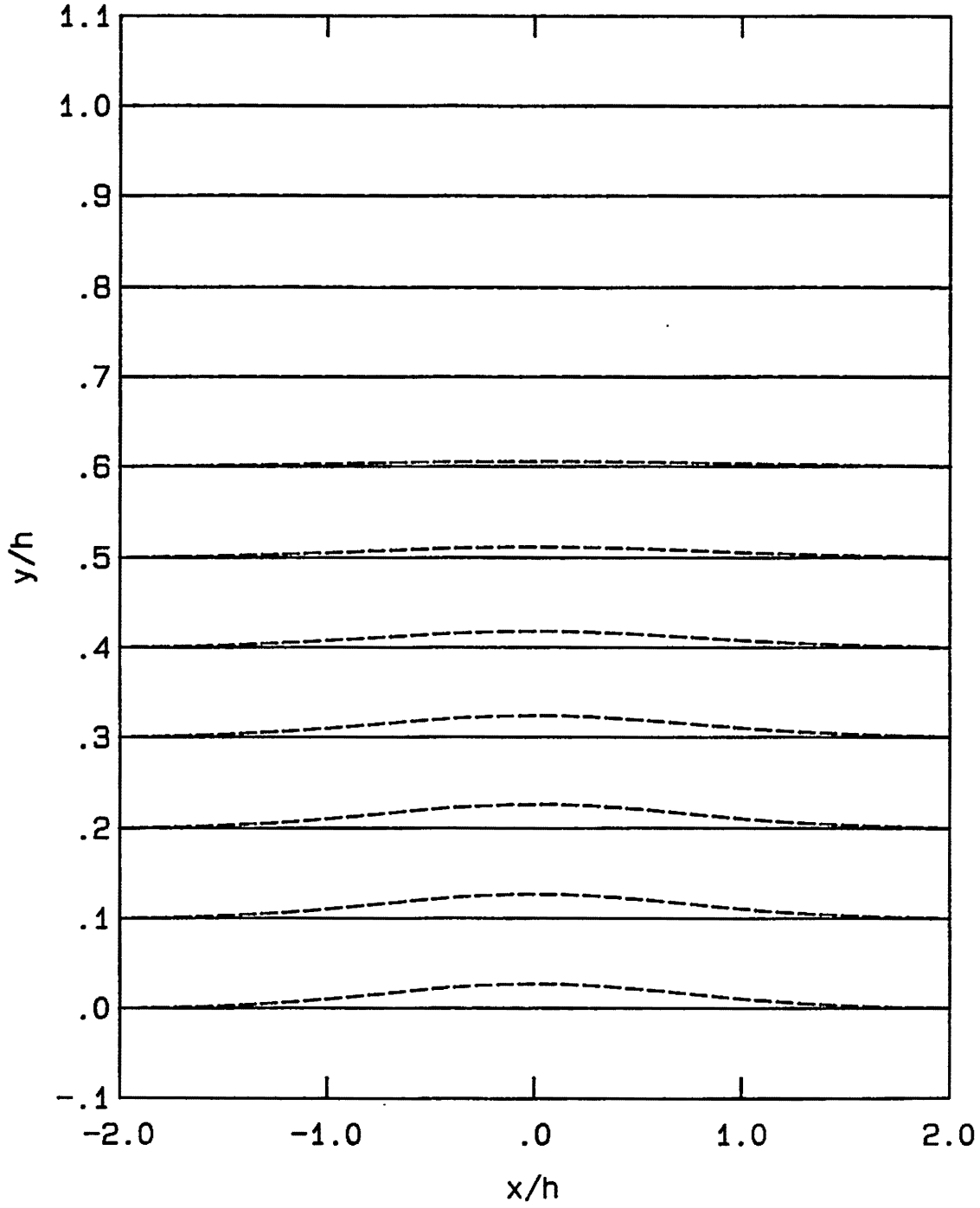

Figure F.6 Vortex Simulation, $\tau_f = 2h/\bar{u}$, $d_0 = 0.5h$

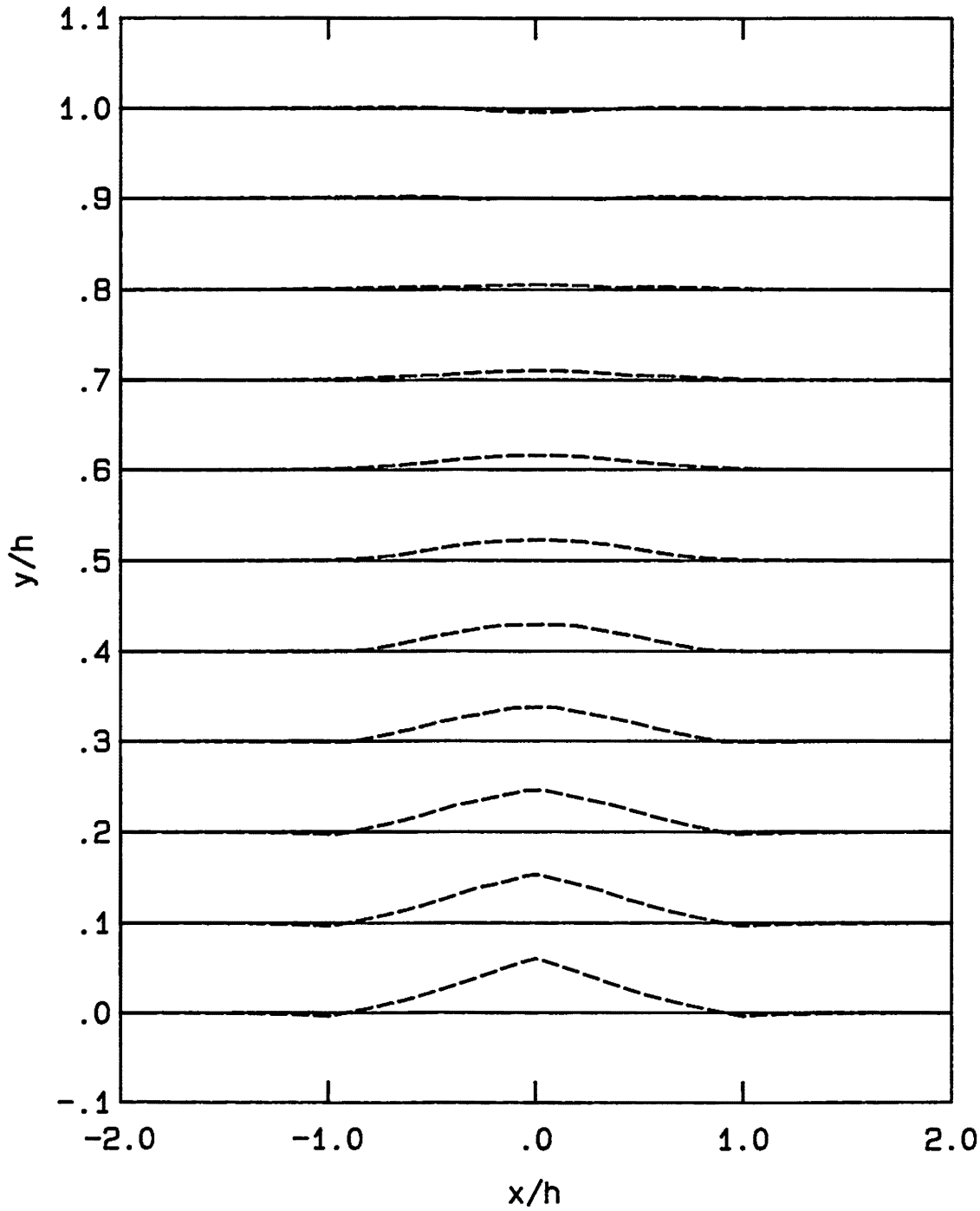

Figure F.7 Vortex Simulation, Unfiltered, d_o = 1.0 h

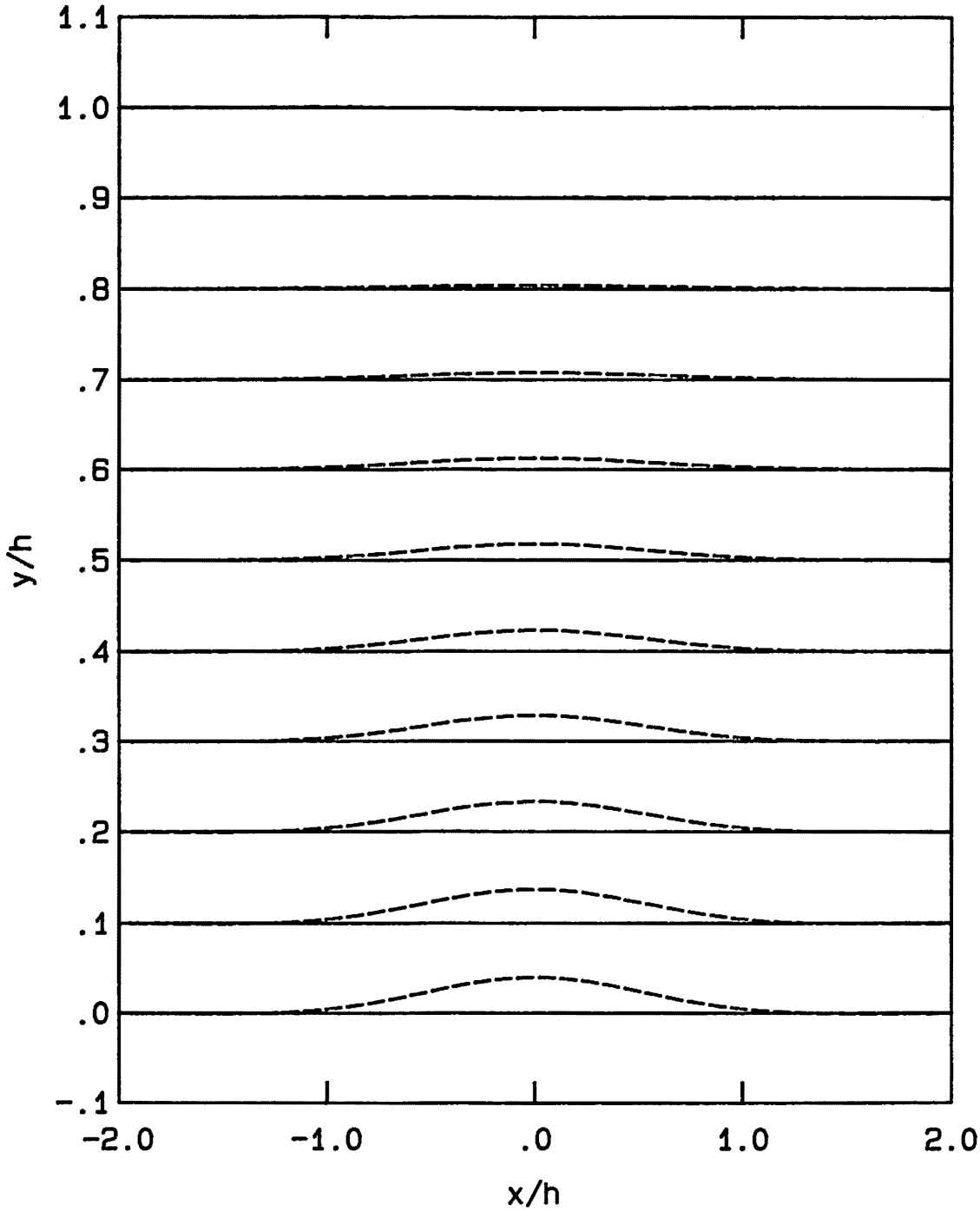

Figure F.8 Vortex Simulation, $\tau_f = h/\bar{u}$, $d_o = 1.0\,h$

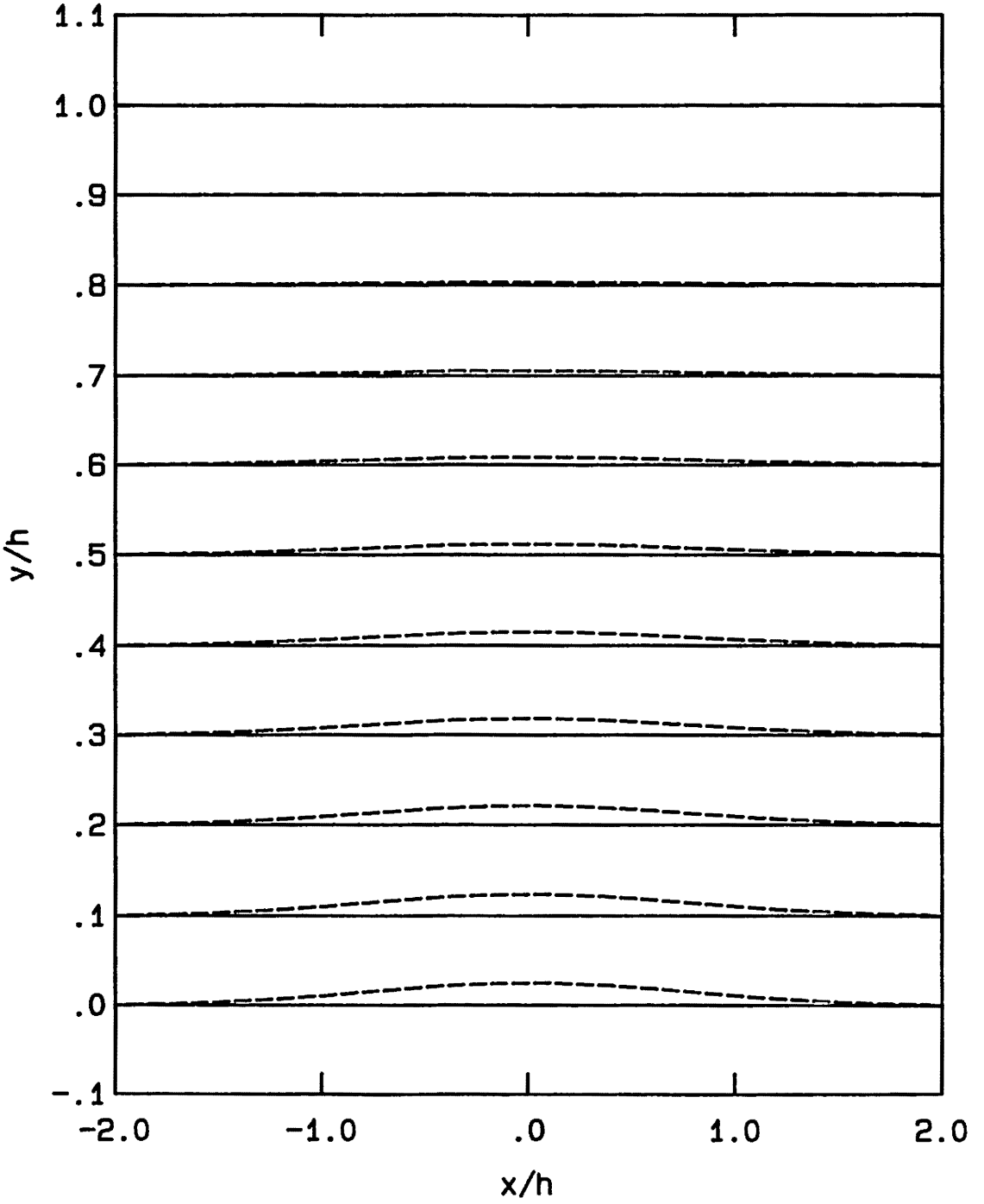

Figure F.9 Vortex Simulation, $\tau_f = 2h/\bar{u}$, $d_o = 1.0h$